ABSTRACT

Title of Document: DENSITY- AND WIND-DRIVEN LATERAL CIRCULATION AND THE ASSOCIATED TRANSPORT OF SEDIMENTS IN IDEALIZED PARTIALLY MIXED ESTUARIES

Shih-Nan Chen, Doctor of Philosophy, 2008

Directed By: Professor Lawrence P. Sanford
Horn Point Laboratory, UMCES
Marine Estuarine Environmental Science

Lateral circulation and the associated transport of sediments in idealized partially mixed estuaries are investigated using a three-dimensional, hydrostatic, primitive equation numerical model (ROMS). The model simulates a straight estuarine channel with a triangular cross-section. Attention is focused on lateral density (salinity) gradients, the major driving force for lateral circulation. Lateral salinity gradients can result from boundary mixing on a slope and differential advection of axial salinity gradients.

Without wind forcing, the numerical experiments suggest that boundary mixing on a slope can drive significant lateral circulation when the water column is stratified. Boundary mixing is at least as important as differential advection for the modeled scenarios, when the two mechanisms are evaluated using the salt balance

equation. Sediments are eroded in the channel and preferentially deposited on the right slope (looking seaward), mainly due to tidal pumping

Both stratification and axial salt transport show strong responses to axial wind forcing. While stratification is always reduced by up-estuary winds, stratification shows an increase-to-decrease transition as down-estuary wind stress increases, due to the competition between wind-induced straining of the axial salinity gradient and direct wind mixing. A horizontal Richardson number modified to include wind straining/mixing is shown to reasonably represent the transition. A regime classification diagram is proposed.

Axial winds also exert important controls on lateral circulation. When the water column mixes vertically, surface Ekman transport is not a significant contributor to lateral circulation. Instead, wind-induced differential advection of the axial salinity gradient establishes lateral salinity gradients that in turn drive lateral circulation. A Hansen-Rattray-like scaling shows good predictive skill for variations in lateral flow. Event-integrated sediment transport is from channel to shoals during down-estuary winds but reversed for up-estuary winds. Accounting for wind-waves results in an order-of-magnitude increase in lateral sediment fluxes.

The effects of wind-waves and seagrass beds on nearshore (< 2m) sediment dynamics are explored separately using a nearshore model (NearCoM). Without seagrass beds, wind-waves greatly enhance sediment resuspension, providing a large sediment source for lateral sediment transport. Seagrass beds attenuate wind-wave energy and trap sediments, thus reducing net sediment loss from the shallow shoal.

DENSITY- AND WIND-DRIVEN LATERAL CIRCULATION AND THE ASSOCIATED TRANSPORT OF SEDIMENTS IN IDEALIZED PARTIALLY MIXED ESTUARIES

By

Shih-Nan Chen

Dissertation submitted to the Faculty of the Graduate School of the
University of Maryland, College Park, in partial fulfillment
of the requirements for the degree of
Doctor of Philosophy
2008

Advisory Committee:
Professor Lawrence P. Sanford, Chair
Professor Shenn-Yu Chao
Professor Carl T. Friedrichs
Professor James T. Kirby
Professor Elizabeth North
Professor James A. Carton, Dean's Representative

Dedication

To my parents, sister, and Tzu-Hsuan

Acknowledgements

This work could never have been accomplished without assistance and encouragement from a large number of people. It has truly been a pleasure to work with my advisor, Larry Sanford, over the last five plus years. Larry gave me freedom to pursue my ideas, supported me along the way, and dragged me back on track in time when I drifted too far. I have also gained greatly from his knowledge and insight in fluid and sediment dynamics. I would like to thank my dissertation committee: Shenn-Yu Chao, Carl Friedrichs, Jeff Halka, Jim Kirby, and Elizabeth North. They have provided timely advice and guidance with patience and kindness throughout my graduate education. There are also a number of other faculty members at Horn Point who were not on my committee but were equally generous with their time and resources; particularly Ming Li, Victoria Coles, Bill Boicourt, Raleigh Hood, Evamaria Koch, and Mike Kemp. I also like to thank Jim Carton who served as Dean's representative during my defense.

Horn Point Laboratory has been a great place to work and study. I'd like to thank the Sanford group: Steve Suttles, Pat Dickhudt, Cindy Higgins, and Yong Kim. It was lots of fun working with you. I'm especially grateful to Steve who was my field work mentor. It was a pleasure to work with him. There are many good friends/roommates who have been cheering for me and significantly improved my English slang vocabulary: Jeremy Testa, Tom Wazniak, Caroline Wicks, Mike Mallonee, Dave Miller, Antti Koskelo (my climbing partner), Tim Carruthers, Jane Thomas, Chris Markin, etc. Many thanks go to the HPL basketball and soccer gangs.

I will miss playing with you. I'd also like to thank other students and staff who work with me during the Ian Morris event.

The Coastal and Estuarine Fluid Dynamics course at Friday Harbor Labs, University of Washington during the summer of 2006 was one of the most important courses in my graduate education. I'd like to thank Rocky Geyer and Parker MacCready for running the course. I have benefited greatly from their profound insights in fluid physics and their enthusiasm for science. My work also benefits from interactions with scientists and students outside Horn Point. They include Bob Chant, Mark Stacey, Malcolm Scully, Jim Lerczak, Dave Ralston, Rich Garvine, Steve Monismith, Arnoldo Valle-Levinson, and all of the students participating in the Friday Harbor course.

My most consistent supporters have always been my mom, dad, sister, Tzu-Hsuan, uncle Gary, aunts Enid, Lynn, and other family members. It did not matter if they were in Taiwan or in the US, they always cared about me and provided me with unqualified support.

Finally, I would like to thank Horn Point Education committee, Maryland Sea Grant, and the National Oceanographic Partnership Program for financial support.

Table of Contents

List of Tables

List of Figures

Chapter 1

Introduction

Lateral circulation is the flow across the primary flow direction. In an estuary this usually means flow across the channel axis. Its magnitude is usually an order of magnitude smaller than the primary axial flow. In spite of its smaller magnitude, lateral circulation plays an important role in estuarine transport processes. Lateral circulation has long been recognized as an effective means to redistribute scalars across estuaries. It thus facilitates lateral mixing which, along with laterally sheared axial flow, drives shear dispersion (Fischer et al. 1979). Dispersion can influence water quality and contaminant/sediment transport in estuarine and coastal waters by controlling the distribution of waterborne materials. More fundamentally, dispersion plays a role in determining the overall estuarine salt budget and thus sets the along-channel (axial) salinity gradient. The axial salinity gradient then drives the estuarine circulation that is often the dominant estuarine transport process. In addition, recent studies have revealed that the advection of momentum by lateral circulation contributes at a leading order to the subtidal, axial momentum balance (Lerczak and Geyer 2004; Scully et al. submitted).

1.1 Driving mechanisms for lateral circulation

When only considering tidal forcing, lateral circulation can be driven by four principal mechanisms. They are: Ekman veering in the bottom boundary layer (Johnson and Ohlsen 1994; Ott and Garrett 2002); centrifugal acceleration in a curved estuarine channel (Kalkwijk and Booij 1986; Chant and Wilson 1997; Lacy and Monismith 2001); boundary mixing on a slope (Phillips 1970; Phillips et al. 1986); and differential advection of the axial salinity gradient (Nunes and Simpson 1985).

These mechanisms may be tentatively categorized into two classes: nondensity- and density-driven. The first two are nondensity-driven, as they rely on axial flow, friction, and Earth rotation or channel geometry. The nondensity-driven lateral circulations result from an imbalance between a weaker Corilois /centrifugal force near the bottom due to friction and a lateral pressure gradient force. The last two, on the other hand, are density-driven. The boundary mixing mechanism requires stratification and near-bottom mixing. On a sloping bottom, isohalines have to be perpendicular to the slope to satisfy a zero normal salt flux. The bending of isohalines then creates a lateral salinity gradient to drive up-slope lateral flows. Differential advection relies on the presence of lateral shear and axial salinity gradient. The depth-averaged tidal currents tend to be stronger in the channel, which generates lateral shear. During floods, for example, the lateral shear advects high salinity water further up-estuary in the channel, creating a lateral salinity (density) gradient to drive lateral circulation. It should be noted that the lateral circulation, whether it is nondensity- or density-driven, will likely interact with salinity field to modify lateral salinity gradient. For example, in stratified flow the Ekman- and centrifugal-forced lateral circulation can tilt the isohalines to generate an adverse salinity gradient that suppresses any further tilting (Chant and Wilson 1997; Lerczak and Geyer 2004). Such feedback effects are complex and are generally not well understood.

The driving mechanisms for lateral circulation are not mutually exclusive. Instead, some of them co-exist and may interact. Therefore, discerning the relatively importance of these mechanisms in different systems is important to advance our understanding of lateral dynamics. In homogeneous systems in which density effects

are not present, Ekman veering and centrifugal acceleration are expected to dominate lateral dynamics (Mied et al. 2002; Kalkwijk and Booij 1986). When an axial salinity gradient is present and the water column is weakly stratified, Lerczak and Geyer (2004) demonstrated that, for a straight channel with a parabolic-shaped cross-section, differential advection and Ekman veering both drive significant amount of lateral circulation while the contribution from boundary mixing is insignificant. When the system is more stratified, however, the principal driving mechanisms are less clear.

Contrasting with the active research on tidally-forced processes, wind-driven lateral processes have received little attention to date in the estuarine literature. Winant (2004) and Sanay and Valle-Levinson (2005) investigated the wind-driven lateral circulation under the simplest possible condition: axial wind forcing over a homogeneous channel. They found that the major clockwise circulating pattern (looking seaward; northern hemisphere) is consistent with Ekman dynamics. However, when salt is present, wind-driven lateral dynamics are largely unknown. While the Ekman veering is still anticipated to drive lateral circulation, in theory wind-driven axial flow interacting with the axial salinity gradient can potentially provide another mechanism. Wind-driven axial flow over laterally varying bathymetry is laterally sheared, with downwind flow on the shoal and upwind flow in the channel (Csanady 1973; Wong 1994). Thus, like tidally-forced differential advection, laterally sheared, wind-driven axial flow can advect the existing axial salinity gradient to create lateral salinity gradients and in turn drive lateral circulation.

Neither the validity of this mechanism nor the influences of stratification and tides on wind-driven lateral circulation have been systematically investigated.

1.2 Lateral sediment dynamics

Lateral circulation can also transport suspended sediments across estuaries. Over tidal time scales, this lateral sediment movement along with axial flow can impact the net axial sediment transport. Over geological time scales, the lateral entrapment of suspended sediment by lateral flow combined with sedimentation may affect channel morphology that could ultimately exert controls on the lateral flow itself. Despite these important implications, very few studies have addressed the effects of lateral circulation on suspended sediment transport. Geyer et al. (1998) observed a turbidity maximum zone skewed toward the right bank (looking seaward) of the Hudson River estuary. This lateral focusing of suspended sediments was explained by the convergence of lateral flows. Fugate et al. (2007) studied lateral sediment dynamics near the salt intrusion in the upper Chesapeake Bay. The found that the ebb intensified lateral circulation tended to focus sediment toward the left shoal, contrary to Geyer et al. (1998)'s findings. Huijts et al. (2006) proposed an analytical model to assess the relative importance of Ekman veering and lateral salinity gradients in lateral sediment trapping. Although the analytical model allows thorough sensitivity analyses, it is somewhat limited because it relies on a prescribed lateral salinity gradient and thus neglects the dynamical feedbacks between salinity and flow fields.

The limited work on lateral sediment transport described above considered only tidal forcing. The roles of wind forcing on lateral sediment transport are largely overlooked. Taking Chesapeake Bay as an example, several field surveys reported higher sedimentation rates in the channel, and the surficial sediment distribution showed a general pattern of a muddy channel with sandy shoals (Kerhin et al. 1988; Colman et al. 1992). Episodic wind events with concurrent wind-wave action on shallow shoals have been hypothesized as an important mode to transport fine sediments across estuary and finally deposit in the channel (Langland and Cronin 2003). However, this hypothesis has not yet been tested, and lateral sediment transport associated with wind events has not been quantified.

1.3 Dissertation outline

The objective of this dissertation work is to explore the driving mechanisms for lateral circulation and the associated transport of suspended sediments in partially mixed estuaries under various forcing conditions. Following Lerczak and Geyer (2004), numerical models with idealized forcings and bathymetries (generic triangular cross-section) are used to carry out process-based experiments. This approach is complementary to analytical models, as it addresses the questions in a fully 3D fashion but still retains some degree of simplicity.

The scope of this work focuses on the creation of lateral salinity gradients and their effects on lateral circulation and sediment transport under tidal and axial wind forcings. The dissertation is organized as follows. Chapter 2 considers only tidal forcing. Chapter 3 and 4 take axial wind forcing into account. Chapter 3 focuses on

how wind-induced straining and mixing exert controls on stratification and axial salt transport. Chapter 4 investigates the importance of stratification and the wind-induced axial salt transport in regulating lateral salinity gradients that in turn drive lateral circulation. The net lateral sediment transport over the wind events is quantified. Two representative cases demonstrating the effects of wind-waves on lateral sediment transport are also presented. In chapter 5, the influences of wind-generated waves and seagrass beds on nearshore sediment dynamics are explored separately using a coupled wave-circulation-sediment model. Finally, a brief summary is given in Chapter 6.

References

Chant, R. J. and E. Wilson, 1997: Secondary circulation in a highly stratified estuary. *Journal of Geophysical Research*, **102,** 23207-23216.

Colman, S. M., J. P. Halka, and C. H. Hobbs, 1992: Patterns and rates of sedimentation in the Chesapeake Bay during the Holocene Rise in sea level, 101-111 pp.

Csanady, G. T., 1973: Wind-induced barotropic motions in long lakes. *Journal of Physical Oceanography*, **3,** 429-438.

Fischer, H. B., E. J. List, R. C. Y. Koh, J. Imberger, and N. A. Brooks, 1979: *Mixing in inland and coastal waters*. Academic Press Inc.

Fugate, D. C., C. T. Friedrichs, and L. P. Sanford, 2007: Lateral dynamics and associated transport of sediments in the upper reaches of a partially mixed estuary, Chesapeake Bay, USA. *Continental Shelf Research*, **27,** 679-698.

Geyer, W. R., R. P. Signell, and G. C. Kineke, 1998: Lateral trapping of sediment in a partially mixed estuary. *Physics of Estuaries and Coastal Seas*, Balkema.

Huijts, K. M. H., H. M. Schuttelaars, H. E. de Swart, and A. Valle-Levinson, 2006: Lateral entrapment of sediment in tidal estuaries: An idealized model study. *Journal of Geophysical Research*, **111,** C12016, doi:10.1029/2006JC003615.

Johnson, G. C. and D. R. Ohlsen, 1994: Frictionally modified rotating hydraulic channel exchange and ocean outflows. *Journal of Physical Oceanography*, **24,** 66-78.

Kalkwijk, J. P. T. and R. Booij, 1986: Adaptation of secondary flow in nearly-horizontal flow. *Journal of Hydraulic Engineering*, **24,** 19-37.

Kerhin, R., J. Halka, D. V. Wells, E. L. Hennessee, P. J. Blakeslee, N. Zoltan, and R. H. Cuthbertson, 1988: The Surficial Sediments of Chesapeake Bay, Maryland: Physical Characteristics and Sediment Budget. Investigation Report 48, 43 pp.

Lacy, J. R. and S. G. Monismith, 2001: Secondary currents in a curved, stratified, estuarine channel. *Journal of Geophysical Research*, **106,** 31283-31302.

Langland, M. and T. M. Cronin, 2003: A summary report of sediment processes in Chesapeake Bay and watershed. U. S. G. S. W. R. I. R. 03-4123, Ed.

Lerczak, J. A. and W. R. Geyer, 2004: Modeling the lateral circulation in straight, stratified estuaries. *Journal of Physical Oceanography*, **34**.

Mied, R. P., R. A. Handler, and T. F. Donato, 2002: Regions of estuarine convergence at high Rossy number: A solution in estuaries with elliptical cross sections. *Journal of Geophysical Research*, **107**.

Nunes, R. A. and J. H. Simpson, 1985: Axial convergence in a well-mixed estuary. *Estuarine, Coastal, and Shelf Science*, **20,** 637-649.

Ott, M. W. and C. Garrett, 2002: Frictional estuarine flow in Juan de Fuca Strait with implications for secondary circulation. *Journal of Geophysical Research*, **103,** 15657-15666.

Phillips, O. M., 1970: On flows induced by diffusion in a stably stratified fluid. *Deep Sea Research*, **17,** 435-443.

Phillips, O. M., J. Shyu, and H. Salmun, 1986: An experiment on boundary mixing: mean circulation and transport rates. *Journal of Fluid Mechanics*, **173,** 473-499.

Sanay, R. and A. Valle-Levinson, 2005: Wind-induced circulation in semienclosed homogeneous, rotating basins. *Journal of Physical Oceanography*, **35,** 2520-2531.

Winant, C. D., 2004: Three-dimensional wind-driven flow in an elongated, rotating basin. *Journal of Physical Oceanography*, **34,** 462-476.

Wong, K. C., 1994: On the nature of transverse variability in a coastal plain estuary. *Journal of Geophysical Research*, **99,** 14,209-14,222.

Chapter 2

Lateral Circulation Driven by Boundary Mixing and the Associated Transport of Sediments in Idealized Partially-Mixed Estuaries[1]

[1]Chen, S.N., Sanford, L.P., 2008. Lateral circulation driven by boundary mixing and the associated transport of sediments in idealized partially-mixed estuaries. Continental Shelf Research, doi:10.1016/j.csr.2008.01.001

Abstract

A three-dimensional, hydrostatic, primitive equation numerical model with modern turbulence closures is used to explore lateral circulation and the associated transport of sediments in idealized, moderately to highly stratified estuaries. The model results suggest that boundary mixing on a sloping bottom can drive a significant amount of lateral circulation. This mechanism has received little attention to date in the estuarine literature. Good agreement with an analytical solution and similar vertical structures of lateral flows to observations from the Hudson River estuary support the importance of the boundary mixing mechanism. Boundary mixing is at least as important as differential advection for the modeled scenarios, when the two mechanisms are evaluated using the salt balance equation for model runs without rotation. Linearly superposing analytical solutions for lagged boundary mixing lateral flow and Ekman-forced lateral flow yields a good representation of the near-bottom lateral flow from the model with rotation. The 2hr lag required for the boundary mixing solution is roughly equal to the vertical diffusion time scale, indicating that lateral flow adjustment depends on development of a bottom mixed layer. Sediment dynamics at cross-sections seaward and landward of the salt intrusion are very different. Seaward of the salt intrusion, sediments are eroded in the channel and preferentially deposited on the right slope (looking seaward), mainly due to the combination of high sediment concentration in the channel during flood with strong upslope transport on that side (tidal pumping). Lateral sediment re-distribution landward of the salt intrusion is negligible due to weak residual lateral circulation.

1. Introduction

Lateral circulation in estuaries results in an exchange of water masses in the cross-channel direction. Despite its typically smaller magnitude compared with along-channel flow, lateral circulation is important for transport processes in estuarine environments. As noted by Fischer (1972) and Smith (1980), it can enhance along-channel dispersion of salt and other tracers and thus can affect the overall salt budget in estuaries. The salt budget in turn determines the along-channel density gradient which ultimately drives estuarine circulation. Lateral circulation can also affect sediment dynamics (Geyer et al., 1998; Woodruff et al., 2001; Huijts et al., 2006; Fugate et al., 2007). Geyer et al. (1998), for example, observed a turbidity maximum zone skewed toward the west side of the Hudson River estuary. Such cross-channel variations were explained by the convergence of lateral flows.

There are various mechanisms that can potentially drive lateral circulation in estuaries. For a straight and stratified estuarine channel, potential driving mechanisms (following the terms defined by Lerczak and Geyer, 2004) are: interactions between barotropic tides and cross-channel variations in bathymetry (Li and O'Donnell, 1997; Li and Valle-Levinson, 1999; Valle-Levinson et al., 2000), Coriolis forcing (Kalkwijk and Booij, 1986; Johnson and Ohlsen, 1994; Ott and Garrett, 2002), differential advection of along-channel density gradients (Smith, 1980; Nunes and Simpson, 1985; Huzzey and Brubaker, 1988), and boundary mixing on a sloping bottom (Wunsch, 1970; Phillips, 1970). Among these, the boundary-mixing mechanism originally proposed for deep ocean mixing has received the least attention. Lerczak and Geyer (2004) used a numerical model to explore the relative importance of the

mechanisms described above under varying stratification. They reported that the contribution from boundary mixing is relatively weak, compared with differential advection and Ekman veering in a well-mixed system. There are also very few observations of boundary mixing in estuarine flows, due in part to the required high resolution of the bottom boundary layer. Phillips et al. (1986) reported a persistent lateral flow from the boundary to the interior at mid-depth (near the halocline), which is consistent with the lateral flow patterns driven by boundary mixing. However, due to limited data, the indication was not conclusive.

Recently, discerning the relative importance of these different mechanisms in different systems has received increasing attention. In a straight, homogeneous tidal channel with mild depth variations, Coriolis forcing that drives lateral flows by veering of the mean along-channel current in the bottom Ekman layer dominates lateral dynamics (e.g. Mied et al., 2002). Differential advection of along-channel density gradients that sets up transverse density gradients and drives bottom divergent lateral flows during flood has been argued to govern lateral dynamics in vertically-mixed systems (Lerczak and Geyer, 2004). In estuaries with strong vertical stratification, however, the main driving mechanisms are less clear.

In this paper, our objectives are to (1) demonstrate that boundary mixing on a sloping bottom can be an important mechanism to drive lateral circulation in moderate to highly stratified estuaries and to (2) explore the associated transport of sediments. Following Lerczak and Geyer (2004)'s approach but using modern turbulence closures, we use a numerical model to investigate lateral dynamics. This paper is organized in the following manner: the boundary mixing process on a slope

is reviewed in section 2. The numerical model is described in section 3. In section 4, evidence is provided for the importance of lateral circulation driven by boundary mixing on a sloping bottom. In section 5 and 6, temporal and spatial variations in flow structure and in sediment dynamics are presented, followed by discussion and conclusions in section 7. Comparison of boundary mixing and differential advection as drivers of lateral circulation is deferred to section 7.1.

2. Boundary mixing on a sloping bottom

In a stratified basin with a sloping bottom, isohalines near the bottom have to be perpendicular to the slope so that net salt flux vanishes at the boundary (no-flux boundary condition):

$$k \left. \frac{\partial \rho}{\partial n} \right|_{z=-H} = 0, \qquad (1)$$

where k is eddy diffusivity (assumed to be non-zero), n is the direction normal to the slope, and ρ is the density of fluid. The tilted isohaline near the bottom then sets up a baroclinic pressure gradient that drives up-slope flows (Wunsch, 1970; Phillips, 1970; Weatherly and Martin, 1978)(Fig. 1). The simplest case is without Coriolis forcing as shown in Fig. 1a, where up-slope flows require compensating return flows from boundary to interior, tending to destratify the fluid. This process occurs during both tidal phases, often forming persistent counter-rotating cells. Including Coriolis forcing adds another layer of complexity. As Fig. 1b shows, during ebbs the isohalines are tilted opposite to the surface tilt, and the ebbing currents induce an up-slope Ekman flow on the left slope looking toward the ocean (down-slope Ekman flow on the right). As a result, up-slope flows on the left are strengthened as the

boundary-mixing-driven (denoted by V_B in Fig. 1b) and the Ekman-driven (denoted by V_E) flows act in concert, whereas up-slope flows on the right are weakened.

The interactions between the boundary-mixing-driven and Ekman-driven flows also influence mixing in the bottom boundary layer. On the right slope during ebbs, for example, the Ekman-forced, down-slope flows are against the boundary-mixing-driven, up-slope flows, leading to flow convergence and possible static instability (Garrett et al., 1993). As a result, the boundary layer and halocline may get thicker. The thicker bottom boundary layer on the right slope during ebbs is dynamically equivalent to what Lentz and Trowbridge (1991) observed during downwelling-favorable flows on the California shelf. These patterns alternate sides when the tide turns.

Both steady state and time-dependent boundary mixing solutions have been derived and applied to shelf seas by several authors (Wunsch, 1970; Weatherly and Martin, 1978; Trowbridge and Lentz, 1991; MacCready and Rhines, 1993; Garrett et al., 1993). With constant eddy viscosity and a turbulent Prandtl number of one (e.g. Garrett et al., 1993), the maximum (vertically), steady-state, up-slope flow (V_B) near the bottom is

$$V_B \approx 0.64 A_v q \cot\theta, \tag{2}$$

where A_v is eddy viscosity, θ is the angle of the sloping bottom with horizon, and q is equivalent to the inverse boundary layer thickness

$$q^4 = \frac{1}{4A_v^{\,2}}(f^2 + N^2 \sin^2\theta), \tag{3}$$

where f is the Coriolis frequency, and N is the background buoyancy frequency. The strength of up-slope flow apparently depends on mixing, stratification in the interior,

and the angle of the slope. Time dependent behavior is important in the stratified interior away from strong boundary frictional effects (e.g. MacCready and Rhines, 1993). However, in subsequent applications of eqs. 2 and 3 in this paper (for comparison to numerical model predictions), we assume a quasi-steady balance within the bottom boundary layer with slowly varying eddy viscosity and stratification.

3. Numerical model

We use the Regional Ocean Model System (ROMS; Haidvogel et al., 2000) to simulate an idealized estuarine channel. ROMS is a hydrostatic, primitive equation model using a curvilinear grid in the horizontal and a stretched, terrain-following coordinate in the vertical. The model domain mimics an estuary-shelf system (Fig. 2). The size of the shelf sea is 50 km across shelf x 48 km along-shelf with a constant slope from 200 m at the offshore boundary to 1 m at the shoreline. A straight, 3.6 km-wide estuarine channel intersects the shelf and extends from x=50 km to 1000 km. The cross-section is triangular shape with a maximum depth of 14 m in the channel and a minimum depth of 1m on the sides. The grid configuration is 192 (along-channel, x-direction) x 101 (cross-channel, y-direction) x 15 (vertical levels). The vertical levels are stretched to have higher resolution near the surface and the bottom (lowest near bottom vertical resolution is 0.6 m). The section of the estuarine channel from the mouth to 150 km is more highly resolved ($\Delta x \sim$ 1 km, $\Delta y \sim$ 200 m). Outside of this area, the grid is telescoped toward the river end ($\Delta x \sim$ 48 km) to obtain a long

channel and along the shelf sea coast ($\Delta y \sim 1.5$ km) to obtain a bigger salt pool on the shelf without increasing computational cost.

The model is forced by M2 tides from the shelf boundaries using the Chapman condition for free-surface and the Flather condition for depth-averaged, boundary-normal velocity (Marchesiello et al., 2001) and by constant freshwater fluxes from the river end. The long channel dissipates tidal energy and thus minimizes reflection of tidal waves, resulting in progressive tides with current amplitude of 0.4 m sec^{-1} in the domain of interest. A weak coastal current (~ 0.05 m sec^{-1}) is specified on the shelf to transport the resulting river plume. Temperature is fixed at 15º C throughout the domain. Salinity at the river end is set to 0, whereas at the shelf boundaries salinity is nudged to an oceanic value of 32. The initial salinity of the shelf water is 32, while the initial salinity of the channel gradually decreases from 32 to 0 from the estuary mouth to the river head. The salt field reaches a steady structure periodically modulated by tides in about 6 days. We found that including a shelf sea in the simulation is beneficial because it avoids specifying estuary mouth boundary conditions that are not known a priori and helps stabilize the salinity structure in the estuarine channel.

We use the $k-\varepsilon$ turbulence closure (Jones and Launder, 1972) with a stability function proposed by Canuto et al. (2001). The $k-\varepsilon$ closure has been shown to perform well for estuarine flows (Burchard and Baumert, 1998; Warner et al., 2005b). Bottom stress is computed by assuming a logarithmic velocity profile in the lowest computational cell and a constant bottom roughness parameter (z_0). The background eddy viscosity and eddy diffusivity are both set to 8×10^{-5} m^2 sec^{-1}. The reason we

use this rather high background value is to obtain a reasonable salt intrusion length (L=128 km for the moderately stratified case). Given the relative weak tidal current of 0.4 m sec^{-1} and freshwater velocity of 0.01 m sec^{-1}, which resembles low-flow conditions in Chesapeake Bay, using a lower background diffusivity of 5 x 10^{-6} m^2 sec^{-1} leads to an unrealistic salt intrusion length of 300 km. While the salt intrusion length is sensitive to background diffusivity, we will show later that the lateral circulation is insensitive to it (section 4.2).

We also incorporate a single layer, single grain size (0.01 mm silt) sediment bed for exploring lateral transport of sediments (section 6). The suspended sediment transport module used here was described, implemented, and tested by Warner et al. (2005b) and Warner et al. (2007) as a part of the Community Sediment Transport Modeling project (CSTM). Flocculation and bed consolidation are excluded for the sake of simplicity. The sediment bed layer is sufficiently thick so that sediment is never depleted. The erosion formulation is the Ariathurai-Partheniades type, and the deposition formulation assumes no critical stress for deposition (e.g. Sanford and Halka, 1993):

$$\begin{aligned} E &= E_0(1-\phi)(\frac{\tau_b}{\tau_c}-1), \\ D &= w_s C \end{aligned} \qquad (4)$$

where E and D are erosion and deposition rate (kg m^{-2} sec^{-1}), E_0 is an erosion rate constant (kg m^{-2} sec^{-1}), ϕ is the porosity, w_s is the particle settling speed (m sec^{-1}), C is the suspended sediment concentration (kg m^{-3}), τ_c is the critical shear stress for erosion, and τ_b is the computed bottom stress. Erosion ceases when τ_b is smaller than

τ_c. The sediment module is called after flow and salt fields reach a steady state. Model parameters are summarized in Table 1.

To obtain various stratifications, we change the freshwater flux while keeping tidal forcing and turbulence closure the same. Through experimentation, we found that lateral circulation patterns under various stratifications (top-bottom salinity differences from 4.7 to 9.5) are qualitatively similar. Hence, we only show two cases here. The two model runs and some solution characteristics are summarized in Table 2. Cross-sectional averaged freshwater flows of 0.01 (moderately-stratified hereafter) and 0.08 m sec^{-1} (highly-stratified hereafter) correspond to salt intrusion length (L) of 126 and 80 km, respectively. The shorter salt intrusion length for the highly-stratified case is expected as higher freshwater discharge pushes more salt out of the estuary, given the same tidal forcing. A cross-sectional profile seaward of the salt intrusion is taken at a location about ¾L from the mouth (denoted by Slice location in Table 2) for each case. At these two locations, top-bottom salinity differences (ΔS) are 4.7 and 9.5 psu, respectively, which is within the observed range of partially-mixed estuaries (e.g. Dyer, 1997).

The tidally-averaged salinity structure along the channel for the moderately-stratified case, shown in Fig. 3a as an example, is consistent with the salt structure of a partially-mixed estuary. The solid vertical line denotes the location where a cross-sectional profile is taken (¾ L), and the vertical profile of tidally-averaged velocity in the channel at ¾ L (Fig. 3b) shows a reasonable estuarine circulation with landward flow near bottom and seaward flow near surface. The dashed vertical line in Fig. 3a is where another cross-sectional profile is taken upstream of the limit of salt (see Table

2). As expected, the corresponding tidally-averaged velocity (Fig. 3b) shows seaward transport over the entire water column.

4. Lateral circulation driven by boundary mixing

In this section, we will show lateral circulation patterns and their comparisons with an analytical model and observations for both moderately and highly-stratified cases (model runs 1 and 2). We aim to demonstrate that boundary-mixing-driven lateral circulation is robust.

4.1 Circulation patterns

Without Coriolis forcing, circulation patterns are symmetric about the channel axis, and near-bottom up-slope flows are equal on both sides. In Fig. 4a, two counter-rotating cells on either side of the channel axis are evident at 2hr after maximum flood for the moderately-stratified ($U_f = 0.01$) case without Coriolis forcing. The isohalines in the interior are flat but are distorted upward before intersecting the sloping bottom at a right angle (the contours in the figures do not appear perpendicular to the boundary because of vertical exaggeration). The up-slope flows and the isohalines perpendicular to the slope are consistent with the boundary mixing mechanism proposed by Wunsch (1970) and Phillips (1970) (Fig. 1a). The magnitude of maximum lateral current (v) is about 4 cm sec^{-1}, whereas the maximum vertical current (w) is about 0.025 cm sec^{-1}. Flow returns (down-slope) near the top of bottom boundary layer. This is partly due to gradual decreases of boundary mixing from the channel to shallow region (vanishes about 3 meter below surface), gradually weakening the up-slope flows. The weakening thus leads to flow convergence along

the slope, forcing boundary water to move to the interior. This mechanism, known as tertiary flows, was demonstrated in laboratory experiments by Phillips et al. (1986). The other reason may be the baroclinic pressure gradient generated by up-slope flow itself. The up-slope flow tilts the flat isohaline upward, which creates a baroclinic force to drive flow from boundary to the interior (Garrett et al., 1993).

Including Coriolis forcing induces axial asymmetry, and the resulting circulation appears to be a superposition of boundary-mixing-driven and Ekman-forced flows. For the moderately-stratified case at 2hr after maximum flood (Fig. 4b; model run 1 in Table 2), up-slope flows can still be seen on both slopes but are stronger on the right slope than on the left. The strengthened lateral flows on the right slope have a maximum magnitude of about 4.7 cm sec^{-1}. The circulation pattern is complex and resembles the superposition of the circulation pattern without Coriolis forcing (Fig. 4a) and a counter-clockwise circulating cell. The counter-clockwise circulation is consistent with bottom Ekman-veering during flood with a return flow higher in the water column. The asymmetrical boundary layer thickness about the channel also indicates the interactions between boundary-mixing-driven and Ekman-forced flows. As in Lentz and Trowbridge (1991)'s observations on the California shelf, the bottom boundary layer is usually thicker during downwelling-favorable currents, such as the condition on the left slope in Fig. 4b and 4c. This is owing to the convergence of up-slope flows driven by boundary mixing and down-slope flows forced by Ekman-veering. Upwelling-favorable conditions appear on the right slope and thus the boundary layer is thinner there.

In the highly-stratified case (Fig. 4c), the circulation patterns are similar to the moderately-stratified case (Fig. 4b), but the boundary layer is thinner than the moderately-stratified case because turbulent mixing is suppressed by the stronger stratification. Also, the influence of a counter-clockwise circulation forced by bottom Ekman-veering is weaker, and the size of the counter-clockwise cell is more confined near the bottom. The weaker Ekman-forced circulation is due to the tilting of isohalines that tends to suppress lateral flow (Chant and Wilson, 1997). Despite the weaker boundary mixing and weaker Ekman-forced flow, the magnitudes of lateral flows (v) do not decrease much with a maximum value of around 3.3 cm sec^{-1}. One of the reasons is that the increased background stratification (N in Eq. (3)) can sustain the boundary-mixing-driven flow when turbulent mixing is decreased (lower eddy viscosity A_v in Eq. 3). The above patterns evolve as the tide changes (see section 5).

4.2 Sensitivity tests and temporal variability without Coriolis forcing

Vertical mixing in stratified fluid is critical to generate the lateral circulation pattern described in this paper. Because this is a difficult process to model, we used different turbulence closures that have been shown to perform well for simulating estuarine flows (Warner et al., 2005b) and refined the vertical resolution to see if the circulation patterns persisted. These tests were carried out for the simplest case without Coriolis forcing. The results showed that the cross-sectional profiles of salinity and lateral circulation at the location of ¾ salt intrusion length (L) are qualitatively the same. Fig. 5(a), for example, contains four time series of near-bottom up-slope flow at 0.8 m above bottom, at a location off the channel (indicated

by the arrowhead in Fig. 4a; about 10 m deep). As can be seen, four time series corresponding to three turbulence closures and lower background diffusivity (5×10^{-6} m^2 sec^{-1}) are nearly identical, except slight variations in the MY 2.5 closure and slightly weaker magnitude in the low background diffusivity case. This suggests that the predicted lateral circulation pattern is not due to a specific turbulence closure or numerical artifact.

Positive values in the time series of Fig. 5a show that up-slope flows are persistent throughout different tidal stages. The up-slope flows fluctuate with tides and display a stronger peak at about 2hr after maximum flood (indicated by thin vertical lines) with a weaker one at about 2hr after maximum ebb for the moderately-stratified condition. The persistent up-slope transport is what we expect from lateral flows driven by boundary mixing because the density gradient set up by boundary mixing is always directed from the high salinity channel to the low salinity, shallow flanks. Two peaks in a tidal cycle are due to enhanced mixing associated with maximum flood and ebb currents. The peak after maximum flood is higher because the flooding tidal current and estuarine circulation act in concert. The 2hr lag is likely the result of the lag in vertical mixing of density following maximum floods and ebbs (see section 7.3 for further discussion). It should be noted that the model results described above are insensitive to our choice of location on the slope, within the stratified region.

A steady state, analytical solution without Coriolis forcing for boundary-mixing-driven flow with a 2hr lag agrees reasonably well with the model results. We apply Eqs. (2) and (3) with instantaneous eddy viscosities from the model at the same

location off the channel. As Fig. 5b shows, without a 2hr-lag the up-slope flow calculated from the analytical solution peaks at maximum floods and ebbs when turbulent mixing is most energetic. With a 2hr phase-shift, the analytical solution corresponds to the model result reasonably well, and the correlation coefficient is about 0.87. The analytical solution tends to overestimate the up-slope flow. This is associated with the assumption of constant eddy viscosity in the analytical solution. Nevertheless, the reasonable agreement between model results and the analytical solution strongly suggests that boundary mixing is the driving mechanism for the lateral circulation shown here.

4.3 With Coriolis forcing: linear superposition of boundary-mixing-driven and Ekman-forced lateral flows

As mentioned in section 4.1, superposition of boundary-mixing-driven and Ekman-forced lateral flows appears to represent the cross-sectional profile of lateral circulation with Coriolis forcing (Fig. 4b and 4c). In Fig. 6a and 6b for the cases with Coriolis forcing, time series of up-slope flow (thick solid lines) show negative values during ebbs, which indicates the influence of Ekman-forced lateral flows (negative; toward left slope during ebb).

To test the simplest possible case of linear superposition, a representation of Ekman-forced lateral circulation is needed. We start with a simple two-layered model, similar to a three-layer model presented by Martin et al. (2005). Fast decay of eddy viscosity above mid-depth allows us to assume that friction terms in the upper-layer, along-channel momentum equation can be neglected. But bottom friction does

contribute at the first order to the lower layer, along-channel momentum balance. Essentially, the layered model assumes that lateral dynamics on tidal timescale are mainly geostrophic. In the lower layer, however, bottom friction slows down along-channel flow, leading to imbalance between Coriolis and pressure gradient forces. This ageostrophic component then drives lateral flow in the lower layer, and continuity requires a return flow in the upper layer. An analytical solution of the two-layer model can be found (Martin et al., 2005)

$$U_1 = \mathrm{Re}\left\{\frac{\partial \eta}{\partial x}\frac{gi}{\omega}e^{i\omega t}\right\}, \tag{5a}$$

$$U_2 = \mathrm{Re}\left\{\frac{\partial \eta}{\partial x}\frac{g}{\omega}\frac{(i - R/\omega)}{(1 + R^2/\omega^2)}e^{i\omega t}\right\}, \tag{5b}$$

$$V_{E1} = \mathrm{Re}\left\{\frac{1}{2}\frac{\partial \eta}{\partial x}\frac{Rfg}{h_1 g'\omega}\frac{(i - R/\omega)}{(1 + R^2/\omega^2)}y(W - y)e^{i\omega t}\right\}, \tag{5c}$$

$$V_{E2} = \mathrm{Re}\left\{-\frac{1}{2}\frac{\partial \eta}{\partial x}\frac{Rfg}{h_2 g'\omega}\frac{(i - R/\omega)}{(1 + R^2/\omega^2)}y(W - y)e^{i\omega t}\right\}, \tag{5d}$$

where subscripts 1 and 2 denote upper and lower layer, U and V_E are along-channel and cross-channel (lateral) velocity, $\partial\eta/\partial x$ is the prescribed barotropic tidal forcing, g is gravitational acceleration, g' is reduced gravity, h is layer thickness, y is cross-channel coordinate, W is channel width, ω is M2 tidal frequency, and R is a Raleigh drag factor. R is expressed by Geyer et al. (2000) as

$$R \approx \frac{2C_D U_T}{h_2} \tag{6}$$

where U_T is the rms along-channel tidal velocity at 2.5 m above bottom, and the drag coefficient (C_D = 0.0022) can be obtained by assuming a logarithmic velocity profile with known bottom roughness parameter (0.5 mm in Table 1) and reference height of

2.5m. General solution characteristics are described in Martin et al. (2005). Solutions for lateral flow (Eq. 5c and 5d) are consistent with bottom Ekman-veering in the lower layer and an opposite-directed, return flow in the upper layer (counter-clockwise circulation during flood, looking seaward). Isohalines tilted against sea-surface slope in the cross-channel direction also qualitatively match the model results (Fig. 4b and 4c). It should be noted that a phase difference between the upper layer axial flow and all other flow components resulting from bottom friction is implicit in the solution (see section 7.3 for further discussion).

To capture first-order effects, we apply this analytical solution to a simple rectangular cross-section with layer thickness roughly equal to model results shown in Fig. 4b and 4c (h_1=5, h_2=9). The reduced gravities (g') are 0.028 and 0.057 for moderately and highly-stratified cases, respectively. The barotropic pressure gradient is chosen to have along-channel velocity of 0.4 m sec^{-1} in the upper layer. The resulting Ekman-forced lateral flow in the lower layer (V_{E2}) reaches largest amplitude (2.2 and 1.2 cm sec^{-1} for these two cases) close to maximum along-channel velocity in the lower layer (U_2). The predicted weaker V_{E2} under the highly-stratified condition is consistent with our observation from Fig. 4 that stratification tends to suppress lateral Ekman flows (g' in the denominator in Eq. 5d). The lower layer in the 2-layer model may be considered as the deep channel in the numerical model from a dynamical standpoint. Thus, peak Ekman-forced lateral flow corresponds to peak along-channel lower layer velocity in the channel.

Linear superposition of the analytical boundary-mixing-driven and Ekman-forced lateral flows is a good representation of the numerical model results. In Fig. 6a

and 6b, analytical solutions of boundary-mixing-driven flow alone (V_B; Eq. 2) and the linear superposition model ($V_B + V_{E2}$; Eq. 2 and 5d) are plotted against the model solutions with Coriolis forcing for both stratified conditions. As can be seen, boundary mixing (V_B; thin solid lines) alone can not explain all the variabilities with correlation coefficients of 0.39 and 0.41. Adding Ekman-forced lateral flow (dashed lines) improves the correlation to 0.88 and 0.69. As Fig. 5 shows, peak boundary-mixing-driven flows lag maximum tidal currents about 2 hours, whereas Ekman-forced flows peak at around maximum tidal currents in the lower layer (positive value during flood). This mismatch of phase and the relative strength of V_B and V_{E2} controls the near-bottom lateral flows. The residuals between the analytical superposition and the full model solution mainly come from the overestimation of boundary-mixing-driven flow using Eq. (2), as shown in Fig. 5b. When we replace V_B by the model-predicted boundary-mixing-driven flows (thick solid line in Fig. 5b), the correlation coefficients are close to 1 (R^2= 0.97 and 0.98). Nevertheless, the good representation by the linear superposition model provides additional support for the potential importance of boundary mixing on lateral dynamics in stratified estuaries.

5. Temporal and spatial variations of flow structure

In this section, we will compare tidal variations of flow structures at two locations for the moderately-stratified case. These two locations (solid and dashed vertical lines in Fig. 3a) represent transport patterns seaward and landward of the salt intrusion (first and second row of model run 1 in Table 2). They are sufficiently far (~

5 x tidal excursion) from the limit of salt to be unaffected by the changing axial gradients near the longitudinal convergence zone.

5.1 Seaward of the salt intrusion

Interactions between boundary-mixing-induced up-slope flow, Ekman-veering, and estuarine circulation exert different controls on near-bottom lateral flows at different tidal phases. Maximum lateral and vertical velocities are around 5 and 0.03 cm sec^{-1}. During maximum flood and ebb (Fig. 7a2 and 7c2), lateral circulation largely resembles Ekman-forced counter-clockwise and clockwise patterns, respectively, but lateral asymmetry of near-bottom flows induced by boundary mixing is evident (stronger lateral flow on the right slope during flood). When along-channel current speed decreases (Fig. 7b2 and 7d2), Ekman-forced flow is weakened, and the up-slope flow driven by boundary mixing is strengthened (roughly 2-hr lag). This leads to net up-slope flow near bottom on both slopes, especially at 2hr after maximum flood (Fig. 7b2). At 2hr after maximum ebb (Fig. 7d2), the net up-slope flow on the right slope is weak because Ekman veering and up-slope flow driven by boundary mixing nearly cancel each other. Although patterns of near-bottom lateral flow reverse from flood to ebb, the lateral flows are stronger during flood. This is due to the influence of estuarine circulation. Near bottom during flood, flooding currents are in concert with estuarine circulation, resulting in stronger Ekman-veering (Fig. 7a1) and boundary mixing. The more energetic mixing in turn drives stronger up-slope flows (Fig. 7b1). During ebb, on the other hand, ebbing currents are against

estuarine circulation near bottom, leading to weaker Ekman-veering and boundary-mixing-induced flows (Fig. 7c1 and 7d1).

The lateral tilting of isohalines is consistent with thermal wind balance (Fig. 7). In the upper part of the cross-section, isohalines are tilted upward to the left shoal for both flood and ebb because the vertical shear of along-channel velocity does not change sign; $\partial u/\partial z < 0$ due to sub-surface maximum of flooding currents caused by estuarine circulation. In the lower part of the cross-section, on the other hand, isohaline tilting oscillates with tides as the vertical shear changes sign. This pattern is consistent with Lerczak and Geyer (2004)'s finding.

5.2 Landward of salt intrusion

Without the influences of salt, lateral circulation is dominated by bottom Ekman-veering (Fig. 8a1 and 8b1). Magnitudes of lateral and vertical velocities (0.7 cm and 0.005 cm sec^{-1}) are considerably weaker than those seaward of the salt intrusion due to weaker tidal current and vertical shear that drives Ekman-forced lateral circulation.

6. Implications for sediment dynamics

In this section, tidally-varying and tidally-averaged sediment transport patterns at two cross-sections for the moderately-stratified case (same as in the section 5) are compared.

6.1 Tidally-varying sediment dynamics

Seaward of the salt intrusion, estuarine circulation has a strong impact on sediment dynamics. During ebb, near bottom currents in the channel are weakened by the opposing estuarine circulation. Therefore, bottom stress in the channel is relatively low (Fig. 7c4 and 7d4). During flood, on the other hand, tidal currents and estuarine circulation are in concert, resulting in peak bottom stress in the channel (Fig. 7a4 and 7b4). Such tidal asymmetry in bottom stress causes high suspended sediment concentrations in the channel during flood and on the slopes during ebb (Fig. 7a3, 7b3, 7c3, and 7d3). Noticeably, there are two secondary bottom stress peaks around depth of 4 m in Fig. 7a4, 7c4, and 7d4. This is due in part to the relatively weak stratification above this depth. The combination of near-bottom lateral flows and tidally asymmetrical suspended sediment distribution then controls the lateral sediment fluxes in Fig. 7a5, 7b5, 7c5, and 7d5 (see below).

In contrast, landward of the salt intrusion bottom stresses at maximum flood and ebb (Fig. 8a4 and 8b4) both peak in the channel but are slightly higher at ebb because the freshwater discharge strengthens ebbing currents. As a result, suspended sediment concentration is highest in the channel, and the distributions are similar on flood and ebb (Fig. 8a3 and 8b3). Due to the absence of stratification, suspended sediments occupy the whole water column, contrasting with the rather confined vertical distribution seaward of the the salt intrusion (e.g. Fig. 7a3). Lateral sediment flux (Fig. 8a5 and 8b5) is one order of magnitude smaller than that seaward of the salt intrusion mainly due to weaker lateral circulation. In the absence of salt and without tidal asymmetry in stress and sediment concentration, lateral sediment flux is thus

controlled by Ekman-forced near-bottom lateral flows, which is toward right slope during flood and reversed during ebb.

6.2 Tidally-averaged transport

The profile of tidally-averaged along-channel velocity seaward of the salt intrusion (Fig. 9a), as expected, has the structure of estuarine circulation, whereas landward of salt intrusion the flow is down-estuary (Fig. 9b) and its cross-sectional average is equal to freshwater velocity (U_f = 0.01). Seaward of the salt intrusion, the tidally-averaged, cross-sectional averaged eddy viscosity is about 4 x 10^{-4}, yielding an Ekman number of 0.02. An Ekman number less than 1 indicates weaker frictional influences than Coriolis forcing. Thus, the along-channel residual flow is vertically segregated with up-estuary flow near bottom and down-estuary flow near surface, as suggested by Kasai et al (2000).

In the upper part of the water column, isohalines are predominantly tilted upward toward the left (Fig. 9c), consistent with an approximate thermal wind balance with the vertical shear. However, the tidally averaged, down-estuary surface flow maximum in Fig. 9a is on the left side (looking seaward), which is opposite to what we expect from Coriolis deflection of the surface flow. This is likely a model artifact caused by the lack of a surface mixed layer (without wind), which results in near surface stratification in the cases presented here. The lateral tilting causes greater suppression of vertical mixing due to stratification on the left shoal and more well-mixed conditions on the right shoal, with correspondingly higher tidally averaged eddy viscosity on the right (0.0014 m^2 sec^{-1}; thick black lines in Fig. 9c). As

a result, the tidally averaged along-channel velocity on the right shoal is more affected by friction, while the velocity on the left shoal is much less affected. In real estuaries there is usually a well-defined surface mixed layer. The presence of a surface mixed layer reduces lateral differences in eddy viscosity and thus eliminates the artifact. Increasing water depth also can eliminate this model artifact because it decreases the effects of bottom friction and thus the effects of lateral differences in eddy viscosity on surface flows. Indeed, when we deepen the whole domain by 4 m, a tidally averaged, down-estuary surface flow maximum on the right side is recovered. Most importantly, the lateral circulation pattern remains unchanged after the depth deepening. Hence, the model artifact does not affect the overall lateral dynamics presented here.

Seaward of the salt intrusion, tidally-averaged lateral circulation (Fig. 9a) is consistent with up-slope flows driven by boundary mixing near bottom and return flows toward the interior at mid-depth. Near surface, lateral flows toward the right are driven by lateral density gradient set up by isohaline tilting. Influences of Ekman-forced lateral flow are nearly absent because Ekman-forced lateral circulation reverses with tides and thus is largely canceled out after tidal averaging. This cancellation is clearly shown at the cross-section landward of salt intrusion where tidally-averaged lateral circulation is extremely weak (max v of 0.016 cm sec^{-1}). The residual circulation is clockwise, following the Ekman-forced pattern during ebb because of slightly stronger ebbing currents.

Net along-channel sediment fluxes at the cross-sections seaward and landward of the salt intrusion are in opposite directions (Fig. 9e and 9f). Seaward of the salt

intrusion, there is a strong up-estuary transport of sediments near the bottom because of enhanced resuspension during the flood tide due to the estuarine circulation. Sediment flux in the interior is largely zero because stratification confines suspended sediments close to the bottom. There are relatively weak down-estuary fluxes on the shallow slopes owing to low sediment concentration and weak down-estuary residual flows. Net sediment flux landward of salt intrusion, in contrast, is predominantly down-estuary as anticipated from net down-estuary axial velocity. But this down-estuary flux is one-order of magnitude smaller and is uniformly distributed over the water column in the absence of stratification. The weak up-estuary fluxes on the shallow regions are probably due to Stoke's transport. The cross-sectional integrations of net sediment fluxes are about 8.4 and -2.7 kg sec^{-1} seaward and landward of salt intrusion, respectively. These opposite-directed net transports favor the development of an estuarine turbidity maximum zone (ETM) near the salt limit (e.g. Sanford et al., 2001).

Net lateral sediment flux seaward of the salt intrusion is up-slope, leading to net sediment erosion in the channel and net deposition on the shallow slopes (Fig. 9g). Net up-slope sediment flux near the bottom is consistent with the residual lateral circulation driven by boundary mixing. The net up-slope flux is higher on the right slope because high sediment concentration in the channel only occurs during flood (Fig. 7a3 and 7b3) when lateral flows are predominantly toward the right slope (Fig. 7a5 and 7b5). The net up-slope flux on the right slope gradually decreases and terminates at about 4 m from the surface where the 6 psu isohaline roughly intersects the right slope. This convergence of up-slope flux not only favors sediment

accumulation below the halocline on the right slope but also drives net lateral flux from the boundary to the interior which can clearly be seen in the center of Fig. 9g. On the left slope, on the other hand, the net up-slope flux as well as the convergence are weaker because the isohalines are predominantly tilted upward toward the left (Fig. 9c). As a result, we anticipate higher sediment deposition on the right slope.

Contrasting with the patterns seaward of the salt intrusion, net lateral sediment flux landward of salt intrusion is at least two-orders of magnitude weaker and generally follows the clockwise, net lateral circulation (Fig. 9h). Thus, sediment re-distribution by lateral circulation should be relatively negligible landward of salt intrusion.

Decomposing tidally averaged lateral sediment flux further confirms that preferential transport of sediments toward the right seaward of the salt intrusion is due to tidal asymmetry in sediment resuspension and lateral flows. Depth-integrated, tidally averaged lateral sediment flux (first term) can be decomposed into mean advective (second term) and tidal pumping fluxes (third term) (e.g. Huijts et al. 2006):

$$\underset{(1)}{\int \left(\overline{v \cdot c}\right) dz} = \underset{(2)}{\int \left(\bar{v} \cdot \bar{c}\right) dz} + \underset{(3)}{\int \left(\overline{v' \cdot c'}\right) dz}, \qquad (7)$$

where v is lateral flow speed, c is suspended sediment concentration, overbar is tidal average, and prime is tidal variation. As Fig. 10a shows, total transport (first term) is to remove sediments out of the channel and preferentially transport sediments toward the right. The mean advective flux tends to distribute sediments evenly about the channel axis. The pumping flux (all positive) is the one responsible for this net rightward transport. This result is expected because resuspended sediment is mostly available in the channel during flood when lateral flows are mainly toward right (Fig.

7a and 7b). Bottom sediment distributions after 60 days of model run illustrate the outcome of such transport patterns (solid line in Fig. 10b). There is net erosion (zero means no change from initial state) in the channel. The eroded sediments from the channel preferentially deposit on the right due to stronger lateral sediment flux and the convergence there (around 2500 m). Landward of salt intrusion, on the other hand, bottom sediments remains unchanged (dashed line in Fig. 10b), as anticipated from extremely weak net lateral sediment fluxes.

7. Discussion and Conclusions

7.1 How important is the boundary mixing mechanism?

We have shown in section 4.2 that without Coriolis forcing, an analytical solution for boundary-mixing-driven lateral flow with a 2hr lag agrees reasonably well with model results. We have also demonstrated in section 4.3 that with Corilois forcing, a linear superposition of boundary-mixing-driven (V_B) and Ekamn-forced lateral flows (V_{E2}) is a good representation of near-bottom lateral flows predicted by the model. These results suggest that boundary mixing can be an important driving mechanism of lateral circulation in stratified estuaries. However, we have not yet considered a third candidate mechanism, differential advection.

For the sake of simplicity and because our focus here is on the boundary mixing mechanism, we consider a system without Coriolis forcing to compare the relative influences of boundary mixing and differential advection. Both boundary mixing and differential advection mechanisms require lateral salinity gradient (s_y) as

a driving force. To evaluate this lateral salinity gradient, we look at the tidally-varying salt balance

$$s_t + us_x + vs_y + ws_z = \left(Ks_z\right)_z, \tag{8}$$

where s is salinity, (u,v,w) is velocity field, and K is vertical eddy diffusivity. Sub-grid horizontal mixing of salt is set to zero, but the advection scheme itself compensates with mild numerical diffusion. Differentiating Eq. (8) with respect to y yields

$$\underset{\text{(i)}}{(s_y)_t} = \underset{\text{(ii)}}{-\left(us_x\right)_y} \underset{\text{(iii)}}{-\left(vs_y\right)_y} \underset{\text{(iv)}}{-\left(ws_z\right)_y} + \underset{\text{(v)}}{\left[\left(Ks_z\right)_z\right]_y}, \tag{9}$$

The first term (i) is the rate of change in lateral salinity gradient, the second term (ii) is the differential advection of longitudinal salinity gradient by lateral shear, the third term (iii) may be interpreted as lateral compression/decompression of salinity gradient, the fourth term (iv) is the tilting of isohalines, and the fifth term (v) is the lateral variations in the vertical diffusive salt flux gradient, which is associated with boundary mixing. Our focus here is to compare the contribution of differential advection (ii) and boundary mixing (v) to the lateral salinity gradient. Thus, we combine (iii) and (iv) into a collective term: lateral advection. Fig. 11 shows how differential advection, boundary mixing, and lateral advection terms contribute to the rate of change of the lateral salinity gradient. The differential advection term changes sign when tide turns, as expected. All four terms vary with comparable magnitude, suggesting that differential advection, boundary mixing, and lateral advection all contribute to the rate of change in lateral salinity gradient. Note however that the variability in the boundary mixing term is most correlated with the variability in the

rate of change of the lateral salinity gradient (R^2=0.6), especially during flood. Thus, these results support our contention that boundary mixing is an important driving mechanism for lateral circulation in estuaries similar to those modeled here.

Several aspects of the above analysis require further investigation. It is not clear how to separate boundary mixing and differential advection mathematically, as they both contribute to lateral salinity gradients and are associated with each other. Also, the above analysis neglects Coriolis forcing. Ekman veering in the bottom boundary layer can modify lateral salinity gradients by tilting isohalines. This makes distinguishing the mechanisms associated with lateral salinity gradient even more complicated. Huijts et al. (2006) presented an analytical model to evaluate relative contributions from differential advection and Coriolis forcing. Due to a prescribed salinity gradient, their model may be more useful for vertically-mixed systems. For more stratified systems in which the lateral salinity gradient varies spatially and temporarily, an analytical solution including all three mechanisms has not been documented in the literature. Finally, though we found in section 4.3 that linearly superposing boundary-mixing-driven and Ekman-forced lateral flows is a good representation of the near-bottom lateral flows predicted by the model, the validity of linear superposition across different estuarine systems (especially under weaker stratification) requires further verification.

7.2 Evidence of boundary mixing in the literature

As mentioned in the introduction, there are very few reports in the literature about boundary mixing on slopes in estuaries. Several cross-sectional snapshots

reported by Phillips et al. (1986) from a dye injection study are consistent with boundary-mixing-driven flow and salt structure, but their conclusion is not definitive. Lerczak and Geyer (2004) reported that lateral circulation driven by boundary mixing was relatively weak compared with differential advection in their modeling study, which contradicts our findings here. The discrepancy may be due to their use of a constant eddy viscosity/diffusivity. In model runs with similar top-bottom salinity differences to ours, their eddy viscosities are 5.4 and 3.3 x 10^{-4} m^2 sec^{-1}, while our values solved by the $k-\varepsilon$ closure are roughly 1-2 and 0.5-1 x 10^{-3} m^2 sec^{-1} within 3 m above the bottom for moderately and highly-stratified cases, respectively. Therefore, in their model runs, boundary mixing is much weaker, which then leads to insignificant lateral flows driven by boundary mixing. This speculation is further confirmed in Fig. 16 of their paper. When they used a modern turbulence closure, isohalines perpendicular to the slopes and the resulting up-slope flows were much clearer.

A field observation from the Hudson River estuary may provide support for boundary-mixing-driven lateral circulation. Lerczak and Geyer (2004) reported that the differential advection mechanism can not explain the observed vertical profile of lateral flow during neap tides in the Hudson River estuary (Fig. 12a). The vertical profile taken at a location on the right of the channel (looking seaward) shows a 3-layer structure during maximum flood and weaker lateral flows during maximum ebb. The vertical profile of lateral flows from our model (Fig. 12b) shows very similar patterns during maximum flood. The 3-layer structure during maximum flood results from the peak Ekman-forced flow enhancing the boundary-mixing-driven flow

toward the right slope near bottom and the return flows toward the left at mid-depth. In contrast, during maximum ebb these two flows are against each other, leading to weaker lateral flows. Although the model and the observations from the Hudson are not directly comparable as bathymetry and forcings are different, the high degree of similarity in lateral flow structure during flood leads us to speculate that boundary mixing may drive significant amount of lateral flows under stratified conditions.

One possible reason that boundary mixing has received little attention in the estuarine literature is the required high vertical resolution in the bottom boundary layer. As shown in Fig. 7, boundary layer height is at most 2-3 meter, and strong boundary-mixing-driven flows are in the lower part of the boundary layer. Another reason may be that boundary mixing is highly time-dependent. We have shown in Fig. 5 and 6 that boundary-mixing-driven flows oscillate with tides and peaks after maximum floods and ebbs. This unsteadiness and the resulting phase differences with other mechanisms, such as Ekman-forced flow, may hinder efforts to distinguish boundary mixing. Relatively steady forcing is probably why reports of boundary mixing are mainly on continental shelves (e.g. Weatherly and Martin, 1978; Lentz and Trowbridge, 1991). Observations with high spatial and temporal resolution are thus required to explore and distinguish the role of boundary mixing on lateral dynamics in stratified estuaries.

7.3 Phase lag between model results and analytical solution for boundary mixing

A relevant time scale that influences boundary mixing is the diffusive time scale. The diffusive time scale controls the speed with which vertical mixing modifies

the density field, which in turn drives the lateral circulation. Given boundary layer heights δ around 3 and 2 m (Fig. 4b and 4c) and averaged eddy diffusivity within the boundary layer K_z about 1.5 x 10^{-3} and 0.75 x 10^{-3} for moderately and highly-stratified cases, respectively, the corresponding diffusive time scales (δ^2 / K_z) are about 1.7 hr and 1.5 hr. These values are consistent with the 2-hour lag between the steady state analytical solution for boundary mixing and the model prediction (Fig. 5b). However, the 2hr lag may also be influenced by other processes, such as tidal acceleration/deceleration. Further investigation is needed.

In the two-layer time-dependent Ekman model (section 4.3), there is a phase difference between the upper layer axial flow and all other flow components (Eq. 5a v. 5b, 5c, and 5d). This phase difference results from the linearized bottom friction parameter R, which affects the lower layer axial flow and lateral flow in both layers as a result. Thus, even though the Ekman model does not resolve the details of vertical mixing in the bottom boundary layer, a phase lag associated with bottom friction is built into the solution. The time scale of this phase lag is $1/R$, approximately 2.5 hours for the cases presented here. So, from a dynamics standpoint, it is appropriate to compare the direct output of the time-dependent Ekman layer model to the lagged output of the steady state boundary mixing model.

7.4. Deficiencies of the model

The model-predicted salinity fields lacks well-defined haloclines. The stratification in Fig. 7 is mostly linear from top-to-bottom. A diffused halocline also appears in realistic estuarine simulations (Li et al., 2005; Warner et al., 2005a). Such

pattern contrasts with the sharp halocline that is often found during highly stratified conditions in real estuaries (e.g. the Hudson; Lerczak and Geyer, 2004). One possible reason for the lack of sharp halocline in our model is related to poor parameterization of interior mixing in the turbulence closures. Internal mixing processes are approximated by a constant and rather high background diffusivity of 8×10^{-5} m^2 sec^{-1} here. Although using a lower background diffusivity of 5×10^{-6} m^2 sec^{-1} sharpens the halocline, it also results in an unrealistic salt intrusion length under the desired tidal currents and freshwater discharge. Adjusting the background diffusivity to simulate damping by stratification (North et al. 2004) is one possible approach for sharpening the halocline. It is also possible that parameterizing the effects of wind stirring and surface wave breaking, which likely contribute to significant upper layer mixing may, lead to more realistic salt structure.

Another limitation of our model is the rather simple bathymetry. Although a triangular shape is more generic than a rectangular one, many coastal plain estuaries feature a gentle shoal and a sharply incised channel. In other words, the angle of the slope changes across the estuary instead of being constant. This laterally varying slope angle can cause local convergence/divergence of boundary-mixing-driven lateral flows and thus complicate the lateral dynamics. The role of boundary mixing under more realistic cross-sectional profiles and different slope angles will be addressed in the future.

7.5 Implications for estuarine morphology

The bottom sediment distribution seaward of the salt intrusion after a 60-day model run shows net erosion in the channel and net deposition preferentially on the right slope (Fig. 10b; looking seaward). The net erosion is due to constant upslope transport of sediments by boundary-mixing-driven flows from the channel. The preferential deposition on the right is mainly due to tidal asymmetry in sediment resuspension and lateral flows (dashed line in Fig. 10a; see section 6.2). Such erosion/deposition patterns over a long time would favor a shallow shoal on the right and the deep channel shifted closer to the left. The resulting axially asymmetrical channel profile is consistent with commonly observed profiles in shallow, coastal plain estuaries, such as the Hudson River estuary, James and York River estuary, and the main stem of Chesapeake Bay (e.g. Geyer et al., 1998; Kerhin et al., 1988). However, the net erosion in the channel predicted by the model contradicts the observed fast deposition there in estuaries like Chesapeake Bay (Hobbs et al., 1992). This discrepancy may result from the dominance of channel-directed sediment transport during storms when strong wind-wave forcing leads to high resuspension on the shoals (Sanford, 1994). Other factors that are not considered here including wind forcing, laterally and longitudinally varying bathymetry, and limited sediment supply in mud pools can complicate the lateral dynamics of suspended sediment transport and thus merit further investigation.

Acknowledgements

We thank the ROMS user community. The original manuscript is much improved because of the efforts from two anonymous reviewers. S.N.C thanks Parker

MacCready, Rocky Geyer, and James Lerczak for many insightful discussions. S.N.C gratefully acknowledges support from a Maryland Sea Grant Fellowship and ONR grant no. A100497 (CSTM). LPS was supported by NSF grant nos. OCE-0536466 (MUDBED) and OCE-0453905 (BITMAXii), and ONR grant no. A100497 (CSTM). This is UMCES publication no. 4141.

References

Burchard, H. and H. Baumert, 1998: The formation of estuarine turbidity maxima due to density effects in the salt wedge. A hydrodynamic process study. *Journal of Physical Oceanography*, **28,** 309-321.

Canuto, V. M., A. Howard, Y. Cheng, and M. S. Dubovikov, 2001: Ocean turbulence I: one-point closure model-Momemtun and heat vertical diffusivities. *Journal of Physical Oceanography*, **31,** 1413-1426.

Chant, R. J. and E. Wilson, 1997: Secondary circulation in a highly stratified estuary. *Journal of Geophysical Research*, **102,** 23207-23216.

Dyer, K. R., 1997: *Estuaries: A Physical Introduction*. 2nd ed. John Wiley & Sons Ltd., 195 pp.

Fischer, H. B., 1972: Mass transport mechanisms in partially stratified estuaries. *Journal of Fluid Mechanics*, **53,** 671-687.

Fugate, D. C., C. T. Friedrichs, and L. P. Sanford, 2007: Lateral dynamics and associated transport of sediments in the upper reaches of a partially mixed estuary, Chesapeake Bay, USA. *Continental Shelf Research*, **27,** 679-698.

Garrett, C., P. MacCready, and P. B. Rhines, 1993: Boundary mixing and arrested Ekman layers: Rotating stratified flow near a sloping boundary. *Annual Review of Fluid Mechanics*, **25,** 291-323.

Geyer, W. R., R. P. Signell, and G. C. Kineke, 1998: *Lateral trapping of sediment in a partially mixed estuary*. *Physics of Estuaries and Coastal Seas*, Balkema.

Geyer, W. R., J. H. Trowbridge, and M. M. Bowen, 2000: The dynamics of a partially mixed estuary. *Journal of Physical Oceanography*, **30,** 2035-2048.

Haidvogel, D. B., H. G. Arango, K. Hedstrom, A. Beckmann, and P. Malanotte-Rizzoli, 2000: Model evaluation experiments in the North Atlantic basin: Simulations in nonlinear terrain-following coordinates. *Dynamics of Atmospheres and Oceans*, **32,** 239-281.

Hobbs, C. H., J. P. Halka, R. T. Kerhin, and M. J. Carron, 1992: Chesapeake Bay Sediment Budget. *Journal of Coastal Research*, **8,** 292-300.

Huijts, K. M. H., H. M. Schuttelaars, H. E. de Swart, and A. Valle-Levinson, 2006: Lateral entrapment of sediment in tidal estuaries: An idealized model study. *Journal of Geophysical Research*, **111,** C12016, doi:10.1029/2006JC003615.

Huzzey, L. M. and J. M. Brubaker, 1988: The formation of longitudinal fronts in a coastal estuary. *Journal of Geophysical Research*, **93,** 1329-1334.

Johnson, G. C. and D. R. Ohlsen, 1994: Frictionally modified rotating hydraulic channel exchange and ocean outflows. *Journal of Physical Oceanography*, **24,** 66-78.

Jones, W. P. and B. E. Launder, 1972: The prediction of laminarization with a two-equation model of turbulence. *International Journal of Heat and Mass Transfter*, **15,** 301-314.

Kalkwijk, J. P. T. and R. Booij, 1986: Adaptation of secondary flow in nearly-horizontal flow. *Journal of Hydraulic Engineering*, **24,** 19-37.

Kasai, A., A. E. Hill, T. Fujiwara, and J. H. Simpson, 2000: Effect of the Earth's rotation on the circulation in regions of freshwater influence. *Journal of Geophysical Research*, **105,** 16961-16969.

Kerhin, R., J. Halka, D. V. Wells, E. L. Hennessee, P. J. Blakeslee, N. Zoltan, and R. H. Cuthbertson, 1988: The Surficial Sediments of Chesapeake Bay, Maryland: Physical Characteristics and Sediment Budget. Investigation Report 48, 43 pp.

Lentz, S. J. and J. H. Trowbridge, 1991: The bottom boundary layer over the northern California shelf. *Journal of Physical Oceanography*, **21,** 1186-1201.

Lerczak, J. A. and W. R. Geyer, 2004: Modeling the lateral circulation in straight, stratified estuaries. *Journal of Physical Oceanography*, **34**.

Li, C. and J. O'Donnell, 1997: Tidally driven residual circulation in shallow estuaries with lateral depth variation. *Journal of Geophysical Research*, **102,** 27915-27929.

Li, C. and A. Valle-Levinson, 1999: A two-dimensional analytic tidal model for a narrow estuary of arbitrary lateral depth variation: The intertidal motion. *Journal of Geophysical Research*, **104,** 23525-23543.

Li, M., L. J. Zhong, and W. C. Boicourt, 2005: Simulations of Chesapeake Bay estuary: Sensitivity to turbulence mixing parameterizations and comparison with observations. *Journal of Geophysical Research*, **110,** C12004.

MacCready, P. and P. B. Rhines, 1993: Slippery bottom boundary layer on a slope. *Journal of Physical Oceanography*, **23,** 5-22.

Marchesiello, P., J. C. McWilliams, and A. Shchepetkin, 2001: Open boundary conditions for long-term integration of regional oceanic models. *Ocean Modeling*, **3,** 1-20.

Martin, W., P. MacCready, and R. Dewey, 2005: Boundary layer forcing of a semidiurnal cross-channel seiche. *Journal of Physical Oceanography*, **35,** 1518-1537.

Mied, R. P., R. A. Handler, and T. F. Donato, 2002: Regions of estuarine convergence at high Rossy number: A solution in estuaries with elliptical cross sections. *Journal of Geophysical Research*, **107**.

North, E. W., S.-Y. Chao, L. P. Sanford, and R. R. Hood, 2004: The Influence of Wind and River Pulses on an Estuarine Turbidity Maximum: Numerical Studies and Field Observations. *Estuaries*, **27,** 132-146.

Nunes, R. A. and J. H. Simpson, 1985: Axial convergence in a well-mixed estuary. *Estuarine, Coastal, and Shelf Science*, **20,** 637-649.

Ott, M. W. and C. Garrett, 2002: Frictional estuarine flow in Juan de Fuca Strait with implications for secondary circulation. *Journal of Geophysical Research*, **103,** 15657-15666.

Phillips, O. M., 1970: On flows induced by diffusion in a stably stratified fluid. *Deep Sea Research*, **17,** 435-443.

Phillips, O. M., J. Shyu, and H. Salmun, 1986: An experiment on boundary mixing: mean circulation and transport rates. *Journal of Fluid Mechanics*, **173,** 473-499.

Sanford, L. P., 1994: Wave-Forced Resuspension of Upper Chesapeake Bay Muds. *Estuaries*, **17,** 148-165.

Sanford, L. P. and J. P. Halka, 1993: Assessing the paradigm of mutually exclusive erosion and deposition of mud, with examples from upper Chesapeake Bay. *Marine Geology*, **114,** 37-57.

Smith, R., 1980: Bouyancy effects upon longitudinal dispersion in wide well-mixed estuaries. *Philosophical Transactions of the Royal Society of London. Series A, Mathematical and Physical Sciences*, **296,** 467-496.

Trowbridge, J. H. and S. J. Lentz, 1991: Asymmetric behavior of an oceanic boundary layer above a sloping bottom. *Journal of Physical Oceanography*, **21,** 1171-1185.

Valle-Levinson, A., C. Li, K. C. Wong, and K. M. M. Lwiza, 2000: Convergence of lateral flow along a coastal plain estuary. *Journal of Geophysical Research*, **105,** 17045-17061.

Warner, J. C., W. R. Geyer, and J. A. Lerczak, 2005: Numerical modeling of an estuary: A comprehensive skill assessment. *Journal of Geophysical Research*, **110,** C05001 (1-13).

Warner, J. C., C. R. Sherwood, H. G. Arango, and R. P. Signell, 2005: Performance of four turbulence closure models implemented using a generic length scale method. *Ocean Modeling*, **8,** 81-113.

Weatherly, G. L. and P. J. Martin, 1978: On the structure and dynamics of the oceanic bottom boundary layer. *Journal of Physical Oceanography*, **8,** 557-570.

Woodruff, J. D., W. R. Geyer, C. K. Sommerfield, and N. W. Driscoll, 2001: Seasonal variation of sediment deposition in the Hudson River estuary. *Marine Geology*, **179,** 105-119.

Wunsch, C., 1970: On oceanic boundary mixing. *Deep Sea Research*, **17,** 293-301.

Table 1 – Model parameters

Parameters	
Bottom roughness parameter (z_0)	0.5 mm
Settling speed (w_s)	0.3 mm sec^{-1}
Critical shear stress (τ_c)	0.05 Pa
Erosion rate constant (E_0)	5 x 10^{-5} kg m^{-2} sec^{-1}
Porosity (ϕ)	0.9
Background eddy viscosity	8 x 10^{-5} m^2 sec^{-1}
Background eddy diffusivity	8 x 10^{-5} m^2 sec^{-1}

Table 2 – Model runs and solution characteristics: Runs 1 and 2 are the moderately and highly-stratified cases, respectively. The first row of run 1 is the solution characteristics seaward of the salt intrusion, and the second row is landward of the salt intrusion. U_f is the freshwater velocity; L is the salt intrusion length defined as the distance between the mouth to 2 psu; ΔS is the top-bottom salinity difference in the channel; U_e is the rms amplitude of estuarine circulation; U_t is the tidal current amplitude at the given cross-section.

Run	U_f (m sec^{-1})	L (km)	Slice location (km)	ΔS (psu)	U_e (m sec^{-1})	U_t (m sec^{-1})
1	0.01	126	90 (solid line in Fig. 3)	4.7	0.11	0.37
	0.01	126	163 (dashed line in Fig. 3)	0	N/A	0.29
2	0.08	80	60	9.5	0.20	0.42

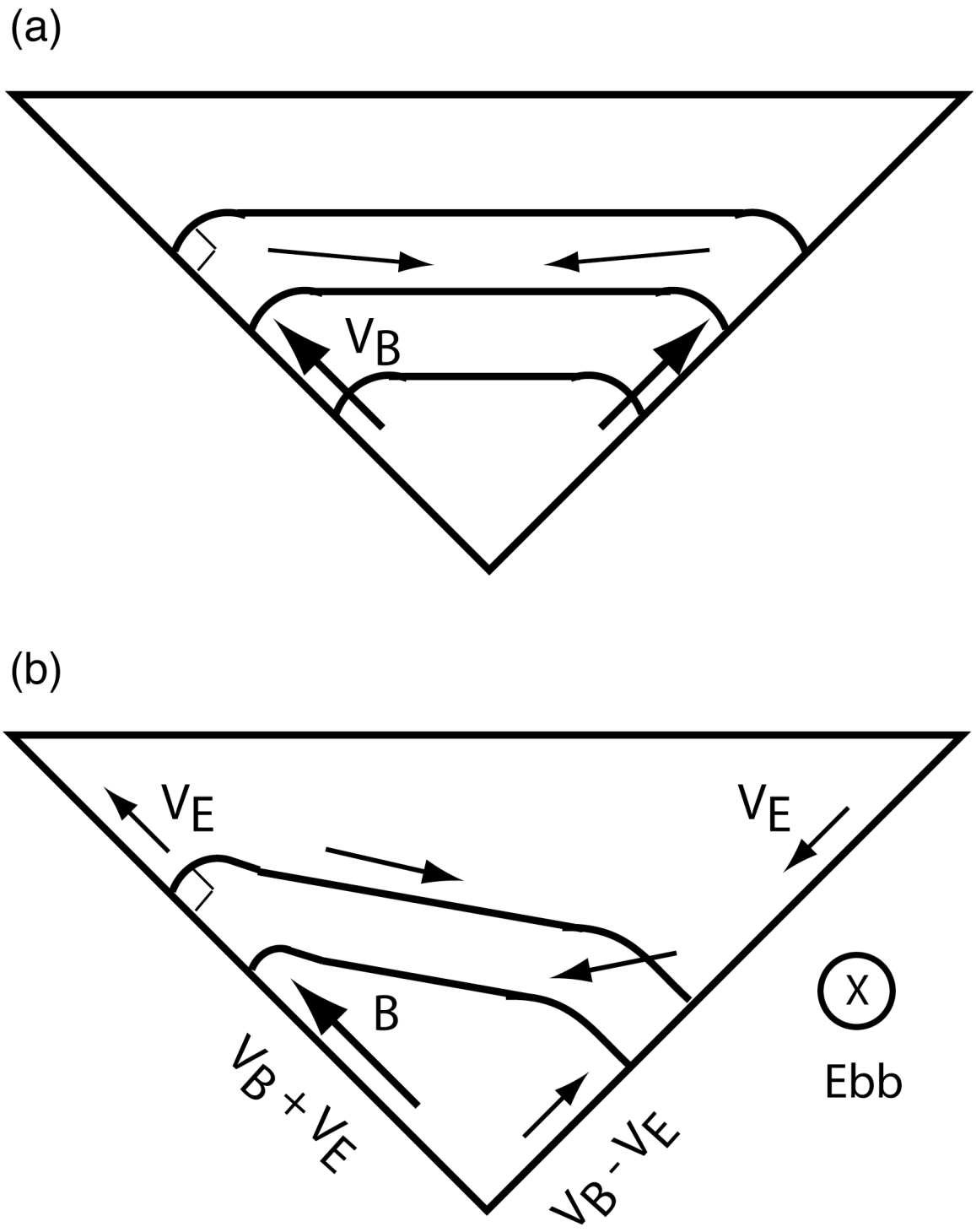

Fig. 1. Schematic diagram of lateral circulation (a) without and (b) with Coriolis forcing. V_B and V_E denote lateral flows driven by boundary mixing and by bottom Ekman veering, respectively. The slope of the triangular channel here is highly exaggerated. In many real estuaries, the cross-channel distance is two-orders of magnitude larger than the depth.

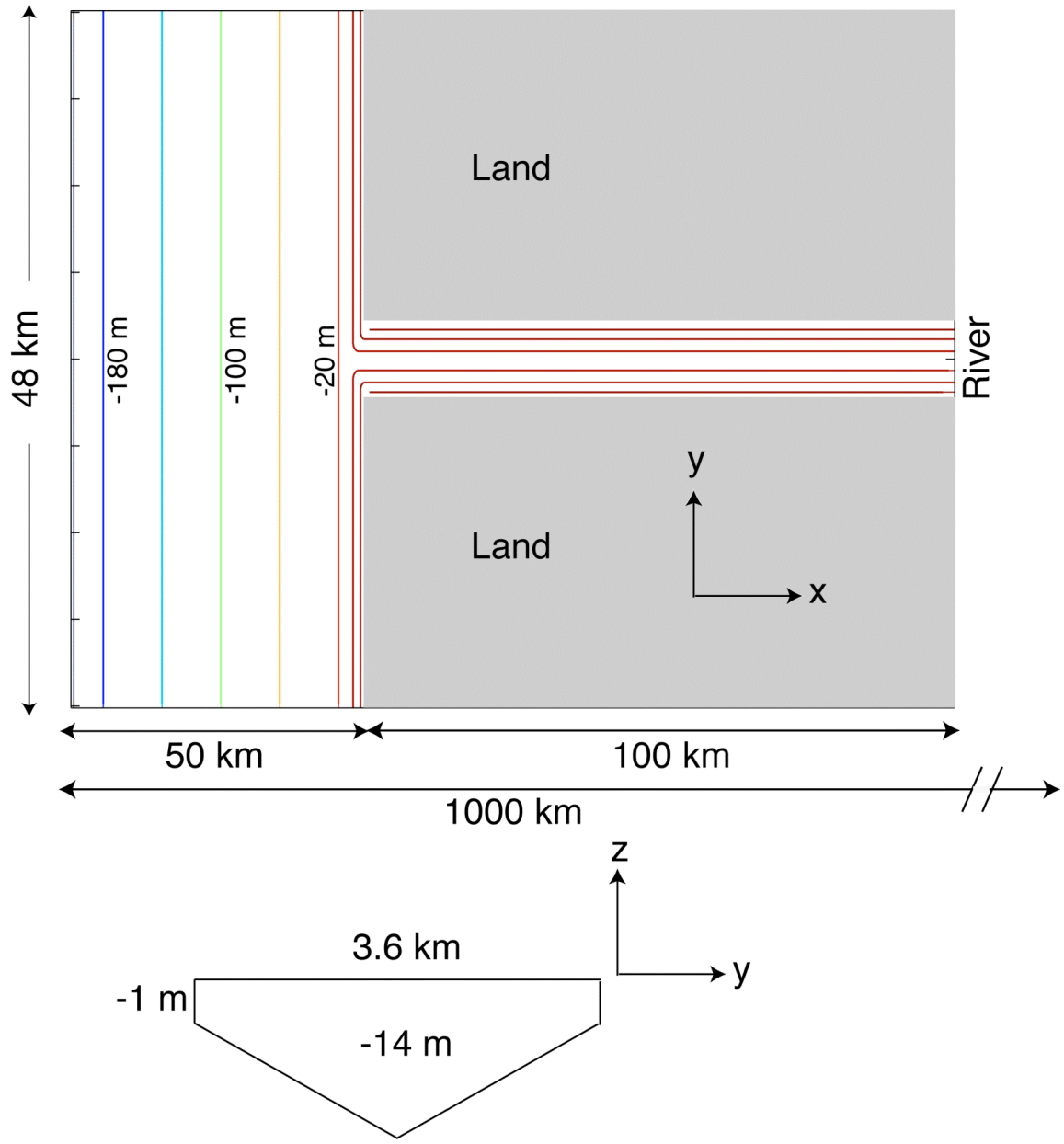

Fig. 2. (a) Plan-view of model domain. The domain mimics a broad continental shelf with a long, straight estuarine channel. The shelf size is 48 km (along-shelf) x 50 km (cross-shelf) with a constant slope from 200 m (off-shelf boundary) to 1 m (land boundary). The estuarine channel extends from x=50 km to about 1000 km. The gray areas are land. Estuarine cross-section is plotted in (b). The channel is triangular-shaped and of 3.6 km-wide. The deep channel is 14 m, and the shallowest area is of 1 m. Note that the domain is scaled disproportionately for better visualization.

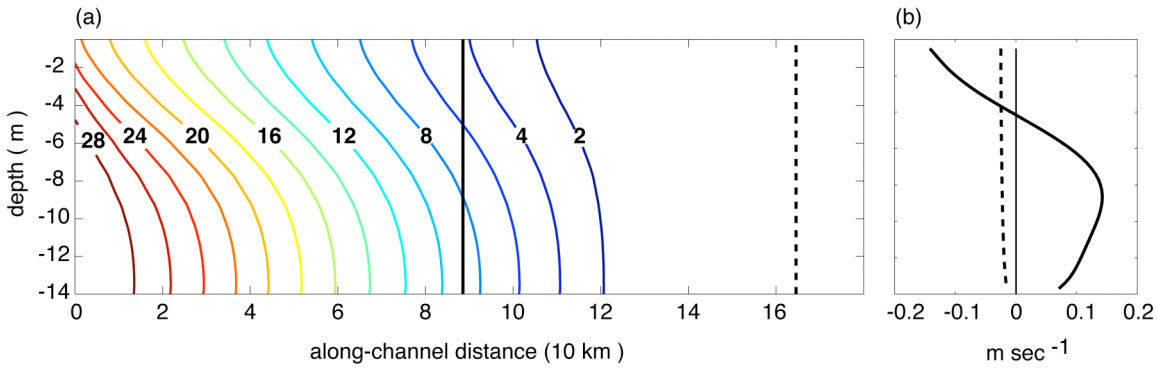

Fig. 3. (a) Tidally averaged salt structure along the channel axis (14 m) starting from the estuary mouth under moderately-stratified conditions (model run 1 in Table 2). The solid and dashed vertical lines are the locations where cross-sectional profiles are taken. These two cross-sections are referred as seaward of salt intrusion (~ ¾ L, slice location 90 km in Table 2) and landward of salt intrusion (slice location 163 km). The distances to the limit of salt (2 psu) from these two cross-sections are both roughly equal to 5 tidal excursions. Vertical profiles of tidally-averaged along-channel velocity at these two locations are plotted in (b).

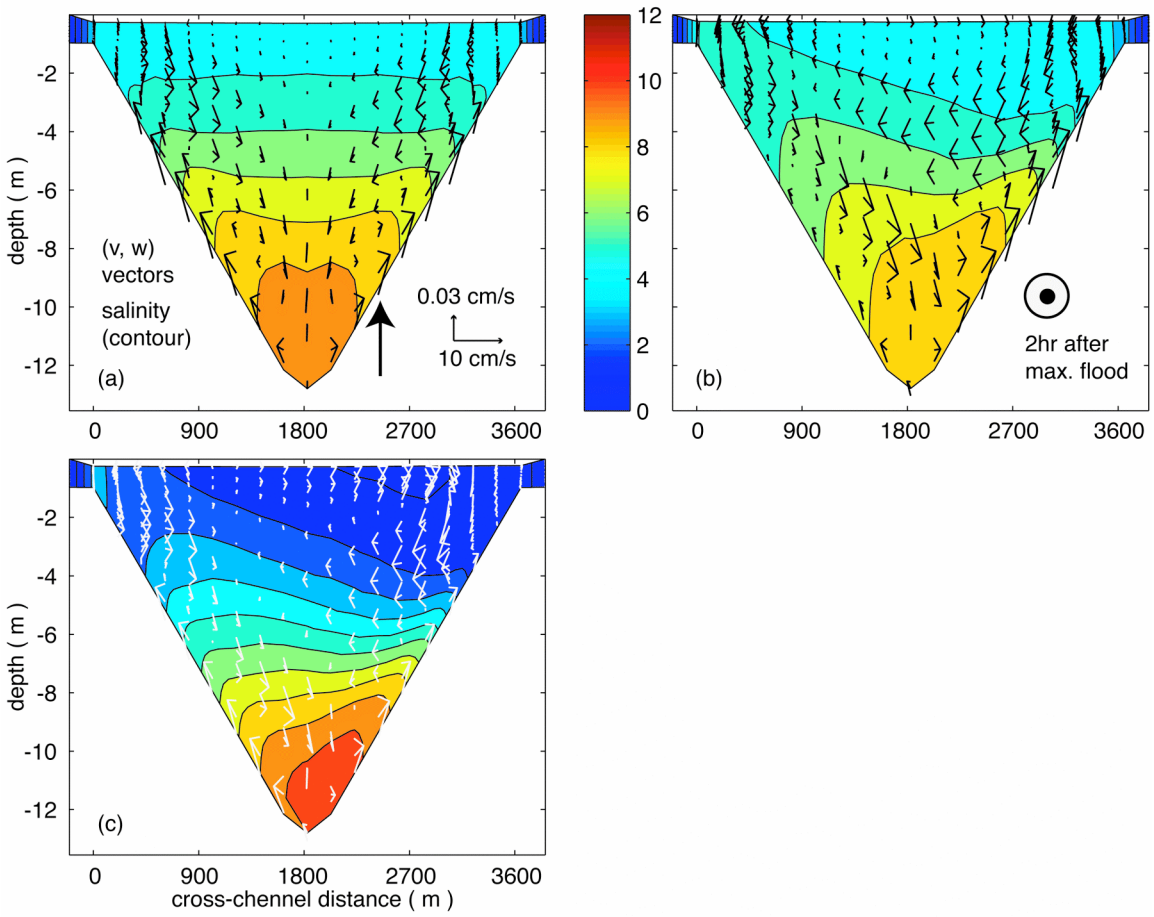

Fig. 4. Cross-sectional profiles of salinity (contoured) and lateral circulation (vectors) for (a) moderately-stratified without Coriolis forcing, (b) moderately-stratified with Coriolis forcing, and (c) highly-stratified with Coriolis forcing cases at 2-hours after maximum flood. All of the cross-sectional profiles presented in this paper are looking seaward. The arrowhead denotes a location off the channel (depth ~ 10 m, 0.8 m above the bottom) where time series of lateral flow velocity are obtained.

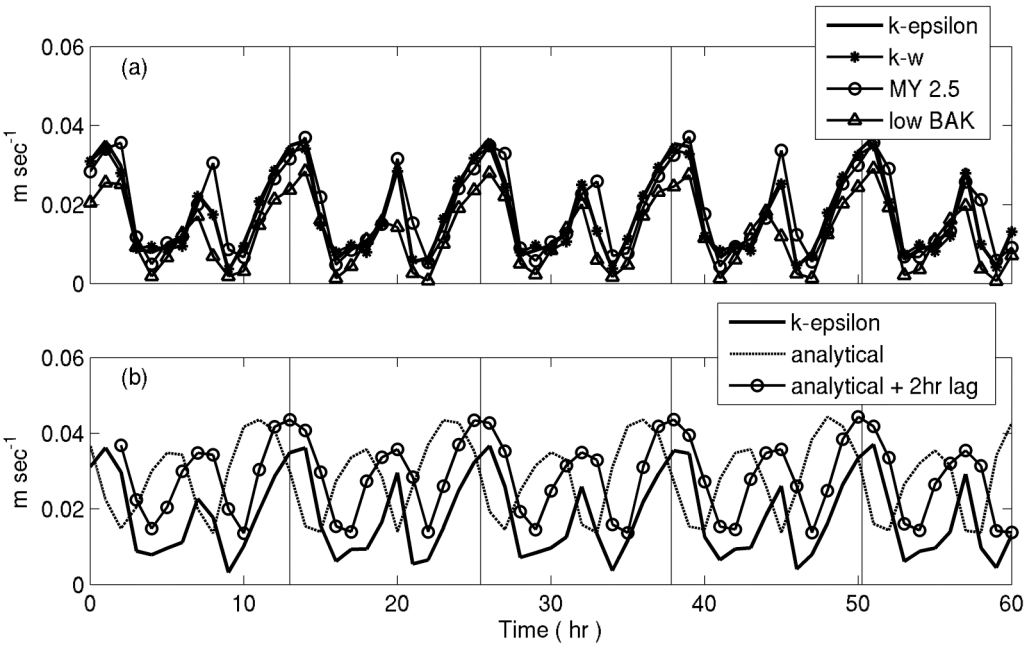

Fig. 5. (a) Comparison of time series of lateral flow velocity with three different turbulence closures and a run with lower background diffusivity of $5x10^{-6}$ (triangle) under the moderately-stratified condition and without Coriolis forcing. In (b) under the same forcing, time series of lateral flow predicted by the model with k-epsilon closure (thick solid line) are plotted against an steady state analytical solution of boundary-mixing-driven flows using tidally-varying eddy viscosities from the model without a 2-hour lag (V_B: dashed line) and with a 2-hour lag (V_B + 2hr lag: thin solid line). The vertical lines are about 2-hour after maximum flood. Noted that the time series are taken at the off-channel location indicated by the arrowhead in Fig. 4 at 3/4 of the salt intrusion length. Positive values are up-slope.

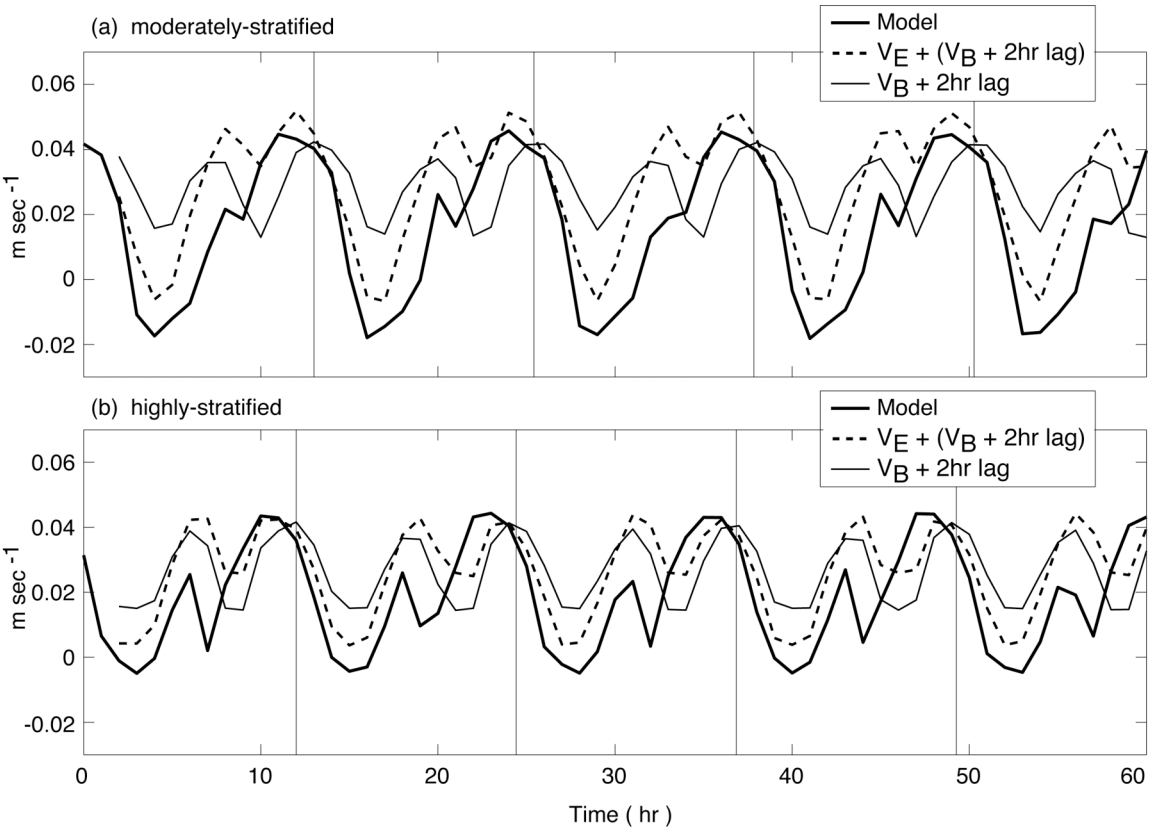

Fig. 6. Time series of lateral flow speed at the same location as in Fig. 5 under the (a) moderately-stratified and (b) highly-stratified conditions when Coriolis forcing is included. The thick solid lines are the model results. The thin solid lines are the analytical solutions for boundary mixing with a 2-hour lag (V_B + 2hr), whereas the dashed lines are linear superposition of two analytical solutions accounting for boundary-mixing-driven and Ekman-forced lateral flows (V_E + (V_B + 2hr)).

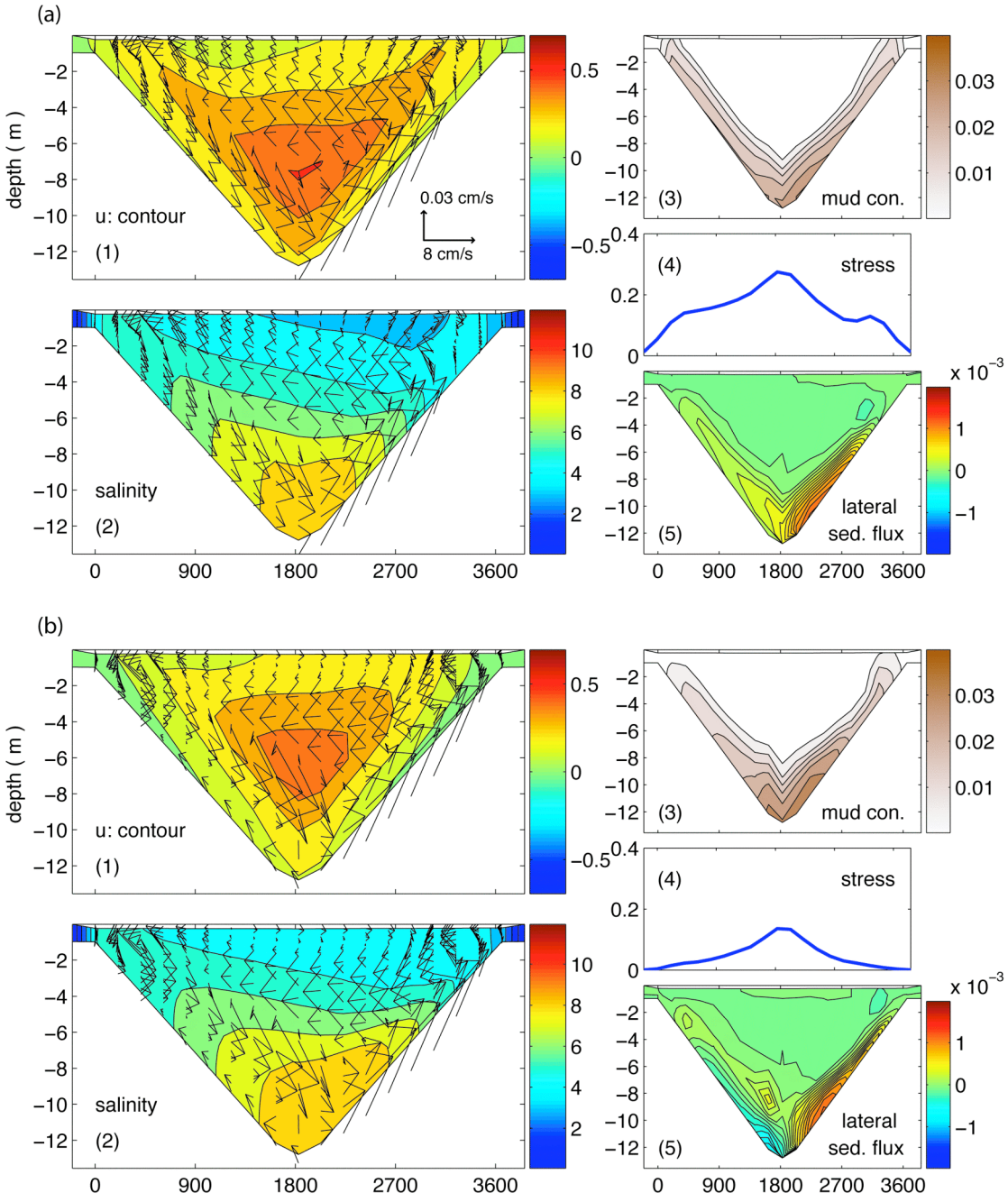

Fig. 7. Cross-sectional profiles of five quantities at the location seaward of the salt intrusion for the moderately-stratified case during (a) maximum flood, (b) 2-hour after maximum flood, (c) maximum ebb, and (d) 2-hour after maximum ebb. Each panel has 5 figures which are numbered from (1) to (5). The upper left (1) is velocity field (u, v, w). Negative values in the colorbar represent ebbs. The lower left (2) is salinity and (v, w). The upper right (3) is suspended sediment concentration (kg m^{-3}). The middle right (4) is bottom stress (Pa). The lower right (5) is lateral sediment flux (kg m^{-2} sec^{-1}). Positive values in the color bar represent transport toward the right slope.

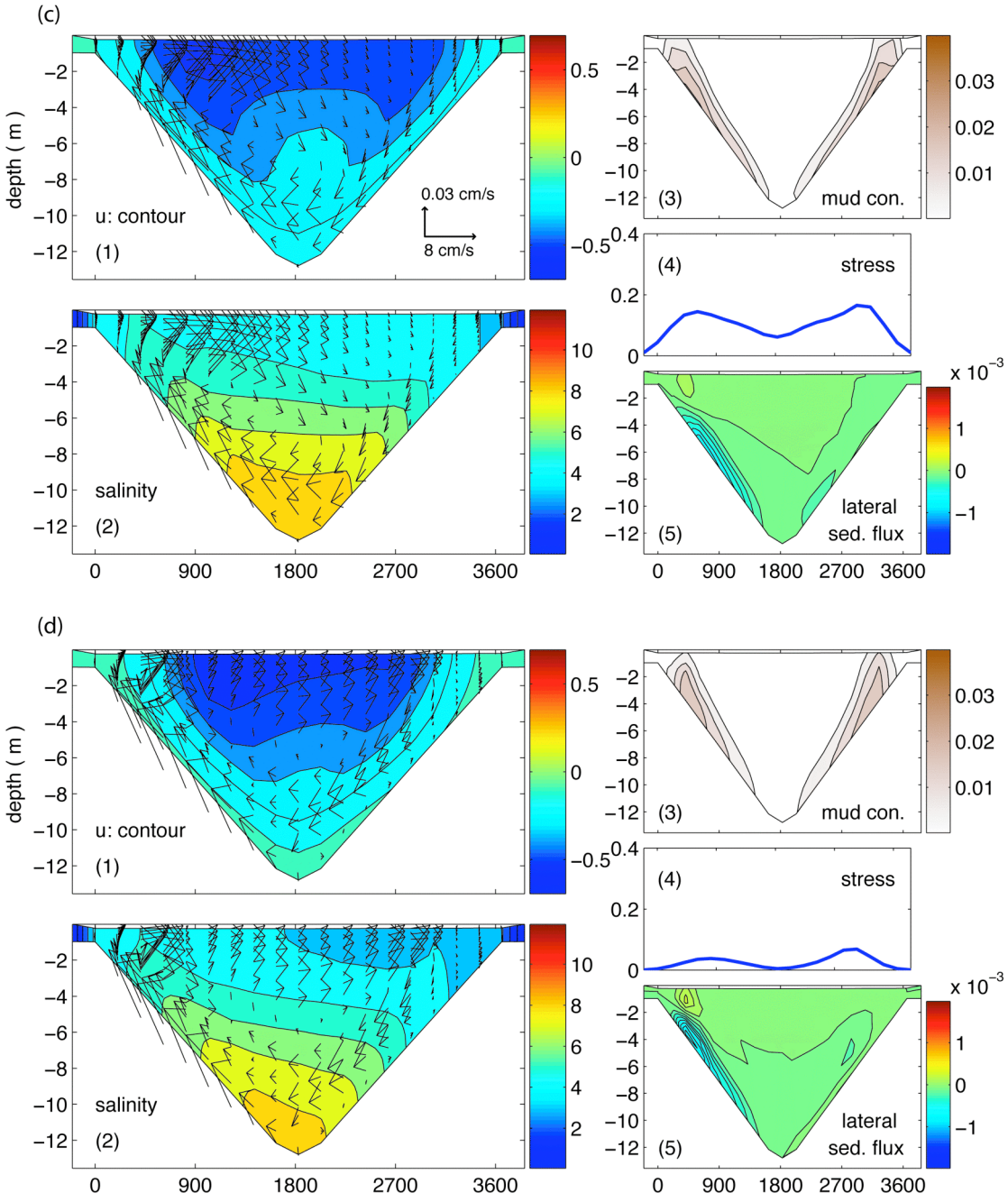

Fig. 7. Cross-sectional profiles of five quantities at the location seaward of the salt intrusion for the moderately-stratified case during (a) maximum flood, (b) 2-hour after maximum flood, (c) maximum ebb, and (d) 2-hour after maximum ebb. Each panel has 5 figures which are numbered from (1) to (5). The upper left (1) is velocity field (u, v, w). Negative values in the colorbar represent ebbs. The lower left (2) is salinity and (v, w). The upper right (3) is suspended sediment concentration (kg m^{-3}). The middle right (4) is bottom stress (Pa). The lower right (5) is lateral sediment flux (kg m^{-2} sec^{-1}). Positive values in the color bar represent transport toward the right slope.

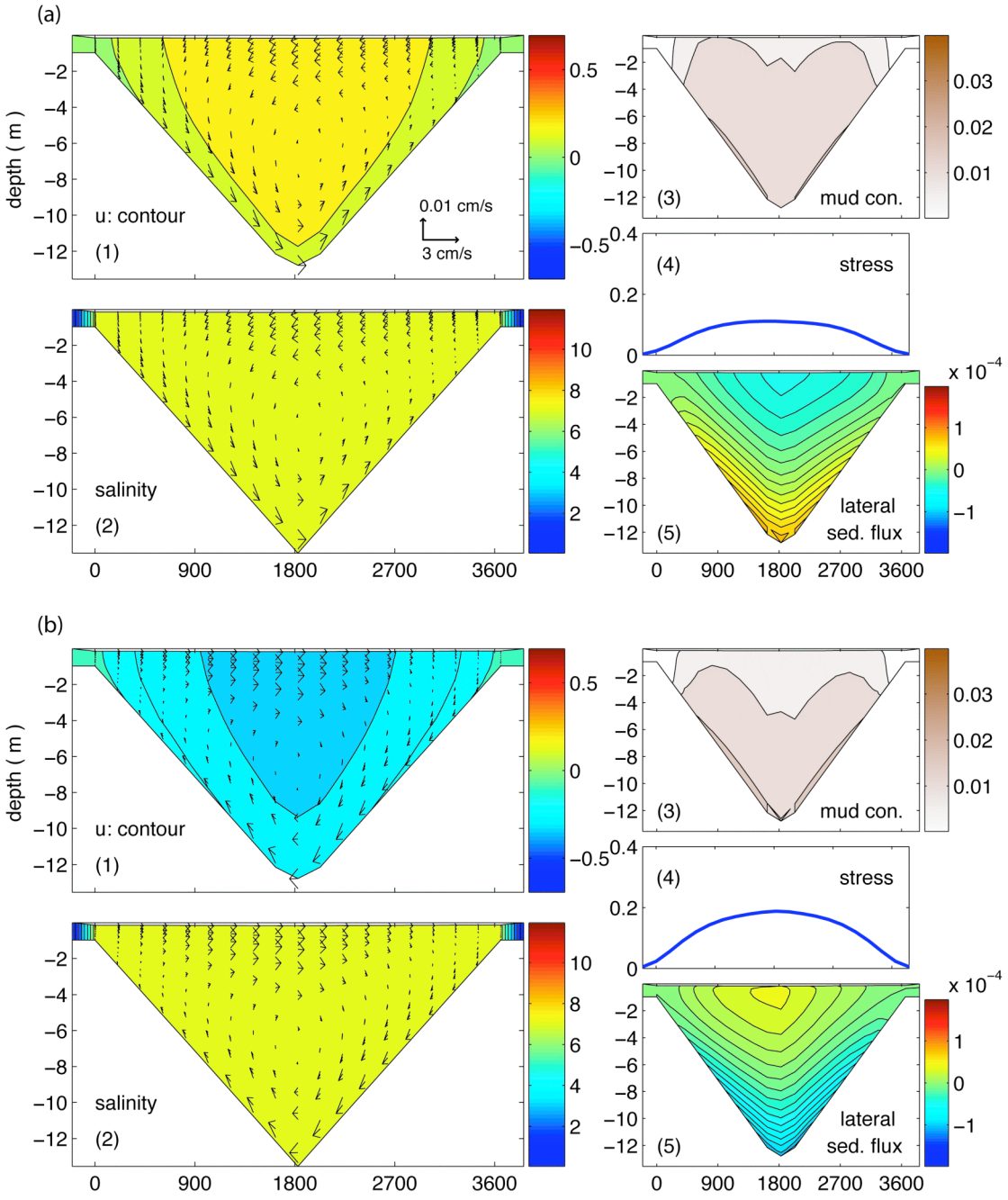

Fig. 8. Same as Fig. 7, but the cross-section is at the location landward of salt intrusion and only (a) maximum flood and (b) maximum ebb are plotted. Lateral sediment flux is one-order of magnitude smaller than that in Figure 7. Salinity at this tidal fresh cross-section (0) is offset by 7.5 for better visualization.

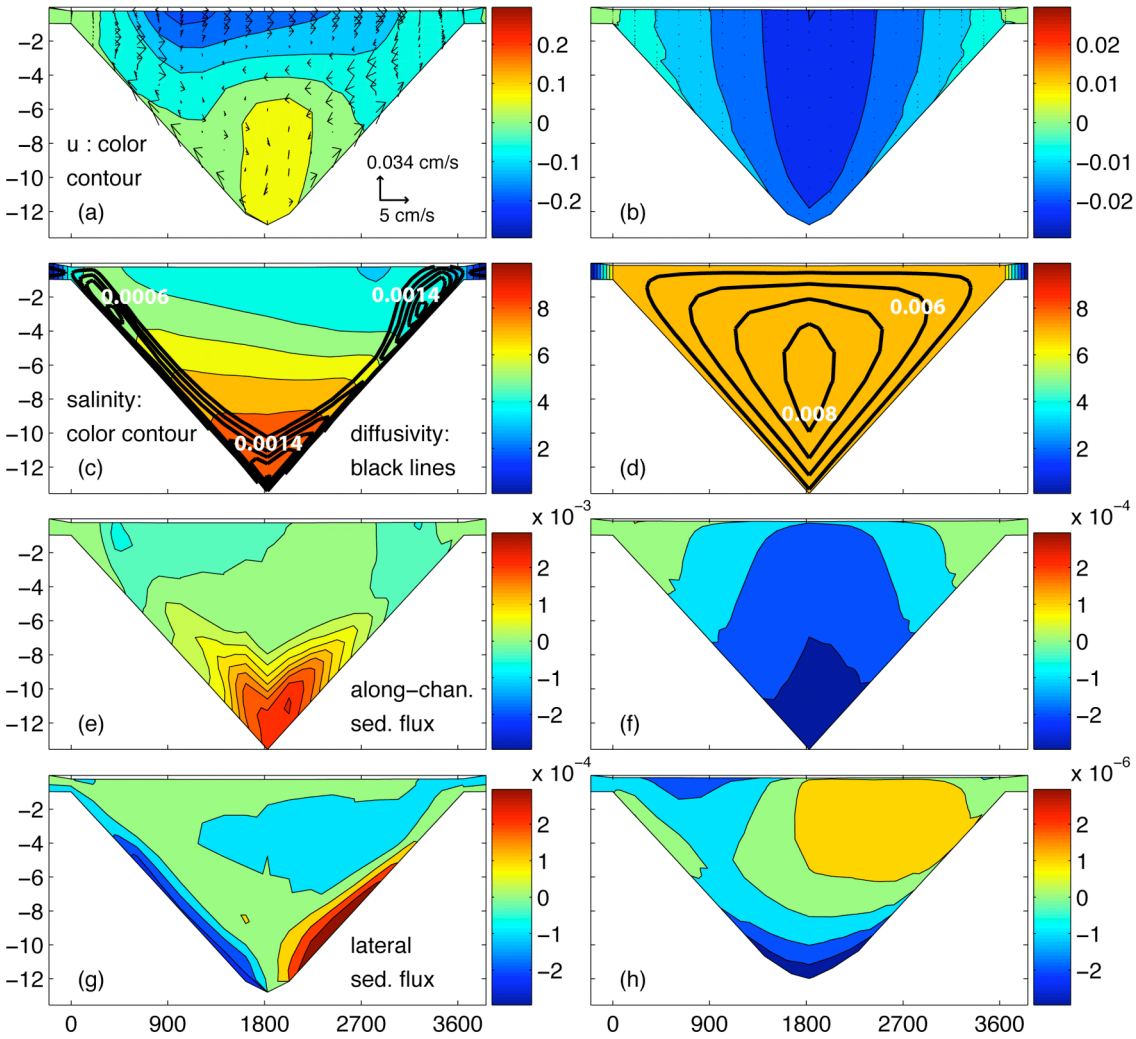

Fig. 9. Cross-sectional profiles of tidally-averaged velocity field (a and b; first row), salinity distribution (c and d; second row), longitudinal sediment fluxes (e and f; third row), and lateral sediment fluxes (g and h; forth row) at the locations seaward of salt intrusion (left column) and landward of salt intrusion (right column). These profiles are for the moderately-stratified case. Noted that color scales on the left and right columns are different. (a) and (e) are one-order of magnitude bigger than (b) and (f). (g) is two-orders of magnitude bigger than (h). In the second row, distributions of eddy diffusivity, indicated by thick black lines and white fonts, are superposed on top of the salinity distribution (color scale). Tidally averaged salinity landward of salt intrusion (d) is offset by 7.5 psu for better visualization.

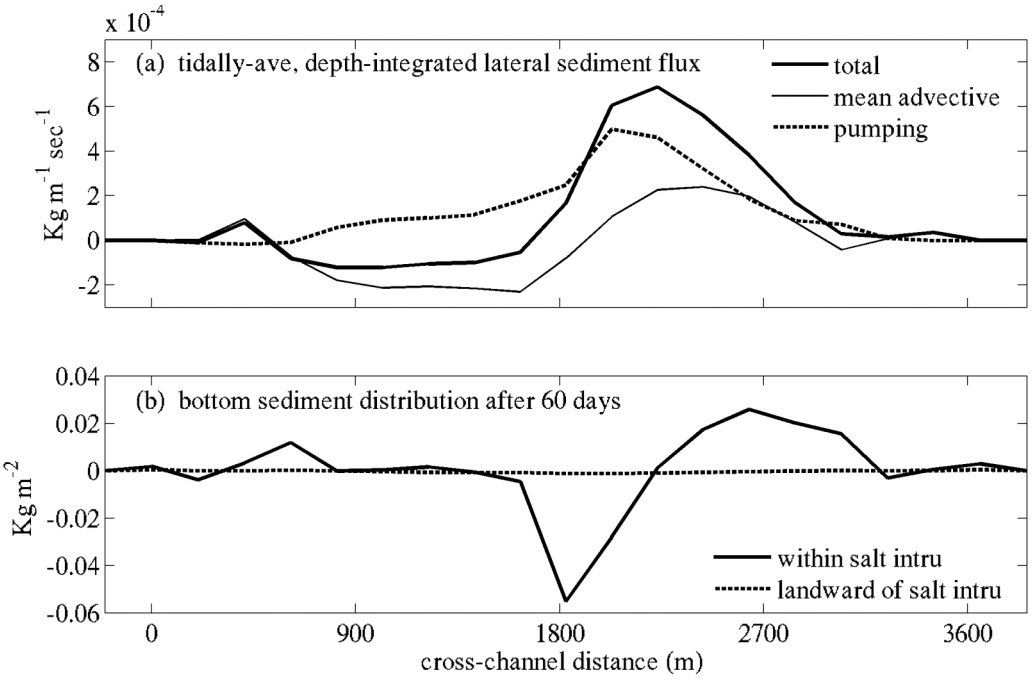

Fig. 10. (a) Decomposition the tidally-averaged, depth-integrated lateral sediment transport (thick solid line, $\int \overline{(v \cdot c)} dz$) into mean advective (thin solid line, $\int \bar{v} \cdot \bar{c} dz$) and tidal pumping (dashed, $\int \overline{(v' \cdot c')} dz$) components. v and c are lateral flows and suspended sediment concentration, respectively. The overbars denote tidal average, and the primes are tidal variations. (b) Comparison of changes in bottom sediment thickness in the cross-channel direction after 60-days model runs. Positive y-values represent net sediment deposition, whereas negative values represent net erosion. The solid and dashed lines are at the location seaward of and landward of salt intrusion, respectively.

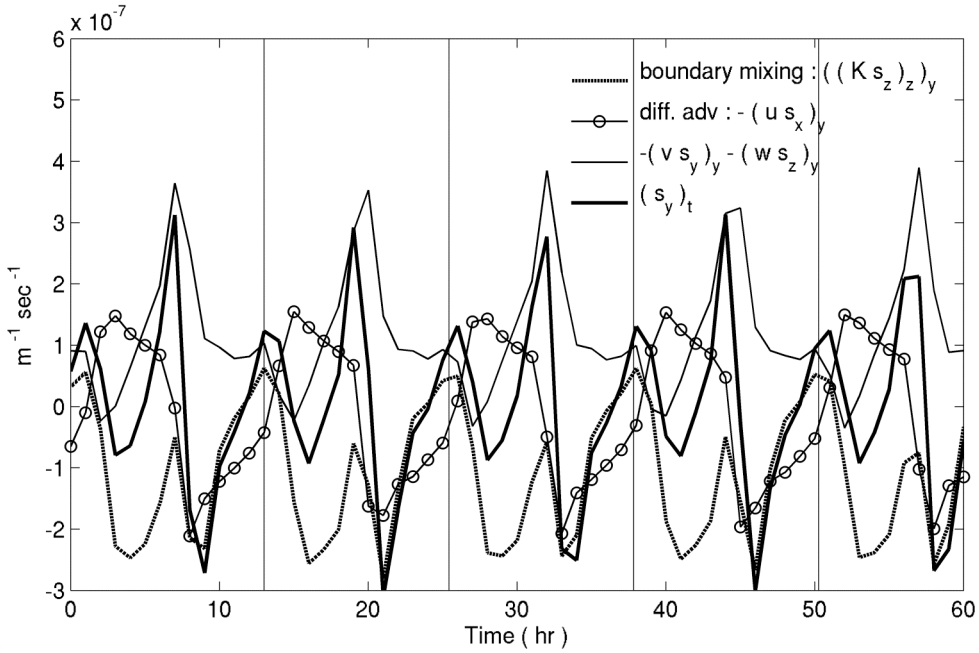

Fig. 11. Comparisons of the relative contribution from boundary mixing (dashed), differential advection (circle), and lateral advection (thin solid line) to the change rate of lateral salinity gradient (thick solid line; $(s_y)_t$). The Coriolis forcing is turned off, as in Fig. 4a (moderately-stratified). Each term is an average of the bottom 2 meters of the water column over all cross-channel locations where the total depth is over 4 m, on the right side of the channel. The vertical lines are about 2-hour after maximum flood.

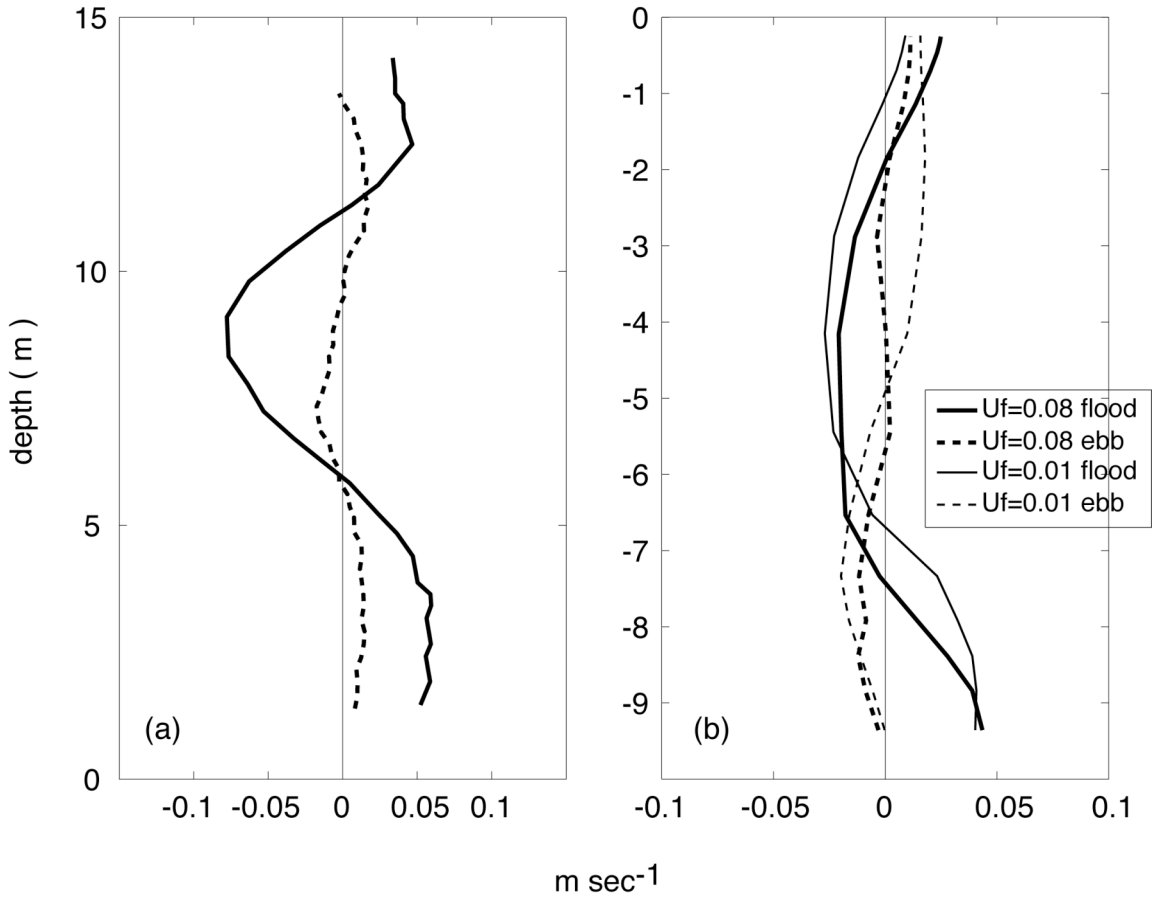

Fig. 12. Vertical profiles of lateral flows at an off-channel location (a) observed in the Hudson River estuary during neap tides at maximum flood (solid) and ebb (dashed) and (b) from the model. (a) is reproduced from Fig. 15 in Lerczak and Geyer (2004). In (b), thick and thin lines separate highly-stratified and moderately-stratified cases. The solid and dashed lines are at maximum flood and ebb, respectively.

Chapter 3

Axial wind effects on stratification and longitudinal salt transport in an idealized, partially mixed estuary[1]

[1]Chen, S.N., Sanford, L.P., 2008. Axial wind effects on stratification and longitudinal salt transport in an idealized, partially mixed estuary. submitted to Journal of Physical Oceanography

Abstract

A 3D hydrodynamic model (ROMS) is used to investigate how axial wind influences stratification and to explore the associated longitudinal salt transport in partially mixed estuaries. The model mimics a straight estuarine channel connecting to a shelf sea. Our results confirm wind straining due to wind-induced, sheared advection of salt. Two parameters are identified to govern the responses of stratification to wind forcing: the Wedderburn number (W) defined as the ratio of wind stress to axial baroclinic pressure gradient force, and the ratio of an entrainment depth to water depth (h_s/H). W controls the effectiveness of wind straining which favors increases/decreases in stratification during down/up-estuary wind. h_s/H determines the portion of the water column affected by direct wind mixing. While stratification is always reduced by up-estuary wind, stratification shows an increase-then-decrease transition when down-estuary wind stress increases. Such transition is a result of the competition between wind straining and direct wind mixing. A horizontal Richardson number modified to include wind straining/mixing is shown to reasonably represent the transition, and a regime diagram is proposed to classify wind's role on stratification. Mechanisms driving salt flux during axial wind events are also explored. At the onset and end of the wind events, barotropic adjustment drives strong transient salt fluxes. Net salt flux is controlled by the responses of subtidal shear dispersion to wind forcing. Moderate down-estuary winds enhance subtidal shear dispersion, whereas up-estuary winds always reduce it. Supporting observations from upper Chesapeake Bay are presented.

1. Introduction

Understanding the dynamics of stratification is of fundamental interest to estuarine research and management. Stratification has been shown to affect phytoplankton blooms (e.g Tyler and Seliger 1978; Cloern 1991), particle trapping in the estuarine turbidity maximum zone (e.g. Geyer 1993), and development/renewal of low dissolved oxygen zone in bottom waters (e.g. Kemp et al. 1992; Stanley and Nixon 1992) through limiting vertical exchange of water masses. More importantly, as illustrated by Knudsen's kinematic estuarine salt balance, stratification determines the volume transport of oceanic water into an estuary. The volume flux of oceanic water and degree of stratification then sets the flushing time of a system, which has important implications for many transport processes.

The classical picture of estuarine stratification depicts a competition between subtidal vertical shear (i.e. gravitational circulation) generated by an along-channel density gradient that tends to flatten the isopycnals and tidal mixing that tends to homogenize the water column (Hansen and Rattray 1965). Building on this foundation, several authors have shown variations of stratification over different time scales, such as the strain-induced periodic stratification (tidal straining) by Simpson et al. (1990) and variations over spring-neap cycles by Sharples et al. (1994) and Stacey et al. (2001).

Wind can modify estuarine stratification at weather-band frequency but its role seems to be ambiguous in the estuarine literature. Wind has long been considered to favor decreases in stratification. As demonstrated in laboratory by Kato and Phillips (1969), wind stress generates a turbulent boundary layer that propagates

downward to erode stratification (termed direct wind mixing here). Several observations and modeling work have documented destratification induced by storm events in estuaries (e.g. Goodrich et al. 1987; Blumberg and Goodrich 1990; Li et al. 2007). Recently, observations from the York River reported a contrary view of wind's role on stratification. Scully et al. (2005) found that estuarine exchange flow and stratification are highly correlated with episodic, axial wind. During moderate down-estuary wind, stratification and exchange flow are increased. During moderate up-estuary wind, opposite patterns occurred. To explain the observations, they proposed a wind straining mechanism: down-estuary wind enhances subtidal vertical shear (i.e. exchange flow), which strains the along-channel density density gradient to increase stratification; up-estuary wind reduces or even reverses the vertical shear, thus tending to decrease stratification.

The ambiguity of wind's role on stratification occurs for down-estuary wind. While down-estuary storm events completely destratified the water column (Goodrich et al. 1987; Li et al. 2007), moderate down-estuary wind increased stratification via wind straining (Scully et al. 2005). This inconsistency implies that there may be a transition from increasing to decreasing stratification by down-estuary wind, depending on wind stress magnitude. It also suggests that axial wind may exert controls on stratification through at least two mechanisms: direct wind mixing and wind straining. Neither the variations of stratification with different wind stress magnitudes nor the interactions between direct wind mixing and wind straining have been systematically investigated. Besides, while the wind straining concept is simple and appealing, the supporting evidence provided by Scully et al. (2005) is based on

small subtidal variations. The reported top-bottom salinity variations were less than 0.8 psu during the 2002 experiment and were at most 1~2 psu in 2003. Heterogeneous advection induced by topographic features in the field and/or spring-neap modulation of tidal mixing may easily bias the results. Thus, the validity of the wind straining mechanism also requires further investigation.

Several studies have shown the significance of wind-driven signals on subtidal flows in estuarine environments (e.g. Weisberg 1976; Wang 1979). Given the wind control on stratification and exchange flow, one would speculate that wind could significantly modulate salt transport. The variability of salt transport will ultimately affect exchange flow because it governs the variability of salt intrusion and thus the large scale salt gradient that drives gravitational circulation. Compared with extensive literature on the salt transport variability induced by spring-neap cycle and seasonal variations in freshwater discharge (e.g. Lewis and Lewis 1983; MacCready 1999; Monismith et al. 2002; Bowen and Geyer 2003; Lerczak et al. 2006), studies of wind-induced salt transport are surprisingly few (Wong and Moses-Hall 1998; Zheng and Weisberg 2006), and the driving mechanism of this transport is not sufficiently documented.

Here, we carry out numerical experiments to investigate three main questions outlined above. We aim to verify the wind straining mechanism, clarify the role of axial wind on stratification, and further explore the salt transport associated with wind. We adopt idealized bathymetry and forcing conditions to reduce complexity but retain turbulence closures to better parameterize mixing. Using a process-based approach, we demonstrate in section 3 that wind control on stratification is largely

determined by interactions between wind straining and direct wind mixing. A horizontal Richardson number modified to include these two effects is shown to reasonably represent wind-induced variations in stratification. In section 4, we decompose the salt flux to separate different salt transport mechanisms affected by wind. The idealized model allows us to focus on the local wind effects, contrasting the study by Wong and Moses-Hall (1998), in which subtidal salt flux results from a mixture of local wind and remote sea-level fluctuations. Finally, a regime diagram to classify axial wind effects on estuarine vertical stratification is proposed.

2. Numerical model

We use the Regional Ocean Model System (ROMS; Haidvogel et al. 2000) to simulate an idealized estuarine channel. ROMS is a hydrostatic, primitive equation model using a curvilinear grid in the horizontal and a stretched, terrain-following coordinate in the vertical. It has been widely used by the coastal ocean modeling community and is capable of simulating many estuarine flows with high skill (e.g. Warner et al. 2005; Li et al. 2005). The model setup here is a slight modification from that described in Chen and Sanford (in press). The model domain consists of a straight estuarine channel and a wide inner shelf (Fig. 1). The size of the shelf is 80 km across shelf x 48 km along-shelf with a constant slope from 200 m at the offshore boundary to 4 m at the shoreline. A 2.8 km-wide estuarine channel intersects the shelf and extends from x=80 km to 400 km. The cross-section is triangular shape with a maximum depth of 14 m in the channel and a minimum depth of 4 m on the sides. This bathymetry is a crude representation of Chesapeake Bay and the channel length

is similar, which allows us to compare the numerical results with the observed response of salt intrusion to wind (see section 4). The grid configuration is 194 (along-channel, x-direction) x 103 (cross-channel, y-direction) x 20 (vertical levels). The vertical levels are stretched with a lowest vertical resolution in the channel of 0.75 m. The estuary is highly resolved ($\Delta x \sim 2$ km, $\Delta y \sim 200$ m). Outside of this area, the grid is telescoped in the cross-channel direction ($\Delta y \sim 1.5$ km) to obtain a bigger salt pool on the shelf without increasing computational cost.

The model is forced by M2 tides from the shelf boundaries and by a constant freshwater flux from the river end (river flow of 0.01 m sec^{-1}). The tidal forcing is achieved by a combination of the Chapman condition for free-surface and the Flather condition for depth-averaged, boundary-normal velocity (Marchesiello et al. 2001). The resulting tide is largely progressive in the region with salt, and the tidal current amplitude is about 0.6 m sec^{-1} in the middle of estuary (half of the salt intrusion). A weak coastal current (~ 0.05 m sec^{-1}) is specified on the shelf to transport the river plume. Temperature is fixed at 15º C throughout the domain. Salinity at the river end is set to 0, whereas at the shelf boundaries salinity is nudged to an oceanic value of 32. The $k-\varepsilon$ turbulence closure (Jones and Launder 1972) is activated with a stability function proposed by Canuto et al. 2001). The $k-\varepsilon$ closure has been shown to perform well for estuarine flows (Burchard and Baumert 1998; Warner et al. 2005). Bottom stress is computed by assuming a logarithmic velocity profile in the lowest computational cell and a constant bottom roughness parameter (z_0) of 0.5mm. The salt field reaches a steady structure periodically modulated by tides in about 120 days.

After the salt structure reaches a steady state, we then perform numerical experiments (Table 1) to investigate axial wind effects on stratification and salt flux. The baseline case (No. 0) is the simplest possible condition: no wind and no Coriolis acceleration. It represents a typical partially-mixed estuary (Fig. 2). The length of estuary, defined by the distance between 2 and 30 psu tidally averaged isohalines in the channel, is about 145 km. At the middle of estuary (denoted by a vertical line in Fig. 2a), the tidally averaged top-bottom salinity difference is 4.5 psu (maximum buoyancy frequency squared is 0.004 sec^{-1}). The vertical profile of tidally averaged, along-channel velocity (Fig. 2b) is as expected consistent with gravitational circulation, with a landward flow near bottom and a seaward flow near surface.

There are 18 wind perturbation experiments (No. 1~18 in Table 1), in which we change wind magnitude, direction and turn on/off Coriolis acceleration while keeping the duration of wind event constant (3 day). The last two scenarios (No. 17 and 18) are with Coriolis acceleration. Our focus here is on axial wind effects. Therefore, the wind direction is either up-estuary (positive) or down-estuary (negative). The wind magnitudes range from one order of magnitude smaller (0.01 Pa) to 2.5 times larger (0.3 Pa) than the appropriately scaled along-channel density gradient. We use the along-channel density gradient as a reference because it is the main driving force to stratify the water column in partially-mixed estuaries. The relative importance between wind stress and scaled baroclinic pressure gradient force forms a non-dimensional parameter, named the Wedderburn number (Monismith 1986).

$$W = \frac{\tau_{wx} L}{\Delta \rho g H^2} \tag{1}$$

where τ_{wx} is the along-channel wind stress (positive is up-estuary), L is the length of the estuary, $\Delta\rho$ is the density change over L, g is the gravitational acceleration, and H is the averaged depth. The Wedderburn number may also be interpreted as the relative strength of wind-driven and gravitational circulations on estuarine residual flows (Geyer 1997). Experiment No. 7 with W equal to -0.85, for example, represents a 3-day down-eatuary wind event with comparable gravitational and wind-driven circulations.

3. Control of wind straining on vertical stratification

3.1. Response of salinity and exchange flow to down and up-estuary wind

To examine wind effects on stratification and exchange flow, we contrast three representative cases for down-estuary (Fig. 3) and up-estuary (Fig. 4) wind. Cases 1 and 2 represent weak wind (Figs. 3a and 4a), cases 7 and 8 represent moderate wind (Figs. 3b and 4b), and cases 15 and 16 represent strong wind (Figs. 3c and 4c). The corresponding Wedderburn numbers represent three categories: $|W| << O(1)$, $\sim O(1)$, and $> O(1)$. Figs. 3 and 4 show snapshots of the along-channel salt distributions during the events, time series of the exchange flow and low-passed maximum buoyancy frequency squared (N^2), and calculated horizontal Richardson numbers (see section 3.2 below). The exchange flow here is calculated as the 33hr low-passed filtered axial velocity at 1 meter above bottom (mab) in the channel minus the equivalent surface velocity.

As down-estuary wind stress increases, both stratification and exchange flow show an increase-then-decrease transition. The along-channel salinity structure during

the weak down-estuary wind (top panel of Fig. 3a) is very similar to the baseline case without wind (Fig. 2). But, during moderate and strong wind (Fig. 3b and 3c) the salinity structures are radically different from the baseline case. The water column is more stratified during moderate down-estuary wind but almost vertically well-mixed during strong down-estuary wind. The increase-then-decrease transition can be seen clearly from the time series. During weak down-estuary wind, both exchange flow and stratification (N^2) increase slightly. During moderate down-estuary wind, N^2 doubles and exchange flow increases from 0.27 to 0.45 (m sec^{-1}). When down-estuary wind stress is 0.3 Pa, N^2 decreases almost to zero and exchange flow decreases to 0.2 m sec^{-1} after a transient pulse. The wave-like fluctuations (pulses) in exchange flow near the onset and the end of events are associated with sea level adjustment to wind forcing (see section 4).

The increase-then-decrease transition is likely the result of competitions between wind straining and direct wind mixing induced by down-estuary wind. Wind straining is accomplished by horizontal advection of salt by wind-forced vertical shear. Scully et al. (2005) proposed that in shallow estuaries down-estuary/up-estuary wind can enhance/reduce exchange flow (i.e. stratifying subtidal vertical shear), which then strains the along-channel density field to increase/decrease stratification. Direct wind mixing favors decreases in stratification as wind stress generates a turbulent boundary layer that propagates downward to erode stratification (Kato and Phillips 1969). For the moderate down-estuary wind case, the signature of wind mixing can be seen from the deepened surface mixed layer. However, the water column is more stratified because the tendency of increasing stratification by wind

straining dominates over the decreasing effects of direct wind mixing. Hence, the increased stratification and exchange flow are consistent with the wind straining patterns observed by Scully et al. (2005). When down-estuary wind stress continues to increase, at some point the stratifying horizontal advection of salt by wind straining can not resist vertical wind mixing. This then leads to decreases in stratification over the whole water column, as illustrated by the strong down-estuary wind case (Fig. 3c). From the time series, exchange flow and stratification co-vary. Near the event onset, a transient wind pulse initially enhances exchange flow and thus increases stratification via straining. As the surface mixed layer deepens with time (around day 129), the water column is mixed, which then feeds back to decrease exchange flow through increased vertical momentum exchange.

The up-estuary wind cases (Fig. 4) are less complicated than the down-estuary wind cases because wind straining and direct wind mixing both favors decreases in stratification. From the along-channel salinity structures and time series, stratification decreases with increases in up-estuary wind stress. Exchange flow follows the same trend because up-estuary wind drives two-layer circulation to oppose gravitational circulation and the well-mixed water column tends to reduce vertical shear. The competition between wind-driven and gravitational circulation is evident during moderate and strong up-estuary wind ($W \sim$ and $> O(1)$) when the exchange flow decreases and reverses sign. Noted that the moderate down-estuary and up-estuary wind cases show very contrasting behaviors under the same wind stress magnitude. Moderate down-estuary wind increases stratification and exchange flow, whereas

moderate up-estuary wind decreases them. Such results highlight the importance of wind straining for regulating stratification.

Axial wind induces not only vertical but also lateral variations in subtidal axial flow and salinity. In a channel with a triangular cross section, the wind-driven flow is down-wind on the shoals and up-wind in the channel with a core of maximum velocity located at the lower half of the water column (Csanady 1973; Wong 1994; Sanay and Valle-Levinson 2005). Without wind, the lateral structure of the subtidal axial flow at the channel midpoint is consistent with vertically segregated gravitational circulation (Fig. 5a). Weak down- and up-estuary winds have a negligible effect on axial flow and stratification (not shown). During moderate down-estuary wind, the vertically segregated exchange is strengthened because wind-driven flow and gravitational circulation are in concert (Fig. 5c). The lateral salinity distribution shows a sharpened halocline and a surface mixed layer (Fig. 5d). These correspond to the increased exchange flow and low-passed N^2 in Fig. 3b. During strong down-estuary wind, in contrast, the subtidal axial flow becomes more laterally segregated and its magnitude is weakened (Fig. 5e). The lateral segregation is consistent with Csanady's analytical solution for wind-driven flow over laterally varying bathymetry, indicating that wind-driven axial flow dominates over gravitational circulation (W~2.5). The weakened axial flow is mainly due to strong vertical mixing, as shown in Fig. 5f. The laterally sheared flow then advects the salinity field to generate a lateral salinity gradient (Fig. 5f). The lateral salinity gradient could also contribute to re-stratification when wind forcing relaxes. During moderate up-estuary wind, the subtidal axial flow is very weak over the whole

channel cross-section because wind-driven flow nearly cancels gravitational circulation (W~0.85; Fig. 5g). The homogeneous salinity distribution is due to a combination of the uniform axial flow and the tendency of mixing aided by wind straining and direct wind mixing (Fig. 5h). The lateral structures during strong up-estuary wind (not shown) are very similar to the moderate up-estuary wind case but with larger flow magnitude (-0.1 m sec^{-1}) and a slightly smaller core of down-estuary flow (gray area).

Next we examine the mechanisms through which axial wind forcing modifies salinity structure. Turbulent mixing is diagnosed with the eddy viscosity profile. In Fig. 6, we compare the time evolutions of instantaneous salinity and eddy viscosity between the moderate to strong down-estuary and up-estuary wind cases at the channel midpoint. In all of the cases, turbulent mixing appears to be initiated from the boundaries. Before wind events (day 127~128), eddy viscosity fluctuates at the M4 frequency with higher values near bottom during flood, indicating that turbulent energy is generated in the tidal bottom boundary layer. During wind events, in all of the cases eddy viscosity near surface increases as the surface mixed layer is deepened. For the moderate down-estuary wind (Fig. 6a), wind straining dominates over direct wind mixing, leading to increases in stratification. The sharpened halocline at the mid-depth damps turbulence extending from the boundaries and thus results in strong mixing concentrating in the surface and bottom boundary layer. For the strong down-estuary wind case (Fig. 6b), on the other hand, wind mixing dominates and the water column is vertically well-mixed. The surface boundary layer appears to have reached mid-depth, and the surface and bottom layers merge when turbulence from the bottom

is intensified (bottom panel of Fig. 6b). The highest eddy viscosity reaches 10^{-2} m^2 sec. Based on Hansen and Rattray (1965), exchange flow is inversely related to effective eddy viscosity. This order-of-magnitude increase in eddy viscosity is therefore consistent with decreases in exchange flow shown by Fig. 3c.

The eddy viscosity profiles during up-estuary wind also suggest turbulence initiated from the boundaries. During moderate and strong up-estuary wind, the water column is rapidly mixed because wind straining and direct wind mixing are working in concert (Figs. 6c and 6d). During the moderate up-estuary wind event, the elevated eddy viscosity near surface and bottom merge at M4 frequency from day 130 (Fig. 6c). This indicates that weak stratification allows turbulence generated from the boundaries to fill the water column. The profiles during moderate and strong up-estuary wind are similar. As up-estuary wind stress increases, the surface boundary layer is deeper (Fig. 6d) and the water column is homogenized right after event onsets (Fig. 6d). These allow turbulence from the boundaries to fill the water column over the whole event period. It is evident that eddy viscosity during the events is much larger than before/after the events. This large eddy viscosity again tends to retard the exchange flows.

3.2. A modified horizontal Richardson number

The above analyses suggest that axial wind could have at least two effects on estuarine stratification: straining via vertically (and/or laterally) sheared advection of salt and direct vertical mixing through turbulent erosion. While direct wind mixing favors decreases in stratification, wind straining could either increase or decrease

stratification, depending on wind direction. During down-estuary wind, wind straining tends to increase stratification and thus competes with direct wind mixing. Opposite behaviors happen during up-estuary wind.

It is natural to ask if we can describe the interaction between straining and mixing to form a parameter to represent the wind-induced variations in stratification. An analysis of estuarine stratification for pure tidal processes by Stacey et al. (2001) provides a scaling foundation to start with. Following Stacey et al. (2001) and assuming that vertical/lateral advection and horizontal diffusion are negligible, we obtain the evolution of vertical stratification ($\partial s/\partial z$) by taking z derivative of the salt transport equation:

$$\frac{\partial}{\partial t}(\frac{\partial s}{\partial z}) + \frac{\partial U}{\partial z}\frac{\partial s}{\partial x} = \frac{\partial^2}{\partial z^2}(K_s\frac{\partial s}{\partial z}), \tag{2}$$

where s is salinity, K_s is the vertical eddy diffusivity for salt, and U is the mean velocity profile. The second and third terms represents the vertically sheared advection of along-channel salinity gradient and vertical mixing, respectively. The relative importance of these two terms then controls the tendency to increase/decrease stratification, and the ratio of these two terms defines a horizontal Richardson number (Ri_x). To account for the axial wind effects on stratification, we need to include wind straining into the second term ($\partial U/\partial z \cdot \partial s/\partial x$) and direct wind mixing into the third term ($\partial^2/\partial z^2 (K_s \partial s/\partial z)$).

Equation (2) can be re-written in terms of buoyancy frequency (N) by multiplying ($-g\beta$) on both sides:

$$\frac{\partial N^2}{\partial t} + \frac{\partial U}{\partial z}N_x^2 = \frac{\partial^2}{\partial z^2}(K_s N^2), \tag{3}$$

where β is the saline expansivity and N_x^2 is defined as $-g\beta\partial s/\partial x$. To estimate the scales of the second and third terms, we integrate (3) twice vertically. The third term, $K_s N^2$, is the vertical buoyancy flux due to turbulent diffusion (B_{turb}). Assuming turbulence is mainly generated from the boundaries, the buoyancy flux may be expressed as turbulent shear production (P) multiplied by a flux Richardson number (R_f) (~0.2; Ivey and Imberger 1991). We further assume that, for the first order approximation, the total vertical buoyancy flux is a sum of the fluxes from surface and bottom boundary layers. Defining appropriate friction velocities near surface and bottom to be u_{*s} ($=\sqrt{\tau_{wx}/\rho}$) and u_{*b} ($=\sqrt{C_D}U_{rms}$) and water depth to be H, the appropriate scale for the vertical buoyancy flux is

$$B_{turb} \sim R_f P_s + R_f P_b = R_f\left(\frac{u_{*s}^3}{kh_s} + \frac{u_{*b}^3}{kh_b}\right) \sim \frac{u_{*s}^3 + u_{*b}^3}{H}. \quad (4)$$

where k is the von Karman constant and h_s and h_b are surface and bottom boundary layer thicknesses. Integrating the sheared advection term in (3) twice vertically yields the horizontal buoyancy flux (B_{shear}), and its scale may be written as

$$B_{shear} = \iint \frac{\partial U}{\partial z} N_x^2 dz dz \sim \Delta U H N_x^2, \quad (5)$$

where ΔU is the scale of vertical shear. Since our focus here is on the subtidal variations, the scale of vertical shear may be defined by the scale of estuarine exchange flow.

The ratio of vertically integrated sheared advection (5) to turbulent mixing (4) then determines a horizontal Richardson number modified to include axial wind straining and direct wind mixing ($Ri_{x,new}$):

$$\frac{B_{shear}}{B_{turb}} \sim \frac{\Delta U H N_x^2}{(u_{*s}^3 + u_{*b}^3)/H} \equiv (Ri_{x,new})^2. \quad (6)$$

In the absence of wind forcing (u_{*s}=0) and scaling the exchange flow by gravitational circulation ($\Delta U \sim H^2 N_x^2 / u_{*b}$), the $Ri_{x,new}$ reverts back to the original Ri_x ($=H^2 N_x^2 / u_*^2$) that was used to represent spring-neap variations in stratification by Stacey et al. (2001). The modified horizontal Richardson number $Ri_{x,new}$ is the ratio of vertically sheared advection of salt by gravitational and wind-driven circulation to tidal and wind mixing. Increasing sheared advection of salt (numerator) stratifies the water column, whereas increasing tidal and wind mixing (denominator) de-stratifies the water column. Therefore, $Ri_{x,new}$ and stratification should co-vary.

In the presence of wind forcing, the modified horizontal Richardson number $Ri_{x,new}$ is a reasonable representation for the variations in stratification. In the bottom panels of Fig. 3a,b,c and Fig. 4a,b,c, we contrast the time variations of two normalized horizontal Richardson numbers, one with wind corrections (solid line) and the other without wind corrections (dashed line). To obtain $Ri_{x,new}$ and Ri_x, we estimate N_x^2 using the distance between 2 and 30 psu isohalines, u_{*s} from wind stress, u_{*b} by $\sqrt{C_d} U_{rms}$ in which C_d is a drag coefficient (3×10^{-3}) and U_{rms} is the rms axial velocity at the lowest vertical grid point about 0.5 mab, and H as the depth in the channel. For all of the down- and up-estuary wind cases (Fig. 3 and Fig. 4), $Ri_{x,new}$ captures the general patterns of wind-induced variations in stratification. When axial wind is weak (Fig. 3a and 4a), $Ri_{x,new}$ shows minor changes, which is consistent with very little changes in stratification. During moderate down-estuary/up-estuary wind conditions, $Ri_{x,new}$ correctly represents increases/decreases in stratification (Fig. 3b

and 4b). Decreases in stratification during strong wind conditions when direct wind mixing dominates (Fig. 3c and 4c) are also captured by $Ri_{x,new}$. On the contrary, the original Ri_x without wind corrections does a poor job representing wind-induced variations in stratification. This is expected because the original Ri_x does not account for wind-induced exchange flow (i.e. straining) and only partially include wind mixing through modified rms axial velocity (u_{*_b}). Above all, the exercises here demonstrate that a horizontal Richardson number modified to include the wind straining/mixing can reasonably represent the variations in stratification. This gives us confidence that our interpretation of axial wind controls on stratification through interactions between wind straining (numerator in Eq. 6) and direct wind mixing (denominator in Eq. 6) is likely correct at least to first order.

4. Influences of axial wind on longitudinal salt flux

In section 3, we have shown that the episodic wind events of a comparable wind stress magnitude with longitudinal density gradient ($W \sim$ and $> O(1)$) can substantially modify subtidal flow and salinity fields. Questions to be addressed next are how episodic, axial wind affects longitudinal salt transport and how an estuary responds. Assessing wind influences on salt transport is fundamental to estuarine dynamics as salt transport controls estuarine length and thus gravitational circulation. Here we choose moderate down- and up-estuary wind as two examples because they show contrasting behaviors in stratification and exchange flow (Fig. 3b and 4b).

4.1. Salt flux decomposition

We decompose the salt flux to gain insight into the driving mechanism of salt transport. The subtidal total salt flux (F_s) is calculated at the midpoint of salt intrusion and is given by

$$F_S = \left\langle \iint uSdA \right\rangle, \tag{7}$$

where the angle bracket is a 33 hr low-passed filter, u is axial velocity, S is salinity, and the cross-sectional integral within the angle bracket represents the instantaneous salt flux. Following Lerczak et al. (2006), the total salt flux is expressed by

$$\begin{aligned} F_S &= \left\langle \iint (u_0 + u_E + u_T)(S_0 + S_E + S_T)dA \right\rangle \\ &\approx \left\langle \iint u_0 S_0 + u_E S_E + u_T S_T dA \right\rangle = Q_f S_0 + F_E + F_T \end{aligned}, \tag{8}$$

in which u and S are decomposed into tidally and cross-sectionally averaged (u_0 and S_0), tidally averaged and cross-sectionally varying (u_E and S_E), and tidally and cross-sectionally varying (u_T and S_T) components. u_0 is defined as the low-passed volume transport divided by the low-passed cross-sectional area. Therefore, Q_f includes the volume transport resulting from correlations between tidal currents and fluctuations in the cross-sectional area (Stokes transport). Without wind forcing, Q_f is negative and equal to the river discharge, but it is not always negative in the presence of wind.

The resulting three terms in Eq. (8) are the salt fluxes due to subtidal cross-sectionally averaged transport ($Q_f S_0$), subtidal shear dispersion (F_E), and tidal oscillatory salt flux (F_T). The salt loss due to river discharge is included in $Q_f S_0$. The salt flux resulting from gravitational circulation is represented by the subtidal shear dispersion. Gravitational circulation advects saltier water up-estuary near bottom and fresher water down-estuary near surface. Thus, its net contribution is usually down-gradient (up-estuary here). Steady wind-driven circulation, which has vertical and

lateral structures (e.g. Fig. 4), also contributes to subtidal shear dispersion. The salt fluxes owing to temporal correlations between u and S are collected into the tidal oscillatory flux (Lerczak et al. 2006). Reducing the total salt flux to three terms in Eq. (8) is a good approximation (estimated error ~12%) because there is no physical reason to expect correlations between terms like $u_E S_T$ (Hunkins 1981; Dyer 1997).

4.2. Axial wind effects on salt flux

The instantaneous salt flux fluctuates with tides, and the modulation by wind is clear in Fig. 7a and 7b. The net effects of moderate axial wind events can be better visualized after removing tides. As defined in Eq. (8), the subtidal total salt flux F_S is the summation of subtidal cross-sectionally averaged transport $Q_f S_0$ (Fig. 7e and 7f), subtidal shear dispersion F_E (Fig. 7c and 7d), and tidally oscillatory flux F_T (Fig 7c and 7d). The subtidal total salt fluxes F_S show two strong pulses with an opposite sign at the onset and the end of the events. Before the wind events, F_S vanishes, indicating that the system is at a steady state. The steady condition is achieved by two down-gradient salt fluxes (F_E and F_T) balancing the salt loss to river discharge ($Q_f S_0 <0$). In the absence of wind, the subtidal shear dispersion, which is mainly contributed from gravitational circulation, dominates the down-gradient salt flux ($F_E/F_T \approx 5$).

The salt flux decomposition reveals that the two pulses in the subtidal total salt flux F_S result from subtidal cross-sectionally averaged transport $Q_f S_0$ (Fig. 7e and 7f). This transport is associated with sea-level (barotropic) adjustment. At the onset of the down-estuary wind, net volume transport is down-estuary as sea level sets down, and salt is flushed out of the estuary. At the end of the event, the sea level relaxes and

salt is transported into the estuary. Each pulse is damped and has a period of roughly 2.3 days (e.g. two local maximums at day 131.7 and 134 in Fig. 7e). This period is similar to the period of the first seiche mode for Chesapeake Bay (Wang 1979), which has a similar channel length. Using a channel length of 320 km and cross-sectionally averaged water depth of 9 m, an estimate of the period of the first seiche mode without frictional damping yields a comparable value of 1.6 day. These results suggest that the two transient pulses of salt transport are most likely due to a damped, first mode barotropic seiche. The damping of the transient seiche is further confirmed when the subtidal volume flux Q_f reverts back to the value of river discharge about 3-days after the event onset with an increased event duration to 10 days (not shown here).

Subtidal shear dispersion increases during the moderate down-estuary wind event but is shut down during the moderate up-estuary wind event (Fig. 7c and 7d). The increased F_E is expected because moderate down-estuary wind enhances estuarine exchange flow (u_E) and increases stratification (S_E) as wind straining out-competes direct wind mixing (Fig. 3b). On the other hand, moderate up-estuary wind shuts down the subtidal shear dispersion because the water column is largely homogenized so that the weakened exchange flow can not drive net salt flux (Fig. 4b). In both cases, there are oscillations in F_E, which are attributed to the adjustment of exchange flow and stratification to the pulsed wind events (middle panels of Fig. 3b and 4b). Contrasting to radically different responses of the subtidal shear dispersion F_E to moderate down- and up-estuary wind, the tidal oscillatory fluxes F_T stay relatively steady during the events.

4.3. Salt content and intrusion length

Following Lerczak et al. (2006), the subtidal, one-dimensional, along-estuary salt conservation equation may be written as

$$A_0(x)\frac{\partial S_0}{\partial t} = -\frac{\partial}{\partial x}\left[Q_f S_0 - A_0 K(x)\frac{\partial S_0}{\partial x}\right], \tag{9}$$

where A_0 is the subtidal cross-sectional area and K is the longitudinal dispersion coefficient which parameterizes the down-gradient salt fluxes (F_E and F_T) as a whole. Thus, the summation of the terms within the bracket represents the subtidal total salt flux F_S at a given location x along the estuary. Integrating Eq. (9) from the channel midpoint up-estuary to a location beyond the salt intrusion yields the change rate of the salt content (M_S) within this range:

$$\frac{\partial M_S}{\partial t} = Q_f S_0 - A_0 K(x)\frac{\partial S_0}{\partial x} = Q_f S_0 + F_E + F_T . \tag{10}$$

Before the event, the system is at steady condition. The salt content change rate is zero. Therefore, the cumulative sum of $\partial M_S/\partial t$ gives the time evolution of the total salt content.

In Fig. 8a and 8b, the salt content change rate (thin solid lines) and salt content (thick solid lines) are plotted together. For the moderate down-estuary wind case (Fig. 8a), the estuary initially loses salt because sea level set-down drives a pulse of down-estuary salt flux ($Q_f S_0 <0$). After the initial pulse, Q_f adjusts back to the river discharge. When the sum of the up-estuary salt fluxes $F_E + F_T$ exceeds $Q_f S_0$ (day 129.3; F_S=0), the estuary starts to gain salt. The salt gain is indicated by the gradual increases of salt content in Fig. 8a. Near the end of the event, the down-estuary wind

ramps down. The relaxation of sea level drives a pulse of salt into estuary, accelerating the salt gain. This is shown by the steep increase of salt content at around day 131. For the moderate up-estuary case (Fig. 8b), the opposite patterns occur, except that the up-estuary salt fluxes (F_E and F_T) play an insignificant role in the total salt flux during the event because F_E is shut down by the up-estuary wind (well-mixed water column). Therefore, after the initial pulse of salt gain, the total salt flux is dictated by the river discharge, and the estuary loses salt.

The two transient pulses near the onset and the end of an event drive comparable salt fluxes in opposite directions. When integrating over an event, they largely cancel each other out. Thus, the responses of sutidal shear dispersion and tidally oscillatory flux to the wind forcing control the net salt gain or loss. In our system, the enhancement/shut-down of subtidal shear dispersion causes the net salt gain/salt loss over the 3-day moderate down-estuary/up-estuary wind event. It should be noted that the salt content decreases/increases very slowly after the moderate down-estuary/up-estuary wind events in order to adjust back to its initial steady condition. Taking the moderate down-estuary wind case as an example, the subtidal shear dispersion F_E decreases gradually after the event (Fig. 7c). About day 140, F_E has a value of 2.107×10^{-3} kg sec^{-1}, which is slightly smaller than the value at steady state (2.172×10^{-3}). This is partly because the estuary has more salt than its steady state, producing to a weaker along-channel salinity gradient. The weaker gradient then drives a slightly weaker gravitational circulation and thus weaker subtidal shear dispersion. The slight imbalance, as can be seen by the slightly negative salt content change rate in Fig. 8a, slowly moves the estuary back to its steady state.

Salt intrusion in the channel may not be a good indicator of the estuarine salt content. Fig. 8c and 8d show the time variations of 2psu locations in the channel (thin lines), on the shoal (dashed; depth of 5 m), and the lateral mean (thick lines) at 0.5 mab. For the down-estuary case, both 2psu locations in the channel and on the shoal capture the general pattern of changes in salt content in Fig. 8a. However, for the up-estuary wind case, the 2psu location in the channel shows an opposite pattern to the changes in salt content in Fig. 8b, while the 2psu location on the shoal displays the correct trend. The laterally averaged 2psu location appears to be a better indicator of the changes in salt content. Nevertheless, these results highlight the inherently three-dimensional nature of the salt structure.

5. Summary and discussion

5.1. Wind straining and direct wind mixing: A conceptual regime diagram

In section 3, we show that axial wind exerts controls on estuarine stratification through two ways: wind straining and direct wind mixing. In estuarine flows, the gravitational exchange driven by the along-channel density gradient plays a central role in maintaining stratification. Therefore, to obtain effective wind straining, the wind-induced exchange flow has to be comparable to gravitational exchange (e.g. Fig. 3). In other words, the Wedderburn number (W) which is a ratio of wind stress to along-channel baroclinic pressure gradient force (Eq. 1) should be a controlling parameter for the effectiveness of wind straining. As for direct wind mixing, one would expect that direct wind mixing prevails when the surface mixed layer occupies a large portion of the water column and merges with the tidal bottom mixed layer

(Fig. 3c and 4c). Thus, a ratio of surface mixed layer thickness to total water depth (h_s/H) may be an important parameter for direct wind mixing. We may use an entrainment depth (h_s; Trowbridge 1992) to represent the surface mixed layer thickness:

$$h_s = \sqrt{2\gamma Ri_c^{1/2} \frac{u_{*s}^2}{N_\infty} \Delta t} \tag{11}$$

where γ is a constant and has a value of 1.22, Ri_c is a critical gradient Richardson number, Δt is wind event duration, and N_∞ represents background stratification.

We then plot the changes in stratification (ΔN^2) and the modified horizontal Richardson number ($Ri_{x,new}$) against these two parameters (W and h_s/H) for all of the 16 non-rotating perturbation experiments in Table 1. We use the steady-state stratification (N_∞^2=0.0045) and one tidal period (Δt=12 hr) to estimate entrainment depth for each experiment. These values are chosen because the eddy viscosity near surface reaches a relatively steady value at roughly 12hr after the event onsets (Fig. 6). The $Ri_{x,new}$ is averaged over the event. For the down-estuary wind cases (Fig. 9a), an increase-then-decrease transition in stratification is clear. Stratification initially increases with $|W|$ (bottom x-axis) as wind straining becomes effective. After reaching a maximum at W around -0.85 and h_s/H around 0.65, stratification begins to decrease as direct wind mixing becomes increasingly important. Direct wind mixing dominates over wind straining and ΔN^2 becomes negative when the entrainment depth occupies the entire water column (h_s/H ~1). For the up-estuary wind cases (Fig. 9b), stratification continues to decrease as W increases and as h_s/H decreases because wind straining and direct wind mixing both favor destratification.

It can also be seen in Fig. 9 that $Ri_{x,new}$ reasonably captures the changes in stratification for both down- and up-estuary wind cases but tends to show steeper initial changes. The steeper changes may be because the average of $Ri_{x,new}$ over the event period includes transient changes in exchange flow (ΔU in Eq. 6). These transient changes at the event onset are strong pulses (e.g. ΔU in Fig. 3 and 4) that may overestimate wind straining effects. It should be noted that $Ri_{x,new}$ is based on a rather crude scaling. It parameterizes complex, time-dependent interactions between tides and wind. Thus, its validity requires further investigation.

Using W and h_s/H as two axes, we may construct a regime diagram to classify wind controls on stratification (Fig. 10). We then place several documented studies as well as our results on the diagram. The region of wind decreasing stratification (shaded) occupies the right quadrant because up-estuary wind tends to reduce or even reverse the stratifying vertical shear. It also extends to the upper part of the left quadrant (W<0, 0.5<h_s/H<1). The importance of direct wind mixing can increase because of either extreme down-estuary wind events (e.g. Goodrich et al. 1987; Li et al. 2007) or mild down-estuary wind acting upon very shallow system (2~3m) like Waquoit Bay (Geyer 1997) and Pamlico River (Stanley and Nixon 1992). The region of wind increasing stratification (ΔN^2>0 in Fig. 9) occupies a small portion of the left quadrant because it requires a relatively shallow surface mixed layer (small h_s/H) and down-estuary wind stress comparable to axial baroclinic pressure gradient force ($|W| \geq O(1)$). Observations by Scully et al. (2005) and North et al. (2004) are most likely in this category. The location for Goodrich et al. (1987) is uncertain because they attributed destratification to shear instability. It is possible that the regime of

wind decreasing stratification would extend to the far left quadrant to account for shear instability. Field observations are needed to verify this regime diagram.

5.2. Comparison with field observations

Observations from the upper Chesapeake Bay provide support for the salt transport patterns described in section 4. In May 2001, a mooring array including a conductivity-temperature chain and an upward-looking ADCP were deployed near the salt intrusion (North et al. 2004). Near the end of the deployment on May 13th, a moderate down-estuary wind event was observed (first panel in Fig. 11). During May 10th to 13th, salinity increased by advection during flood tides and decreased during ebb tides (second panel). The near-bottom subtidal axial velocity was very weak (third panel) because the mooring was located near the convergence zone (ETM). However, at the onset of the down-estuary wind event on May 13th, salinity at 3 depths and water level decreased, while down-estuary subtidal velocity increased and occupied the whole water column. This was followed by increased salinity and stratification and strong up-estuary subtidal flows near bottom. The initial decreases in salinity/water level and increases in down-estuary flows are consistent with our finding of down-estuary transient volume and salt transport due to barotropic adjustment. The subsequent increases in salinity and up-estuary flows can be explained by a combination of enhanced subtidal shear dispersion and sea-level relaxation near the end of the event. The net salt gain, indicated by the increased salinity, also agrees with our model predictions.

The numerical experiments carried out by North et al. (2004) showed initial salt loss/gain during a down/up-estuary wind event similar to our results. The salt flux decomposition here further reveals that this initial response is due to barotropic adjustment. We relate the adjustment with the first barotropic seiche mode, meaning that the two strong pulses of salt fluxes near the onset and the end of an event are most likely sensitive to the channel length and depth. Therefore, the subtidal, cross-sectionally averaged salt transport may be less important in shorter and/or deeper systems. In addition, when integrating over the whole event period, the two transient pulses largely cancel out. This suggests that the responses of subtidal shear dispersion F_E and tidal oscillatory flux F_T to wind determine the net salt loss or gain. In our system ($F_E/F_T \approx 5$), moderate down/up-estuary wind increases/decreases F_E and thus results in net salt gain/loss. The above discussion implies that extra care should be taken when applying the Hansen and Rattray (1965)'s theory of longitudinal salt transport because the transient pulses of salt flux are not included. Applying to a long time series, as done by Ralston et al. (in press), would be more appropriate because the transient effects likely cancel out.

5.3. Influences of Earth rotation

We evaluate the influences of Earth rotation by comparing the salt transport mechanisms between non-rotating (No. 7 and 8) and rotating (No. 17 and 18) moderate down- and up-estuary wind cases. At the mid-estuary cross-section, the time series of subtidal total salt flux (F_S), subtidal shear dispersion (F_E), and tidal oscillatory flux (F_T) show the same patterns with very similar magnitudes as the non-

rotating cases shown in Fig. 7. There are two minor differences: first, the salt intrusion length with rotation is slightly shorter (137 against 145 km); second, rotation as expected induces variations in the lateral structures of the subtidal shear dispersion F_E and oscillatory flux F_T. For example, during the non-rotating, moderate down-estuary wind, F_E is mostly up-estuary (positive) and has a maximum core near the channel bottom (Fig. 12a). This is expected because the exchange flow enhanced by wind advects saltier water up-estuary near bottom and fresher water down-estuary near surface. During the non-rotating, moderate up-estuary wind, F_E is largely zero because water column is homogenized (Fig. 12c). When rotation is included, lateral distribution of F_E is tilted in a manner consistent with Coriolis deflection of exchange flow (Fig. 12b). Most importantly, the magnitudes of F_E with rotation (Fig. 12b and 12d) are very similar to those without rotation (Fig. 12a and 12c). The insignificant influences of rotation are expected because the internal Rossby radius in our system is about 6 km, which is 2 times larger than the channel width.

Acknowledgements

We thank the ROMS code developer/user community and the financial support from ONR through the Community Sediment Transport Modeling (CSTM) project. The Ri_x analyses were inspired by Mark Stacey's lectures during the Friday Harbor Summer School in 2006. S.N.C thanks Bob Chant, Rocky Geyer, Malcolm Scully, and Steven Monismith for many valuable suggestions and Steve Suttles for processing field data. This is UMCES publication no. xxxx.

References

Blumberg, A. E. and D. M. Goodrich, 1990: Modeling of Wind-Induced Destratification in Chesapeake Bay. *Estuaries*, **13,** 236-249.

Bowen, M. M. and W. R. Geyer, 2003: Salt transport and the time-dependent salt balance of a partially stratified estuary. *Journal of Geophysical Research*, **108,** 3158.

Burchard, H. and H. Baumert, 1998: The formation of estuarine turbidity maxima due to density effects in the salt wedge. A hydrodynamic process study. *Journal of Physical Oceanography*, **28,** 309-321.

Canuto, V. M., A. Howard, Y. Cheng, and M. S. Dubovikov, 2001: Ocean turbulence I: one-point closure model-Momemtun and heat vertical diffusivities. *Journal of Physical Oceanography*, **31,** 1413-1426.

Chen, S. N. and L. P. Sanford, 2008: Lateral circulation driven by boundary mixing and the associated transport of sediments in idealized partially-mixed estuaries. *Continental Shelf Research***,** doi:10.1016/j.csr.2008.01.001.

Cloern, J. E., 1991: Tidal stirring and phytoplankton bloom dynamics in an estuary. *Journal of Marine Research*, **49,** 203-221.

Csanady, G. T., 1973: Wind-induced barotropic motions in long lakes. *Journal of Physical Oceanography*, **3,** 429-438.

Dyer, K. R., 1997: *Estuaries: A Physical Introduction*. 2nd ed. John Wiley & Sons Ltd., 195 pp.

Geyer, W. R., 1993: The Importance of Suppression of Turbulence By Stratification On the Estuarine Turbidity Maximum. *Estuaries*, **16,** 113-125.

——, 1997: Influence of wind on dynamics and flushing of shallow estuaries. *Estuarine, Coastal, and Shelf Science*, **44,** 713-722.

Goodrich, D. M., W. C. Boicourt, P. Hamilton, and D. W. Pritchard, 1987: Wind-Induced Destratification in Chesapeake Bay. *Journal of Physical Oceanography*, **17,** 2232-2240.

Haidvogel, D. B., H. G. Arango, K. Hedstrom, A. Beckmann, and P. Malanotte-Rizzoli, 2000: Model evaluation experiments in the North Atlantic basin: Simulations in nonlinear terrain-following coordinates. *Dynamics of Atmospheres and Oceans*, **32,** 239-281.

Hansen, D. V. and M. Rattray, 1965: Gravitational circulation in straits and estuaries. *Journal of Marine Research*, **23,** 104-122.

Hunkins, K., 1981: Salt dispersion in the Hudson estuary. *Journal of Physical Oceanography*, **11,** 729-738.

Ivey, G. N. and J. Imberger, 1991: On the nature of turbulence in a stratified fluid. Part I: The energetics of mixing. *Journal of Physical Oceanography*, **21,** 650-658.

Jones, W. P. and B. E. Launder, 1972: The prediction of laminarization with a two-equation model of turbulence. *International Journal of Heat and Mass Transfter*, **15,** 301-314.

Kato, H. and O. M. Phillips, 1969: On the penetration of a turbulent layer into a stratified fluid. *Journal of Fluid Mechanics*, **37,** 643-655.

Kemp, W. M., P. A. Sampou, J. Garber, J. Tuttle, and W. R. Boynton, 1992: Seasonal Depletion of Oxygen From Bottom Waters of Chesapeake Bay: Roles of Benthic and Planktonic Respiration and Physical Exchange Processes. *Marine Ecology Progress Series*, **85,** 137-152.

Lerczak, J. A., W. R. Geyer, and R. J. Chant, 2006: Mechanisms driving the time-dependent salt flux in a partially stratified estuary. *Journal of Physical Oceanography*, **36,** 2296-2311.

Lewis, R. E. and J. O. Lewis, 1983: The principal factors contributing to the flux of salt in a narrow, partially stratified estuary. *Estuarine and Coastal Marine Science*, **16,** 599-626.

Li, M., L. J. Zhong, and W. C. Boicourt, 2005: Simulations of Chesapeake Bay estuary: Sensitivity to turbulence mixing parameterizations and comparison with observations. *Journal of Geophysical Research*, **110,** C12004.

Li, M., L. J. Zhong, W. C. Boicourt, S. L. Zhang, and D. L. Zhang, 2007: Hurricane-induced destratification and restratification in a partially-mixed estuary. *Journal of Marine Research*, **65,** 169-192.

MacCready, P., 1999: Estuarine adjustment to changes in river flow and tidal mixing. *Journal of Physical Oceanography*, **29,** 708-726.

Marchesiello, P., J. C. McWilliams, and A. Shchepetkin, 2001: Open boundary conditions for long-term integration of regional oceanic models. *Ocean Modeling*, **3,** 1-20.

Monismith, S. G., 1986: An experimental study of the upwelling response of stratified reservoirs to surface shear stress. *Journal of Fluid Mechanics*, **171,** 407-439.

Monismith, S. G., W. Kimmerer, J. R. Burau, and M. T. Stacey, 2002: Structure and flow-induced variability of the subtidal salinity field in northern San Francisco Bay. *Journal of Physical Oceanography*, **32,** 3003-3019.

North, E. W., S.-Y. Chao, L. P. Sanford, and R. R. Hood, 2004: The Influence of Wind and River Pulses on an Estuarine Turbidity Maximum: Numerical Studies and Field Observations. *Estuaries*, **27,** 132-146.

Sanay, R. and A. Valle-Levinson, 2005: Wind-induced circulation in semienclosed homogeneous, rotating basins. *Journal of Physical Oceanography*, **35,** 2520-2531.

Scully, M. E., C. T. Friedrichs, and J. M. Brubaker, 2005: Control of Estuarine Stratification and Mixing by Wind-induced Straining of the Estuarine Density Field. *Estuaries*, **28,** 321-326.

Sharples, J., J. H. Simpson, and J. M. Brubaker, 1994: Observations and modelling of periodic stratification in the Upper York River Estuary, Virginia. *Estuarine, Coastal, and Shelf Science*, **38,** 301-312.

Simpson, J. H., J. Brown, J. Matthews, and G. Allen, 1990: Tidal straining, density currents, and stirring in control of estuarine stratification. *Estuaries*, **13,** 125-132.

Stacey, M. T., J. R. Burau, and S. G. Monismith, 2001: Creation of residual flows in a partially stratified estuary. *Journal of Geophysical Research*, **106,** 17,013-17,037.

Stanley, D. W. and S. W. Nixon, 1992: Stratification and bottom-water hypoxia in the Pamlico River estuary. *Estuaries*, **15,** 270-281.

Trowbridge, J. H., 1992: A simple description of the deepening and structure of a stably stratified flow driven by a surface stress. *Journal of Geophysical Research*, **97,** 15,529-15,543.

Tyler, M. A. and H. H. Seliger, 1978: Annual subsurface transport of red tide dinoflagellate to its bloom area - water circulation patterns and organism distribution in Chesapeake Bay. *Limnology and Oceanography*, **23,** 227-246.

Wang, D.-P., 1979: Wind-Driven Circulation in the Chesapeake Bay, Winter 1975. *Journal of Physical Oceanography*, **90,** 564-572.

Warner, J. C., W. R. Geyer, and J. A. Lerczak, 2005: Numerical modeling of an estuary: A comprehensive skill assessment. *Journal of Geophysical Research*, **110,** C05001 (1-13).

Warner, J. C., C. R. Sherwood, H. G. Arango, and R. P. Signell, 2005: Performance of four turbulence closure models implemented using a generic length scale method. *Ocean Modeling*, **8,** 81-113.

Weisberg, R. H., 1976: The nontidal flow in the Providence River of Narragansett Bay: A stochastic approach to estuarine circulation. *Journal of Physical Oceanography*, **6,** 721-734.

Wong, K. C., 1994: On the nature of transverse variability in a coastal plain estuary. *Journal of Geophysical Research*, **99,** 14,209-14,222.

Wong, K. C. and J. E. Moses-Hall, 1998: The tidal and subtidal variations in the transverse salinity and current distributions across a coastal plain estuary. *Journal of Marine Research*, **56,** 489-517.

Zheng, L. and R. H. Weisberg, 2006: Tide, buoyancy, and wind-driven circulation of the Charlotte Harbor estuary: A model study. *Journal of Geophysical Research*, **109**.

Table 1. Wind perturbation experiments. Positive is up-estuary. Winds were applied for 3 days (128 to 131).

Down-estuary wind				Up-estuary wind			
No.	τ_{wx} (Pa)	W	f (sec^{-1})	No.	τ_{wx} (Pa)	W	f (sec^{-1})
0	0	0	0				
1	-0.01	-0.08	0	2	0.01	0.08	0
3	-0.04	-0.34	0	4	0.04	0.34	0
5	-0.07	-0.60	0	6	0.07	0.60	0
7	-0.1	-0.85	0	8	0.1	0.85	0
9	-0.15	-1.27	0	10	0.15	1.27	0
11	-0.2	-1.79	0	12	0.2	1.79	0
13	-0.25	-2.11	0	14	0.25	2.11	0
15	-0.3	-2.53	0	16	0.3	2.53	0
17	-0.1	-0.80	10^{-4}	18	0.1	0.80	10^{-4}

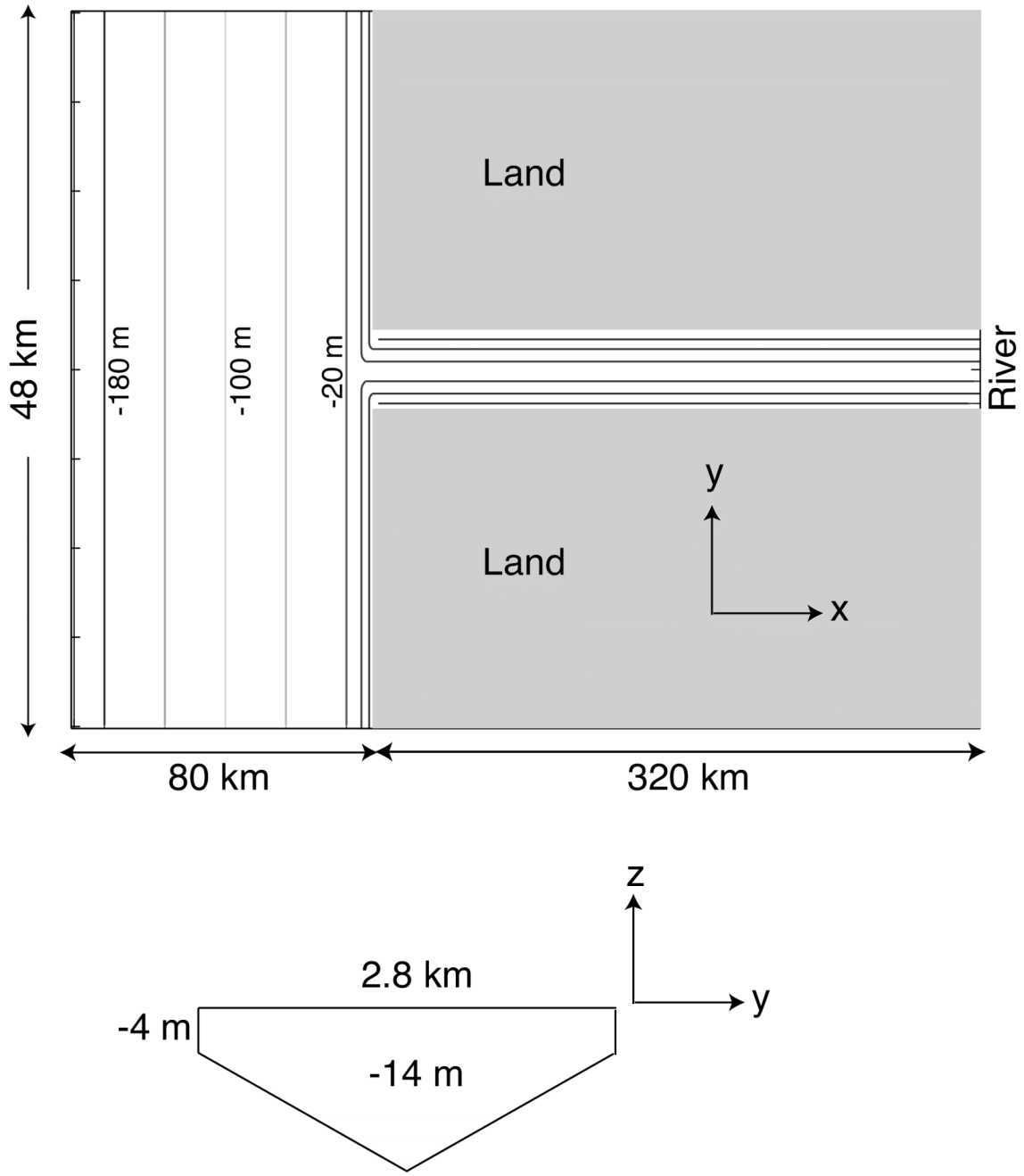

Fig. 1. Plan-view of model domain (top) and estuarine channel cross-section (bot). The domain mimics a broad continental shelf with a long, straight estuarine channel. The shelf size is 48 km (along-shelf) x 80 km (cross-shelf) with a constant slope from 200 m (off-shelf boundary) to 4 m (land boundary). The estuarine channel extends from x=80 km to 400 km. The gray areas are land. The channel is triangular-shaped, 2.8 km-wide, 14 m deep in the center, and 4 m deep on the sides. Note that the domain is scaled disproportionately for better visualization.

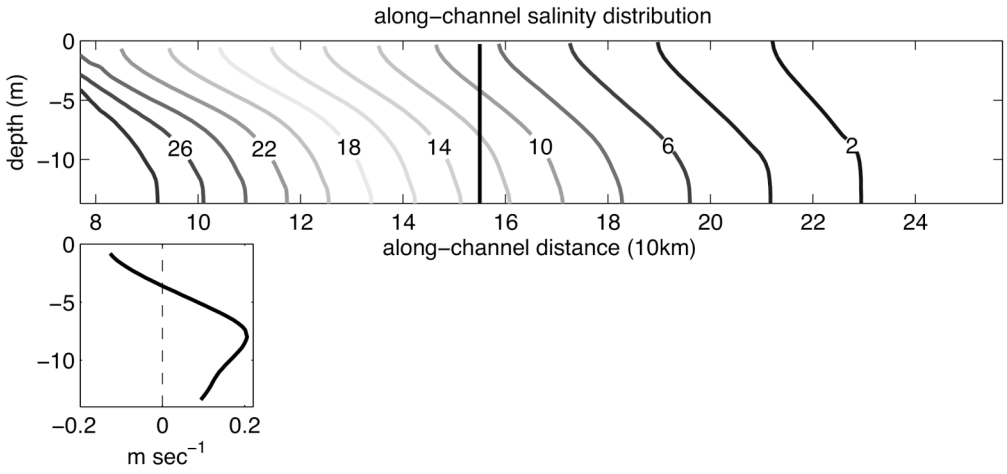

Fig. 2. Along-channel salt structure (top) and vertical profile of tidally-averaged, steady-state along-channel velocity (bot) at the channel midpoint for the baseline case (model run 0 in Table 1). The vertical line in the top panel is the channel midpoint, defined as half of the salt intrusion length (~ 145 km).

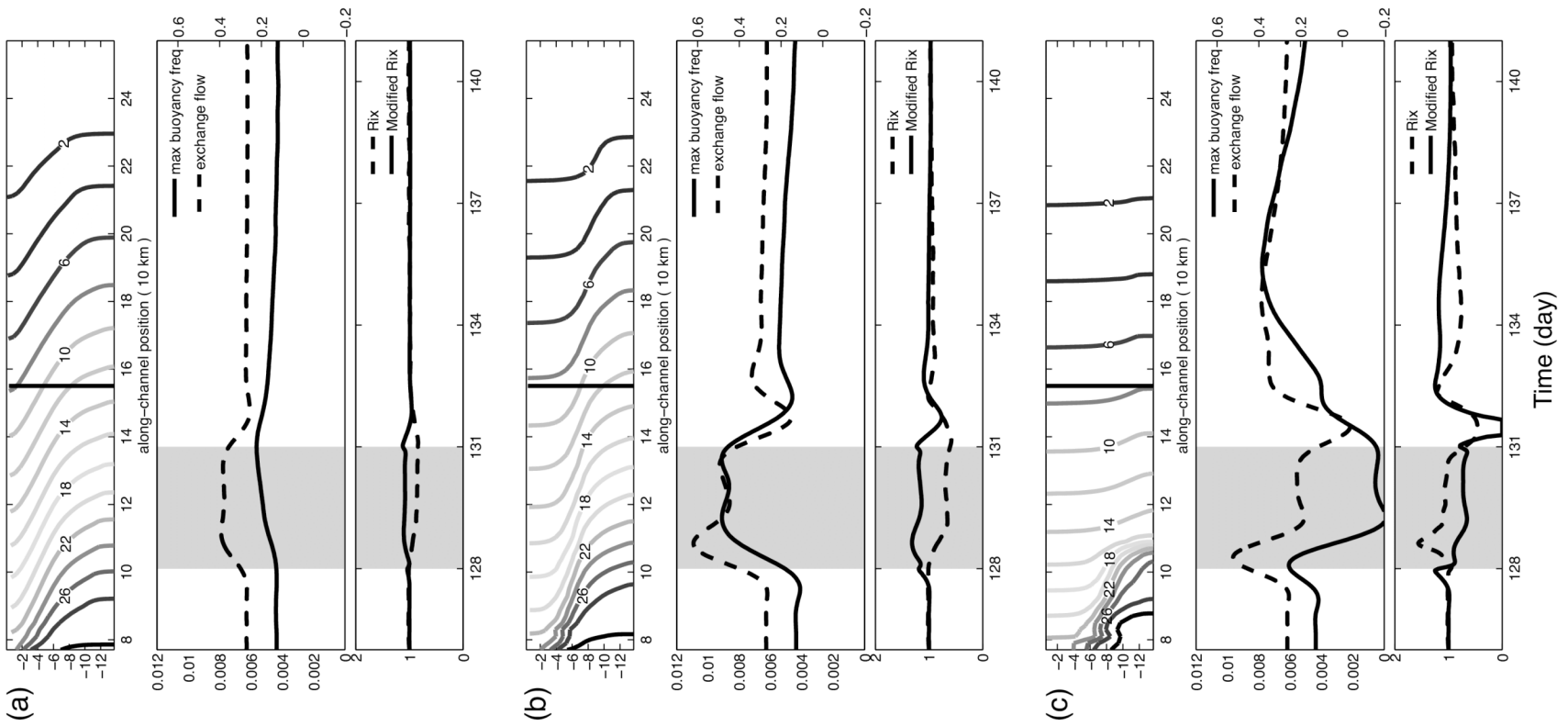

Fig. 3. Salinity distribution and time series under 3-day (days 128~131, shaded in gray) events of weak (a; 0.01Pa), moderate (b; 0.1Pa), and strong (c; 0.3Pa) down-estuary wind. These three cases correspond to experiments No. 1, 7, and 15 in Table 1, with absolute values of the Wedderburn numbers of 0.08, 0.85, and 2.5, respectively. Each panel has 3 figures. The top is a snapshot of along-channel salinity distribution at day 130; the middle is 33hr low-passed time series of maximum buoyancy frequency squared (solid) and exchange flows (dashed); the bottom is 33hr low-passed time series of normalized horizontal Richardson number without (dashed) and with (solid) wind straining/mixing corrections (Eq. 6). The time series are from the channel midpoint, denoted by vertical lines in the salinity distributions.

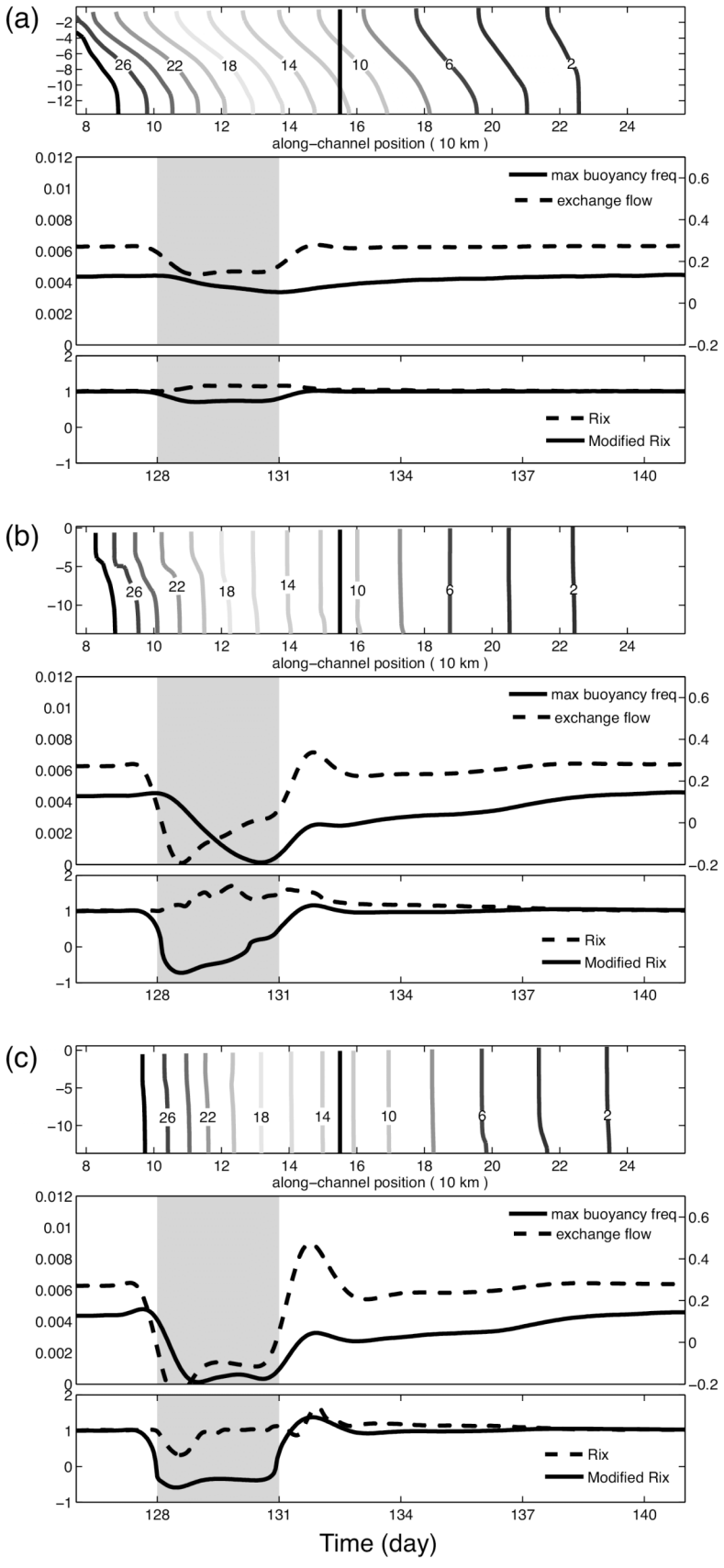

Fig. 4. Same as Fig. 3 but for up-estuary wind. The three cases correspond to experiments No. 2, 8, and 16 in Table 1, respectively.

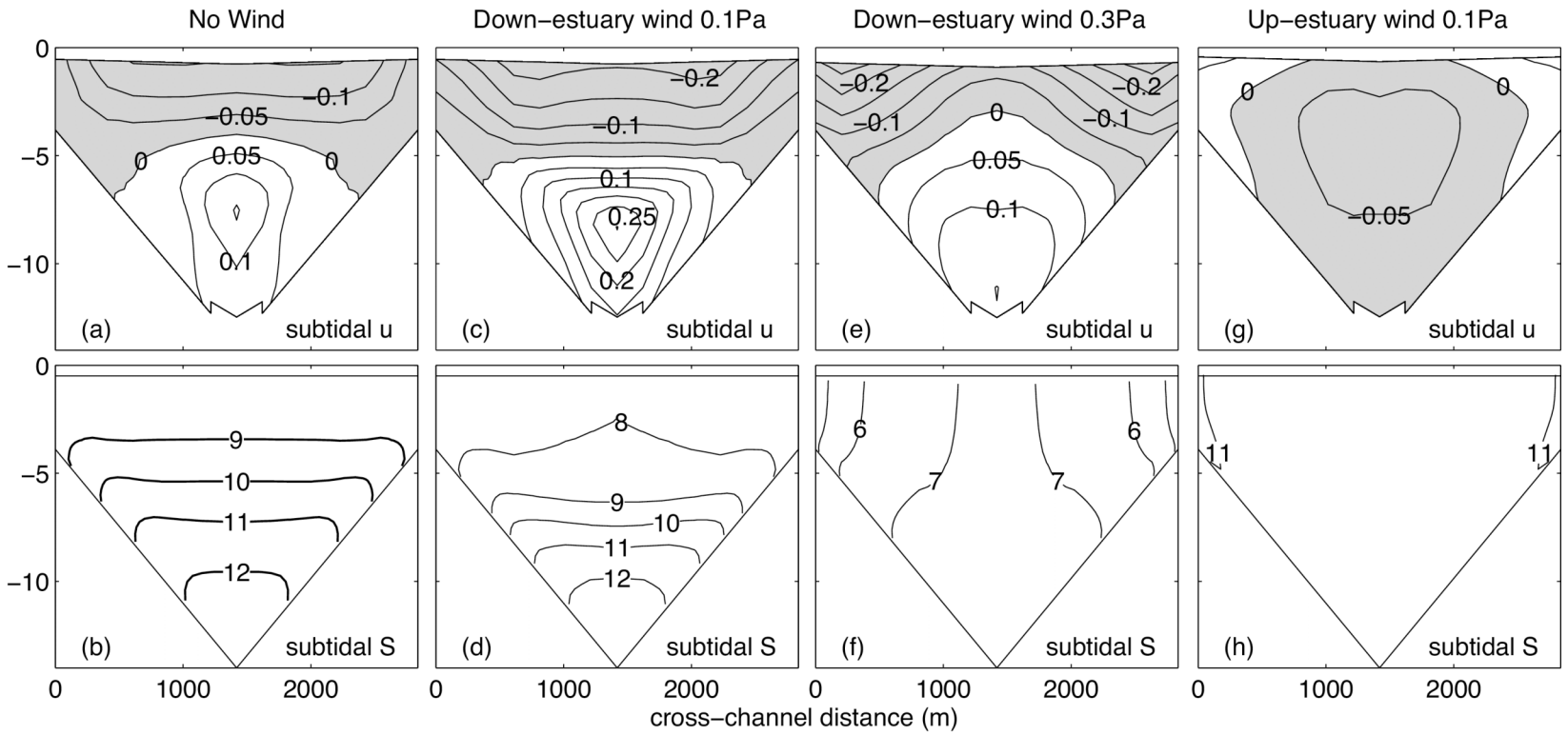

Fig. 5. Cross-sectional distributions (looking seaward) of subtidal axial velocity (top panels) and salinity (bottom panels) at the channel midpoint at day 130. The four columns are under no-wind, moderate (0.1Pa) down-estuary wind, strong (0.3Pa) down-estuary wind, and moderate (0.1Pa) up-estuary wind conditions, respectively.

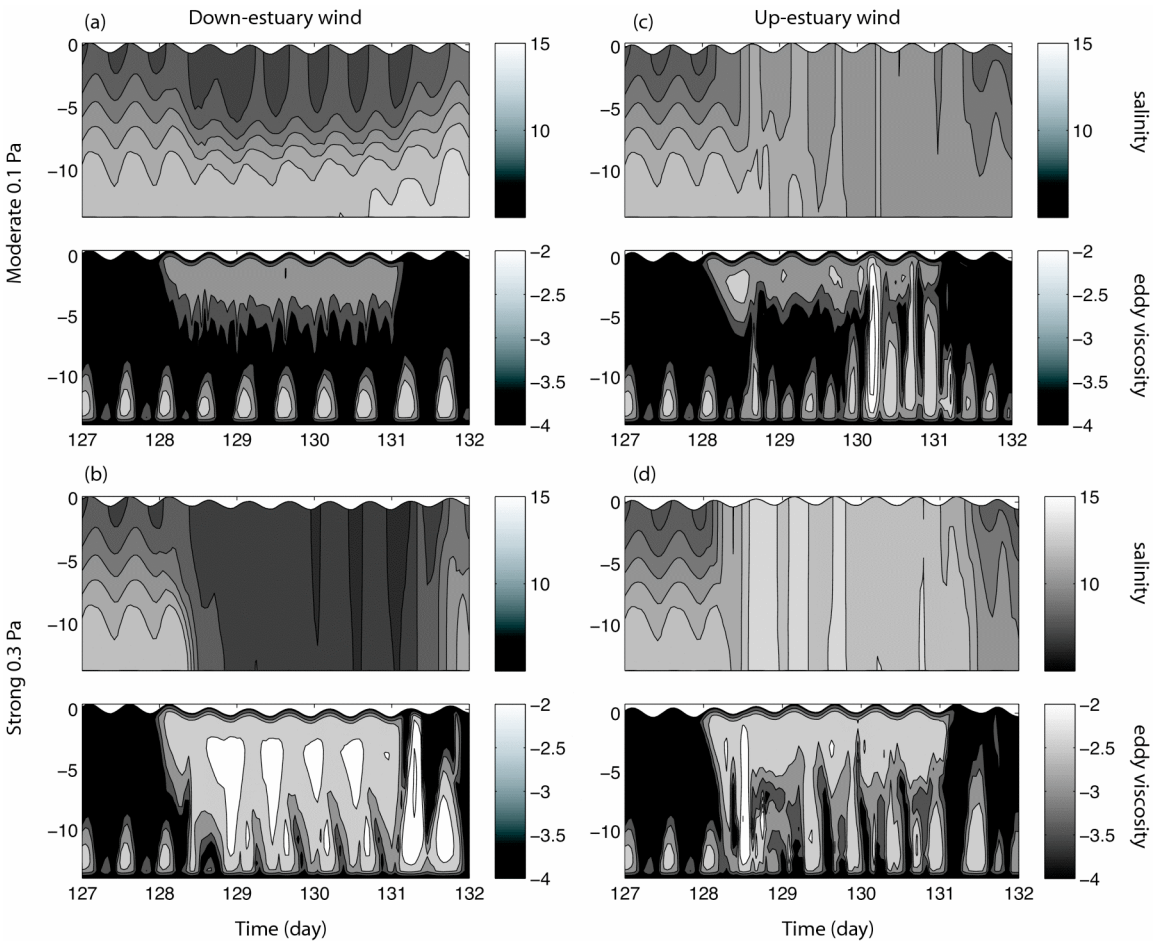

Fig. 6. Time series of instantaneous salinity and eddy viscosity at the channel midpoint for four cases. The upper left (a) is moderate down-estuary wind; lower left (b) is strong down-estuary wind; upper right (c) is moderate up-estuary wind; lower right (d) is strong up-estuary wind.

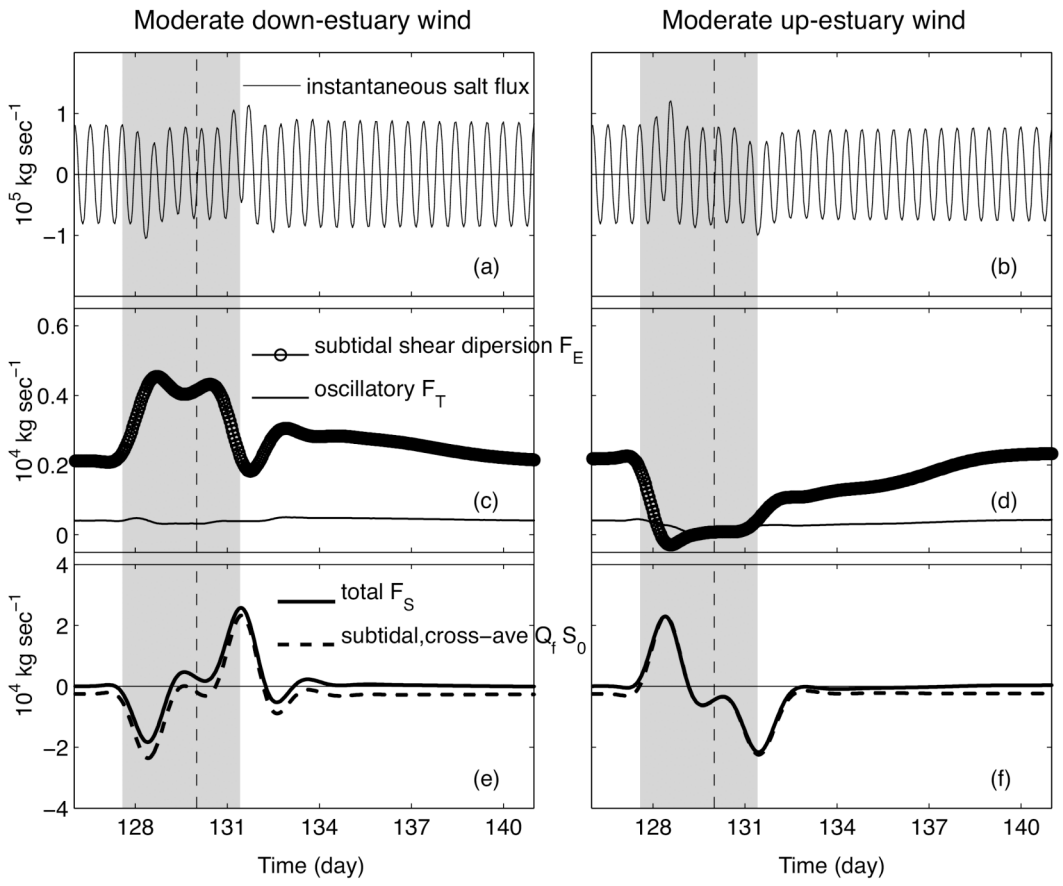

Fig. 7. Time series of salt fluxes for the moderate down-estuary wind (left; a,c,e) and up-estuary wind (right; b,d,f) cases. The top panels (a, b) are instantaneous salt fluxes. The middle panels (c, d) are subtidal shear dispersion (circle) and tidal oscillatory fluxes (thin lines). The bottom panels (e, f) are subtidal total salt fluxes (thick lines) and subtidal cross-sectionally averaged fluxes (dashed). The wind event is shaded in gray. Note that the vertical scales of the middle and bottom panels are different.

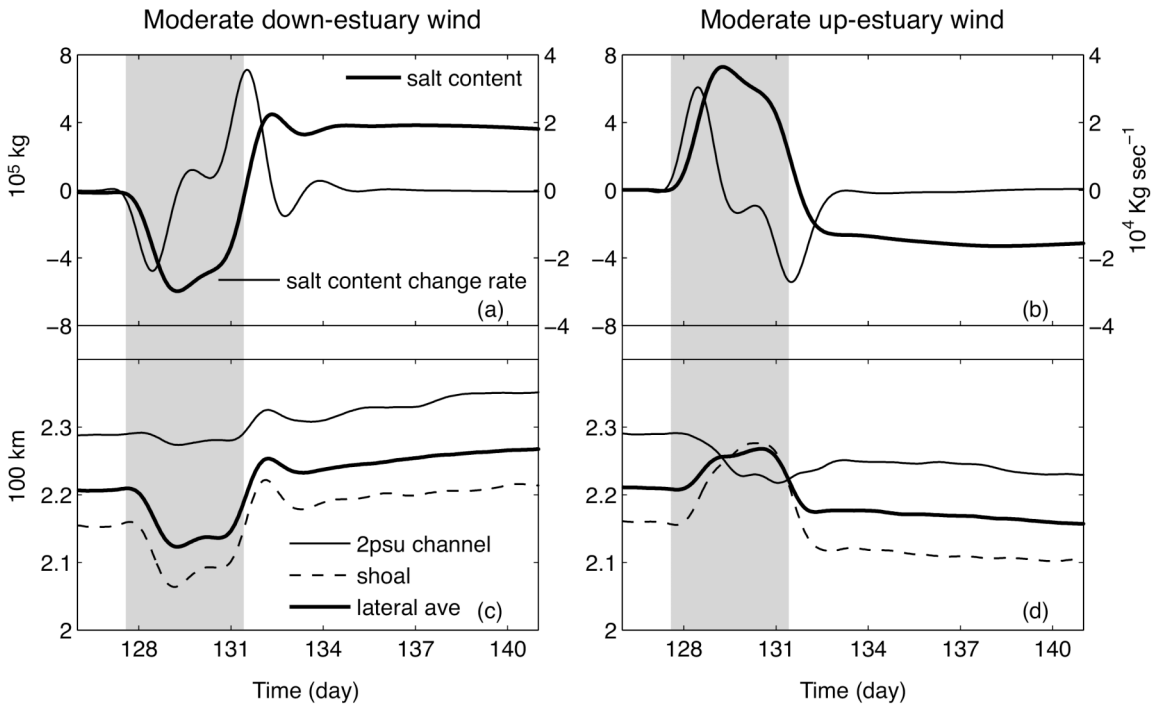

Fig. 8. Time series of the salt content and the salt content change rate (top panels; a, b) and the 2 psu locations at 0.5 m above bottom (bottom panels; c, d) for the moderate down-estuary wind (left) and up-estuary wind (right) cases. In (a) and (b), the scales for salt content (thick lines) are on the left axis and for salt content change rate (thin lines) are on the right axis. In (c) and (d), the 2psu locations are calculated in the channel (thin lines; 14 m), on the shoal (dashed lines; 5 m), and by laterally averaging (thick lines).

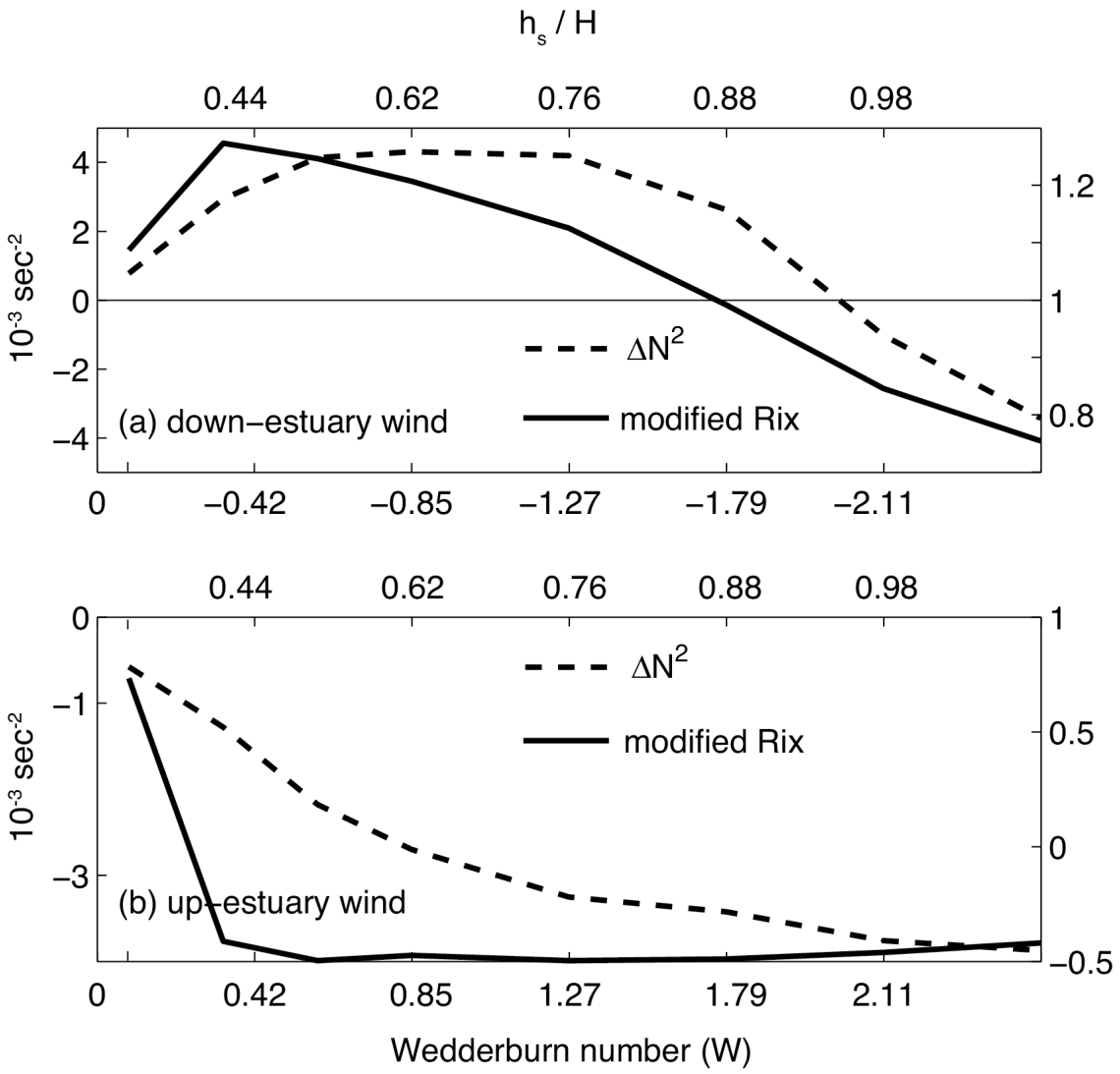

Fig. 9. Changes in stratification (ΔN^2; dashed line) and the modified horizontal Richardson number (solid line; Eq. 6) with two parameters, W (bottom x-axes) and h_s/H (top x-axes), for all 16 non-rotating perturbation experiments in Table 1. The top (a) and bottom (b) panels are down- and up-estuary wind cases, respectively. ΔN^2 and the modified Ri_x are averaged over the events. Note that the top x-axis does not change linearly because the entrainment depth, h_s, is not a linear function of wind stress.

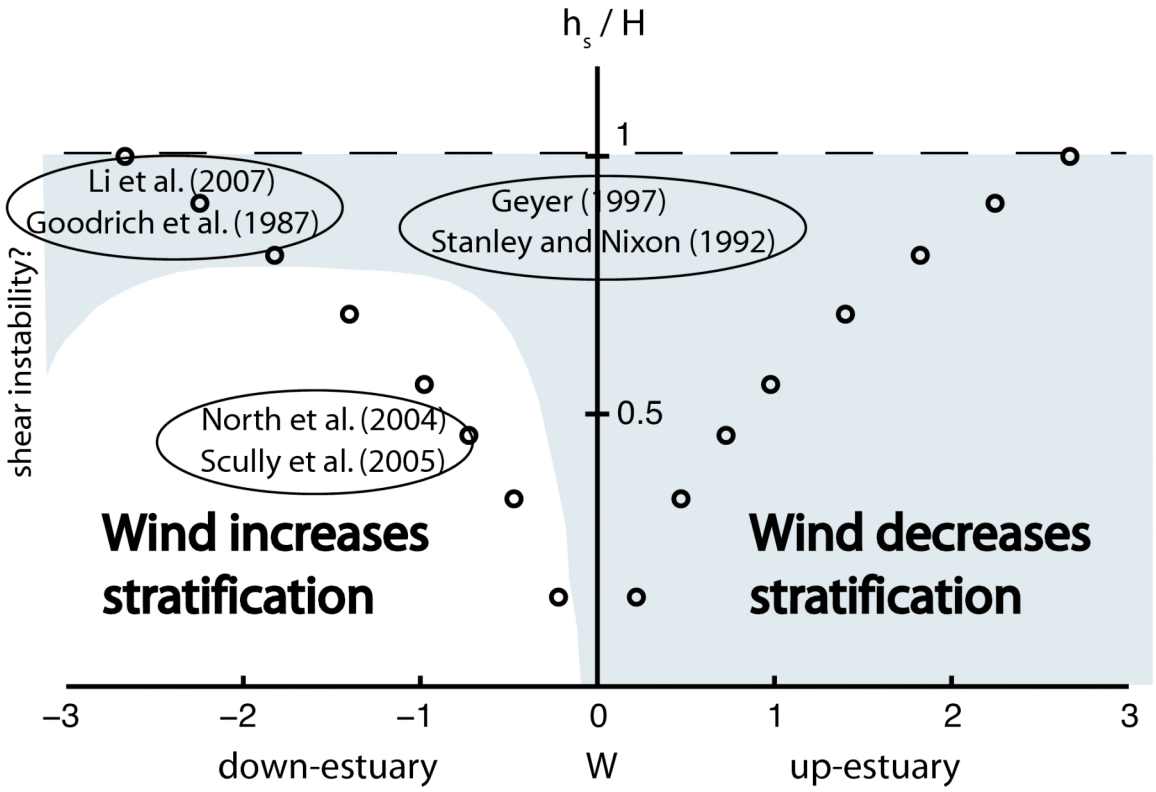

Fig. 10. A regime diagram to classify axial wind effects on stratification. The y-axis is the ratio of entrainment depth (h_s) to water depth (H); the x-axis is the Wedderburn number W. Positive is up-estuary. The circles are the 16 non-rotating experiments in Table 1. The regime of wind decreasing stratification is shaded, and the regime of wind increasing stratification is white. The ovals represent the approximate locations of data presented in the cited references.

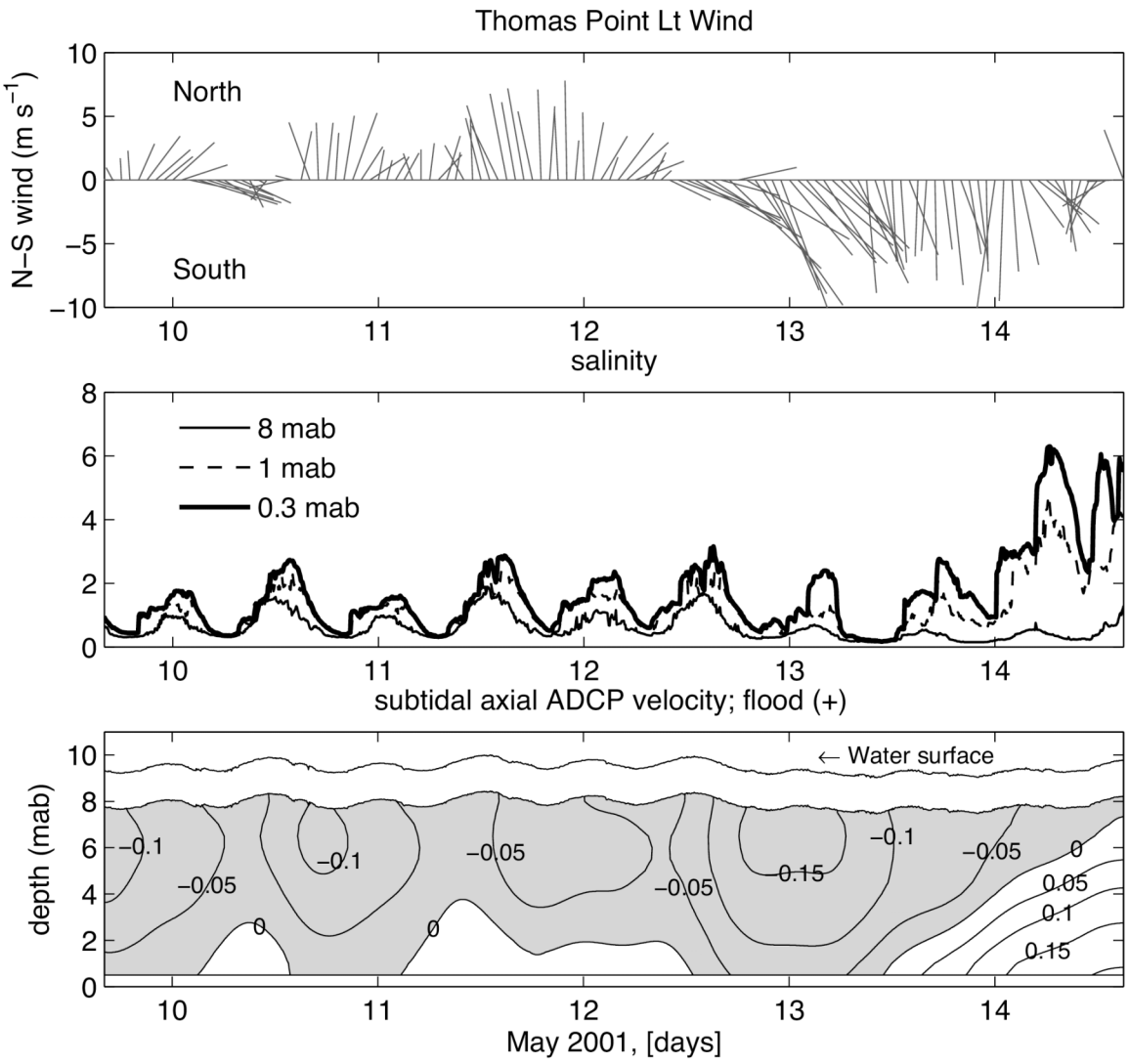

Fig. 11. Time series of axial wind (top), salinity at three depths (middle), and 33hr low-passed axial velocity (bottom) from a moored conductivity-temperature chain and an upward looking ADCP. The mooring was deployed for 5 days at a location near the salt intrusion of Chesapeake Bay in May 2001 (39º19'63" N, 76º12'37" W). The wind record is from Thomas Point Light (38º53'54" N, 76º26'12" W). The conductivity-temperature sensors were 0.3, 1, and 8 meters above bottom.

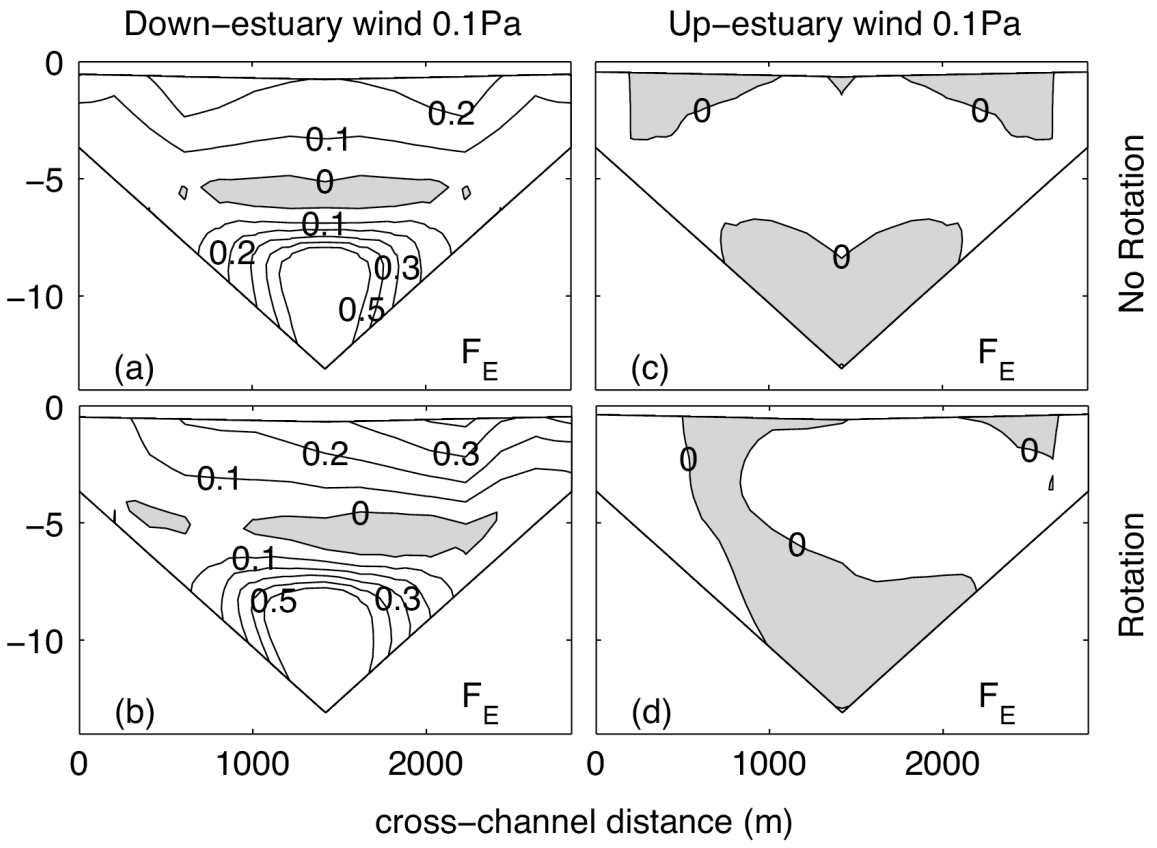

Fig. 12. Cross-sectional distributions (looking seaward) of subtidal shear dispersion F_E for non-rotating (top panels; a, c) and rotating (bottom panels; b,d) moderate wind conditions, taken at the channel midpoint at day 130. The left and right columns are under moderate down-estuary wind and up-estuary wind conditions, respectively (No. 7, 8, 17, and 18). The units of the contour are 10^4 kg sec^{-1}.

Chapter 4

Lateral circulation driven by axial wind events and the concurrent lateral sediment transport in an idealized, partially mixed estuary

Abstract

A 3D hydrodynamic model (ROMS) is used to investigate lateral circulation driven by axial wind events and to explore the associated transport of sediments in a partially mixed estuary. The channel is straight and with a triangular cross-section. The model results suggest that, when the water column mixes vertically, Ekman transport due to axial winds is not a significant contributor to lateral circulation. Instead, differential advection of the axial salinity gradient by wind-driven axial flow is responsible for controlling lateral salinity gradients that in turn drive bottom-divergent lateral circulation during down-estuary wind and bottom-convergent lateral circulation during up-estuary winds. The wind-induced and tidally-induced lateral shear interacts to drive the variability of lateral flow. A Hansen-Rattray-like scaling is derived and shows good predictive skills for lateral flow. Lateral sediment flux and the event-integrated sediment transport are from channel to shoals during down-estuary winds but reversed for up-estuary winds. Potential impacts of wind-generated waves on lateral sediment transport are evaluated with two cases representing typical event conditions of Chesapeake Bay. Accounting for wind-wave effects shows an order-of-magnitude increase in lateral sediment fluxes.

1. Introduction

Lateral circulation has long been recognized as an effective means to distribute scalar (e.g. salt) across estuaries (Fischer et al. 1979). It thus affects scalar dispersion rates, which set the residence time of a system and can potentially impact estuarine bio-geochemical processes. Recently, redistribution of momentum by lateral circulation was also identified to contribute at the leading order to the subtidal, axial momentum balance (Lerczak and Geyer 2004; Scully et al. submitted). Thus, lateral circulation also has a direct effect on residual axial circulation, and understanding the dynamics of lateral circulation is important to better comprehend how estuaries function.

To examine the dynamics of lateral circulation, most of the attention has been placed on tidally-forced processes. In the presence of tides, lateral circulation can be driven by: interactions between barotropic tides with bathymetry (Valle-Levinson et al. 2000); centrifugal acceleration in a curved, estuarine channel (Chant and Wilson 1997; Lacy and Monismith 2001); Ekman veering in bottom boundary layer (Ott and Garrett 2002); boundary mixing on a slope (Chen and Sanford 2008); and differential advection of axial salinity gradient (Nunes and Simpson 1985; Lerczak and Geyer 2004). Analytical models aiming to discern the relative importance of some of the above mechanisms have also been solved by prescribing the lateral density gradient (e.g. Huijts et al. 2006).

In comparison with active research on tidally-forced processes, lateral circulation driven by wind forcing has received less attention. Winant (2004) and Sanay and Valle-Levinson (2005) investigated the wind-driven lateral circulation for

homogeneous channels without tides. They found that the major clockwise circulating pattern (looking seaward; northern hemisphere) is consistent with Ekman dynamics. However, when salt is present, neither the wind-driven lateral circulation nor its interactions with tides are well studied.

While Ekman dynamics is still expected to drive lateral circulation in the presence of salt, theoretically wind-driven axial circulation can provide another driving mechanism for lateral circulation. This mechanism is similar to the tidally-induced differential advection. Key ingredients for differential advection mechanism are a presence of axial salinity gradient and lateral shear in axial flow. For pure tidally-forced case, depth-averaged tidal currents tend to be stronger in the channel, which generates lateral shear. During floods, for example, this lateral shear then advects high salinity water further up-estuary in the channel, creating a lateral baroclinic pressure gradient to drive lateral circulation (see Lerczak and Geyer 2004). Wind-driven axial flow over laterally varying bathymetry can also generate lateral shear. Csanady (1973) and Wong (1994) demonstrated that wind-driven flow is downwind on the shoal and upwind in the channel. Therefore, wind-induced lateral shear acting on axial salinity gradient theoretically can create lateral salinity gradient to drive lateral circulation.

Lateral circulation can also transport suspended sediments across estuaries. This lateral transport integrated over time and combined with sedimentation may affect channel morphology. Although there are increasing amount of work on lateral sediment transport, the focus was again mainly on tidally-forced processes (Geyer et al. 1998; Huijts et al. 2006; Fugate et al. 2007; Chen and Sanford 2008). Lateral

sediment transport during episodic wind events are largely overlooked, even though in microtidal estuaries wind and tidal energy inputs can be comparable (Zhong and Li 2006). Taking Chesapeake Bay as an example, several field surveys reported higher sedimentation rates in the channel, and the surficial sediment distribution showed a general pattern of muddy channel with sandy shoals (Kerhin et al. 1988; Colman et al. 1992). Wind events with concurrent wind-generated wave action on shallow shoals have been hypothesized to transport fine-grain sediments across estuary and deposit in the channel (Langland and Cronin 2003). However, this hypothesis has not yet been tested, and the lateral sediment transport associated with wind events has not been quantified.

In this study, we carry out idealized, numerical experiments to investigate lateral circulation and the associated transport of sediments during axial wind events. Our main focus is on the driving mechanism for lateral circulation when an axial salt gradient is present. In section 2, we briefly describe the model setup and the designs of numerical experiments. In section 3, we demonstrate that, when the stratification is weak, wind-induced differential advection described above is indeed an important mechanism and the rotation effect (Ekman) is relatively weak. In addition, the interactions between wind-induced and tidally-induced differential advection control the variability of lateral flow. In section 4, we quantify the lateral sediment fluxes during wind events with different applied stresses. Two cases with wind-wave forcing which represent typical event conditions in Chesapeake Bay are also included to evaluate the potential impacts of wind-waves on lateral sediment transport. Finally, in

section 5, a schematic diagram for wind-induced differential advection and its interactions with tides are presented.

2. Numerical Model

We use the Regional Ocean Model System (ROMS; Haidvogel et al. 2000) to simulate an idealized estuarine channel. ROMS is a hydrostatic, primitive equation model using a curvilinear grid in the horizontal and a stretched, terrain-following coordinate in the vertical. It has been widely used by the coastal ocean modeling community and is capable of simulating many estuarine flows with high skill (e.g. Warner et al. 2005; Li et al. 2005). The model domain consists of a straight estuarine channel and a wide inner shelf (Fig. 1). The size of the shelf is 80 km across shelf x 48 km along-shelf with a constant slope from 200 m at the offshore boundary to 4 m at the shoreline. A 2.8 km-wide estuarine channel intersects the shelf and extends from x=80 km to 400 km. The cross-section is triangular shape with a maximum depth of 14 m in the channel and a minimum depth of 4 m on the sides. This bathymetry is a crude representation of Chesapeake Bay and the channel length is similar. The grid configuration is 194 (along-channel, x-direction) x 103 (cross-channel, y-direction) x 20 (vertical levels). The vertical levels are stretched with a lowest vertical resolution in the channel of 0.75 m. The estuary is highly resolved ($\Delta x \sim$ 2 km, $\Delta y \sim$ 200 m). Outside of this area, the grid is telescoped in the cross-channel direction ($\Delta y \sim$ 1.5 km) to obtain a bigger salt pool on the shelf without increasing computational cost.

Implementations of open boundary conditions and tidal forcing are described in Chen and Sanford (2008). The resulting tide is largely progressive in the region with salt, and the tidal current amplitude is about 0.6 m sec^{-1} in the middle of estuary (half of the salt intrusion). A constant river flow of 0.01 m sec^{-1} is imposed at the river end. The $k-\varepsilon$ turbulence closure (Jones and Launder 1972) is activated with a stability function proposed by Canuto et al. 2001). Chen and Sanford (2008) applied a nearly identical model setup to investigate tidally driven lateral circulation and found that both flow and salinity fields are insensitive to the choice of closures among $k-\varepsilon$, $k-\omega$, and MY2.5. The salinity field reaches a steady structure periodically modulated by tides in 120 days.

We incorporate a single layer, single grain size sediment bed to explore lateral sediment transport. The sediment bed is sufficiently thick so that sediment is never depleted. The erosion formulation is the Ariathurai-Partheniades type, and the deposition is continuous with a constant settling speed of 0.3 mm s^{-1}. Details of the sediment transport module can be found in Chen and Sanford (2008). Without surface gravity waves, bottom stress is computed by assuming a logarithmic current profile in the lowest computational cell and a constant bottom roughness parameter (z_0) of 0.5mm. With surface gravity waves, a maximum combined wave-current bottom stress is computed using Madsen 1994 formulations with prescribed wave height, period, angle, and the same z_0 for consistency. The wave number is approximated by using the 6^{th}-degree polynomial by Dean and Dalrymple (1991).

After the salt structure reaches a steady state, we then perform numerical experiments (Table 1) to investigate the dynamics of lateral circulation driven by

axial wind and the associated transport of sediments. Following Chen and Sanford (submitted), we design the experiments based on a nondimensional number, the Wedderburn number (W). The Wedderburn number is a ratio of wind stress divergence to baroclinic pressure gradient force (Monismith 1986)

$$W = \frac{\tau_{wx} L}{\Delta\rho g H^2} \tag{1}$$

where τ_{wx} is the axial wind stress (positive is up-estuary), L is the length of the estuary, $\Delta\rho$ is the density change over L, g is the gravitational acceleration, and H is the averaged depth. W thus indicates the relative strength of wind-driven and gravitational circulations on subtidal axial flows (Geyer 1997). For example, when $|W| > 1$, wind-driven circulation is expected to have significant influences on the cross-sectional structures of subtidal axial flows and therefore subtidal salinity field.

There are 17 numerical experiments (Table 1). The baseline case (No. 0) is the simplest possible condition: no wind, no Coriolis acceleration, and no waves. In the 16 wind perturbation experiments, we change wind magnitude, direction and turn on/off Coriolis acceleration and wave forcing while keeping the duration of wind event constant (3 day). The wind direction is either up-estuary (positive) or down-estuary (negative). The wind stresses range from 0.1 to 0.3 Pa, bracketing $|W|$ from about unity to 2.5. Conditions with $|W| << 1$ are not considered here because Chen and Sanford (submitted) found that such weak wind stresses have minor effects on stratification and subtidal velocity/salinity fields. Wind is ramped up and down 5-hr before the event onset and end. Wind stress is constant from 5-hr after day 128 to 5-hr before day 131. Cases No. 15 and 16 account for the influences of wind-generated

waves. We choose wind stress of 0.1 Pa (~ wind speed of 8 m sec^{-1} based on Large and Pond 1981) as an example because it represents a typical event condition in wide estuaries like Chesapeake Bay (Lin et al. 2002). Two empirical formulas are used to estimate fetch-limited wind-wave (Resio et al. 2002; Goda 2003). Approximating fetch by the distance from the mouth to the middle of estuary where we evaluate the lateral dynamics, both formulas yield similar estimates of 1m wave height (H_s) and 3.5 sec wave period (T_s). These estimates are consistent with the observed typical values in Chesapeake Bay (Lin et al. 2002) and are used to derive the combined wave-current bottom stress in the sediment transport component.

The model simulates a partially-mixed estuary. The length of estuary, defined by the distance between 2 and 30 psu tidally averaged isohalines in the channel, is about 145 km. At the middle of estuary (denoted by a vertical line in Fig. 2a), the tidally averaged top-bottom salinity difference is 4.5 psu. The vertical profile of tidally averaged, along-channel velocity (Fig. 2b) is as expected consistent with gravitational circulation, with a landward flow near bottom and a seaward flow near surface. For cross-sectional structures (Fig. 2c and 2d), the isohalines are mostly horizontal in the interior but intersects the bottom slope at a right angle, and the near-bottom lateral flows are up-slope at both maximum ebb and flood. These patterns are consistent with the lateral circulation driven by boundary mixing on a slope (Chen and Sanford 2008). Bottom stress shows flood-ebb asymmetry due to the presence of gravitational circulation (Fig. 2e). Detailed lateral dynamics for the baseline case is described in Chen and Sanford (2008).

3. Dynamics of lateral circulation during wind events

3.1 Cross-sectional structures of flow and salinity field at different tidal phases

To examine the dynamics of lateral circulation during wind events, we contrast two representative wind forcing regimes and begin with the simplest condition without rotation. Case 1 and 2 represent moderate wind condition when wind-driven axial circulation is comparable to gravitational circulation (Fig. 3), whereas case 9 and 10 represent strong wind condition when wind-driven flow dominates (Fig. 4). These two regimes also provide contrasting behaviors in stratification. During moderate wind, the wind-induced straining of along-estuary salinity field exerts important controls on stratification, leading to enhanced stratification during down-estuary wind but a unstratified condition during up-estuary wind (Scully et al. 2005; Chen and Sanford, submitted). During strong wind, on the other hand, wind stress is large enough to penetrate the water column, leading to unstratified conditions for both down- and up-estuary wind (Chen and Sanford, submitted). The wind controls on stratification have profound influences on lateral circulation.

The general wind responses consist of a transient adjustment period when sea-level is set up or down by wind, a quasi-steady period during the event, and an another transient adjustment after the event. The adjustment period is about one day (day 128-129 and 131-132). Cross-sectional profiles described below are taken during the quasi-steady period (day 129.875, 130, and 130.125 for max. ebb, slack, and max. flood, respectively).

During moderate down-estuary wind, the water column stays stratified. Below the halocline at around 6m, the up-slope directed, near-bottom lateral flows and the flat interior isohalines tilted normal to the slope at different tidal phases (Fig. 3abc) are similar to the baseline case (Fig. 2), suggesting that boundary mixing still drives a significant amount of lateral circulation. Above the halocline (i.e. surface mixed layer), lateral circulation pattern is more complex. However, two circulation cells symmetric about the channel axial with lateral flow divergent at around 6m are persistent. The salinity is vertically uniform with this layer. The surface-averaged salinity at the channel axis is persistently 0.5 to 0.9 psu higher than that on the shoals. The baroclinic pressure gradient thus increases with depth, which then drives the two circulation cells. Maximum lateral flows do not change significantly over a tidal cycle, ranging from 2.0 to 2.3 cm sec^{-1}. Axial velocity is strongly sheared near surface during maximum ebb (Fig. 3a1) and shows a strong subsurface maximum during maximum flood (Fig. 3c1) because wind-driven circulation reinforces gravitational circulation (see section 3.2).

During moderate up-estuary wind, water column is unstratified. Two symmetric circulation cells with lateral flow convergent near the bottom are apparent throughout the tidal phases (Fig. 3def). Lateral salinity gradient is reversed with slightly higher salinity on the shoals (0.38~0.43 psu shoal-channel differences), which then drives the bottom-convergent lateral circulation. Lateral flows here are stronger than those during moderate down-estuary wind. Maximum lateral flows do not change much over a tidal cycle, ranging from 4.3 to 4.8 cm sec^{-1}. In comparison

with moderate down-estuary wind case, the vertical shear in axial velocity is reduced mainly because wind-driven axial flow nearly cancels gravitational circulation.

Contrasting with the stratified condition during moderate down-estuary wind, the water column is largely unstratified during strong down-estuary wind (Fig. 4abc). Lateral circulation also shows a very different pattern. It consists of two symmetric circulation cells with lateral flow divergent near the bottom. Surface-averaged salinity at the center is persistently higher than that on the shoals (~2.5psu). This sets up a baroclinic pressure gradient force that increases with depth. The pressure gradient force then drives the bottom-divergent lateral circulation. While the bottom-divergent pattern persists at different tidal phases, its magnitude increases from 2.5 cm sec^{-1} at maximum ebb (Fig. 4a) to 4.8 cm sec^{-1} at maximum flood (Fig. 4c). The lateral flow magnitude appears to vary coherently with the lateral salinity gradient and lateral shear of axial velocity ($\partial u/\partial y$; see section 3.3).

Cross-sectional structures of flow and salinity fields during strong up-estuary wind (Fig. 4def) are similar to those during moderate up-estuary wind (Fig. 3def) but with larger magnitudes. Lateral circulation features two symmetric circulation cells with lateral flow convergent near the bottom. The surface-averaged salinity on the shoals is persistently 1~1.2 psu higher than that in the channel, reversing the lateral salinity gradient and thus driving near-bottom lateral flows toward the channel. The magnitude of lateral flow displays considerable tidal variations. Maximum lateral flow decreases from 11.0 cm sec^{-1} at maximum ebb to 5.1 cm sec^{-1} at maximum flood, which is opposite to the increasing trend from ebb to flood during strong down-

estuary wind. Again, the lateral flow magnitude appears to vary coherently with lateral salinity gradient and lateral shear.

3.2. Wind modifications on lateral shear in axial velocity and lateral salinity gradient

Results from the previous section suggest that, when the water column is unstratified, salinity on the shoals is persistently higher/lower than that in the channel during up-/down-estuary wind, leading to a bottom-convergent/bottom-divergent lateral circulation pattern. Such persistent salinity gradient over a tidal cycle is inconsistent with the gradient reversal ($\partial s/\partial y$ change sign) between flood and ebb expected from the pure tidally-driven differential advection mechanism (Nunes and Simpson 1985; Lerczak and Geyer 2004). The inconsistency thus implies wind modifications of lateral shear.

To examine the wind influences on lateral shear, we first look at the cross-sectional structures of subtidal axial velocity (Fig. 5). In a channel with a triangular cross section, we expect subtidal axial flow to show considerable lateral variations during wind events because pure wind-driven flow is down-wind on the shoals and up-wind in the channel (Csanady 1973; Wong 1994; Sanay and Valle-Levinson 2005).Without wind, the subtidal axial flow at the channel midpoint is primarily vertically segregated, consistent with gravitational circulation (Fig. 5a). In general, down-estuary wind enhances the magnitude of subtidal flow because wind-driven flow and gravitational circulation are in concert (Fig. 5b and 5c). The subtidal flow during moderate down-estuary wind shows little lateral variations because the water column is stratified (Fig. 3abc). This is analogous to the “weakly frictional” regime of

density-driven exchange flows by Valle-Levinson et al. (2003). However, the subtidal flow indeed shows large lateral variations during strong down-estuary wind (Fig. 5c). The subtidal flow becomes more laterally segregated when wind-driven axial flow dominates (W~2.5) and the water column is unstratified. This enhanced subtidal lateral shear could then advect the salinity gradient further down-estuary on the shoals to withstand the tendency of reversing gradient during ebbs, which then leads to a persistently saltier channel region.

Moderate and strong up-estuary wind reverses the subtidal lateral shear. During moderate wind, the subtidal axial flow is weak because wind-driven flow nearly cancels gravitational circulation (W~0.85; Fig. 5d). However, the subtidal flow is up-estuary on the shoals and down-estuary in the channel, revealing the wind influences. As the wind-driven flow dominates during strong wind, reversal of the subtidal lateral shear becomes apparent (W~2.5; Fig. 5e). The reversed, laterally sheared flow could then advect salt further up-estuary on the shoals and down-estuary in the channel to create shoal regions with persistently higher salinity, as shown in Fig. 3def and Fig. 4def.

The wind modulations of lateral shear described above are confirmed by the time series. The lateral shear ($\partial u/\partial y$) is averaged over the left half of the cross-section (looking seaward). Thus, a positive value means that the axial velocity increases toward the channel axial. The subtidal lateral shear does not change much during moderate down-estuary wind (Fig. 6a; from day 129-131) but increases from 0.5×10^{-4} before the event to 1.2×10^{-4} (sec^{-1}) during strong down-estuary wind (Fig. 6c). For up-estuary wind cases, on the other hand, the subtidal lateral shear changes

sign and decreases to -0.6 x 10^{-4} during moderate wind (Fig. 6e) and to -1.3 x 10^{-4} (sec^{-1}) during strong wind (Fig. 6g). Note however that the transient effects within about 1 day after the event onset and end also have strong signals. These transient effects are due to sea-level adjustment (Chen and Sanford, submitted). For example, in the beginning of a down-estuary wind event, sea-level starts to tilt up toward the mouth, accompanying with a net down-estuary volume transport. This transient down-estuary flow is stronger in the channel and hence reduces/reverses lateral shear (Fig. 6a and 6c after day 128). Nevertheless, when the water column is unstratified, the enhancement/reversal of subtidal lateral shear by down-/up-estuary wind after the transient adjustment is clear.

The snapshots of the cross-sectional structures shown in Fig. 5 also imply that wind modification of lateral shear controls the lateral salinity gradient through diffrential advection. This implication is supported by the good correspondence between lateral shear and lateral salinity differences (ΔS). ΔS is computed by differentiating the salinity between channel and shoal and then averaging over the entire surface layer (<5m). Positive ΔS indicates the channel region is saltier. When the water column is unstratified, after the transient adjustment during day 128-129, the changes in subtidal lateral shear generally correspond to the changes in ΔS. During strong down-estuary wind, lateral shear and ΔS both increase (Fig. 6cd), whereas during up-estuary winds lateral shear and ΔS both change sign and decrease (Fig. 6ef and 6gh). The stronger up-estuary wind stress leads to larger changes in lateral shear and in ΔS. However, when the water column is stratified, there is no clear relationship between lateral shear and ΔS (Fig. 6ab). Although lateral shear and

ΔS appear to correlate with each other during the adjustment period (day 128-129) for the up-estuary wind cases, such correlation may be partially spurious. During the adjustment period, the water column changes from stratified to unstratified condition (not shown here; Chen and Sanford, submitted). Therefore, vertical mixing alone could increase ΔS. This is why the transient reversal of lateral shear for strong down-estuary wind does not correspond to a decrease in ΔS (Fig. 6cd).

3.3. Interactions between wind-induced and tidally-induced lateral shear

It is apparent in Fig. 6 that lateral shear fluctuates with tides (thin lines). The magnitude of lateral shear is larger during floods for strong down-estuary wind (3rd vertical line in Fig. 6c) but is larger during ebbs for strong up-estuary wind (1st vertical line in Fig. 6g). Such pattern is a result of interactions between wind-induced and tidally-induced lateral shear. In our definition, positive lateral shear means axial velocity increases toward the channel axis. When the subtidal lateral shear is positive, such as during strong down-estuary wind, flooding currents will further enhance the existing lateral shear whereas ebbing currents will reduce it (Fig. 6c). The opposite occurs during up-estuary winds when the subtidal lateral shear is negative (Fig. 6e and 6g). Such interactions do not exist during moderate down-estuary wind simply because the wind modification of lateral shear is small (Fig. 5b and Fig. 6a). The interactions between wind-induced and tidally-induced lateral shear create a tidal asymmetry in lateral shear which has an important control on the magnitude of lateral flows (see below).

3.4. A Hansen-Rattrary-Like scaling

Our analyses in section 3.2 suggest that, when the water column is unstratified, axial wind exerts a leading order control on lateral shear, which in turn controls the lateral salinity gradient that drives lateral circulation. It is shown in section 3.3 that the wind-induced lateral shear interacts with tides to generate tidal variations in lateral shear. So the question to be addressed next is whether the tidal variations in lateral shear drives the variability of lateral flow, as hinted in Fig. 4.

To answer this question, we seek a linkage between lateral flow and lateral shear. Since the lateral circulation pattern of two circulation cells symmetric about the channel axial and the concurrent salinity distribution are very similar to those resulted from tidally driven differential advection, a scaling analysis for the pure tidal process provided by Lerczak and Geyer (2004) may be applicable to our cases with wind forcing. Assuming that the pressure gradient force balances the vertical stress divergence in lateral momentum equation, Smith (1980) and Nunes and Simpson (1985) gave the scale of lateral flow driven by differential advection (v_{DA}) as

$$v_{DA} \sim \frac{1}{48}\frac{g\beta H^3}{A_v}s_y, \qquad (2)$$

where g is the gravitational acceleration, H is the water depth, A_v is the vertical eddy viscosity, s is salinity, and β is the saline expansion. Note that v_{DA} scaling has the same functional form as the gravitational circulation derived by Hansen and Rattray (1965) because the same momentum balance was used in the axial direction. It is clear in Eq. (2) that the lateral salinity gradient (s_y) is the driving force for lateral circulation. The two-layer lateral flow viewing from half of the cross-section (e.g. Fig. 4c) also largely resembles a "sideway" gravitational circulation.

Lerczak and Geyer (2004) argued that lateral salinity gradient scales with lateral shear via

$$s_y \sim u_y s_x / \omega, \tag{3}$$

where ω is the tidal frequency. The link between s_y and u_y in Eq. (3) comes from an equation governing the time evolution of s_y (e.g. Chen and Sanford 2008):

$$\underset{\text{(i)}}{(s_y)_t} \approx \underset{\text{(ii)}}{-u_y s_x} \underset{\text{(iii)}}{- v_y s_y} \underset{\text{(iv)}}{- w_y s_z} + \underset{\text{(v)}}{\left[\left(K s_z\right)_z\right]_y}, \tag{4}$$

in which (u,v,w) is the velocity field and K is the vertical eddy diffusivity. For our cases, when the water column is unstratified, the last two terms associated with isohaline tilting and boundary mixing are negligible. Assuming that s_x and s_y are of the same order of magnitude, the differential advection term (ii) is likely larger than the lateral compression term (iii). Consequently, Eq. (4) reduces to $(s_y)_t \approx -u_y s_x$ which can be readily integrated to yield Eq. (3). Plugging Eq. (3) into Eq. (2), the scale of lateral flow becomes

$$v_{DA} \sim \frac{1}{48}\frac{g\beta H^3}{A_v} s_y \sim \frac{1}{48}\frac{g\beta H^3}{A_v \omega} s_x u_y. \tag{5}$$

This scaling simply states that the laterally sheared advection of axial salinity gradient ($u_y s_x$) controls the changes in lateral salinity gradient that in turn drives lateral flows.

Next we test this scaling against the model results to see if the tidal variations in lateral shear drive the variability of lateral flow. The strength of lateral flow is diagnosed by the cross-sectionally averaged lateral velocity magnitude ($\bar{v}$)

$$\bar{v} = \frac{1}{A}\int |v| \cdot dA. \tag{6}$$

To obtain v_{DA}, we estimate the axial salinity gradient by the distance between 2 and 30 psu in the channel, A_v by the cross-sectionally averaged eddy viscosity from the closure, H as the channel depth, and u_y by the cross-sectionally averaged value as in Fig. 6.

During strong winds after the transient adjustment, v_{DA} and $\bar{v}$ are in good agreements (Fig. 7b and 7d from day 129-131). The predicting skills (Willmott 1981; Li et al. 2005) are 0.92 and 0.83 for strong down- and up-estuary wind, respectively (Table 2). The good agreement strongly suggests that variation in lateral flows is driven by lateral shear. For strong down-/up-eatuary wind, the lateral flow magnitude peaks at flood/ebb when the magnitude lateral shear reaches its maximum. This maximum occurs when wind-induced and tidally-induced lateral shear are in concert (section 3.2). For moderate up-estuary wind, the skill of v_{DA} scaling is marginal, with a value of 0.3. The decrease of predicting skill is not unexpected. During moderate up-estuary wind, the lateral shear is weak due to the comparable wind-driven and gravitational circulations (Fig. 5d). This weak lateral shear thus requires longer time than the strong up-estuary wind case to reverse the lateral salinity gradient. In other words, the flow and salinity fields are likely still under adjustment during the event (e.g. after day 129 in Fig. 6ef). For moderate down-estuary wind, the v_{DA} scaling as expected has no predicting skill (0.05; Fig. 6a) because differential advection is not the main driving mechanism for lateral circulation. It should be noted that the v_{DA} scaling is very sensitive to water depth (H). Using the averaged depth to compute v_{DA} improves the skill for the moderate up-estuary wind case from 0.3 to 0.5 but underestimates the lateral flow magnitudes during strong wind cases (skill decreases

to around 0.6; Table 2). Nevertheless, it is clear that the v_{DA} scaling captures most of the lateral flow variability when the water column is unstratified, especially during strong winds. This therefore provides a strong support for the importance of lateral shear in driving lateral circulation during wind events.

3.5. Influences of Earth rotation

Including Earth rotation induces axial asymmetry in lateral circulation, but, when the water column is unstratified, the lateral circulation patterns are similar to those without rotation. During strong down-/up-estuary wind, both non-rotating and rotating cases show a pattern of two lateral circulation cells with flow divergent/convergent near the bottom (Fig. 8cd and 8gh). The circulation cells in the rotating cases are slightly asymmetrical about the channel axis (Fig. 8d and 8h). Similar comparison results are found during moderate up-estuary wind. The bottom-convergent lateral circulation can still be seen when rotation is included (Fig. 8f), but the right side of the cell is stronger than the left side (looking seaward) and the axial asymmetry in lateral circulation is also larger than the strong wind cases. The similarity in lateral circulation pattern between non-rotating and rotating cases breaks down when the water column is stratified. During moderate down-estuary wind, the lateral circulation with rotation is radically different from that without rotation (Fig. 8ab). With rotation, the circulation is dominated by a counter-clockwise circulation which is consistent with Ekman veering in the bottom boundary layer during floods..

The magnitudes and temporal variations of lateral flows are also similar between non-rotating and rotating cases when the water column is unstratified. The

magnitude is diagnosed by the cross-sectionally averaged lateral flow velocity (Eq. 6). During strong winds, the time series of lateral flow with/without rotation are nearly identical, especially after the transient adjustment (day 129-131 in Fig. 9b and 9d). The correlation coefficients are 0.88 and 0.86 for strong down- and up-estuary wind, respectively. During moderate up-estuary wind, the lateral flow magnitude with rotation is on average 49% higher than that without rotation, and the correlation coefficient diminishes slightly to 0.66. Nonetheless, the magnitude and temporal variations in lateral flow with rotation still generally resembles those without rotation. Again, the similarity between non-rotating and rotating cases breaks down under a stratified condition, as illustrated by the cross-sectional structure in Fig. 8ab. During moderate down-estuary wind, the lateral flow magnitude with rotation is on average 82% higher than that without rotation, and the correlation coefficient is low with a value of 0.28.

4. Lateral sediment transport

4.1. Patterns of lateral sediment transport at different tidal phases

We begin our exploration of lateral sediment transport by examining the cross-channel distribution of bottom shear stress that mobilizes the sediments. The interactions between tidal currents, wind-driven flow, and gravitational circulation control the bottom stress distribution which varies with wind direction and exhibit considerable tidal variations. During down-estuary winds, bottom stress peaks in the channel during flood when the flooding currents, wind-driven circulation, and gravitational circulation are all directed up-estuary in the channel (Fig. 3c and 4c). As

expected, bottom stress is weak at slack, but there is still a small peak in the channel (Fig. 3b and 4b) because the presence of down-estuary wind strengthens the subtidal axial velocity (Fig. 5bc; section 3.2). At ebbs, the peak of bottom stress in the channel disappears because ebbing currents are now against the up-estuary-directed subtidal flow there (Fig. 3a and 4a). But there are two secondary peaks on the shoals where ebbing currents and down-estuary-directed subtidal flow are working together. While the stress distributions at different tidal phases are similar between moderate and strong down-estuary winds, the stress magnitude is larger during strong wind simply because of the larger wind-driven flow.

The interactions between tides, wind, and gravitational circulations in controlling stress distribution described above reverse for the up-estuary wind cases. During up-estuary winds, the subtidal axial flow is up-estuary on the shoals and down-estuary in the channel (Fig. 5de). Therefore, bottom stress peaks in the channel at ebbs when ebbing currents strengthens the down-estuary-directed subtidal flow in the channel (Fig. 3d and 4d). Two secondary peaks on shoals occur at floods as flooding currents and the up-estuary-directed subtidal flow are coherent there (Fig. 3f and 4f).

The transport direction of lateral sediment flux is dictated by the near-bottom lateral flows. This is anticipated because the sediment fluxes are larger near the bottom where the suspended sediment concentration is higher. Sediments are transported from channel to shoals during down-estuary winds (Fig. 3abc and 4abc), whereas the transport direction is reversed, becoming from shoals to channel during up-estuary winds (Fig. 3def and 4def). Although moderate and strong down-estuary

winds both induce channel-to-shoals transport, the near-bottom lateral flows as a transport agent are driven by different mechanisms (boundary mixing and differential advection, respectively; section 3) and the sediment fluxes during moderate down-estuary wind are confined close to the bottom due to stratification. The lateral sediment fluxes during strong winds are larger than those during moderate winds because of a combination of larger bottom stress and stronger lateral flows.

The magnitude of lateral sediment flux also varies within a tidal cycle. In general, the flux magnitude peaks when the bottom stress peaks in the channel (Fig. 3c, 3d, 4c, 4d). Such pattern is due in part to the tidal asymmetry in the strength of bottom stress. However, during strong winds, the coincidence of peak lateral flow and bottom stress also appears to be important (Fig. 4c and 4d). The peak of bottom stress in the channel occurs as the subtidal axial flow and the tidal currents are toward the same direction. This timing also matches the occurrence of maximum lateral shear when the tidally-induced and subtidal lateral shears are of the same sign (section 3.3). The maximum lateral shear then drives the strongest lateral circulation that, in conjunction with peak bottom stress, leads to a maximum lateral sediment flux in a tidal cycle.

4.2. Integrated transport during events

To measure the net lateral sediment transport, we integrate the lateral sediment fluxes over depth, average over half of the channel width, and low-passed filter to define a net transport rate (T: kg m^{-1} sec^{-1}) as

$$T = \left\langle \frac{2}{W} \int_{W/2}^{W} \int_{-h}^{\eta} v \cdot C \cdot dz dy \right\rangle, \qquad (7)$$

where the angle bracket represents 33hr low-passed filter, C is the suspended sediment concentration, η and h are the surface elevation and water depth at a given cross-channel location, and W is the channel width. The transport rate is calculated at the right half of the cross-section. Thus, a positive value means a transport from channel to shoals.

After the transient adjustment, the net lateral sediment transport during the event is toward shoals/channel during down-/up-estuary winds. The magnitude of net transport is as expected larger during strong winds (section 4.1). Before the event, the steady-state transport driven by boundary mixing (Chen and Sanford 2008) is from channel to shoals with $T = 1.8 \times 10^{-4}$. During moderate and strong down-estuary wind, this channel-to-shoal transport rate increases to a maximum value of 4.1×10^{-4} and 2.3×10^{-3}, respectively (Fig. 10ab). For both cases, the strongest signal however occurs after the event with $T = 4.1 \times 10^{-4}$ and 3.8×10^{-3}. During moderate and strong up-estuary winds, on the other hand, the net transport is from shoals to channel after day 129 with maximum $T = -4.9$ and -7.4×10^{-4}, respectively (Fig. 10de). Note that for strong up-estuary wind, there is a pulse of transport from channel to shoal after the event onset. This initial pulse is consistent with the positive lateral salinity gradient in Fig. 6h. This suggests that, before the lateral salinity gradient is reversed, the salinity in the channel is still higher than that on the shoals, which then drives this transient channel-to-shoal transport. It is also noteworthy that the lateral sediment transport happens in pulses (thin lines in Fig. 10). The largest transport occurs at floods/ebbs

during down-/up-estuary winds after the transient adjustment, as described in section 4.1.

4.3. Influences of surface gravity waves

Including surface gravity waves greatly increases the magnitude of lateral sediment transport. As mentioned in model setup (section 2), two numerical experiments (No. 15 and 16) accounting for wind-generated waves under moderate winds are carried out to evaluate the influences of surface gravity waves on lateral sediment transport. With waves, the bottom stresses increase exponentially toward the shoals during both moderate down- and up-estuary winds, indicating the dominance of wave-induced bottom stresses (solid lines in Fig. 11). In the channel, the bottom stresses with waves (solid lines) match those without waves (dashed) because the wave orbital velocity has decayed before reaching the channel bottom. High suspended sediment concentration on the shoals is apparent, strongly contrasting with the limited concentration across the entire cross-section in the cases without waves (Fig. 3c and 3f). The sediment transport direction remains channel-to-shoal during down-estuary wind and shoal-to-channel during up-estuary wind, but the magnitude of lateral sediment flux is an order of magnitude larger with waves (Fig. 11ab and Fig. 3cf). During moderate up-estuary wind, high suspended sediment concentration reaches the mid-depth near the channel due to the convergence of sediment fluxes (Fig. 11b).

An order of magnitude increase in net transport rate with waves can be clearly seen from the time series. During moderate down-estuary winds, the net transport rate

increases from 4.1 x 10^{-4} without waves (Fig. 10a) to a maximum value of 1.5 x 10^{-3} with waves (Fig. 10c). During moderate up-estuary winds, on the other hand, the shoal-to-channel transport rate increases from 4.9 x 10^{-4} without waves (Fig. 10d) to a maximum value of 6.4 x 10^{-3} with waves (Fig. 10f). Note that, in the presence of waves, the maximum magnitude of net transport during up-estuary wind is much larger than that during down-estuary wind. This is because the highest suspended sediment concentration and largest lateral salinity gradient (thus lateral flow) both locate on the shoals during up-estuary wind (Fig. 3def and Fig. 11b).

5. Discussion and Summary

5.1. Driving mechanism for lateral circulation during axial wind events

Our model results suggest that the driving mechanisms for lateral circulation during axial wind events are different between stratified and unstratified conditions. When the water column is stratified, the lateral flow and salinity structures below halocline closely resemble those driven by the boundary mixing mechanism (Chen and Sanford 2008), and the rotation effect is important. When the water column is unstratified, the lateral circulation and its variability are driven by the interactions between wind-induced and tidally-induced differential advection, and the rotation effect is relatively weak.

The controls of lateral salinity gradient by the interactions between wind-induced and tidally-induced differential advection can be illustrated by a schematic diagram. Under a simplest condition without wind, tides, and rotation, the subtidal lateral structure of an isohaline is distorted by the density-driven gravitational

circulation, forcing high salinity water up-estuary in the channel (Fig. 12a). Adding axial wind forcing with a stress comparable or larger than the baroclinic pressure gradient force ($|W| \sim or > 1$) significantly modifies the lateral structure of subtidal axial flow (e.g. Fig. 5). Down-estuary wind increases subtidal lateral shear, whereas up-estuary wind reverses it. The increase/reversal of lateral shear advects the axial salinity gradient to create a saltier channel/shoal region during down-/up-estuary wind (Fig. 12b). This wind-induced differential advection is supported by the good correspondence between the subtidal lateral shear and the averaged, channel-shoal salinity difference (ΔS) during the events in Fig. 6. The resulting lateral salinity gradient then drives the persistent bottom-divergent/-convergent lateral circulation (Fig. 12b; also Fig. 3def and Fig. 4). When the tides are included, the wind-induced and tidally-induced lateral shear interact to generate tidal variations (Fig. 12c). During down-estuary wind, flooding currents further enhance the lateral shear while ebbing currents reduce it. The opposite occurs during up-estuary wind. Therefore, a larger lateral salinity gradient occurs when the wind-induced and tidally-induced differential advection are in concert, which in turn drives a stronger lateral flow.

To further validate the link between lateral shear and lateral flow, a Hasen-Rattray-like scaling (v_{DA} Eq. 5) is used to predict the model outputs of lateral flow magnitude (Fig. 7). The predicting skills and the correlation coefficients between v_{DA} and $\bar{v}$ for the non-rotating cases are summarized in Table 2. It is apparent that, when stratification is weak (unshaded area), the v_{DA} scaling is a reasonable predictor. The skills and correlations are especially high during strong winds (No. 7-10). The good predicting skills thus provide a strong support for our assertion that the interactions

between wind-induced and tidally-induced lateral shear drive the variability of lateral flows.

When rotation is included and when the water column is unstratified, the similarities in lateral flow structure, magnitude, and temporal variations between non-rotating and rotating cases suggest that lateral circulation is primarily driven by the mechanism described above rather than the Ekman dynamics (Fig. 8 and 9). This statement is particularly precise during strong winds when the lateral salinity gradient set by wind is larger. The weak rotation (Ekman) effect is most likely due to the weak stratification. When the water column is unstratified, the boundary layers that confine the Ekman transport likely merge and occupy the entire depth. A simple estimate of boundary layer thickness with $\sqrt{2A_v/f}$ (f is the Coriolis parameter; A_v is the cross-sectionally averaged eddy viscosity) yields a value of around 9-10m which is clearly sufficient to cause the Ekman transport in the surface and bottom layers to merge with each other. The comparable boundary layer thickness and water depth also implies that the time scale for transferring momentum in the vertical is shorter than the rotation time scale (1/f) at most of the cross-channel locations. Therefore, the Ekman veering that gives rise to lateral flow is reduced (Lentz 2001).

In summary, the wind-induced differential advection can be an important driving mechanism for lateral circulation during wind events when: (1) $|W| \sim or > 1$, which allows axial wind to significantly alter lateral salinity gradient through laterally sheared advection ($u_y s_x$ in Eq. 5); and (2) the stratification is weak. The weak stratification not only reduces the Ekman transport but also allows the baroclinic pressure gradient force to develop with depth, which then drives the bottom-

divergent/-convergent lateral circulation. This mechanism, to the best of author's knowledge, has not yet been documented in the literatures. Its absence in the analytical models such as Huijts et al. (2008) is due to the fact that, to reach a tangible analytical solution, the lateral density gradient is often prescribed and the problem is often reduced to 2D. However, our results demonstrate that the lateral density gradient is dynamically linked to axial salt transport by axial wind. In other words, salt and flow fields have to be considered/solved together. We are also not awere of any field observations on particularly the reversal of lateral salinity gradient during up-estuary winds. The lack of observations is likely because the field effort targeted to adequately resolve the lateral dimension is rare. The only relevant study is by Sanay (2003), in which she modeled a problem similar to ours but without tides. She found similar higher salinity shoals during up-estuary winds, but the resulting lateral flow magnitude in her simulations was unrealistically large (10-20 cm sec^{-1}), probably due to the lack of tidal mixing/stirring to reduce lateral salinity gradient. Nevertheless, in the presence of axial salt gradient, the mechanisms driving lateral circulation during wind events are clearly not well understood. The wind-induced differential advection proposed here thus serves as a first attempt and its validity requires future field investigations.

5.2. Total lateral sediment transport during wind events and the implications

To quantify the total lateral sediment transport of an event, we integrate the net transport rate (Eq. 7) from the event onset to one day after the event ends (day 128-132) to properly account for the transient adjustments (e.g. Fig. 10b). The total

transport and the event-averaged transport rate are summarized in Table 3. The total transport is from channel to shoal for down-estuary winds but is reversed for up-estuary winds. This pattern is dictated by the near-bottom lateral flow. Including wind-wave forcing greatly increases the total transport because wind-wave action on the shoals leads to a much larger sediment source. The influence of wind-waves is particularly strong during up-estuary wind, as shown by the order-of-magnitude increase in transport (see section 4.3).

The implications of the transport patterns described above are: (1) lateral circulation during up-estuary winds can provide a mechanism to move fine sediments from shoals to channel. The lateral circulation driven by tidally-induced differential advection and boundary mixing tends to favor net transport from shoals to channel (Lerczak and Geyer 2004; Chen and Sanford 2008), which can not explain the net depositional channel region and the constant channel dredging in coastal plain estuaries like Chesapeake Bay (Colman et al. 1992). Transport during up-estuary wind events thus provides a plausible explanation; (2) when wind-wave forcing is included, frequent up-estuary wind events are not required to result in a net depositional channel. The total transport after a 3-day event needs around 45-day of background channel-to-shoal transport to compensate (Table 3). Such result highlights the importance to revolve episodic events with wind-wave coupling, which thus merits further investigations; and (3) the transient effects during the adjustment period can be important. While the instantaneous sediment fluxes are stronger during stronger wind stresses (Fig. 10), the total transport may not show the same trend. For example, the total transport during strong up-estuary wind is actually slightly lower

than moderate up-estuary wind (Table 3). This is due to the initial pulse of channel-to-shoal transport during the transient adjustment (Fig. 10e; day 128-129). Such result also implies that limited sediment supply, as opposed to unlimited condition here, may further complicate the sediment transport pattern during wind events. A more realistic sediment bed model is thus needed for future investigations on event-driven transport.

Acknowledgements

We thank the ROMS code developer/user community and the financial support from ONR through the Community Sediment Transport Modeling (CSTM) project.

References

Canuto, V. M., A. Howard, Y. Cheng, and M. S. Dubovikov, 2001: Ocean turbulence I: one-point closure model-Momentum and heat vertical diffusivities. *Journal of Physical Oceanography*, **31,** 1413-1426.

Chant, R. J. and E. Wilson, 1997: Secondary circulation in a highly stratified estuary. *Journal of Geophysical Research*, **102,** 23207-23216.

Chen, S. N. and L. P. Sanford, 2008: Lateral circulation driven by boundary mixing and the associated transport of sediments in idealized partially-mixed estuaries. *Continental Shelf Research***,** doi:10.1016/j.csr.2008.01.001.

Chen, S. N. and L. P. Sanford: Axial wind effects on stratification and longitudinal salt transport in an idealized, partially mixed estuary. *Submitted to Journal of Physical Oceanography*.

Colman, S. M., J. P. Halka, and C. H. Hobbs, 1992: Patterns and rates of sedimentation in the Chesapeake Bay during the Holocene Rise in sea level, 101-111 pp.

Csanady, G. T., 1973: Wind-induced barotropic motions in long lakes. *Journal of Physical Oceanography*, **3,** 429-438.

Dean, R. G. and R. A. Dalrymple, 1991: *Water Wave Mechanics for Engineers and Scientists*. World Scientific.

Fischer, H. B., E. J. List, R. C. Y. Koh, J. Imberger, and N. A. Brooks, 1979: *Mixing in inland and coastal waters*. Academic Press Inc.

Fugate, D. C., C. T. Friedrichs, and L. P. Sanford, 2007: Lateral dynamics and associated transport of sediments in the upper reaches of a partially mixed estuary, Chesapeake Bay, USA. *Continental Shelf Research*, **27,** 679-698.

Geyer, W. R., 1997: Influence of wind on dynamics and flushing of shallow estuaries. *Estuarine, Coastal, and Shelf Science*, **44,** 713-722.

Geyer, W. R., R. P. Signell, and G. C. Kineke, 1998: *Lateral trapping of sediment in a partially mixed estuary*. *Physics of Estuaries and Coastal Seas*, Balkema.

Goda, Y., 2003: Revisiting Wilson's formulas for simplified wind-wave prediction. *Journal of Waterway, Port, Coastal and Ocean Engineering*, **129,** 93-95.

Haidvogel, D. B., H. G. Arango, K. Hedstrom, A. Beckmann, and P. Malanotte-Rizzoli, 2000: Model evaluation experiments in the North Atlantic basin: Simulations in nonlinear terrain-following coordinates. *Dynamics of Atmospheres and Oceans*, **32,** 239-281.

Hansen, D. V. and M. Rattray, 1965: Gravitational circulation in straits and estuaries. *Journal of Marine Research*, **23,** 104-122.

Huijts, K. M. H., H. M. Schuttelaars, H. E. de Swart, and A. Valle-Levinson, 2006: Lateral entrapment of sediment in tidal estuaries: An idealized model study. *Journal of Geophysical Research*, **111,** C12016, doi:10.1029/2006JC003615.

Huijts, K. M. H., H. M. Schuttelaars, H. E. de Swart, and C. T. Friedrichs, 2008: Analytical study of the transverse distribution of along-channel and transverse residual flows in tidal estuaries. *Continental Shelf Research*, doi:10.1016/j.csr.2007.09.007

Jones, W. P. and B. E. Launder, 1972: The prediction of laminarization with a two-equation model of turbulence. *International Journal of Heat and Mass Transfter*, **15,** 301-314.

Kerhin, R., J. Halka, D. V. Wells, E. L. Hennessee, P. J. Blakeslee, N. Zoltan, and R. H. Cuthbertson, 1988: The Surficial Sediments of Chesapeake Bay, Maryland: Physical Characteristics and Sediment Budget. Investigation Report 48, 43 pp.

Lacy, J. R. and S. G. Monismith, 2001: Secondary currents in a curved, stratified, estuarine channel. *Journal of Geophysical Research*, **106,** 31283-31302.

Langland, M. and T. M. Cronin, 2003: A summary report of sediment processes in Chesapeake Bay and watershed. U. S. G. S. W. R. I. R. 03-4123, Ed.

Large, W. G. and S. Pond, 1981: Open ocean momentum flux measurements in moderate to strong winds. *Journal of Physical Oceanography*, **11,** 324-336.

Lentz, S. J., 2001: The influence of stratification on the wind-driven cross-shelf circulation over the North Carolina shelf. *Journal of Physical Oceanography*, **31,** 2749-2760.

Lerczak, J. A. and W. R. Geyer, 2004: Modeling the lateral circulation in straight, stratified estuaries. *Journal of Physical Oceanography*, **34**.

Li, M., L. J. Zhong, and W. C. Boicourt, 2005: Simulations of Chesapeake Bay estuary: Sensitivity to turbulence mixing parameterizations and comparison with observations. *Journal of Geophysical Research*, **110,** C12004.

Lin, W., L. P. Sanford, and S. E. Suttles, 2002: Wave measurement and modeling in Chesapeake Bay. *Continental Shelf Research*, **22,** 2673-2686.

Madsen, O. S., 1994: Spectral wave-current bottom boundary layer flows. *Proceedings 24th International Conference on Coastal Engineering, ASCE, Kobe*, **1,** 384-398.

Monismith, S. G., 1986: An experimental study of the upwelling response of stratified reservoirs to surface shear stress. *Journal of Fluid Mechanics*, **171,** 407-439.

Nunes, R. A. and J. H. Simpson, 1985: Axial convergence in a well-mixed estuary. *Estuarine, Coastal, and Shelf Science*, **20,** 637-649.

Ott, M. W. and C. Garrett, 2002: Frictional estuarine flow in Juan de Fuca Strait with implications for secondary circulation. *Journal of Geophysical Research*, **103,** 15657-15666.

Resio, D., S. Bratos, and E. Thompson, 2002: Meteorology and wave climate. USACE Coastal Engineering Manual.

Sanay, R., 2003: Wind-induced exchange in semi-enclosed bains, Department of Ocean, Earth, and Atmospheric Sciences, Old Dominion University.

Sanay, R. and A. Valle-Levinson, 2005: Wind-induced circulation in semienclosed homogeneous, rotating basins. *Journal of Physical Oceanography*, **35,** 2520-2531.

Scully, M. E., C. T. Friedrichs, and J. M. Brubaker, 2005: Control of Estuarine Stratification and Mixing by Wind-induced Straining of the Estuarine Density Field. *Estuaries*, **28,** 321-326.

Smith, R., 1980: Bouyancy effects upon longitudinal dispersion in wide well-mixed estuaries. *Philosophical Transactions of the Royal Society of London. Series A, Mathematical and Physical Sciences*, **296,** 467-496.

Valle-Levinson, A., C. Reyes, and R. Sanay, 2003: Effects of bathymetry, friction, and rotation on estuary-ocean exchange. *Journal of Physical Oceanography*, **33,** 2375-2393.

Valle-Levinson, A., C. Li, K. C. Wong, and K. M. M. Lwiza, 2000: Convergence of lateral flow along a coastal plain estuary. *Journal of Geophysical Research*, **105,** 17045-17061.

Warner, J. C., W. R. Geyer, and J. A. Lerczak, 2005: Numerical modeling of an estuary: A comprehensive skill assessment. *Journal of Geophysical Research*, **110,** C05001 (1-13).

Willmott, C. J., 1981: On the validation of models. *Physical Geography*, **2,** 184-194.

Winant, C. D., 2004: Three-dimensional wind-driven flow in an elongated, rotating basin. *Journal of Physical Oceanography*, **34,** 462-476.

Wong, K. C., 1994: On the nature of transverse variability in a coastal plain estuary. *Journal of Geophysical Research*, **99,** 14,209-14,222.

Zhong, L. and M. Li, 2006: Tidal energy fluxes and dissipation in the Chesapeake Bay. *Continental Shelf Research*, **26,** 752-770.

Table 1. Wind perturbation experiments. Postive is up-estuary. The event duration is 3 days (day 128 to 131). τ_{wx} is the wind stress, W is the Wedderburn number, f is the Coriolis parameter, and H_s is the wave height.

Down-estuary wind					Up-estuary wind				
No.	τ_{wx} (Pa)	W	f (sec^{-1})	H_s (m^{-1})	No.	τ_{wx} (Pa)	W	f (sec^{-1})	H_s (m^{-1})
0	0	0	0	0					
1	-0.1	-0.85	0	0	2	0.1	0.85	0	0
3	-0.15	-1.27	0	0	4	0.15	1.27	0	0
5	-0.2	-1.79	0	0	6	0.2	1.79	0	0
7	-0.25	-2.11	0	0	8	0.25	2.11	0	0
9	-0.3	-2.53	0	0	10	0.3	2.53	0	0
11	-0.1	-0.80	10^{-4}	0	12	0.1	0.80	10^{-4}	0
13	-0.3	-2.4	10^{-4}	0	14	0.3	2.4	10^{-4}	0
15	-0.1	-0.85	0	1	16	0.1	0.85	0	1

Table 2. Predicting skills of v_{DA} scaling (Eq. 5) and the correlation coefficients (R^2) between v_{DA} and $\bar{v}$ (Eq. 6). N is the buoyancy frequency. The unit for N^2 is 10^{-3} sec^{-2}. The *skill1* is when v_{DA} is computed using channel depth, whereas the *skill2* is when using averaged depth. The gray shading indicates the cases with comparable stratification to the baseline condition (No. 0).

Down-estuary wind					Up-estuary wind				
No.	N^2	*skill1*	*skill2*	R^2	No.	N^2	*skill1*	*skill2*	R^2
0	4.0	—	—	—					
1	7.2	0.05	0.11	0.4	2	0.18	0.30	0.50	0.42
3	2.3	0.12	0.31	0.5	4	0.20	0.60	0.56	0.54
5	0.40	0.45	0.77	0.68	6	0.14	0.73	0.57	0.60
7	0.22	0.87	0.64	0.81	8	0.14	0.72	0.52	0.75
9	0.18	0.92	0.62	0.94	10	0.11	0.83	0.60	0.80

Table 3. Lateral sediment transport characteristics for experiment No. 1, 2, 9, 10, 15, 16. The total transport is the net transport rate (*T* in Eq. 7) integrated from the event onset to one day after the event ends (day 128-132) in order to account for the transient effects. The event-averaged transport rate is the total transport divided by the period of time-integral (4 days here). The units of the total transport and the event-averaged transport rate are kg m^{-1} and 10^{-4} kg m^{-1} sec^{-1}, respectively. Positive means from channel to shoal.

	No Wind	Down-estuary wind			Up-estuary wind		
		0.1 Pa	0.3 Pa	0.1Pa+wave	0.1 Pa	0.3 Pa	0.1Pa+wave
Total transport	–	100.0	566.6	256.0	-39.2	-31.1	-724.0
Event-ave transport rate	1.84	2.86	16	7.33	-1.12	-0.89	-21

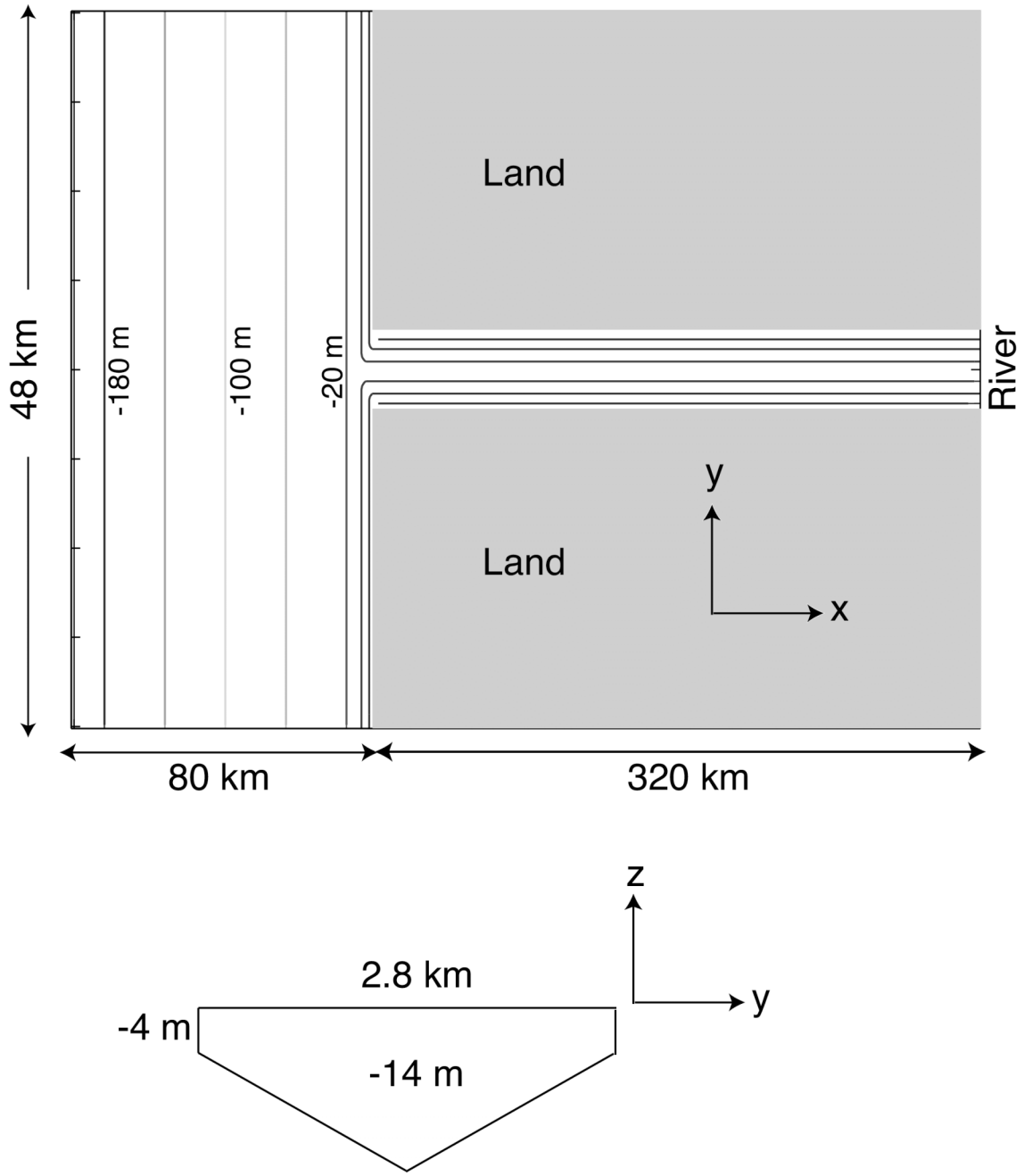

Fig. 1. Plane-view of model domain (top) and the estuarine channel cross-section (bot). The domain mimics a broad continental shelf with a long, straight estuarine channel. The shelf size is 48 km (along-shelf) x 80 km (cross-shelf) with a constant slope from 200 m (off-shelf boundary) to 4 m (land boundary). The estuarine channel extends from x=80 km to about 400 km. The gray areas are land. The channel is triangular-shaped and of 2.8 km-wide. The deep channel is 14 m, and the shallowest area is of 4 m. Note that the domain is scaled disproportionately for better visualization.

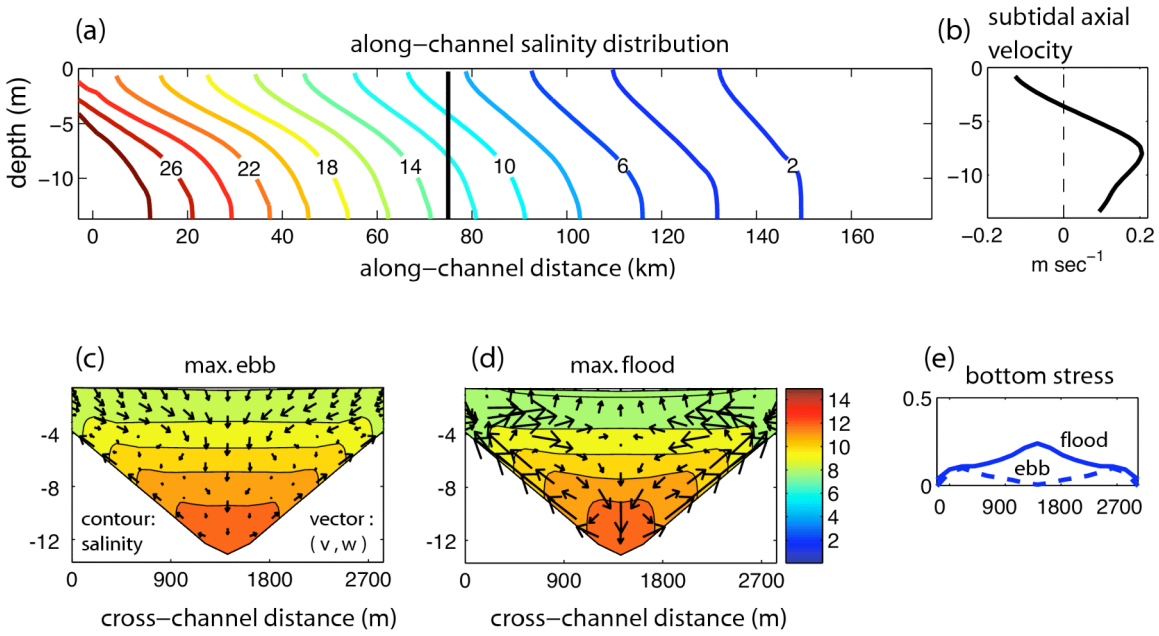

Fig. 2. Along-channel salt structure (a), vertical profile of subtidal axial velocity (b), cross-sectional structures of salinity (color contour) and lateral circulation (vectors) at maximum ebb (c) and flood (d), and lateral distribution of bottom shear stress (e) at maximum flood (solid line) and ebb (dashed line) for the baseline case (No. 0 in Table 1). Slices (b)(c)(d)(e) are taken at the channel midpoint indicated by the vertical line in (a). The channel midpoint defined as half of the salt intrusion length (~145 km).

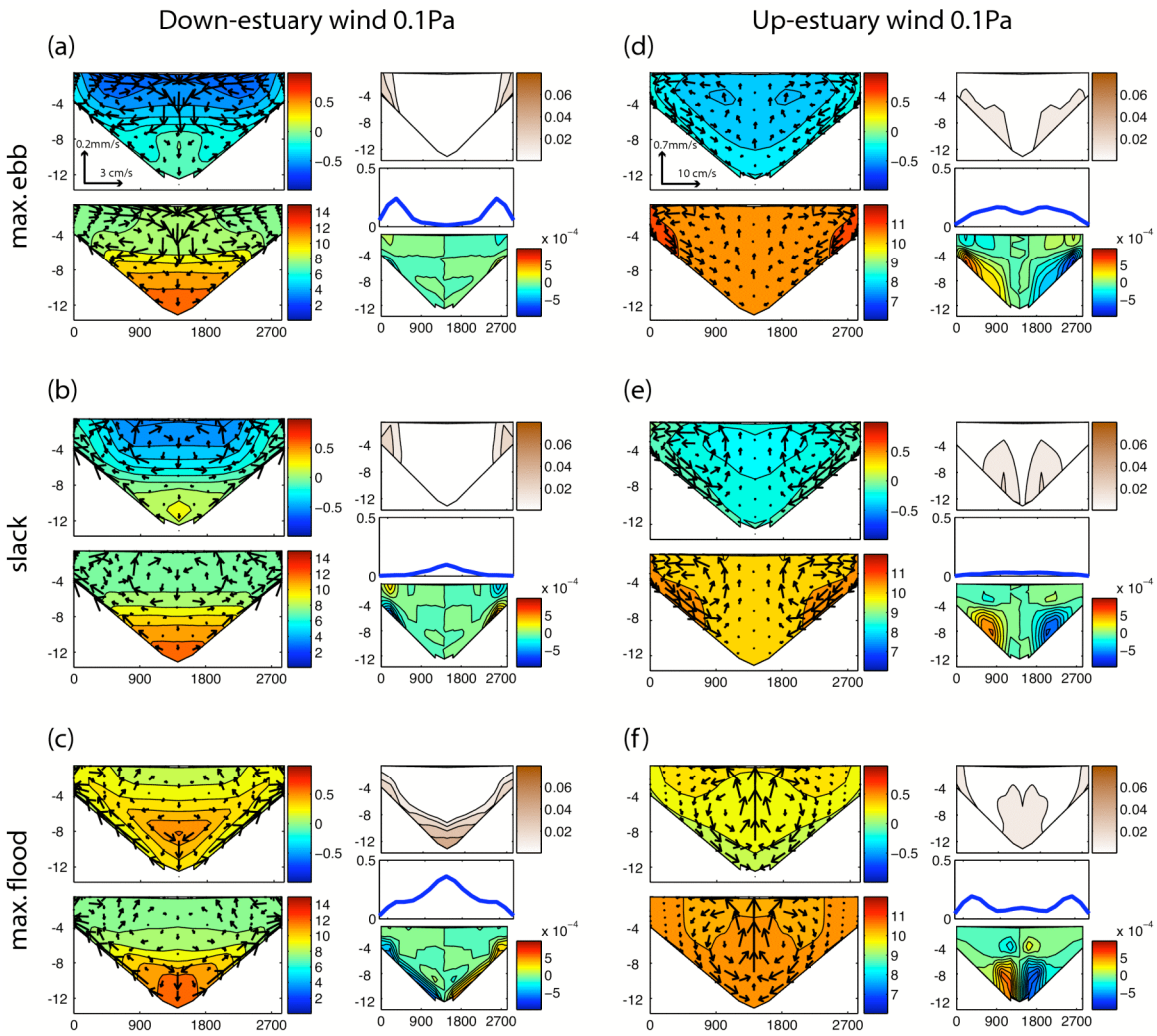

Fig. 3. Cross-sectional structures (looking seaward) of five variables for the moderate down-estuary (abc) and up-estuary (def) wind cases (No. 1 and 2 in Table 1). The profiles are taken at maximum ebb (top row), around slack (middle), and at maximum flood (bottom). Each panel (for example, Fig. 3a) has 5 small figures: The upper left is velocity field (u, v, w). Negative values in the colorbar represent ebbs. The lower left is salinity and (v, w). The upper right is suspended sediment concentration (kg m^{-3}). The middle right is bottom stress (Pa). The lower right is lateral sediment flux (kg m^{-2} sec^{-1}). Positive values in the color bar represent transport toward the right. Again the slices are taken at the channel midpoint.

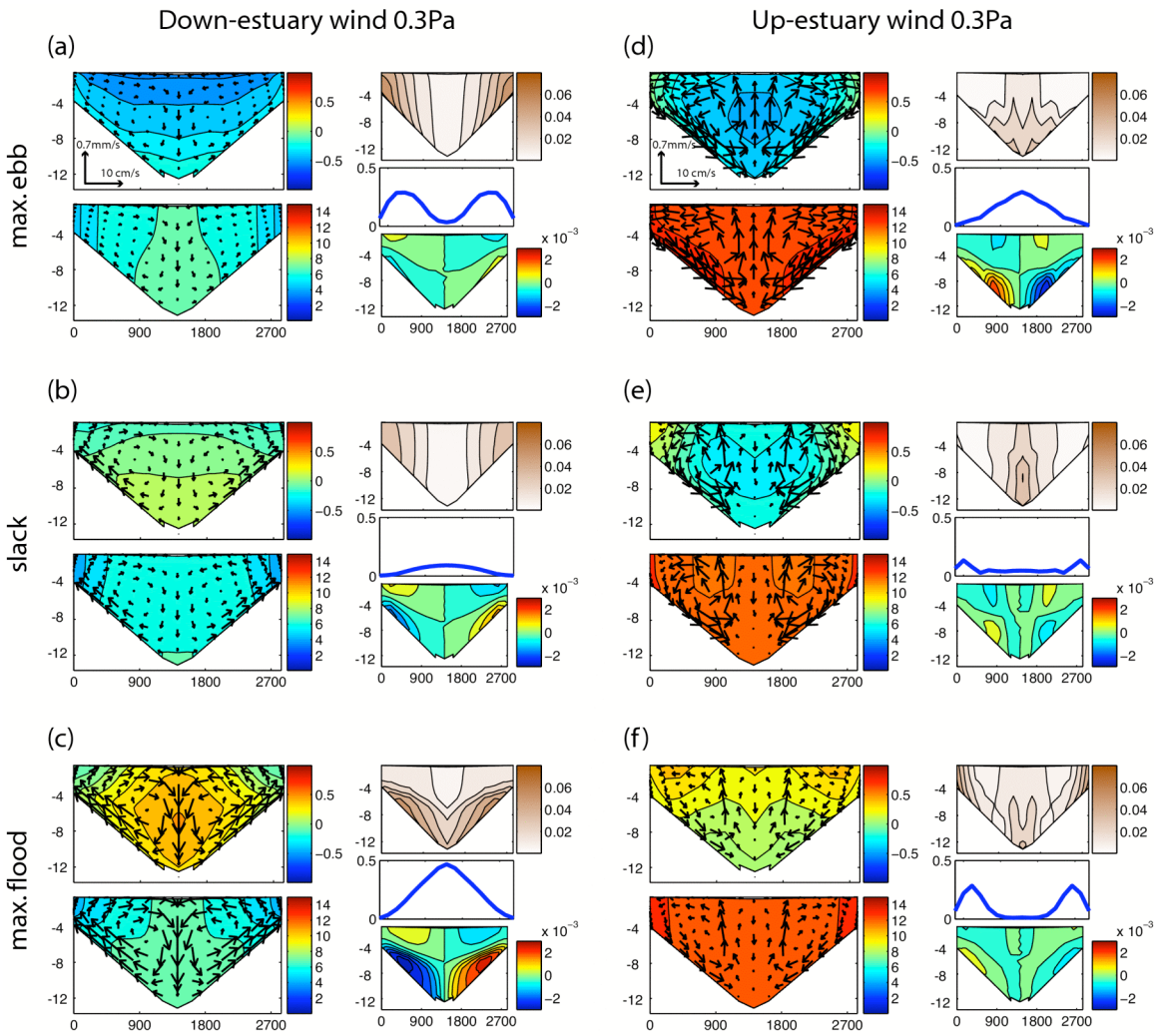

Fig. 4. Same as Fig. 3 but for the strong down-estuary (abc) and up-estuary (def) wind cases (No. 9 and 10 in Table 1).

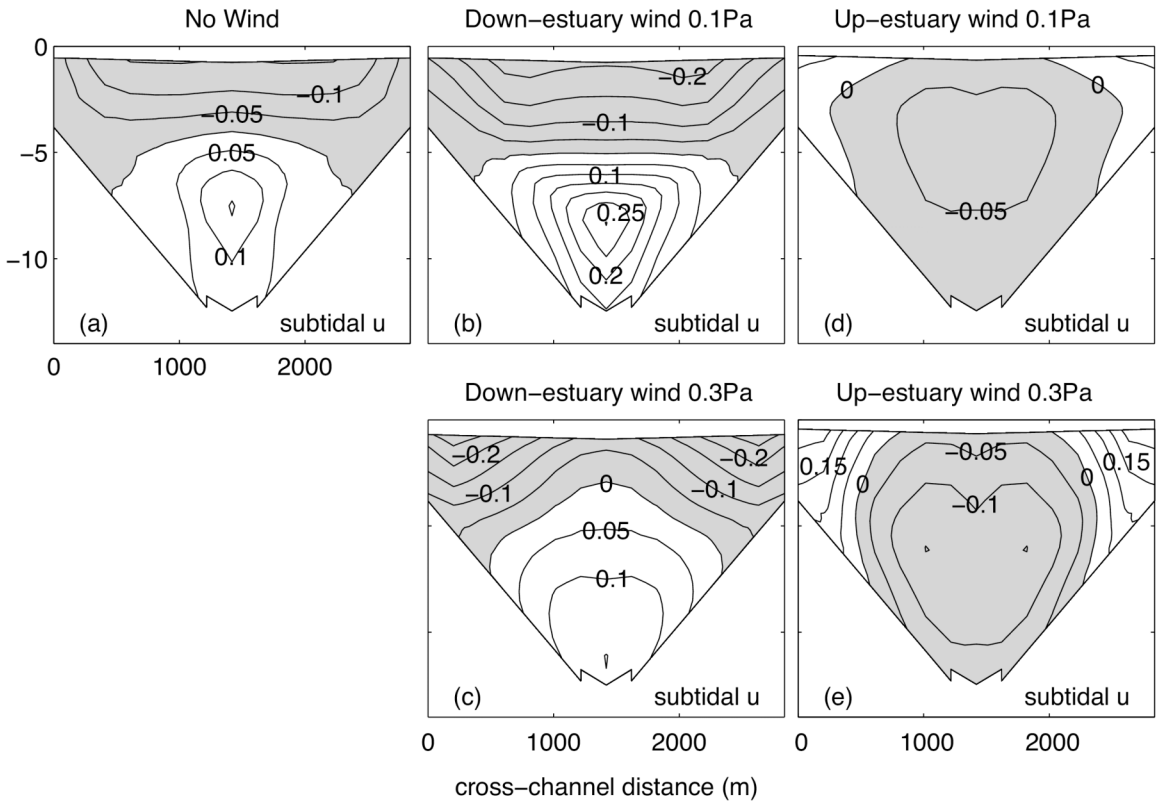

Fig. 5. Cross-sectional structures of subtidal axial velocity at the channel midpoint at day 130. The five panels represent no-wind (a), moderate down-estuary wind (b), strong down-estuary wind (c), moderate up-estuary wind (d), and strong up-estuary wind (e) cases. The gray shading indicates down-estuary (negative).

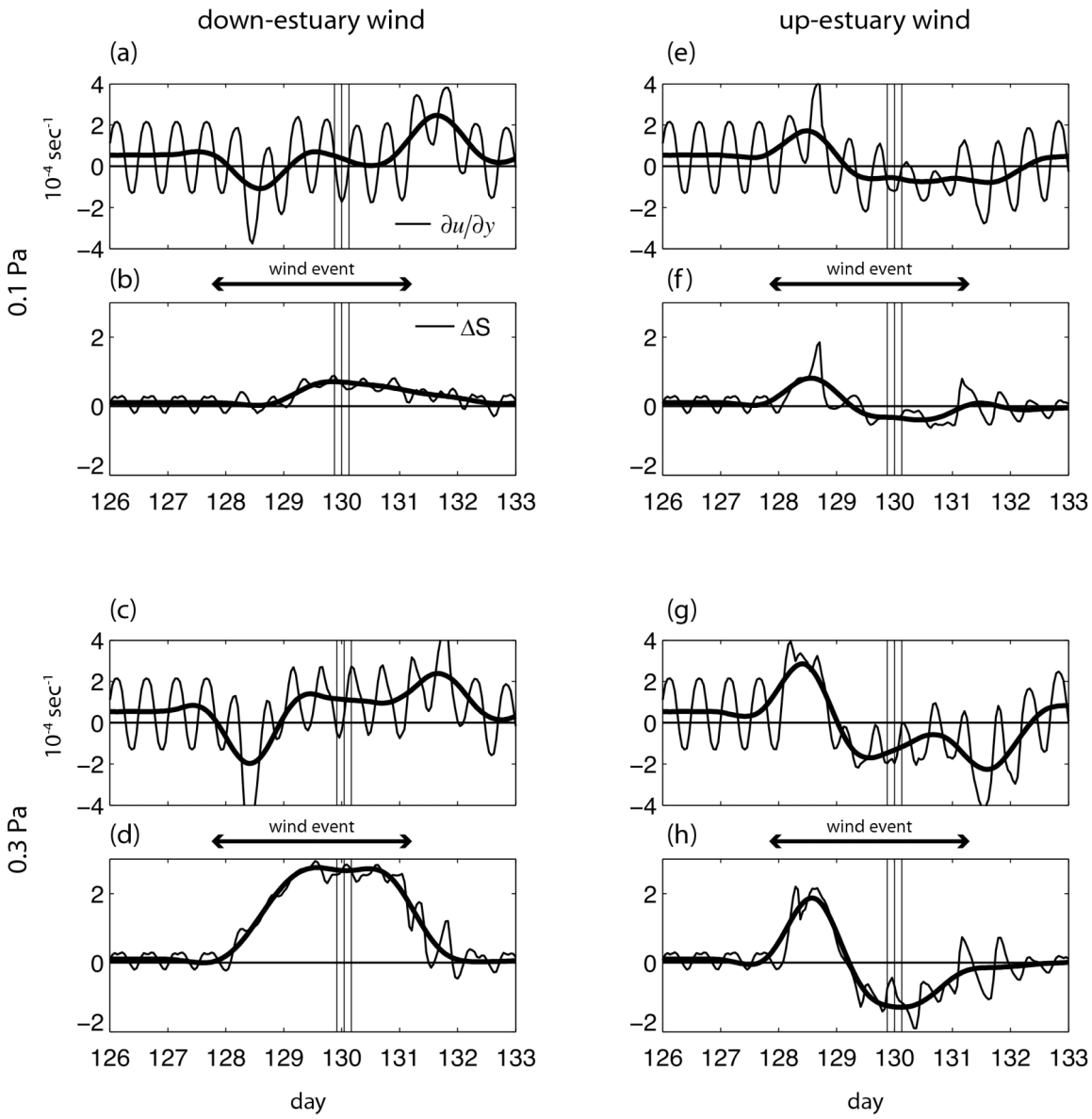

Fig. 6. Time series comparisons between lateral shear in axial velocity ($\partial u/\partial y$; a,c,e,g) and channel-shoal salinity difference (ΔS; b,d,f,h). The left and right columns are for down-estuary and up-estuary wind, respectively. The top two rows are with moderate wind, whereas the bottom two are with strong wind. There are three vertical lines in each panel. They correspond to maximum ebb, slack, and maximum flood when the cross-sectional profiles in Fig. 3 and 4 are taken. The thick line in each panel represents the subtidal signal (33hr low-pass filtered).

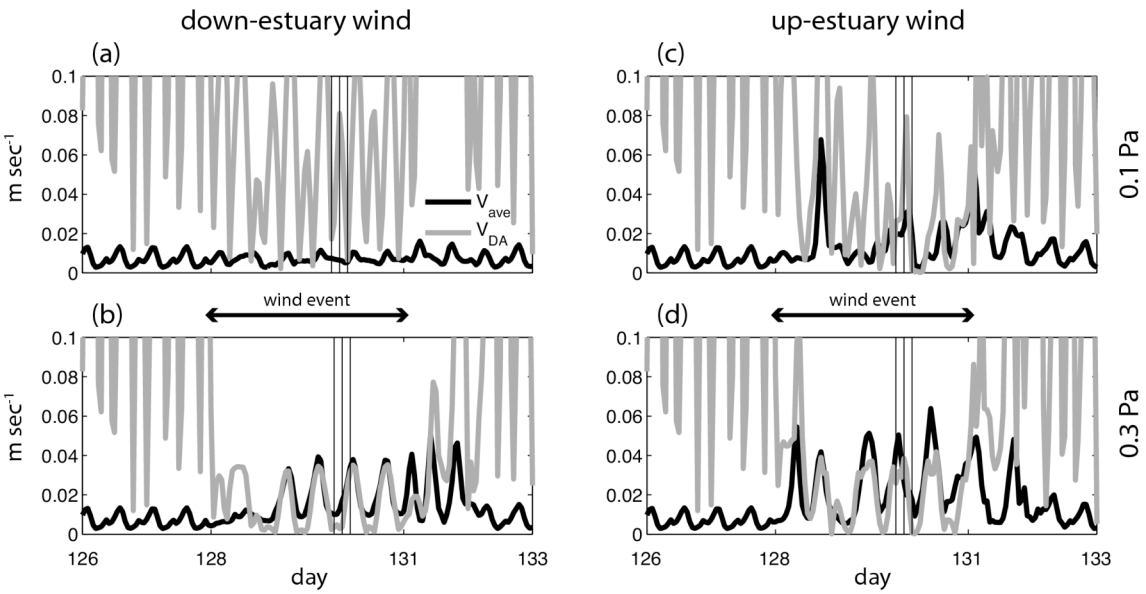

Fig. 7. Time series comparisons between lateral flow magnitude ($\bar{v}$ in Eq. 6; black lines) and the Hansen-Rattray-Like scaling (v_{DA} in Eq. 5; gray lines). (a) to (d) correspond to moderate down-estuary wind, strong down-estuary wind, moderate up-estuary wind, and strong down-estuary wind, respectively.

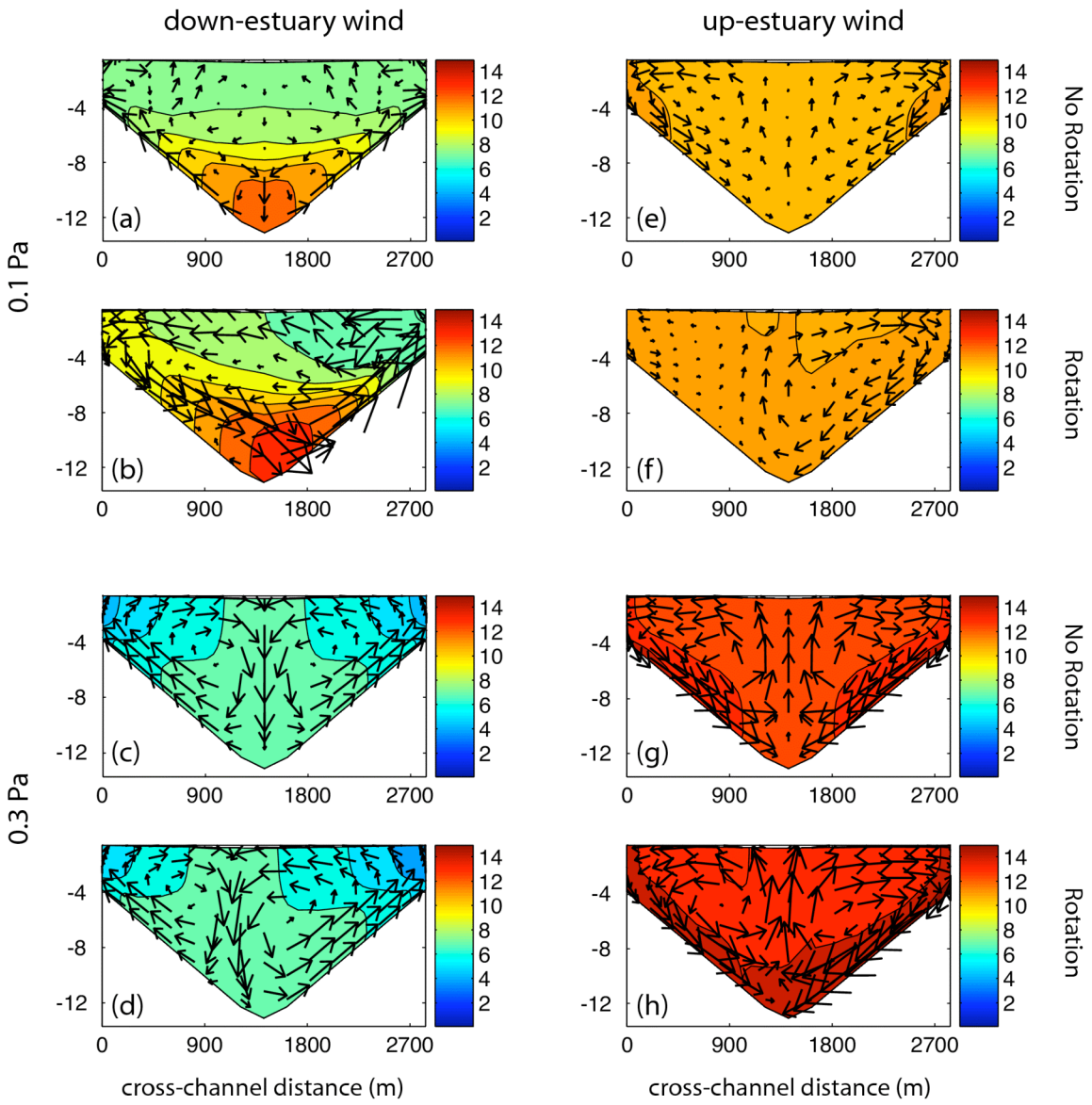

Fig. 8. Comparisons of the cross-sectional structures of salinity (color contour) and lateral circulation (vectors) between the cases without rotation (a,c,e,g) and with rotation (b,d,f,h) at maximum ebb. The left column is for down-estuary, and the profiles are taken at maximum flood. The right column is for up-estuary wind, and the profiles are taken at maximum ebb. The top two rows are with moderate wind forcing, whereas the bottom two are with strong wind forcing. Noted that the vector scale for moderate down-estuary wind case is 4-times larger than the rest of the cases.

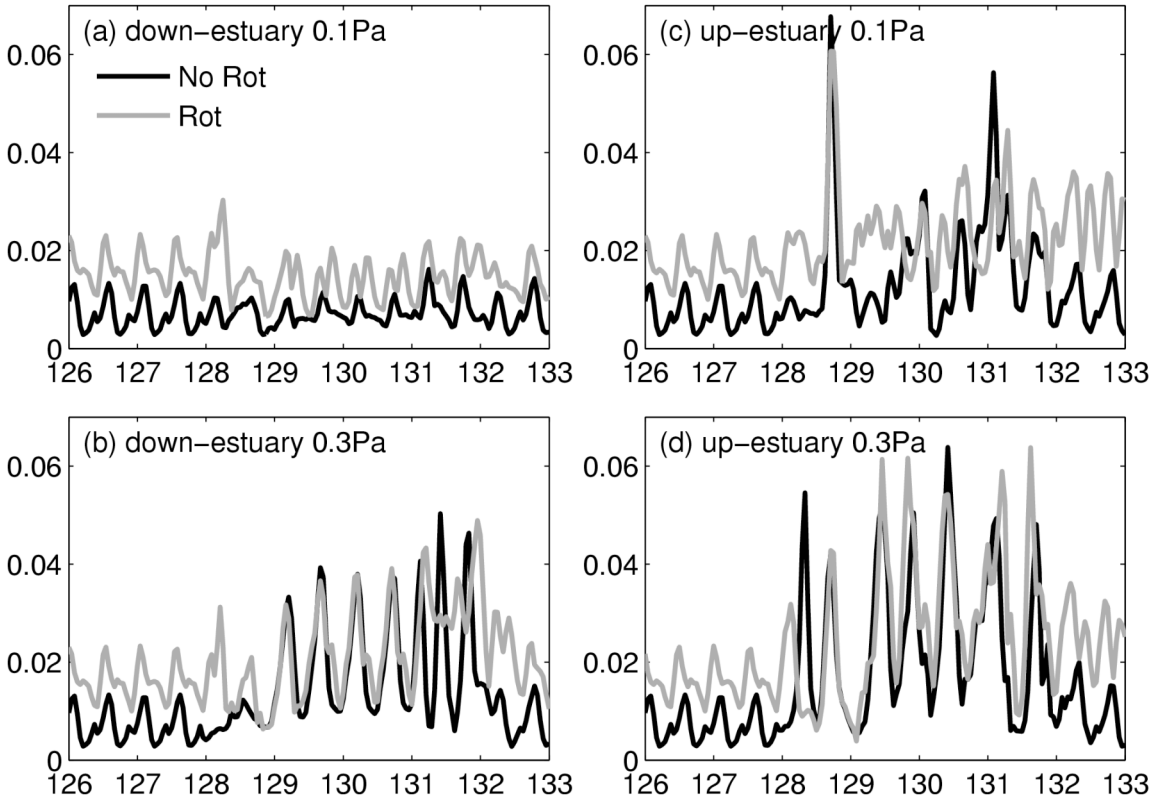

Fig. 9. Time series comparisons between lateral flow magnitude ($\bar{v}$ in Eq. 6) without rotation (black lines) and with rotation (gray lines). (a) to (d) correspond to moderate down-estuary wind, strong down-estuary wind, moderate up-estuary wind, and strong down-estuary wind, respectively.

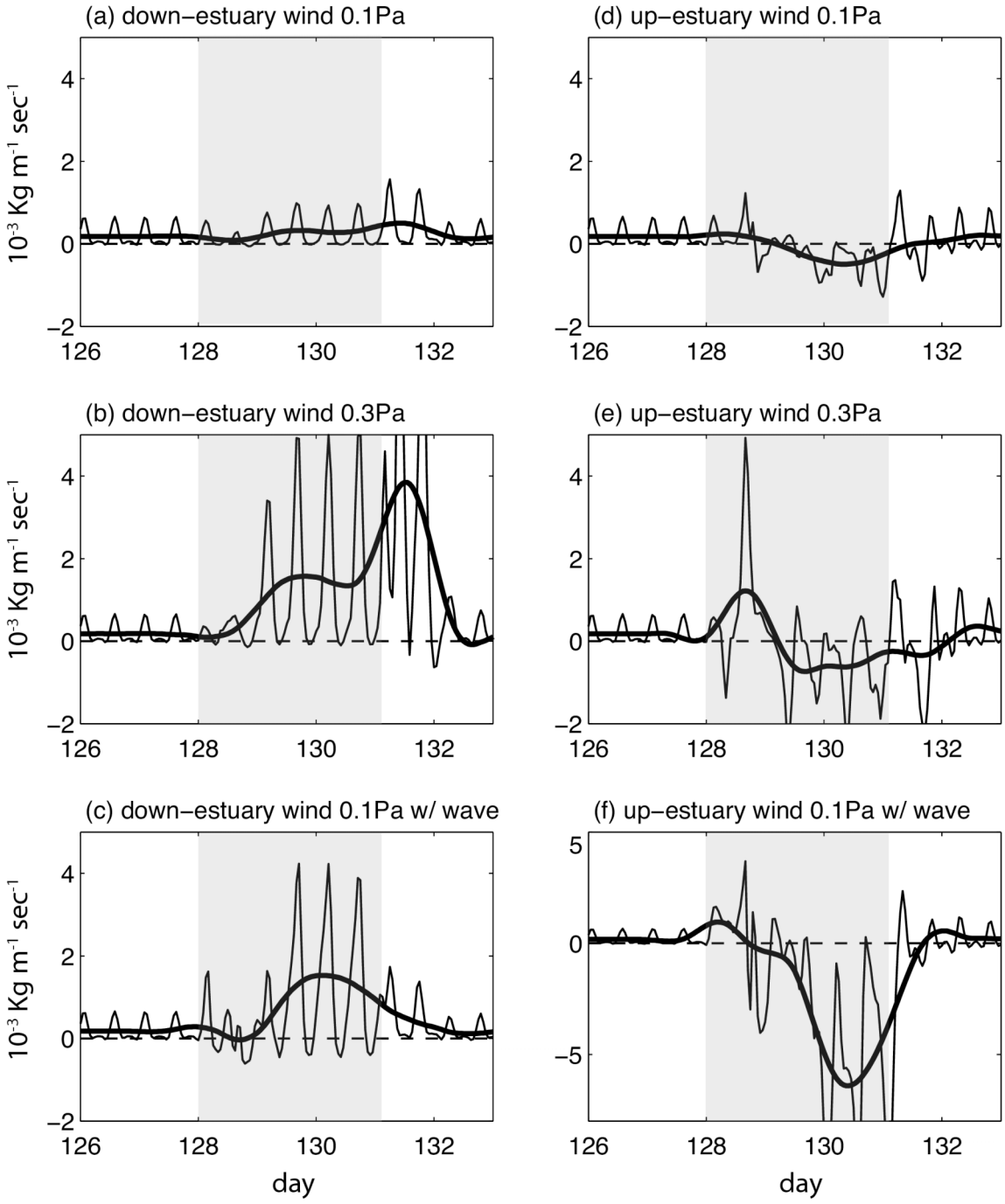

Fig. 10. Time series of the net lateral sediment transport rate (L in Eq. 7; thick lines). The left and right columns are for down-estuary and up-estuary wind. The rows from top to bottom are moderate wind (a,d), strong wind (b,e), and moderate wind with wind-wave forcing (c,f), respectively. The thin line in each panel is the depth-integrated, cross-sectionally averaged lateral sediment flux. Note that the scale of y-axis in (f) is different. The gray shading represents the event period.

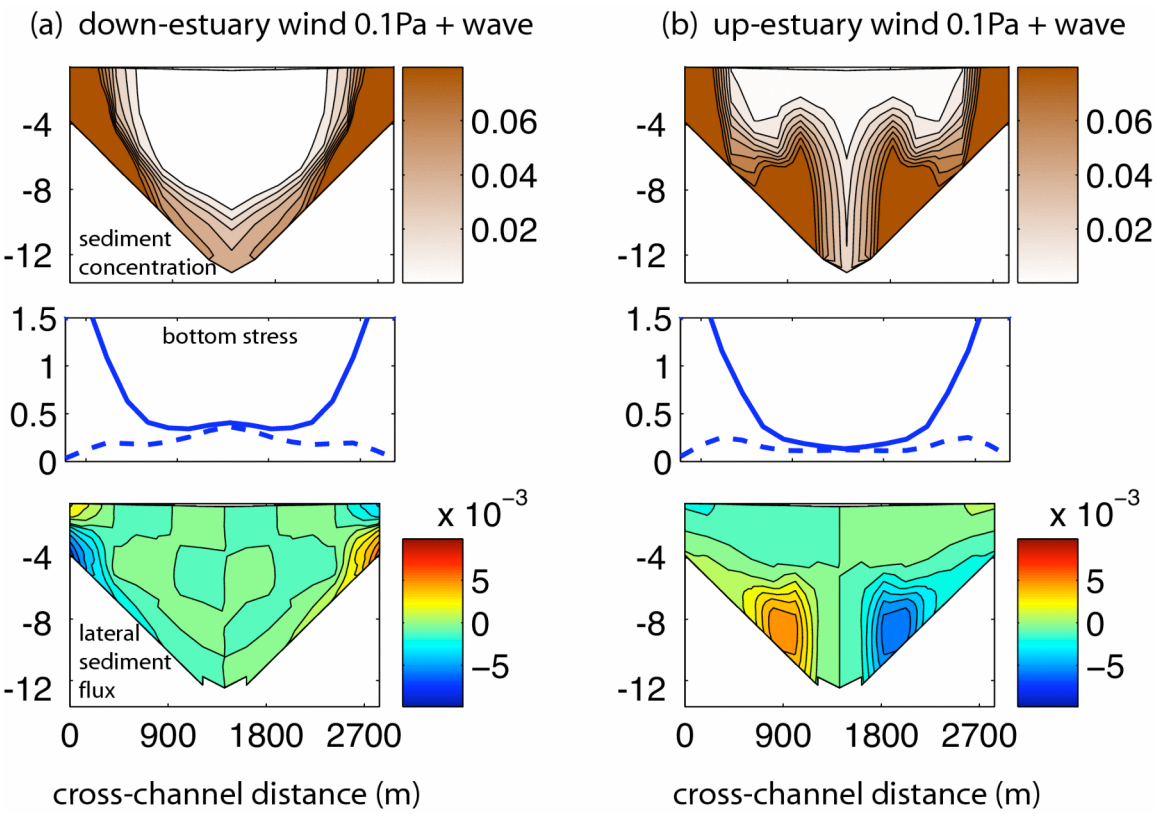

Fig. 11. Cross-sectional structures of suspended sediment concentration (top), bottom stress (middle), and lateral sediment flux (bottom) for moderate down-estuary wind (a) and moderate up-estuary wind (b) in the presence of wind-wave forcing (No. 15 and 16 in Table 1). Only the profile at maximum flood is shown because the profiles at other tidal phases are qualitatively the same (wave-dominated). The solid and dashed lines in the middle panels represent bottom stress distribution with and without wind-waves.

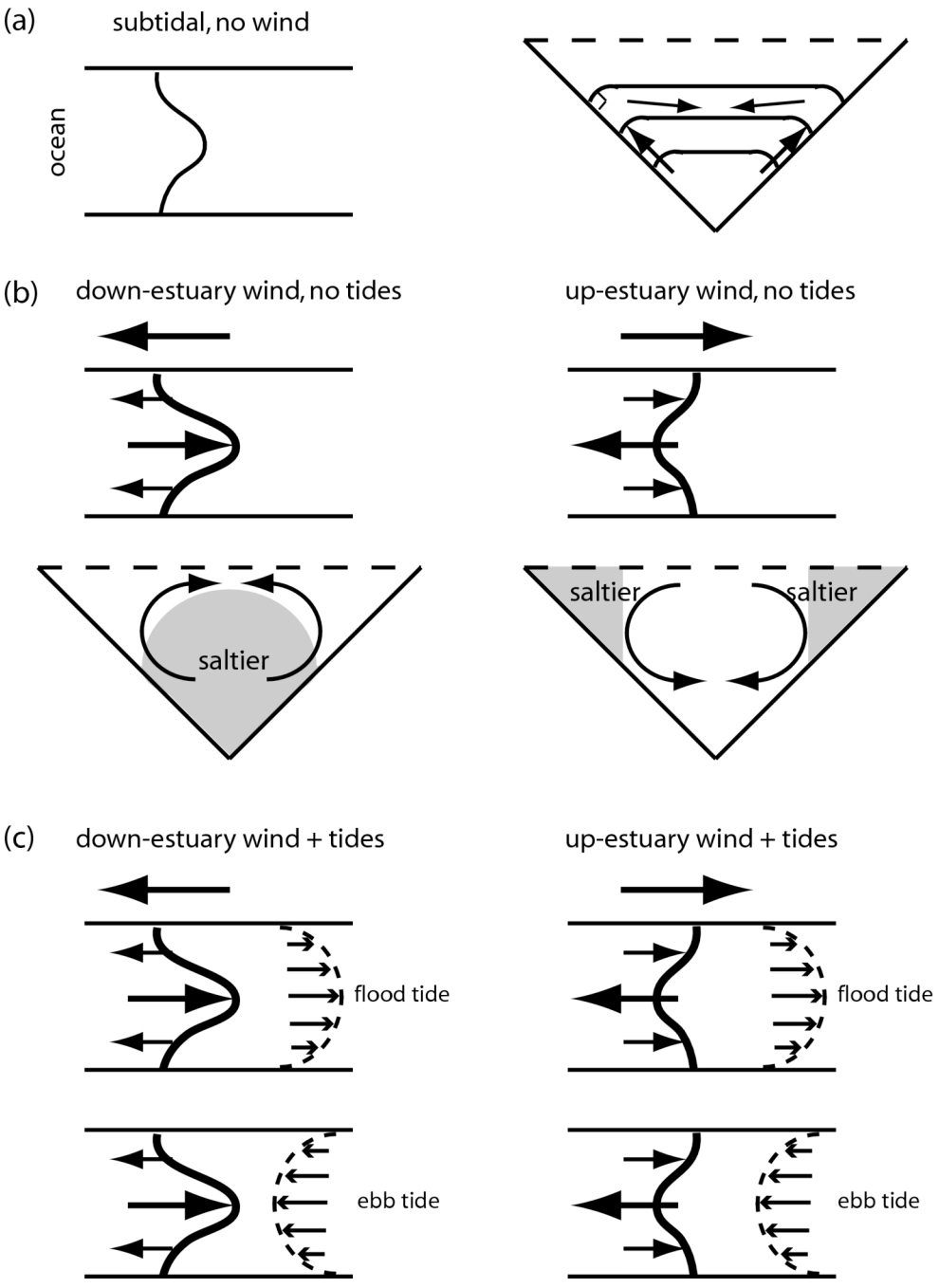

Fig. 12. Schematic diagram for the evolution of an isohaline (plan view of a straight channel) from without wind and tides (a), adding axial winds (b), to with wind and tides (c). The mechanism of wind-induced differential advection is illustrated in (b), and the interactions between wind-induced and tidally-induced lateral shear are shown in (c).

Chapter 5

A Nearshore Model to Investigate the Effects of Seagrass Bed Geometry on Wave Attenuation and Suspended Sediment Transport[1]

[1]Chen, S.N., Sanford, L.P., Koch, E.W., Shi, F., North, E.W., 2007. A nearshore model to investigate the effects of seagrass bed geometry on wave attenuation and suspended sediment transport. Estuaries and Coasts 30, 296-310.

Abstract

The effects of seagrass bed geometry on wave attenuation and suspended sediment transport were investigated using a modified Nearshore Community Model (NearCoM). The model was enhanced to account for cohesive sediment erosion and deposition, sediment transport, combined wave and current shear stresses, and seagrass effects on drag. Expressions for seagrass drag as a function of seagrass shoot density and canopy height were derived from published flume studies of model vegetation. The predicted reduction of volume flux for steady flow through a bed agreed reasonably well with a separate flume study. Predicted wave attenuation qualitatively captured seasonal patterns observed in the field: wave attenuation peaked during the flowering season and decreased as shoot density and canopy height decreased. Model scenarios with idealized bathymetries demonstrated that, when wave orbital velocities and the seagrass canopy interact, increasing seagrass bed width in the direction of wave propagation results in higher wave attenuation, and increasing incoming wave height results in higher relative wave attenuation. The model also predicted lower skin friction, reduced erosion rates, and higher bottom sediment accumulation within and behind the bed. Reduced erosion rates within seagrass beds have been reported, but reductions in stress behind the bed require further studies for verification. Model results suggest that the mechanism of sediment trapping by seagrass beds is more complex than reduced erosion rates alone; it also requires suspended sediment sources outside of the bed and horizontal transport into the bed.

1. Introduction

Deciphering the effects of seagrasses on water and sediments has been an active and challenging research area. Previous work has focused on the role of seagrass in reducing flow speed (Fonseca et al. 1982; Fonseca and Fisher 1986; Gambi et al. 1990; Koch 1993; Rybicki et al. 1997), modifying flow and turbulence structure (Ackerman and Okubo 1993; Nepf 1999; Ghisalberti and Nepf 2002; Abdelrhman 2003; Ghisalberti and Nepf 2004), altering sediment geochemical characteristics (Scoffin 1970; Wanless 1981; Wigand et al. 1997), attenuating wave energy (Fonseca and Cahalan 1992; Koch 1996; Kobayashi et al. 1993; Mendez et al. 1999), and affecting sediment dynamics (Ward et al. 1984; Almasi et al. 1987; Lopez and Garcia 1998; Gacia et al. 1999; Gacia and Duarte 2001). Recently, integration of the above perspectives has received increasing attention (Koch et al. 2006). Numerical models may help address the complex nature of this problem.

Teeter et al. (2001) review the physical, biological, and sedimentological complexities involved in constructing a complete wave-flow-seagrass-sediment model and present relevant equations as a point of departure. Teeter et al. state that the primary limitations on developing such a model are computational power and information on frictional damping of flow by seagrass blades and bottom sheltering effects on sediment resuspension by seagrass beds. Wave and flow damping by aquatic vegetation has been the focus of several recent modeling studies. These studies have focused on development of expressions and parameterizations for 1-dimensional or 2-dimensional frictional drag, in terms of a vegetation Reynolds number or canopy height and vegetation density. The drag force of the vegetation on

waves or steady currents is usually expressed as

$$F = \frac{1}{2}\rho \overline{f} a u_b^2 \quad \text{or} \quad F = \rho C_d a U^2 \tag{1}$$

where F is force per volume, ρ is density, a is projected area perpendicular to the flow direction per unit water volume, $\overline{f}$ and C_d are the bulk drag coefficients for waves and steady currents, respectively, u_b is the amplitude of the wave induced velocity just above the bottom, and U is the steady current speed at some reference height (depth-averaged velocity here). For purposes of comparison, the different approaches in the literature to estimating the bulk drag of seagrass may be categorized as Kobayashi-type models (Kobayashi 1993; Mendez et al. 1999; Mendez and Losada 2004) and Nepf-type models (Nepf 1999; Ghisalberti and Nepf 2004).

Kobayashi et al. (1993) presented an analytical solution of wave height decay through vegetation based on linear wave theory, a Reynolds number dependent drag parameterization, and constant depth. The projected area per unit volume $a = N \cdot b_v$, where N = the number of shoots per unit bottom area and b_v is defined as the plant area per unit height. Kobayashi et al. compared their model to flume studies on artificial kelp stands whit N = 1100 and 1490 m^{-2}, and b_v = 5.2 10^{-2} m, yielding a = 57.2 and 77.5 m^{-1}, respectively. The flume studies consisted of 60 runs with varying water depths (0.45-0.52 m), wave periods (0.714-2.0 s), and wave heights (0.036-0.1934 m). They used the bulk drag coefficient ($\overline{f}$) to calibrate the model for 60 runs and then correlated $\overline{f}$ with Reynolds number ($R = Ud/\nu$, where ν is the kinematic viscosity of the water). They found that $\overline{f}$ decreases with increasing Reynolds number, and the relationship can be approximated by

$$\overline{f} = 0.08 + \left(\frac{2200}{R}\right)^{2.4} \quad (2)$$

Mendez et al. (1999) and Mendez and Losada (2004) expanded Kobayashi's solution by including swaying motion of the seagrass, wave breaking, and variable depth, and parameterized their model based on careful flume experiments. They allowed for swaying motion of the seagrass by changing the characteristic velocity in Eqn. (1) to the relative velocity between plant and water. They reported another empirical relationship between bulk drag and Reynolds number:

$$\overline{f} = 0.4 + \left(\frac{4600}{R}\right)^{2.9} \quad (3)$$

Given the same Reynolds number, the bulk drag coefficient in Mendez et al. (1999) is higher than that in Kobayashi et al. (1993) because a lower velocity relative to the plant, when accounting for plant motion, requires a higher drag coefficient to maintain the same amount of wave energy attenuation. Their model fit to the data has a better correlation coefficient than Kobayashi et al.'s model. This suggests that the swaying motion of plants might need to be considered for optimal drag estimation.

Nepf (1999) used a different approach to explore the drag of vegetation on steady currents. She ignored the flexibility of the vegetation, mimicking the seagrass shoots using arrays of cylinders (width d = 6.4 mm). The projected area $a = nd$, where n is the number of shoots per unit bottom area and d is a typical shoot diameter; this definition of a is equivalent to the Kobayashi-type models. Based on observations for pairs of cylinders by Bokaian and Geoola (1984), she assumed that the bulk drag coefficient is a function of vegetation density as represented by the fractional volume occupied (ad). Numerical simulations were then performed for both random and

staggered arrays of cylinders with different element spacings (i.e., different values of *ad*). She showed that the bulk drag coefficient is relatively constant for *ad* up to 0.01 and declines steadily beyond this density (Fig. 6 in Nepf, 1999). In the density-independent range ($0.001<ad<0.01$), the spacing between cylinders is too large for the wake behind an upstream cylinder to influence the drag of a downstream cylinder. In the steady-decline range ($0.01<ad<0.1$) the drag coefficient decreases due to turbulent wake interference that delays the point of separation on a downstream cylinder and subsequently leads to a lower drag (Kundu and Cohen, 2002). In this model $\overline{f}$ was argued to be a weak function of Reynolds number.

Ghisalberti and Nepf (2004) considered the effects of canopy submergence on flow, turbulence, and drag. They found a significant reduction in drag relative to the Nepf (1999) expression when the top of the canopy was submerged, attributed to vortex shedding by the free end of the submerged grass blades. The bulk drag coefficient was approximately 64% of its value for emergent plants, depending weakly on the depth of the shear layer inside the canopy. However, they did not explore the effects of changing the degree of submergence. All of their experiments were carried out with canopy heights set at 30% of the water depth.

There are two main differences between these two types of models. First, Kobayashi-type models are for oscillatory flow (waves) while Nepf-type models are for steady currents. Therefore, the Reynolds numbers are different as the characteristic velocities are wave orbital velocity and uniform current speed, respectively. Second, in Kobayashi-type models the bulk drag is a function of Reynolds number that reflects the nature of the flow around a single shoot of

vegetation. In contrast, the bulk drag in Nepf's model is a function of density that reflects the properties of the whole bed.

All of these studies were vertically two-dimensional, measuring or modeling a vertical slice through a grass bed in the direction of wave propagation or flow, with flow prevented from diverging around the bed. Thus, while they were all instructive and valuable, they did not consider spatially varying seagrass bed geometry (e.g., less than complete seagrass coverage), spatially varying shorelines and bathymetries, or combinations of waves and currents. In addition, although there have been several observational studies that indicate reduced sediment resuspension in seagrass beds due to lower shear stresses and enhanced sediment deposition (Lopez and Garcia 1998; Gacia and Duarte 2001), there have been almost no modeling studies of sediment transport in seagrass beds.

The model described by Teeter et al. (2001), as implemented at least partially in Teeter (2001), is an exception. It is quite comprehensive, including wind forcing, wave forcing, seagrass-enhanced drag, and sediment transport, but it depends extensively on empirical parameterizations based on local observations. For example, Teeter (2001) implemented this model for Laguna Madre, TX, representing vegetation drag by a fixed roughness (Nikuradse sand grain roughness $k_n \sim 0.2$ m) which was tuned to give reasonable agreement with field observations, but is not applicable to seagrass beds in other locations with other combinations of waves and currents.

We have developed a new, more flexible, approach for modeling interactions between waves, currents, and sediment transport in seagrass systems. The new model

reduces the empiricism of the Teeter et al. approach by estimating wave and current drag that depends on seagrass density and height, based on Nepf (1999). It also considers 3-dimensional spatial variability in bed geometry and bathymetry, allows for both wave and current influences, considers the nearshore currents generated by wave breaking, calculates total bottom shear stress based on vector addition of wave and current stresses, and estimates fine sediment resuspension, deposition, and transport in and near seagrass beds. In the remainder of this paper, we describe the model development with an emphasis on drag estimation, validate it against flume studies of flow reduction by Gambi et al. (1990) and against field observations of wave damping, and present several model scenarios exploring the effects of seagrass bed geometries on wave attenuation, tidal current modification, and sediment trapping.

2. Methods

2.1. Numerical modeling of waves and currents

We adapted the Nearshore Community Model (NearCoM) system and integrated a curvilinear nearshore circulation model SHORECIRC (Shi et al., 2003; Shi et al. 2006) and a wave driver REF/DIF-1 (Kirby et al., 2005) into the system. NearCoM aims to predict waves, circulations, and sediment transport in the nearshore ocean. SHORECIRC numerically solves the depth-integrated 2D horizontal equations and incorporates a semi-analytical solution for the vertical current profile (Svendsen et al. 2000). REF/DIF-1 accounts for shoaling, refraction, energy dissipation, and diffraction as waves propagate over variable bathymetry and determines short-wave

forcing to drive currents in SHORECIRC. Our enhancements to the system include estimating seagrass effects on drag and turbulence, calculating the vector sum of wave and current bottom stresses, and adding a fine sediment transport module.

2.2. Seagrass effects on drag

For the model presented here, we adopted and modified the vegetation form drag expression of Nepf (1999), which was developed based on laboratory experiments with steady flows through rigid seagrass mimics. The primary reason for using this expression is that it explicitly accounts for the effects of seagrass shoot density over a realistic range of densities. The dominant seagrass species in the field studies to which we compare our model predictions was *Ruppia maritima* (leaf width ~ 1.5 mm), with a fractional volume (*ad*) that fluctuated seasonally between about 0.0014 and 0.003. This range of *ad* is within the density-independent regime of Nepf (1999), but it is three orders of magnitude smaller than the values reported in Kobayashi et al. (1993) and Mendez et al. (1999) for their laboratory studies of seagrass wave drag. We apply the Nepf (1999) approach because we prefer to use steady flow drag data in comparable seagrass densities rather than wave drag data from a much higher seagrass density, and because we use the same basic drag formulation for both steady flow and wave forcing in our model.

Bottom shear stress (τ_{cs}) for steady currents is written using a standard quadratic law:

$$\tau_{cs} = \rho C_d U^2 \qquad (4)$$

where ρ is flow density, U is depth-averaged flow velocity, and C_d is the drag coefficient. Assuming that seagrass blades may be modeled as rigid cylinders, Nepf (1999) partitioned total drag into skin friction due to the bottom stress at the sediment-water interface and form drag by the seagrass blades. She expressed the drag coefficient as

$$C_d = (1 - ad)C_B + \frac{1}{2}\overline{C_D}ad(\frac{h}{d}) \tag{5}$$

where a is the projected plant area per unit volume, d is shoot diameter, h is water depth, ad represents the fractional volume occupied by seagrasses, C_B is a skin friction drag coefficient (set equal to 0.001 here), and $\overline{C_D}$ is the bulk drag coefficient for seagrass, which Nepf (1999) determined from experiments. The first term on the right-hand side of Eqn. (5) represents skin friction, whereas the second term represents form drag. We modified her calculation of a to allow seagrasses to only occupy part of the water column, so $a = nld/h$, where n is the number of seagrass shoots per unit area and l is the canopy height. Rearranging Eqn. (5), the drag coefficient for current becomes

$$C_d = (1 - \frac{nld^2}{h})C_B + \frac{1}{2}\overline{C_D}(nhd)(\frac{l}{h}) \tag{6}$$

Thus, C_d is a function of canopy height, shoot density, shoot diameter, and water depth. In Nepf (1999)'s model, $\overline{C_D}$ is a function of fractional volume (ad). We approximate the curve in Fig. 6 of Nepf (1999) as

$$\overline{C_D} \approx \begin{cases} 1.17, & 10^{-3} < ad < 10^{-2} \\ -0.255\ln(ad), & 10^{-2} < ad < 10^{-1} \end{cases} \tag{7}$$

Nepf (1999)'s model is for an emergent canopy. We account for submergence by scaling the form drag by the ratio of the canopy height to the water depth. A further reduction in drag may be needed to account for free-end effects at the top of submerged canopies (Ghisalberti and Nepf 2004). However, we have not made any additional modification to the Nepf (1999) expression because the experiments of Ghisalberti and Nepf were limited to deeply submerged canopies. It is reasonable to expect that the drag reduction they observed would be less for a less submerged canopy, but there is no data on the effects of different depths of submersion. Thus, Eqn. (6) is adopted as a reasonable starting approximation, pending additional data.

In Nepf's experiments the velocity was measured at 7.5 cm above the bottom, whereas the reference height in SHORECIRC is set at 1 m, requiring conversion of her drag coefficient to one that is relevant for SHORECIRC. SHORECIRC treats all drag as if it were generated by bottom boundary layer turbulence (Eqn. 4). Although Nepf's expression (Eqns. 5 and 6) only assumes that a small part of the drag is generated by bottom boundary layer turbulence, the form of her total drag coefficient is operationally the same as for bottom boundary layer drag. Thus, we make the required conversion by assuming a logarithmic turbulent bottom boundary layer velocity profile and solving for a bottom roughness coefficient z_0 consistent with C_d from Eqn. (6) at a reference height of z = 7.5 cm. Using this value of z_0 and a new reference height z = 1 m, we calculate the tidal current drag coefficient for SHORECIRC as

$$C_d = \left[\frac{k}{\ln(\frac{z}{z_0})}\right]^2 \qquad (8)$$

where $k = 0.4$ is the von Karman constant. This does not mean that the velocity profile within an actual grass bed is logarithmic. In fact, a recently study by Ghisalberti and Nepf (2002) shows that that the flow structure within and just above an unconfined canopy resembles a mixing layer rather a boundary layer. However, resolving the vertical structure of the flow in the grass bed is beyond the scope of our study; we only want to parameterize the drag of the bed on the flow, for which purpose our approach is a reasonable approximation.

We used field observations to determine the seagrass bulk drag for waves in REF/DIF-1. Bottom shear stress due to pure wave action (τ_w) is expressed in terms of the wave friction factor (f):

$$\tau_w = \frac{1}{2}\rho f u_b^2 \tag{9}$$

where

$$f = (1 - ad) f_B + \frac{1}{2}\overline{f} ad \left(\frac{h}{d}\right) \tag{10}$$

where u_b is wave orbital velocity near bottom, f_B is the wave skin friction factor, and $\overline{f}$ is a bulk drag representing the effects of seagrasses on waves. f_B was calculated using a bottom roughness equivalent to the value of $C_B = 0.001$ used in SHORECIRC, following procedures in U.S. Army Corps of Engineers (2002), while $\overline{f}$ was determined using field observations and assuming the functional form of Eqn. (7) with an adjustable multiplicative coefficient (see below). As in Eqn. (6), f depends on the ratio of canopy height to water depth (l/h) through the fractional volume ($ad = nd^2 l/h$).

2.3. Combining wave and current bottom stresses

Once the drag coefficient and wave friction factors are estimated through Eqn. (6) and (10), current and wave fields are calculated by SHORECIRC and REF/DIF-1. With this updated current and wave field (wave height and period) and with known bottom sediment grain size, skin friction shear stress due to pure current (τ_{cs}) and wave motions (τ_{ws}) are obtained using the techniques in U.S. Army Corps of Engineers (2002). Then we apply vector summation of the two skin friction components to calculate maximum skin friction shear stress (τ_{ms}):

$$\tau_{ms} = \sqrt{(\tau_{ws} + \tau_{cs}\left|\cos\phi_{wc}\right|)^2 + (\tau_{cs}\sin\phi_{wc})^2} \qquad (11)$$

where ϕ_{wc} is the angle between current and wave propagation and can be calculated from SHORECIRC and REF/DIF-1. Because we are interested in the maximum potential for sediment movement, the absolute value of $\cos\phi_{wc}$ is used in Eqn. (11) to guarantee maximum vector summation regardless of the direction of wave orbital motion. This vector summation ignores enhanced turbulence due to nonlinear wave-current interactions in the bottom boundary layer (Grant and Madsen 1979). However, given the high uncertainty of seagrass drag estimation and turbulence structure in seagrass beds, Eqn. (11) is a reasonable first order approximation for combined wave-current bottom stress.

2.4. Sediment transport modeling

We developed and incorporated a suspended sediment transport module based on North et al. (2004). The module accounts for erosion and deposition with a simple parameterization of consolidation for single-grain-size cohesive sediments. We solve

for changes in bottom sediment per unit area (B in kg m^{-2}) over time t at each grid point using

$$\frac{dB}{dt} = D - E - \gamma B \qquad (12)$$

where D and E are the deposition and erosion rate (kg $m^{-2}s^{-1}$), respectively, and γ is a first order consolidation rate (s^{-1}; set equal to zero here). The formulation states that the amount of erodible sediment per unit area increases by deposition but decreases by erosion and consolidation. The deposition rate is calculated as

$$D = W_s C \qquad (13)$$

where the settling velocity (W_s) is equal to 0.03 cm s^{-1} (a typical value for fine suspended sediment in Chesapeake Bay; Sanford et al. 2001) and C is depth-averaged suspended sediment concentration (kgm^{-3}). The erosion rate may be expressed as

$$E = M(\frac{\tau_{ms}}{\tau_c} - 1)\tilde{H}(\tau_{ms} - \tau_c)\tilde{H}(B + 2\frac{dB}{dt}) \qquad (14)$$

where τ_c is critical shear stress for erosion (e.g. 0.15 Pa for fine sand), M is an empirical constant ($5x10^{-5}$ kg $m^{-2}s^{-1}$ here), and $\tilde{H}$ is the Heaviside step function ($\tilde{H}$=1 when its argument is > 0 and $\tilde{H}$=0 when its argument is ≤ 0). The first step function in Eqn. (14) represents the initiation of sediment motion when the maximum bottom shear stress exceeds the critical value, while the second step function prevents over-erosion and negative values of B.

Given the erosion and deposition rates in each model cell, a third-order accurate numerical scheme QUICKEST (Leonard 1979) is used to solve the depth-averaged transport equation for suspended sediments (Clarke and Elliot 1998):

$$\frac{\partial (hC)}{\partial t} + \frac{\partial (hUC)}{\partial x} + \frac{\partial (hVC)}{\partial y} = \frac{\partial}{\partial x}(hK_x \frac{\partial C}{\partial x}) + \frac{\partial}{\partial y}(hK_y \frac{\partial C}{\partial y}) + E - D \quad (15)$$

where h is water depth, U and V are depth-averaged velocity components, and K_x and K_y are diffusion coefficients. The QUICKEST scheme reduces overshoot problems near strong gradients in concentration. This feature is particularly important because the presence of seagrass could lead to abrupt changes in bottom shear stress, which may in turn cause strong gradients in suspended sediment concentrations.

It should be noted that depth-averaged transport formulations used here effectively assume a vertically uniform sediment concentration profile. In reality, we expect sediment concentrations to be higher near bottom, which can be approximately compensated for by increasing the value of W_s in Eqn. (13). Different vertical profiles of turbulent mixing inside and outside the seagrass bed (Nepf and Vivoni 2000) would change the respective vertical profiles of suspended sediment concentration, slightly biasing the estimates of sediment deposition as a result. However, because we intend to explore only first-order effects of seagrass beds on currents, waves and sediments, depth-averaged transport formulations are adopted as a reasonable approximation.

2.5. Model validation

Two model configurations were used for model validation. In the first, we set up the model to test the effects of seagrass under current-only conditions (using SHORECIRC only). Because we are particularly interested in modeling the effects of seagrass beds that cover only part of the model domain, such that water may flow around the bed rather than

being forced through it or over it, we use the data of Gambi et al. (1990) for comparison. Gambi et al. studied flow speed reduction by *Zostera marina* L. (eelgrass, shoot diameter d=0.28 cm) in a seawater flume, with the seagrass bed occupying only 20% of the width of the flume. SHORECIRC was configured to mimic the relative dimensions of their flume experiments. The actual model domain was considerably larger because of computational constraints, but the ratios of the domain length, domain width, and the horizontal extent of the eelgrass bed were scaled exactly (1 m seagrass bed length in the flume is scaled to 3,200 m in the model). The canopy height was not scaled by the same factor; a canopy height of 0.75 m with 1 m water depth was used to mimic the flume bed and give a realistic drag coefficient. This does not affect the model-data comparison because we are interested only in the scaled horizontal structure of the flow field. Flow was driven using an upstream flux boundary condition, with no flow through the domain sidewalls, to generate the same free-stream velocities as Gambi et al. The eelgrass parameters they reported were used to calculate the drag coefficient for SHORECIRC based on Eqs. 6 and 7. We computed the volume flux reduction within the eelgrass bed from just upstream of the bed to the end of bed where flow reached a steady condition. The volume flux reduction is defined as

$$(1 - \int U dz / \int U_{control} dz) \times 100 \qquad (16)$$

where $U_{control}$ is the up-stream velocity. We choose combinations of two shoot densities (600 and 1200 shoots m^{-2}) and two free-stream velocities (10 and 20 cm s^{-1}). Comparisons are shown in Fig. 1. The model-predicted values for the four different combinations agree reasonably well with Gambi et al.'s results, without any

parameter tuning. As expected, the eelgrass bed with higher shoot density results in higher volume flux reductions. The model-predicted volume flux reduction increases rapidly behind the leading edge of the eelgrass bed and levels off approximately halfway into the bed.

In the second model validation exercise, the model was configured to test the effects of seagrass on wave attenuation (using RED/DIF-1 only). We used field observations to determine the magnitude of the wave form drag, because equivalent data to that of Nepf (1999) on the relationship between seagrass density and wave form drag ($\overline{f}$) is not available. The field observations were carried out in Duck Point Cove, near Bishop's Head Point, Maryland, in mesohaline Chesapeake Bay (Newell and Koch 2004). A time series of wave height and seagrass parameters were measured in different months at two adjacent sites parallel to the shoreline, one vegetated with *R. maritima* and the other unvegetated. The size of *R. maritima* bed was about 600 m in the alongshore direction and 200 m in the crossshore direction, and a pressure sensor was located at the center in average water depth of 1 m. Assuming the same incident wave climates at the two sites, we can plot wave height measurements at the unvegetated site against the vegetated site to evaluate wave attenuation by the *R. maritima* bed. Assuming that $\overline{f}$ is a function of fractional volume (ad) and has similar functional form to that for steady current (Eq. 7), we change the height of the $\overline{f}$ curve to obtain the observed wave attenuations in October. The calibrated $\overline{f}$ is written as

$$\overline{f} \approx \begin{cases} 0.253, & 10^{-3} < ad < 10^{-2} \\ -0.055\ln(ad), & 10^{-2} < ad < 10^{-1} \end{cases} \qquad (17)$$

We validated the October-derived calibration by applying observed seagrass parameters for May and June, then calculating the corresponding wave friction factors and comparing the model-predicted wave heights with observations. Table 1 summarizes the slopes and goodness of linear fits from the field observations and the calibrated model. A slope less than 1 indicates wave attenuation. Both the October calibration run and May validation run slopes agree well with the data, which show mild wave attenuation. Wave attenuation by the seagrass bed peaked in June when the seagrass canopy occupied the whole water column. The model qualitatively captures this trend (June attenuation > May and October) although the model tends to slightly underestimate wave attenuation in June.

This approach has the advantage that a wider range of vegetation density is covered with one empirical parameter ($\overline{f}$). This is particularly useful for simulating seasonally or geographically varying seagrass populations. The underestimation of wave attenuation in June may be due to a different response to oscillatory forcing, the flexibility of real seagrass blades (i.e., in June the reproductive stems may have different flexibility from the vegetative stems in other months), a Reynolds number dependence for which we have not accounted, or additional drag force due to sediment bed forms. The drag partitioning for current and waves here assumes a flat sediment bed due to a lack of field measurements on bed forms. Further study is needed to understand the influence of these effects, and a wide range of realistic vegetation densities, on the bulk drag of seagrass. For the present purpose, the qualitative reproduction of changing wave drag due to seasonal changes in seagrass morphology is considered sufficient.

2.6. Model setup and scenarios

The model domain is set at 720 m in the shore-normal direction and 5,400 m in the shore-parallel direction with a 10 x 30 m grid resolution. Two bathymetries are set up: a flat bottom with 1 m depth and a sloping bottom with 2.5 m depth offshore and 0.05 m depth at the shoreline. When present, tidal currents are assumed to be primarily in shore-parallel direction with a maximum magnitude of about 20 cm s21. Tidal currents are simulated by imposing flux boundary conditions through the upstream and downstream boundaries of the domain at semidiurnal frequency. A 4-s sinusoidal wave enters the domain from the offshore boundary with wave heights varying between 0.1 and 0.4 m, at an incident angle of either 0^o (scenarios 1-3) or 10^o (scenario 4) counterclockwise from the shore-normal direction. The domain of the sediment module is smaller than the entire SHORECIRC/ REFDIF-1 domain to avoid anomalous physical forcing near the boundaries, and a looping boundary condition is applied in the shore-parallel direction so that the sediment flux leaving one end of the domain equals the flux entering the other end of the domain. Bottom sediments are initialized with B = 3 kg m^{-2} uniformly distributed throughout the domain. This avoids depletion of the bottom sediment supply over the duration of a run and the corresponding additional complexity. In addition to the scenarios reported here, the sediment transport module was verified to conserve mass when suspended sediments and bottom sediments are totaled.

Model scenarios were designed to investigate the effects of seagrass bed geometry on wave transformations and sediment transport. Model scenarios include

three flat bottom cases with varying width, length, and position of the seagrass bed and one sloping bottom case with three different bed geometries (Table 2). The seagrass parameters observed in June for *R. maritima* are applied (density is 1,270 m^{-2}; canopy height is 1 m). The circulation, wave, and sediment modules are turned on in all scenarios, and we look at several output quantities.

The first two scenarios examine the effect of seagrass bed width and alongshore extents on reduction of the wave energy flux reaching the shoreline. Wave energy flux (F) is the rate at which wave energy is transported in the horizontal direction and can be expressed as

$$F = EC_g = (\frac{1}{8}\rho g H^2)C_g \qquad (18)$$

where E is the wave energy density, C_g is group velocity, ρ is water density, g is the gravitational constant, and H is wave height. In these two scenarios we change the geometry of the seagrass bed and calculate the ratio of F with and without seagrasses, averaged over the entire shoreline. The percentage of wave energy flux reduction is then $(1-F_{with}/F_{without})$ x 100.

The third scenario examines the effect of seagrass bed location (distance offshore) on reduction of bottom stress over the total domain. Because we are interested in the influences of the seagrass bed on the total force acting on the bottom sediments in the domain, we define the total bottom stress as the skin friction shear stress integrated over the whole domain. The ratio of total bottom stress with and without the seagrass bed is used to calculate the percentage reduction. In the third scenario, the percent bottom stress reduction is compared as the mid point of the bed is moved from an inshore position toward the offshore boundary, with bed width and

length fixed.

The last scenario (with a sloping bottom) is more realistic than the constant depth scenarios. It examines the overall influence of seagrass presence and extent on tidal currents, waves, and sediment transport in more detail. We examine changes in wave height, skin friction shear stress, suspended sediment, and bottom sediment over both space and time through two tidal cycles. Cases considered are no seagrass, a seagrass bed of limited extent, and a seagrass bed covering the full domain.

3. Results

Larger seagrass bed width in the direction of wave propagation results in higher wave attenuation, and relative wave attenuation increases as incoming wave height increases. Figure 2 shows changes in wave energy flux reduction when the crossshore bed width is varied but the bed occupies the entire domain in the alongshore direction (scenario 1). The results are presented with respect to only the crossshore direction, since there is no alongshore variation. Wave energy flux reduction increases with crossshore width but levels off as maximum width is approached. The increase in energy flux reduction is obviously due to the increase in seagrass wave drag as the bed becomes wider. The energy flux reduction levels off at large bed width simply because not much wave energy is left to dissipate, so the rate of change decreases.

Percent energy flux reduction also increases with increasing wave height. This is because a larger wave height exerts a higher stress on the bottom, proportional to the wave orbital velocity squared. The wave energy dissipation rate is proportional to

the product of stress and wave orbital velocity for rough turbulent flow (Dean and Dalrymple 1991), so wave energy dissipation is proportional to orbital velocity (wave height) cubed, while wave energy flux is only proportional to wave height squared. Wave energy dissipation is proportionately more effective for higher waves.

Increasing seagrass bed length alongshore (perpendicular to wave propagation) linearly reduces the wave energy flux at the shoreline. Figure 2 shows changes in wave energy flux reduction on the shoreline for scenario 2, in which we change the alongshore length of the bed while keeping the crossshore width fixed. As expected, wave energy flux reduction is linearly proportional to the alongshore seagrass bed length. Again, percent energy flux reduction increases with incident wave height.

With fixed seagrass bed geometry and a flat bottom, moving the bed away from the shoreline reduces the total force exerted on the bottom. Figure 3 presents the skin friction distribution and the percent reduction in total force acting on bottom sediments as the position of the bed is moved from inshore towards the offshore boundary (scenario 3), with a fixed bed width of 100 m and length covering the whole domain in the alongshore direction. In the upper panel of Fig. 3, 0.2-m waves are applied in the shore-normal direction, and as the bed is moved toward the shoreline, the abrupt reduction in skin friction (indicating the area occupied by seagrass) is moved accordingly. It should be noted that the skin frictions at the shoreline for different bed locations are about the same. This may be due to very weak nonlinearities in wave energy dissipation in this flat bottom scenario and due to the absence of wave diffraction because the seagrass bed covers the entire alongshore

domain. In the lower panel of Fig. 3, the percent of total bottom stress reduction is calculated according to the previous section. The total bottom stress with a seagrass bed is the integral average of skin friction distribution over the crossshore distance, as shown in Fig. 3. It can be seen that total bottom stress reduction increases approximately linearly with the offshore distance of the bed. It makes sense that total force acting on bottom sediments is reduced by moving the bed offshore because the affected area between the bed and shoreline increases linearly with the distance of the bed offshore. The smaller waves that emerge from the seagrass bed act over this entire area. Again, larger waves result in proportionately higher bottom stress reduction.

Seagrass bed geometry also influences sediment dynamics, in ways that are more complex than the reduction in bottom stress alone. In the fourth scenario, the more realistic sloping bottom case, we compare model runs with no seagrass, a seagrass bed 200-m wide and 1,800-m long, and a seagrass bed that covers the entire width of the domain and is 1,800-m long. Figure 4 shows crossshore transects of wave height and skin friction shear stress across the center of the seagrass bed at slack tide. In the upper panel of Fig. 4, wave shoaling and then breaking as waves propagate shoreward can be seen without the seagrass bed. This wave height evolution corresponds to the increase and quick drop of skin friction shear stress shown in the lower panel of Fig. 4. In both cases with seagrass beds, wave height and skin friction shear stress within and behind the bed are greatly reduced. The breaking zone and the peak of skin friction shear stress for the case with a 200-m wide bed are moved shoreward. When the crossshore domain is fully occupied by the seagrass bed,

the breaking zone disappears. Differences between all three cases in deeper water near the offshore boundary are relatively small. The reason is that short period wave orbital velocity decays with depth, making bottom friction less effective to dissipate wave energy in deeper areas. Interactions between seagrass beds and waves in deeper water depend on wave period; longer period waves interact more effectively with seagrass beds in deeper water.

Reduced skin friction has important implications from the standpoint of sediment transport. To demonstrate this, we put a line in Fig. 4 to indicate the critical shear stress (about 0.15 Pa; U.S. Army Corps of Engineers 2002) for fine sands (0.2 mm). Sediments start to move when shear stress exceeds a critical value (Eq. 14). As shown in Fig. 4, the distances over which the critical stress is exceeded are about the same with or without the seagrass beds. The erosion rate is proportional to the distance between the lines of wave-induced skin friction and critical shear stress (Eq. 14), so erosion rate is greatly reduced within and behind the seagrass beds. This implies that, without advection of sediment from external sources, suspended sediment concentrations within and behind the beds may be lower than those with no seagrass bed. Although greatly simplified, these model results illustrate that seagrass bed geometries can have profound effects on waves and can subsequently influence sediment dynamics.

To further examine the effects of seagrass beds on sediment dynamics, we compare the time series of six variables associated with sediments between the 200-m wide bed case and the no seagrass case (Fig. 5) over 2 full tidal cycles. The variables are bottom sediments, suspended sediment concentration, skin friction shear stress,

current magnitude, erosion rate, and deposition rate. In Fig. 5, each panel contains three lines that represent the averaged values of each variable offshore of the bed, within the bed (or where the bed would be), and between the bed and the shoreline. As can be seen in Fig. 5, current magnitudes show semidiurnal tidal signals and, when the seagrass bed is not present, they decrease shoreward due to increased bottom friction. Current magnitudes at the onshore position during floods are slightly smaller than ebbs because flooding tides are against wave-induced alongshore currents (toward positive y direction). When a 200-m wide bed is added, current magnitude inside the bed is reduced and becomes smaller than either offshore or onshore. Tidal signals are very weak in the other variables, especially for shallower locations, indicating that the sediment dynamics in the system are dominated by waves. Most importantly, averaged suspended sediment concentration, skin friction shear stress, erosion rate, and deposition rate are lower and there is more bottom sediment at both the seagrass bed and onshore positions when the seagrass bed is present. This result confirms the anticipation of lower suspended sediment concentration from Fig. 4 and suggests that seagrass beds can protect bottom sediments from being eroded not only inside the bed itself but also the area behind it.

The spatial distributions of predicted suspended and bottom sediments indicate that the mechanism of sediment trapping by seagrass beds requires not only reduced erosion but also a suspended sediment source outside the bed and horizontal transport into the bed. Figure 6 shows a snapshot of distributions of suspended (lower panels) and bottom sediments (upper panels) with and without the seagrass bed at maximum flood. For the no seagrass case, suspended sediment concentration

increases shoreward with little alongshore variation, causing bottom sediments to decrease. This pattern again indicates the dominance of wave-induced erosion. Adding a 200-m wide seagrass bed induces both alongshore and crossshore variations of suspended and bottom sediment distributions, as can be seen in Fig. 6. Due to higher drag of the bed, tidal currents are forced to flow around it, resulting in a bulge of suspended sediments at the upstream offshore corner of the bed. A similar pattern is observed at the downstream offshore corner when tides change direction. In general, suspended sediment concentration within the bed is lower than that either onshore or offshore, but advection of suspended sediments by tidal currents can locally increase the concentration within the bed. As for bottom sediments, local scouring is evident at the corners of the bed on the nearshore side. The scouring could be due to enhanced tidal flow speed between the shoreline and the bed. We found no published field observations to support such scouring and suspect that this effect may be exaggerated by the wall boundary condition in the model. There are generally more bottom sediments within the bed than on either side, mostly near the upper and lower edges. The sediment trapping is due to import of higher suspended sediment concentration by tidal currents from outside, deposition of these sediments, and lower wave-induced erosion rates inside. Animating the model results confirms that sediment trapping appears to occur at the upstream edge on each half tidal cycle, when tidal currents are advecting higher suspended sediment concentrations from outside into the seagrass bed.

4. Discussion

4.1. Estimating bulk drag of seagrass on waves

Several general statements can be made from the results of the model scenarios with a flat bottom (Figs. 2–3). Larger seagrass bed width in the direction of wave propagation results in higher wave attenuation (indicated by percentage of energy flux reduction) and less energy on the shoreline. The total force acting on the bottom (indicated by percentage of bottom stress reduction) in the whole domain decreases as the seagrass bed is moved offshore. Relative wave attenuation and bottom stress reduction increase with incoming wave height.

These statements are generally valid as long as there is a significant interaction between wave orbital velocity and the seagrass canopy. This qualification may be interpreted as a generalization of suggestions by Ward et al. (1984), Fonseca and Cahalan (1992), and Koch (2001). They pointed out that wave attenuation should be higher when seagrass occupies a large portion of the water column. For the flat bottom cases, seagrass canopy occupied the entire water column (June case), and the decay of orbital velocity is negligible (at 1 m depth, 4 s waves are close to shallow water waves). In the sloping bottom case 1-m seagrass canopy only occupied part of the water column in the deepest region (2.5 m), and orbital velocity decayed at least 25%. This is why the differences in wave height (Fig. 4) between no seagrass and full crossshore width cases are relatively small at the deepest region but increasing toward shallower regions. Although a flume study (Fonseca and Cahalan 1992) and field observation (Koch 1996) indirectly support this hypothesis, wave attenuation has also been observed when seagrass only occupies a small portion of the water column (Granata et al. 2001 observations at a depth of 15 m). Systematic observations on the

effects of seagrass bed geometry on waves with different wave heights and periods are needed to verify the model predictions and to better understand the processes.

Wave attenuation by seagrass may have implications for shoreline protection. A few authors have postulated that seagrass beds could reduce the energy that reaches shorelines, and potentially protect shorelines from being eroded (van Katwijk and Hermus 2000). Using the observed seagrass parameters of June, our model results show significant reductions of wave energy flux at the shoreline in both the flat and sloping bottom scenarios (Figs. 2 and 4). Seagrass presence varies spatially, seasonally, and interannually in temperate environments, whereas shoreline erosion is usually associated with wave events that occur episodically (Wilcock et al. 1998) over annual or decadal time scales (Kamphuis 1987). Timing between wave events and seagrass growth probably influences the potential for seagrass beds to protect shorelines. Without knowing this timing, it is difficult to evaluate the net influence of seagrass on shoreline protection based on the results presented here. Other factors such as spectral or directional distributions of wave energy may need to be considered in order to better address this question. REF/DIF is capable of modeling spectral wave forcing as well as multiple wave incident angles (Kirby and Tuba Ozkan 1994) and will be addressed in the future.

4.2. Sediment dynamics

Model results presented in this paper have two main implications for sediment dynamics. Sedimentary processes are altered within the seagrass bed and probably behind it. Results from scenario 3 (Fig. 3) show that, in wave-dominated

environments, the total force acting on bottom sediments decreases as the seagrass bed is moved offshore due to increases in the affected area behind the bed. This suggests that seagrass beds may stabilize bottom sediments in the zone between the bed and shoreline, which is consistent with Hine et al. (1987)'s observation that disappearance of a seagrass community allowed rapid onshore and alongshore sand transport in the nearshore zone. Comparison between cases without and with a 200-m wide bed (Fig. 5) shows lower skin friction shear stress, lower erosion rate, and higher level of bottom sediments at locations within and behind the bed. Within the bed, our result is consistent with Lopez and Garcia (1998)'s findings of reduced shear stress and consequently lower suspended sediment transport (partly due to lower suspended sediment concentration) in the vegetated area. Reduced erosion rate as well as bottom sediment retention are also supported by field observations (Gacia and Duarte 2001). Gacia and Duarte found that the presence of *Posidonia oceanica* enhances sediment stability by preventing resuspension. Quantitative evidence does not exist to support the model-predicted reduction in skin friction shear stress and erosion and sediment retention between the bed and shoreline. Further studies are required for verification.

The second implication of our results for sediment dynamics stems from the 3-dimensional nature of our modeling approach: sediment trapping in the seagrass bed requires horizontal transport of suspended sediment from outside of the bed into the bed. The concept of the seagrass bed as a depositional environment has been suggested by several authors (e.g., Grady 1981; Ward et al. 1984; Almasi et al. 1987), and the proposed mechanism for this accumulation may be summarized as reduced

shear stress due to loss of momentum in a seagrass bed leading to reduction in resuspension and increased sediment accumulation (Koch et al. 2006). This connection between lower momentum and reduced resuspension (lower erosion rate) is supported by our results. Our results also suggest that linkages from reduced resuspension to increased accumulation are not trivial and may not occur everywhere within the bed. Sediment accumulation at one location could occur when the suspended sediment concentration is high enough that the deposition rate exceeds the erosion rate. Sediment accumulation at the upper and lower edges of the bed in Fig. 6 illustrates this point. At these two edges, accumulation occurs when high concentrations of suspended sediments from outside are transported into the bed where reduced shear stresses allow deposition. The amount of accumulated sediments then gradually decreases with distance into the bed until the sediment source from outside is used up. Further into the bed, original sediments remain but there is no new accumulation. In short, the model results clearly demonstrate that sediment accumulation requires both sediment sources (outside the bed here) and a transport mechanism (tidal current here), both of which may vary spatially within the bed. The reduction in suspended sediment transport capacity (concentration multiplied by streamwise velocity) in a vegetated area reported by Lopez and Garcia (1998) indirectly supports accumulation at the bed edge. Direct observations on spatial patterns of accumulation within seagrass beds are few, and most of them focus on sediment grain size distributions (e.g., Scoffin 1970; Wanless 1981; Granata et al. 2001). It should be noted that the spatial distribution of bottom sediment presented here may not match field observations precisely because the model does not account

for limited supplies of surficial sediments and mixed sediment grain sizes. More observations that resolve spatial patterns of erosion and deposition are needed to enhance our understanding of the interactions between seagrass, sediment, and the physics of nearshore environments.

Acknowledgements

This research was supported in part under award (NA16RG2207/SA07-5-28051S) from Maryland Sea Grant, National Oceanic and Atmospheric Administration, U.S. Department of Commerce, by Cooperative Institute for Coastal and Estuarine Environmental Technology - CICEET (Grant No. W912HZ-05-C-0033), and by the U.S. Army Corps of Engineers (Contract No. 00-366). The statements, findings, conclusions, and recommendations are those of the authors and do not necessarily reflect the views of Maryland Sea Grant, the National Oceanic and Atmospheric Administration or U.S. Department of Commerce. S. N. Chen was partially supported by a graduate fellowship from Horn Point Laboratory. We would like to thank Dr. James T. Kirby who made the Nearshore Community Model available to us. This is UMCES publication no. 4077.

References

Abdelrhman, M. A. 2003. Effects of eelgrass Zostera marina canopies on flow and transport. *Marine Ecological Progress Seriess*, **248**, 67-83.

Ackerman, J. D. and A. Okubo. 1993. Reduced mixing in a marine macrophyte canopy. *Functional Ecology*, **7**, 305-309.

Almasi, M. N., C. M. Hoskin, J. K. Reed, and J. Milo. 1987. Effects of natural and artificial *Thalassia testudinum* on rates of sedimentation. *Journal of Sedimentary Petrology*, **57**, 901-906.

Bokaian, A. and F. Geoola. 1984. Wake-induced galloping of two interfering circular cylinders. *Journal of Fluid Mechanics*, **146**, 383-415.

Clarke, S. and A. J. Elliott. 1998. Modelling suspended sediment concentration in the firth of forth. *Estuarine Coastal And Shelf Science*, **47**, 235-250.

Dean, R. G. and R. A. Dalrymple. 1991. Water wave mechanics for engineers and scientists. World Scientific.

Fonseca, M. S., J. S. Fisher, J. C. Zieman, and G. W. Thayer. 1982. Influence of the seagrass, *Zostera marina*, on current flow. *Estuarine Coastal and Shelf Science*, **15**, 351-364.

Fonseca, M. S. and J. S. Fisher. 1986. A comparison of canopy friction and sediment movement between four species of seagrass with reference to their ecology and restoration. *Marine Ecology Progress Series*, **29**, 15-22.

Fonseca, M. S. and J. A. Cahalan. 1992. A preliminary evaluation of wave attenuation for four species of seagrass. *Estuarine, Coastal and Shelf Science*, **35**, 565-576.

Gacia, E., T. C. Granata, and C. M. Duarte. 1999. An approach to the measurement of particle flux and sediment retention within seagrass (*Posidonia oceanica*) meadows. *Aquatic Botany*, **65**, 255-268.

Gacia, E. and C. M. Duarte. 2001. Sediment retention by a Mediterranean *Posidonia oceanica* meadow: the balance between deposition and resuspension. *Estuarine, Coastal and Shelf Science*, **52**, 505-514.

Gambi, M. C., A. R. M. Nowell, and P. A. Jumar. 1990. Flume observations on flow dynamics in *Zostera marina* (eelgrass) beds. *Marine Ecology Progress Series*, **61**, 159-169.

Grant, W. D. and O. S. Madsen. 1979. Combined wave and current interaction with a rough bottom. *Journal of Geophysical Research-Oceans and Atmospheres*, **84**, 1797-1808.

Ghisalberti, M. and H. M. Nepf. 2002. Mixing layers and coherent structures in vegetated aquatic flows. *Journal of Geophysical Research*, **107**, 1-11.

Ghisalberti, M. and H. M. Nepf. 2004. The limited growth of vegetated shear layers. Water Resources Research, **40**, W07502.

Grady, J. R., 1981. Properties of seagrass and sand flat sediments from the intertidal zone of St. Andrew Bay, Florida. *Estuaries*, **4**, 335-344.

Granata, T. C., T. Serra, J. Colomer, X. Casamitjana, C. M. Duarte, and E. Gacia. 2001. Flow and particle distributions in a nearshore meadow before and after a storm. *Marine Ecology Progress Series*, **218**, 95-106.

Hine, A. C., M. W. Evans, R. A. Davis, and D. Belknap. 1987. Depositional response to seagrass mortality along a low-energy, barrier island coast: West-Central Florida. *Journal of Sedimentary Petrology*, **57**, 431-439.

Kamphuis, J. W. 1987. Recession rate of glacial till bluffs. *Journal of Waterway Port Coastal and Ocean Engineering-ASCE*, **13**, 60-73.

Kirby, J. T., R. A. Dalrymple, and F. Shi. 2005. Combined refraction/diffraction model, REF/DIF 1, Version 3.0, Documentation and User's Manual, Research Report, Center for Applied Coastal Research. University of Delaware, Newark.

Kirby, J. T. and H. Tuba Ozkan. 1994. Combined refraction/diffraction model for spectral wave conditions, REF/DIF S, Version 1.1, Documentation and User's Manual, Research Report, Center for Applied Coastal Research. University of Delaware, Newark.

Kobayashi, N., A. W. Raichle, and T. Asano. 1993. Wave attenuation by vegetation. *Journal of Waterway Port Coastal and Ocean Engineering-ASCE*, **119**, 30-48.

Koch, E. W. 1993. Hydrodynamics of flow through seagrass canopies. Ph.D Dissertation, University of South Florida, St. Petersburg, USA.

Koch, E. W. 1996. Hydrodynamics of a shallow *Thalassia testudinum* bed in Florida, USA, p. 105-110. *In* J. Kuo, R. C. Phillips, D. I. Walker, and H. Kirkman (eds.), Seagrass Biology – Proceedings of an International Workshop, Western Australia Museum, Perth, Australia.

Koch, E. W. 2001. Beyond light: Physical, geological and geochemical parameters as possible submersed aquatic vegetation habitat requirements. *Estuaries*, **24**, 1-17.

Koch, E. W., J. D. Ackerman, and J. Verduin. 2006. Fluid dynamics in seagrass ecology: from molecules to ecosystems, p. 193-225 *In* A. W. D. Larkum, R. J. Orth, and C. M. Duarte (eds.), Seagrasses: Biology, Ecology and Conservation. Springer Verlag.

Kundu, P. K. and I. M. Cohen. 2002. Fluid Mechanics, 2nd edition, Academic Press, San Diego.

Leonard, B. P. 1979. Stable and accurate convective modeling procedure based on quadratic upstream interpolation. *Computer Methods in Applied Mechanics and Engineering*, **19**, 59-98.

Lopez, F. and M. Garcia. 1998. Open-channel flow through simulated vegetation: suspended sediment transport modeling. *Water Resources Research*, **34**, 2341-2352.

Mendez, F. J. and I. J. Losada. 2004. An empirical model to estimate the propagation of random breaking and nonbreaking waves over vegetation fields. *Coastal Engineering*, **51**, 103-118.

Mendez, F. J., I. J. Losada, and M. A. Losada. 1999. Hydrodynamics induced by wind waves in a vegetation field. *Journal of Geophysical Research-Oceans*, **104**, 18383-18396.

Nepf, H. M. 1999. Drag, turbulence and diffusion in flow through emergent vegetation. *Water Resources Research*, **35**, 479-489.

Nepf, H. M. and E. R. Vivoni. 2000. Flow structure in depth-limted, vegetated flow. Journal of Geophysical Research, **105**, 28,547-28,557.

Newell, R. I. E. and E. W. Koch. 2004. Modeling seagrass density and distribution in response to changes in turbidity stemming from bivalve filtration and seagrass sediment stabilization. *Estuaries*, **27**, 793-806.

North, E. W., S. Y. Chao, L. P. Sanford, and R. R. Hood. 2004. The influence of wind and river pulses on an estuarine turbidity maximum: numerical studies and field observations in Chesapeake Bay. *Estuaries*, **27**, 132-146.

Ota, T., N. Kobayashi, and J. T. Kirby. 2004. Wave and current interactions with vegetation. Proceedings of 29th International Conference on Coastal Engineering, Lisbon, September, pp. 508-520.

Peterson, C. H., R. A. Luettich Jr, F. Michelli, and G. A. Skilleter. 2004. Attenuation of water flow inside seagrass canopies of differing structure. *Marine Ecology Progress Series*, **268**, 81-92.

Rybicki, N. B., H. L. Jenter, V. Carter, R. A. Baltzer, and M. Turtora. 1997. Observations of tidal flux between a submersed aquatic plant stand and the adjacent channel in the Potomac River near Washington, DC. *Limnology and Oceanography*, **42**, 307-317.

Sanford, L. P., S. E. Suttles, and J. P. Halka. 2001. Reconsidering the physics of the Chesapeake Bay estuarine turbidity maximum. *Estuaries*, **24**, 655-669.

Scoffin, T. P. 1970. The trapping and binding of subtidal carbonate sediments by marine vegetation in Bimini Lagoon, Bahamas. *Journal of Sedimentary Petrology*, **40**, 249-273.

Shi, F., I. A. Svendsen, J. T. Kirby, and J. M. Smith. 2003. A curvilinear version of a Quasi-3D nearshore circulation model. *Coastal Engineering*, **49**, 99-124.

Shi, F., J. T. Kirby, and D. Hanes. 2006. An efficient semi-implicit scheme for a quasi-3D nearshore circulation model in generalized curvilinear coordinates, submitted to *Coastal Engineering*.

Svendsen, I.A., K. Haas, and Q. Zhao. 2000. Quasi-3D nearshore circulation model, SHORECIRC, Version 1.3.6, Documentation and User's Manual, Center for Applied Coastal Research. University of Delaware, Newark.

Teeter, A. M. 2001. Sediment resuspension and circulation of dredged material in Laguna Madre, Texas. Technical Report, U.S. Army Engineer Research and Development Center, Vicksburg, MS, U.S.A.

Teeter, A. M., B. H. Johnson, C. Berger, G. Stelling, N. W. Scheffner, M. H. Garcia, and T. M. Parchure. 2001. Hydrodynamic and sediment transport modeling with emphasis on shallow-water, vegetated areas (lakes, reservoirs, estuaries and lagoons). *Hydrobiologia*, **444**, 1-24.

U.S. Army Corps of Engineers, 2002. Coastal Engineering Manual. Engineer Manual 1110-2-1100, U.S. Army Corps of Engineers, Washington, D.C. (in 6 volumes).

van Katwijk, M. M. and D. C. R. Hermus. 2000. Effects of water dynamics on *Zostera marina*: transplantation experiments in the intertidal Dutch Wadden Sea. *Marine Ecology Progress Series*, **208**, 107-118.

Wanless, H. R. 1981. Fining upwards sedimentary sequences generated in seagrass beds. *Journal of Sedimentary Petrology*, **51**, 445-454.

Ward, L. G., W. M. Kemp, and W. E. Boynton. 1984. The influence of waves and seagrass communities on suspended particulates in an estuarine embayment. *Marine Geology*, **59**, 85-103.

Wigand, C., J. C. Stevenson, and J.C. Cornwell. 1997. Effects of different submersed macrophytes on sediment biogeochemistry. *Aquatic Botany*, **56**, 233-244.

Wilcock, P. R., D. S. Miller, R. H. Shea, and R. T. Kerkin. 1998. Frequency of effective wave activity and the recession of coastal bluffs: Calvert Cliffs, Maryland. *Journal Of Coastal Research*, **14**, 256-268.

Table 1. Linear fits (zero intercept) of unvegetated (x axis) versus vegetated (y axis) wave heights from field observations, for comparison to the calibrated model in May, June, and October, 2001.

	May		June		October	
	Slope	R^2	Slope	R^2	Slope	R^2
Observation	0.97	0.84	0.75	0.81	0.95	0.96
Model	0.95	—	0.88	—	0.92	—

Table 2. Model scenarios

Scenario	Bathymetry	Cross-shore Bed Width (m)	Along-shore Bed Length (m)	Position	Output Quantities
1	Flat (1 m)	0 to 700 (50m interval)	Full along-shore domain	Offshore edge of the bed fixed at the offshore boundary	% of wave energy flux reduction
2	Flat (1 m)	100	300 to full along-shore domain (300m interval)	Offshore edge of the bed fixed at the offshore boundary; Center of the bed fixed at the center of along-shore domain	Same as above
3	Flat (1 m)	100	Full along-shore domain	Center of the bed located 50 to 650 m from the offshore boundary (50m interval)	% of total bottom stress reduction
4	Sloping (2.5m offshore, 0.05m onshore)	0	0		Wave height and skin friction shear stress
		200	1800	Center of the bed located 550m from the offshore boundary	Same as above
		Full cross-shore domain	1800	Center of the bed located 360m from the offshore boundary	Same as above

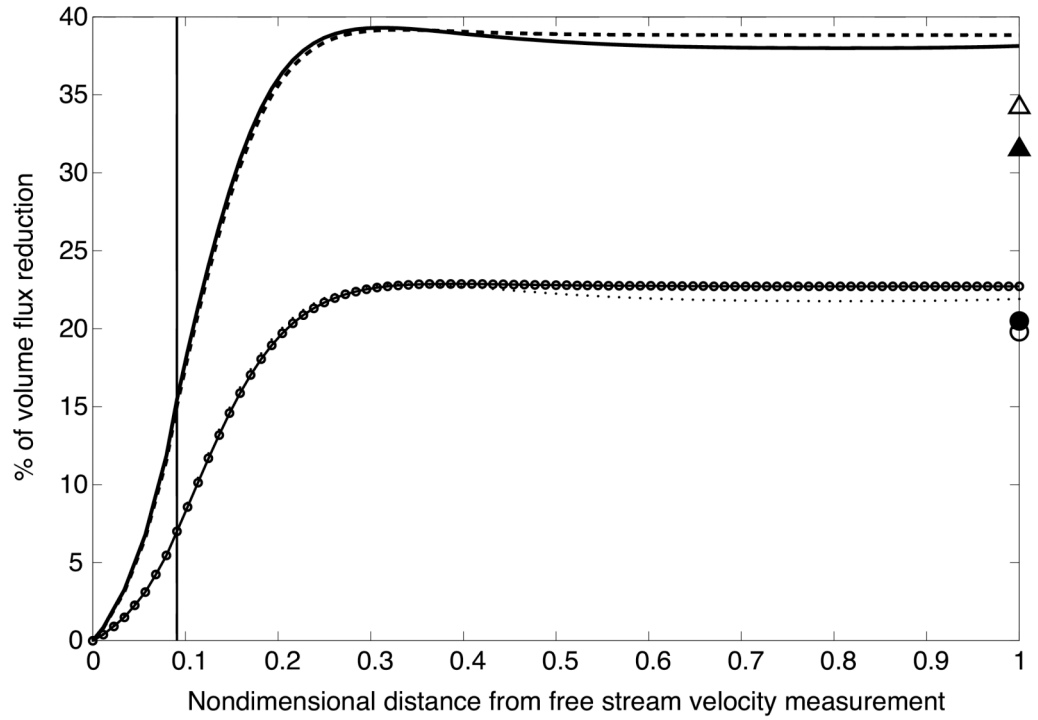

Fig. 1. Comparison of flow speed reduction in a seagrass bed between the model prediction (4 curves) and flume data (4 discrete points: 2 triangles and 2 circles) reported by Gambi et al. (1990). The percentage of volume flux reduction is used as an indicator of flow speed reduction and is plotted against the relative distance beyond (downstream of) the free-stream velocity measurements. Relative distance is normalized by the distance between the free-stream measurement and the end of the bed. The leading edge of the seagrass bed is indicated by the vertical line. The solid and dashed curves are model predictions for shoot density 1,200 m^{-2} with 10 and 20 cm s^{-1} free-stream velocity, respectively. The dotted and circle curves are model predictions for shoot density 600 m^{-2} with 10 and 20 cm s^{-1} free-stream velocity, respectively. The solid and open triangles represent Gambi et al.'s results for shoot density 1,200 m^{-2} with 10 and 20 cm s^{-1} free-stream velocities, respectively, whereas the solid and open circles are Gambi et al.'s results for 600 m22 with 10 and 20 cm s^{-1}.

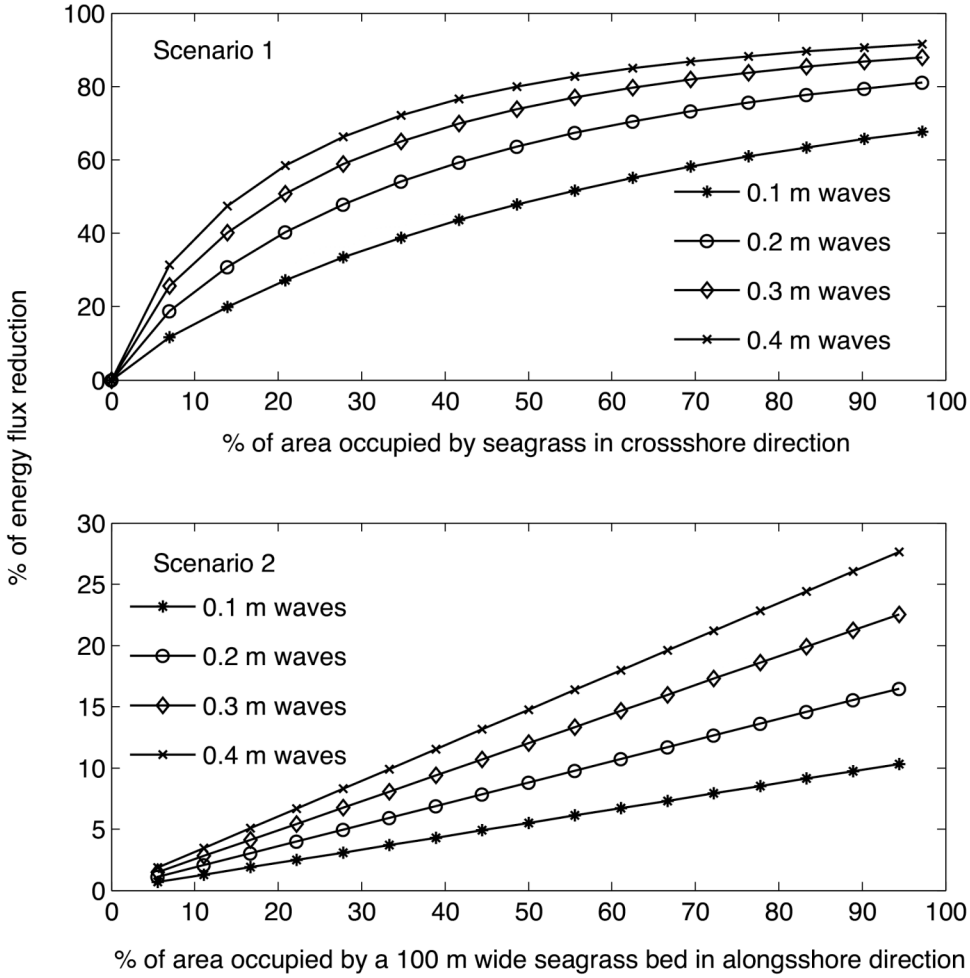

Fig. 2. Changes in wave energy flux reduction (indicator of wave attenuation) on the shoreline when the crossshore and alongshore seagrass bed width increases (see scenario 1 and 2 in Table 2 for details). Incident wave angles are zero degree (shorenormal direction). Seagrass parameters (shoot density and canopy height) in June were used.

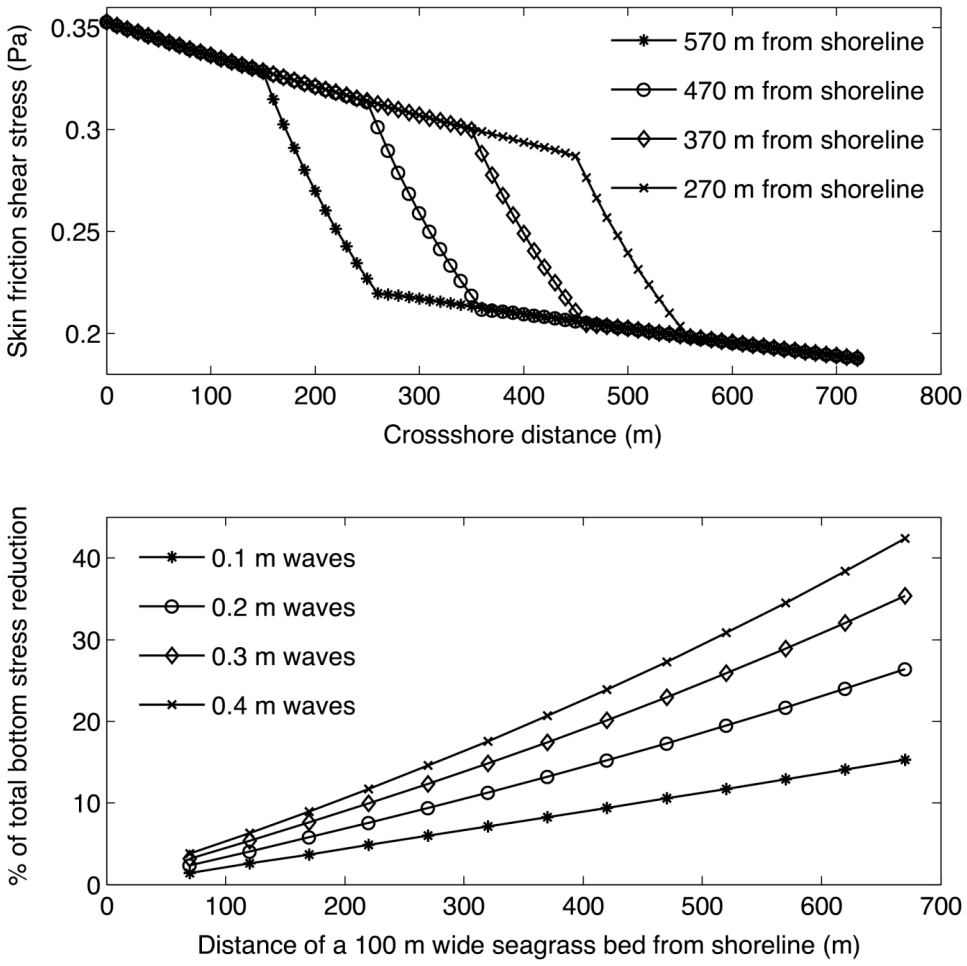

Fig. 3. Skin friction evolution when 0.2 m waves propagate along a central transect from the offshore boundary to shoreline (upper panel) and total bottom stress reduction (lower panel) when a seagrass bed is moved away from shoreline (scenario 3 in Table 2). Wave and seagrass parameters are the same as Fig. 2.

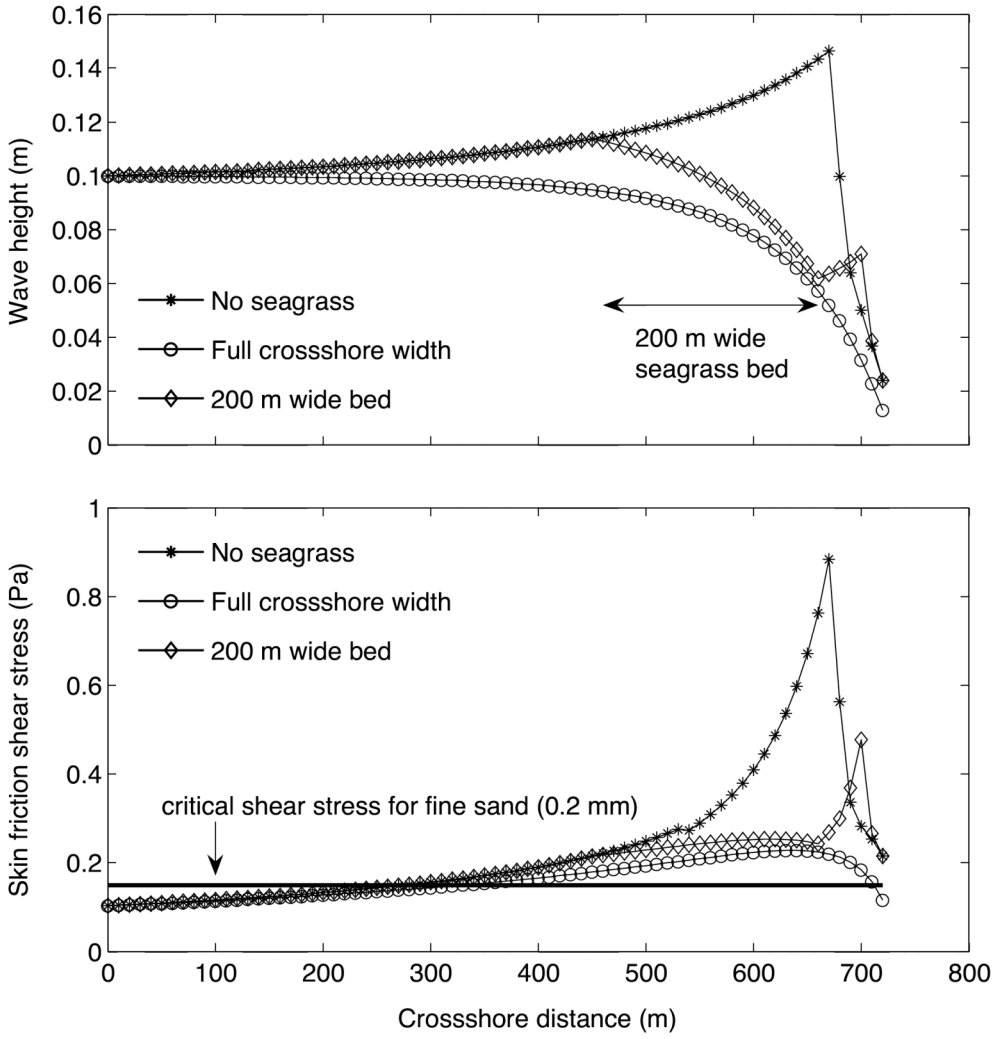

Fig. 4. Wave height evolution when waves propagate along a central transect from the offshore boundary to shoreline (upper panel) and the corresponding changes in skin friction shear stress (lower panel) under three seagrass bed configurations. See scenario 4 in Table 2 for details. Seagrass parameters in June were used.

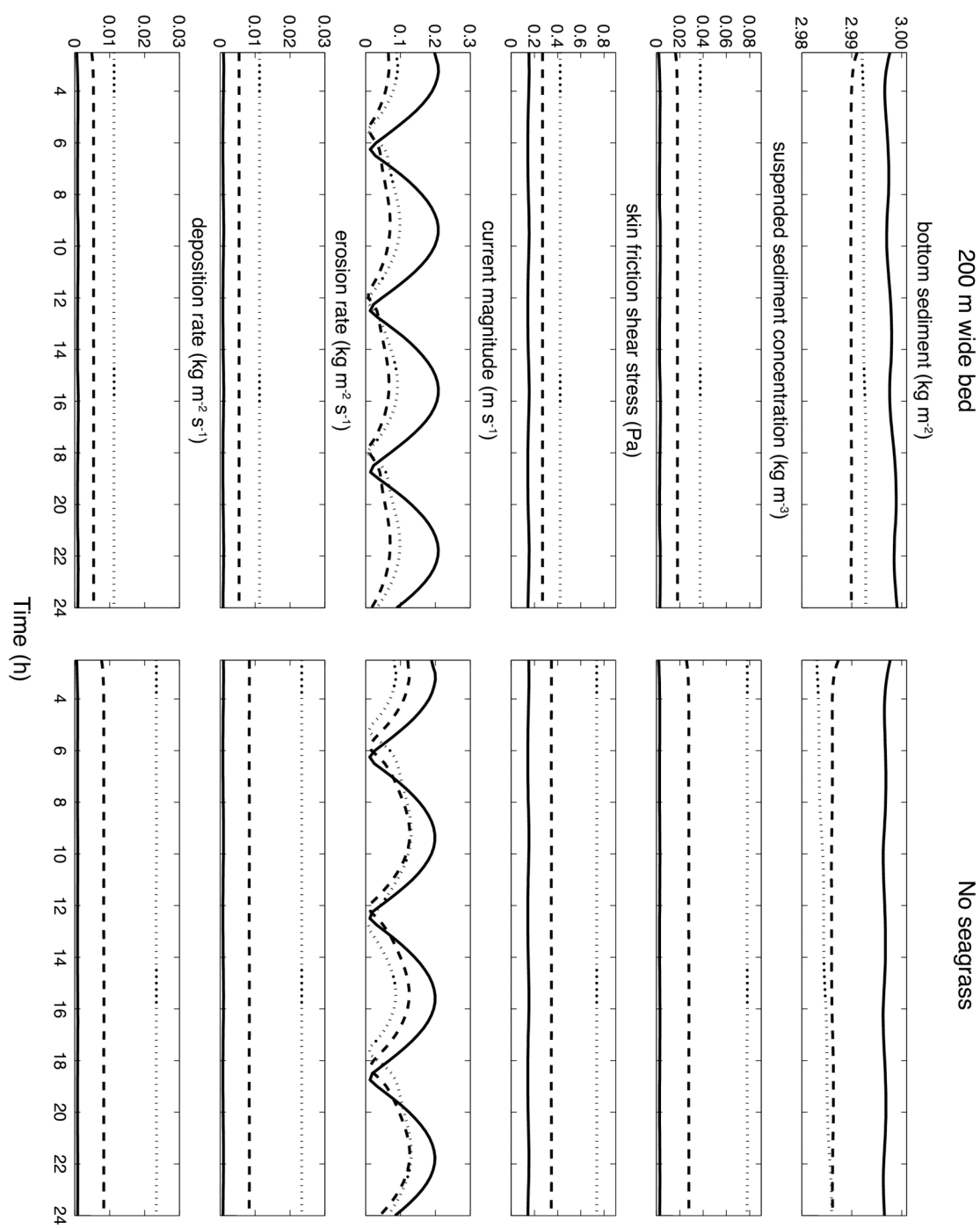

Fig. 5. Time series comparing a 200 m wide bed with a no seagrass case, as described in scenario 4. Predictions are from the central transect shown in Fig. 6. The solid line here represents the spatial average of each variable from the offshore boundary to the offshore edge of the bed (450 m from offshore boundary); the dashed line is the spatial average within the bed (from 450 to 650 m); the dotted line is the spatial average over the rest of the domain. Seagrass parameters in June were used.

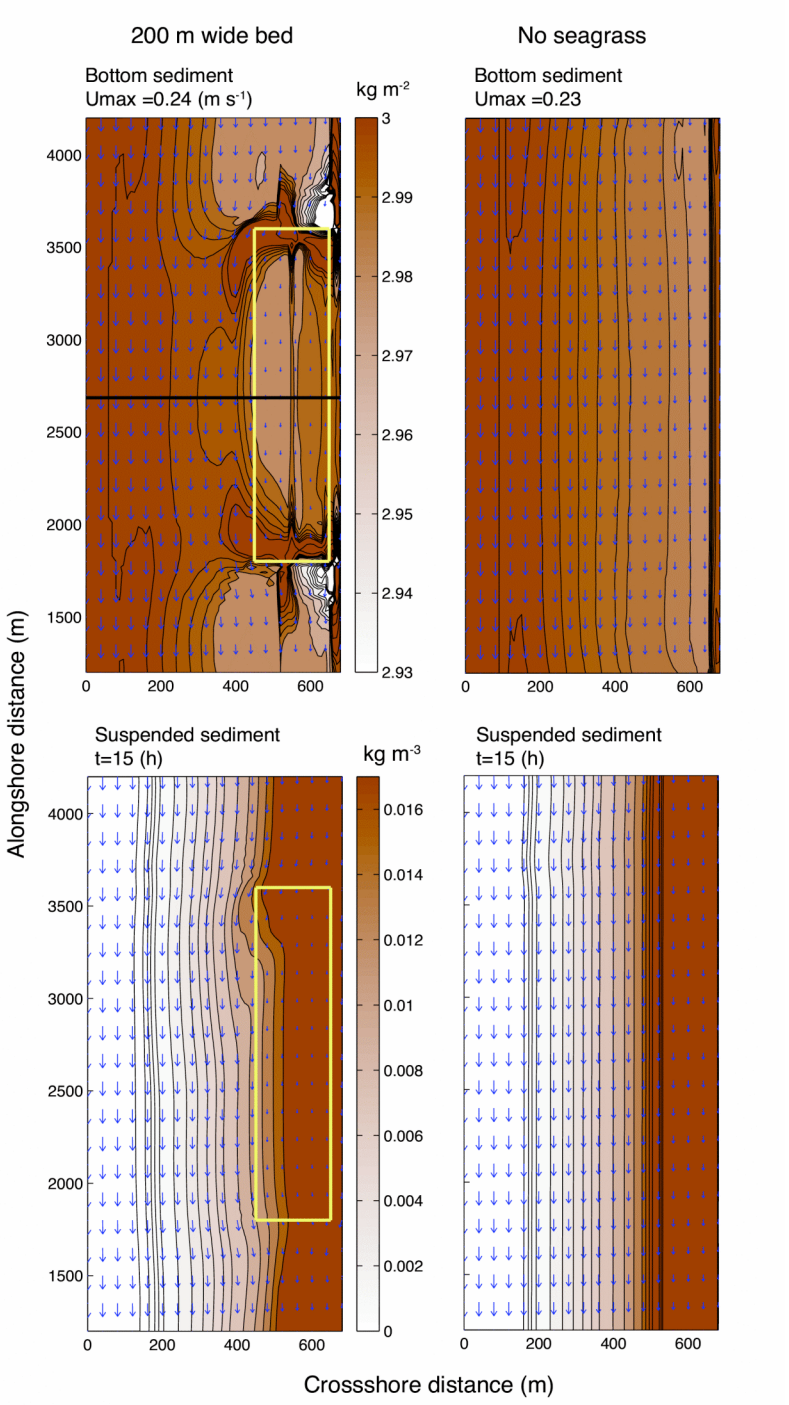

Fig. 6. Snapshot (top-view of model domain) of the distribution of bottom sediments (upper panels) and suspended sediment concentrations (bottom panels) comparing a 200 m wide bed with a no seagrass case. M2 tide is forced in the alongshore direction, while 0.1 m, 4 s waves propagate from offshore boundary with 10 degree incident angle (counter-clockwise from shore-normal direction). The current direction and magnitude are indicated by vectors, and bottom sediment and suspended sediment concentrations are shown in the contours. Seagrass parameters in June were used.

Chapter 6

Summary

A three-dimensional, hydrostatic, primitive equation numerical model (ROMS) has been used to investigate the lateral circulation and the associated transport of sediments in idealized partially mixed estuaries. The model simulates a straight estuarine channel with a triangular cross-section. The idealized setup is similar to that in Lerczak and Geyer 2004, but the turbulence closures are retained to better parameterize vertical mixing and for sensitivity tests. Tidal and axial wind forcings are considered. Attention is focused on lateral density (salinity) gradients, the major driving forces for lateral circulation. Lateral salinity gradients can result from boundary mixing on a sloping bottom and differential advection of axial salinity gradients.

When considering tidal forcing only, the numerical experiments suggest that boundary mixing on a sloping bottom can drive a significant amount of lateral circulation when the water column is stratified. This mechanism has received little attention to date in the estuarine literature. Good agreement with an analytical solution and similar vertical structures of lateral flows to observations from the Hudson River estuary support the importance of the boundary mixing mechanism. Boundary mixing is at least as important as differential advection for the modeled scenarios, when the two mechanisms are evaluated using the salt balance equation. Sediments are eroded in the channel and preferentially deposited on the right slope (looking seaward), mainly due to the combination of high sediment concentration in the channel during flood with strong upslope transport toward the right slope (i.e. tidal pumping).

When axial wind forcing is included, both vertical stratification and axial salt transport show strong wind modulations. Two parameters are identified to govern the responses of stratification to wind forcing: the Wedderburn number (W) defined as the ratio of wind stress to axial baroclinic pressure gradient force, and the ratio of an entrainment depth set by a Richardson number criteria to total water depth (h_0/H). The Wedderburn number controls the effectiveness of wind-induced horizontal buoyancy flux (wind straining) which favors increases/decreases in stratification during down/up-estuary wind. h_0/H determines the portion of the water column affected by direct wind mixing. While stratification is always reduced by up-estuary winds, stratification shows an increase-to-decrease transition as down-estuary wind stress increases. Such transition is a result of the competition between wind straining and mixing. A horizontal Richardson number modified to include wind straining/mixing is shown to reasonably represent the regime transition, and a regime diagram is proposed to classify wind's role on stratification. Mechanisms driving axial salt fluxes during axial wind events are also explored. At the onset and end of the wind events, barotropic adjustment drives strong transient salt fluxes. Net salt flux is controlled by the responses of subtidal shear dispersion to wind forcing. Moderate down-estuary winds enhance subtidal shear dispersion, whereas up-estuary winds always reduce it. Supporting observations from upper Chesapeake Bay are presented.

Wind modulations of stratification and axial salt transport exert important controls on lateral circulation. When the water column mixes vertically, Ekman transport due to axial winds is not a significant contributor to lateral circulation. Instead, the wind-induced, differential advection of axial salinity gradients (i.e.

laterally varying axial salt transport) is responsible for controlling lateral salinity gradients that in turn drive bottom-divergent/-convergent lateral circulation during down-/up-estuary winds. The wind-induced and tidally-induced lateral shears interact to drive the variability of lateral flow. A Hansen-Rattray-like scaling is derived and shows good predictive skills for the variations in lateral flow. Lateral sediment flux and the event-integrated sediment transport are from channel to shoals during down-estuary winds but reversed for up-estuary winds. The potential impacts of wind-generated waves on lateral sediment transport are evaluated with two cases representing typical event conditions in Chesapeake Bay. Accounting for wind-wave effects results in an order-of-magnitude increase in lateral sediment fluxes.

Nearshore processes (depths within 2m) neglected in the model described above (chapters 2-4) are explored separately using a coupled wave-circulation-sediment nearshore model (NearCoM). Attention is focused on how seagrass beds commonly found in shallow estuarine waters affect suspended sediment transport. Seagrass drag on waves and current is parameterized as a function of shoot density and shoot height. Without seagrass beds, wind-wave events greatly enhance sediment resuspension, providing a large sediment source for lateral sediment transport. Seagrass beds attenuate wind-wave energy, thus reducing bottom stress and erosion rate not only within the bed but also in the region between bed and shoreline. Higher bottom sediment accumulations are found within the bed. Spatial patterns of accumulations suggest that effective sediment trapping requires suspended sediment sources outside of the bed and horizontal transport into the bed.

6.1. Future work

This dissertation documents two mechanisms that can be important in driving lateral circulation but have been overlooked in the estuarine literature. One is boundary mixing on a sloping bottom, and the other is wind-induced, differential advection of axial salinity gradients. While these two mechanisms are robust in the simulated partially mixed estuaries, their validity and importance need to be verified in the field. Cross-channel arrays of moored current and temperature-conductivity profilers and/or high resolution, cross-channel shipboard surveys are in need to resolve these mechanisms (e.g. Lerczak et al. 2006; Fugate et al. 2007). Perhaps more importantly, we need synthesis efforts to explore how different mechanisms compete to drive lateral circulation under different conditions. Degree of stratification, although it is a dependent variable, appears to be critical in separating boundary mixing and differential advection.

The proposed regime diagram to classify wind's role on stratification through the interactions between straining and direct mixing requires further examinations as well. One component neglected in this picture is the variations in tidal mixing. In the study by Scully et al. (2005) which motivates the numerical experiments in Chapter 3, both spring-neap and wind-straining-induced variations in stratification can be seen. Questions such as whether the tendency toward increasing stratification by down-estuary winds can overcome strong mixing during spring tides remain unanswered and are subjects for future research. Another obvious extension of this work is to include the effects of cross-channel winds. Cross-channel winds can directly drive lateral circulation, and the resulting vertically sheared lateral flow can potentially

strain the salinity field to affect stratification. Moreover, cross-channel winds induced by summer time sea breeze and the concurrent wind-generated waves have been documented to significantly impact the temporal variations of suspended sediment concentration in South San Francisco Bay (Schoellhamer 1996). Can the wind-wave-forced resuspension and lateral circulation forced by cross-channel winds transport significant amount of sediments across estuaries? The roles of cross-channel as well as axial winds on lateral dynamics are still largely uncertain.

As for lateral sediment dynamics, while our goals are to elucidate transport mechanisms and to capture leading order patterns, the sediment transport component in this work with single grain size and unlimited supply is apparently a simplification. Processes such as mixed sediment bed, limited sediment supply, and bed consolidation/armoring (Sanford 2008) are neglected, and all of them can potentially affect lateral sediment dynamics. For example, we demonstrate in Chapter 4 that the event-integrated sediment transport is from shoals to channel during up-estuary winds, largely following the direction of near bottom lateral flows. However, the initial responses of lateral sediment fluxes to up-estuary winds favors an opposite transport direction (i.e. day 128-129 in Fig. 10 (d)(e)(f) of Chapter 4). If bottom sediment supply is limited, sediments may be depleted after the initial response, thus leading to a net channel-to-shoal transport. In addition, we show that accounting for wind-waves results in an order-of-magnitude increase in lateral sediment flux. This calculation does not include gravity-driven, downslope sediment transport. Recent observations on a New Zealand shelf provided new evidences that suspended sediment concentration of 2-4 kg m^{-3} ($O(0.1)$ of typical fluid mud) with a shelf slope

of 10m decent over 1km horizontal distance can contribute significantly to cross-shelf sediment transport (Ma et al. 2008; Wright and Friedrichs 2006). These reported values are of similar magnitudes to the predicted suspended sediment concentration in our model (~1 kg m-3) and bottom slope (10m/1.4km). To properly account for gravity-driven sediment transport, influences of sediment concentration on fluid density need to be included. More fundamentally, the importance of gravity-driven lateral sediment transport in estuaries requires further investigations.

Lastly, as demonstrated in Chapter 5, nearshore sediment resuspension due to wave and tidal forcing with/without the presence of seagrass is highly variable. Investigating whether this nearshore environment serves as a source or sink for suspended sediment in deeper offshore waters would require modeling both environments simultaneously, which is not possible with the distinct modeling frameworks used in this dissertation. Therefore, a dynamically consistent modeling framework such as a direct coupling of ROMS and SWAN models with seagrass wave/current drag is required to further quantify exchanges between deeper waters and shallow shoals.

References

Fugate, D. C., C. T. Friedrichs, and L. P. Sanford, 2007: Lateral dynamics and associated transport of sediments in the upper reaches of a partially mixed estuary, Chesapeake Bay, USA. *Continental Shelf Research*, **27,** 679-698.

Lerczak, J. A. and W. R. Geyer, 2004: Modeling the lateral circulation in straight, stratified estuaries. *Journal of Physical Oceanography*, **34**.

Lerczak, J. A., W. R. Geyer, and R. J. Chant, 2006: Mechanisms driving the time-dependent salt flux in a partially stratified estuary. *Journal of Physical Oceanography*, **36,** 2296-2311.

Sanford, L. P., 2008: Modeling a dynamically varying mixed sediment bed with erosion, deposition, bioturbation, consolidation, and armoring. *Computer & Geosciences*, doi:10.1016/j.cageo.2008.02.011.

Schoellhamer, D. H., 1996: Factors affecting suspended-solids concentrations in South San Francisco Bay, California. *Journal of Geophysical Research*, **101,** 12087-12095.

Scully, M. E., C. T. Friedrichs, and J. M. Brubaker, 2005: Control of Estuarine Stratification and Mixing by Wind-induced Straining of the Estuarine Density Field. *Estuaries*, **28,** 321-326.

References

Abdelrhman, M. A. 2003. Effects of eelgrass Zostera marina canopies on flow and transport. *Marine Ecological Progress Seriess*, **248**, 67-83.

Ackerman, J. D. and A. Okubo. 1993. Reduced mixing in a marine macrophyte canopy. *Functional Ecology*, **7**, 305-309.

Almasi, M. N., C. M. Hoskin, J. K. Reed, and J. Milo. 1987. Effects of natural and artificial *Thalassia testudinum* on rates of sedimentation. *Journal of Sedimentary Petrology*, **57**, 901-906.

Blumberg, A. E. and D. M. Goodrich, 1990: Modeling of Wind-Induced Destratification in Chesapeake Bay. *Estuaries*, **13,** 236-249.

Bokaian, A. and F. Geoola. 1984. Wake-induced galloping of two interfering circular cylinders. *Journal of Fluid Mechanics*, **146**, 383-415.

Bowen, M. M. and W. R. Geyer, 2003: Salt transport and the time-dependent salt balance of a partially stratified estuary. *Journal of Geophysical Research*, **108,** 3158.

Burchard, H. and H. Baumert, 1998: The formation of estuarine turbidity maxima due to density effects in the salt wedge. A hydrodynamic process study. *Journal of Physical Oceanography*, **28,** 309-321.

Chant, R. J. and E. Wilson, 1997: Secondary circulation in a highly stratified estuary. *Journal of Geophysical Research*, **102,** 23207-23216.

Chen, S. N. and L. P. Sanford, 2008: Lateral circulation driven by boundary mixing and the associated transport of sediments in idealized partially-mixed estuaries. *Continental Shelf Research***,** doi:10.1016/j.csr.2008.01.001.

Chen, S. N. and L. P. Sanford: Axial wind effects on stratification and longitudinal salt transport in an idealized, partially mixed estuary. *Submitted to Journal of Physical Oceanography*.

Clarke, S. and A. J. Elliott. 1998. Modelling suspended sediment concentration in the firth of forth. *Estuarine Coastal And Shelf Science*, **47**, 235-250.

Cloern, J. E., 1991: Tidal stirring and phytoplankton bloom dynamics in an estuary. *Journal of Marine Research*, **49,** 203-221.

Colman, S. M., J. P. Halka, and C. H. Hobbs, 1992: Patterns and rates of sedimentation in the Chesapeake Bay during the Holocene Rise in sea level, 101-111 pp.

Csanady, G. T., 1973: Wind-induced barotropic motions in long lakes. *Journal of Physical Oceanography*, **3,** 429-438.

Dyer, K. R., 1997: *Estuaries: A Physical Introduction*. 2nd ed. John Wiley & Sons Ltd., 195 pp.

Dean, R. G. and R. A. Dalrymple, 1991: *Water Wave Mechanics for Engineers and Scientists*. World Scientific.

Fischer, H. B., 1972: Mass transport mechanisms in partially stratified estuaries. *Journal of Fluid Mechanics*, **53,** 671-687.

Fischer, H. B., E. J. List, R. C. Y. Koh, J. Imberger, and N. A. Brooks, 1979: *Mixing in inland and coastal waters*. Academic Press Inc.

Fonseca, M. S., J. S. Fisher, J. C. Zieman, and G. W. Thayer. 1982. Influence of the seagrass, *Zostera marina*, on current flow. *Estuarine Coastal and Shelf Science*, **15**, 351-364.

Fonseca, M. S. and J. S. Fisher. 1986. A comparison of canopy friction and sediment movement between four species of seagrass with reference to their ecology and restoration. *Marine Ecology Progress Series*, **29**, 15-22.

Fonseca, M. S. and J. A. Cahalan. 1992. A preliminary evaluation of wave attenuation for four species of seagrass. *Estuarine, Coastal and Shelf Science*, **35**, 565-576.

Fugate, D. C., C. T. Friedrichs, and L. P. Sanford, 2007: Lateral dynamics and associated transport of sediments in the upper reaches of a partially mixed estuary, Chesapeake Bay, USA. *Continental Shelf Research*, **27,** 679-698.

Gacia, E., T. C. Granata, and C. M. Duarte. 1999. An approach to the measurement of particle flux and sediment retention within seagrass (*Posidonia oceanica*) meadows. *Aquatic Botany*, **65**, 255-268.

Gacia, E. and C. M. Duarte. 2001. Sediment retention by a Mediterranean *Posidonia oceanica* meadow: the balance between deposition and resuspension. *Estuarine, Coastal and Shelf Science*, **52**, 505-514.

Gambi, M. C., A. R. M. Nowell, and P. A. Jumar. 1990. Flume observations on flow dynamics in *Zostera marina* (eelgrass) beds. *Marine Ecology Progress Series*, **61**, 159-169.

Garrett, C., P. MacCready, and P. B. Rhines, 1993: Boundary mixing and arrested Ekman layers: Rotating stratified flow near a sloping boundary. *Annual Review of Fluid Mechanics*, **25,** 291-323.

Geyer, W. R., 1993: The Importance of Suppression of Turbulence By Stratification On the Estuarine Turbidity Maximum. *Estuaries*, **16,** 113-125.

——, 1997: Influence of wind on dynamics and flushing of shallow estuaries. *Estuarine, Coastal, and Shelf Science*, **44,** 713-722.

Geyer, W. R., R. P. Signell, and G. C. Kineke, 1998: Lateral trapping of sediment in a partially mixed estuary. *Physics of Estuaries and Coastal Seas*, Balkema.

Geyer, W. R., J. H. Trowbridge, and M. M. Bowen, 2000: The dynamics of a partially mixed estuary. *Journal of Physical Oceanography*, **30,** 2035-2048.

Ghisalberti, M. and H. M. Nepf. 2002. Mixing layers and coherent structures in vegetated aquatic flows. *Journal of Geophysical Research*, **107**, 1-11.

Ghisalberti, M. and H. M. Nepf. 2004. The limited growth of vegetated shear layers. Water Resources Research, **40**, W07502.

Goda, Y., 2003: Revisiting Wilson's formulas for simplified wind-wave prediction. *Journal of Waterway, Port, Coastal and Ocean Engineering*, **129,** 93-95.

Goodrich, D. M., W. C. Boicourt, P. Hamilton, and D. W. Pritchard, 1987: Wind-Induced Destratification in Chesapeake Bay. *Journal of Physical Oceanography*, **17,** 2232-2240.

Grady, J. R., 1981. Properties of seagrass and sand flat sediments from the intertidal zone of St. Andrew Bay, Florida. *Estuaries*, **4**, 335-344.

Grant, W. D. and O. S. Madsen. 1979. Combined wave and current interaction with a rough bottom. *Journal of Geophysical Research-Oceans and Atmospheres*, **84**, 1797-1808.

Granata, T. C., T. Serra, J. Colomer, X. Casamitjana, C. M. Duarte, and E. Gacia. 2001. Flow and particle distributions in a nearshore meadow before and after a storm. *Marine Ecology Progress Series*, **218**, 95-106.

Haidvogel, D. B., H. G. Arango, K. Hedstrom, A. Beckmann, and P. Malanotte-Rizzoli, 2000: Model evaluation experiments in the North Atlantic basin: Simulations in nonlinear terrain-following coordinates. *Dynamics of Atmospheres and Oceans*, **32,** 239-281.

Hansen, D. V. and M. Rattray, 1965: Gravitational circulation in straits and estuaries. *Journal of Marine Research*, **23,** 104-122.

Hine, A. C., M. W. Evans, R. A. Davis, and D. Belknap. 1987. Depositional response to seagrass mortality along a low-energy, barrier island coast: West-Central Florida. *Journal of Sedimentary Petrology*, **57**, 431-439.

Hobbs, C. H., J. P. Halka, R. T. Kerhin, and M. J. Carron, 1992: Chesapeake Bay Sediment Budget. *Journal of Coastal Research*, **8,** 292-300.

Huijts, K. M. H., H. M. Schuttelaars, H. E. de Swart, and A. Valle-Levinson, 2006: Lateral entrapment of sediment in tidal estuaries: An idealized model study. *Journal of Geophysical Research*, **111,** C12016, doi:10.1029/2006JC003615.

Huijts, K. M. H., H. M. Schuttelaars, H. E. de Swart, and C. T. Friedrichs, 2008: Analytical study of the transverse distribution of along-channel and transverse residual flows in tidal estuaries. *Continental Shelf Research*, doi:10.1016/j.csr.2007.09.007

Hunkins, K., 1981: Salt dispersion in the Hudson estuary. *Journal of Physical Oceanography*, **11,** 729-738.

Huzzey, L. M. and J. M. Brubaker, 1988: The formation of longitudinal fronts in a coastal estuary. *Journal of Geophysical Research*, **93,** 1329-1334.

Ivey, G. N. and J. Imberger, 1991: On the nature of turbulence in a stratified fluid. Part I: The energetics of mixing. *Journal of Physical Oceanography*, **21,** 650-658.

Jones, W. P. and B. E. Launder, 1972: The prediction of laminarization with a two-equation model of turbulence. *International Journal of Heat and Mass Transfter*, **15,** 301-314.

Johnson, G. C. and D. R. Ohlsen, 1994: Frictionally modified rotating hydraulic channel exchange and ocean outflows. *Journal of Physical Oceanography*, **24,** 66-78.

Kato, H. and O. M. Phillips, 1969: On the penetration of a turbulent layer into a stratified fluid. *Journal of Fluid Mechanics*, **37,** 643-655.

Kalkwijk, J. P. T. and R. Booij, 1986: Adaptation of secondary flow in nearly-horizontal flow. *Journal of Hydraulic Engineering*, **24,** 19-37.

Kamphuis, J. W. 1987. Recession rate of glacial till bluffs. *Journal of Waterway Port Coastal and Ocean Engineering-ASCE*, **13**, 60-73.

Kasai, A., A. E. Hill, T. Fujiwara, and J. H. Simpson, 2000: Effect of the Earth's rotation on the circulation in regions of freshwater influence. *Journal of Geophysical Research*, **105,** 16961-16969.

Kemp, W. M., P. A. Sampou, J. Garber, J. Tuttle, and W. R. Boynton, 1992: Seasonal Depletion of Oxygen From Bottom Waters of Chesapeake Bay: Roles of

Benthic and Planktonic Respiration and Physical Exchange Processes. *Marine Ecology Progress Series*, **85,** 137-152.

Kerhin, R., J. Halka, D. V. Wells, E. L. Hennessee, P. J. Blakeslee, N. Zoltan, and R. H. Cuthbertson, 1988: The Surficial Sediments of Chesapeake Bay, Maryland: Physical Characteristics and Sediment Budget. Investigation Report 48, 43 pp.

Kirby, J. T., R. A. Dalrymple, and F. Shi. 2005. Combined refraction/diffraction model, REF/DIF 1, Version 3.0, Documentation and User's Manual, Research Report, Center for Applied Coastal Research. University of Delaware, Newark.

Kirby, J. T. and H. Tuba Ozkan. 1994. Combined refraction/diffraction model for spectral wave conditions, REF/DIF S, Version 1.1, Documentation and User's Manual, Research Report, Center for Applied Coastal Research. University of Delaware, Newark.

Kobayashi, N., A. W. Raichle, and T. Asano. 1993. Wave attenuation by vegetation. *Journal of Waterway Port Coastal and Ocean Engineering-ASCE*, **119**, 30-48.

Koch, E. W. 1993. Hydrodynamics of flow through seagrass canopies. Ph.D Dissertation, University of South Florida, St. Petersburg, USA.

Koch, E. W. 1996. Hydrodynamics of a shallow *Thalassia testudinum* bed in Florida, USA, p. 105-110. *In* J. Kuo, R. C. Phillips, D. I. Walker, and H. Kirkman (eds.), Seagrass Biology – Proceedings of an International Workshop, Western Australia Museum, Perth, Australia.

Koch, E. W. 2001. Beyond light: Physical, geological and geochemical parameters as possible submersed aquatic vegetation habitat requirements. *Estuaries*, **24**, 1-17.

Koch, E. W., J. D. Ackerman, and J. Verduin. 2006. Fluid dynamics in seagrass ecology: from molecules to ecosystems, p. 193-225 *In* A. W. D. Larkum, R. J. Orth, and C. M. Duarte (eds.), Seagrasses: Biology, Ecology and Conservation. Springer Verlag.

Kundu, P. K. and I. M. Cohen. 2002. Fluid Mechanics, 2nd edition, Academic Press, San Diego.

Lacy, J. R. and S. G. Monismith, 2001: Secondary currents in a curved, stratified, estuarine channel. *Journal of Geophysical Research*, **106,** 31283-31302.

Langland, M. and T. M. Cronin, 2003: A summary report of sediment processes in Chesapeake Bay and watershed. U. S. G. S. W. R. I. R. 03-4123, Ed.

Large, W. G. and S. Pond, 1981: Open ocean momentum flux measurements in moderate to strong winds. *Journal of Physical Oceanography*, **11,** 324-336.

Lentz, S. J. and J. H. Trowbridge, 1991: The bottom boundary layer over the northern California shelf. *Journal of Physical Oceanography*, **21,** 1186-1201.

Lentz, S. J., 2001: The influence of stratification on the wind-driven cross-shelf circulation over the North Carolina shelf. *Journal of Physical Oceanography*, **31,** 2749-2760.

Leonard, B. P. 1979. Stable and accurate convective modeling procedure based on quadratic upstream interpolation. *Computer Methods in Applied Mechanics and Engineering*, **19**, 59-98.

Lerczak, J. A. and W. R. Geyer, 2004: Modeling the lateral circulation in straight, stratified estuaries. *Journal of Physical Oceanography*, **34**.

Lerczak, J. A., W. R. Geyer, and R. J. Chant, 2006: Mechanisms driving the time-dependent salt flux in a partially stratified estuary. *Journal of Physical Oceanography*, **36,** 2296-2311.

Lewis, R. E. and J. O. Lewis, 1983: The principal factors contributing to the flux of salt in a narrow, partially stratified estuary. *Estuarine and Coastal Marine Science*, **16,** 599-626.

Li, C. and J. O'Donnell, 1997: Tidally driven residual circulation in shallow estuaries with lateral depth variation. *Journal of Geophysical Research*, **102,** 27915-27929.

Li, C. and A. Valle-Levinson, 1999: A two-dimensional analytic tidal model for a narrow estuary of arbitrary lateral depth variation: The intertidal motion. *Journal of Geophysical Research*, **104,** 23525-23543.

Li, M., L. J. Zhong, and W. C. Boicourt, 2005: Simulations of Chesapeake Bay estuary: Sensitivity to turbulence mixing parameterizations and comparison with observations. *Journal of Geophysical Research*, **110,** C12004.

Li, M., L. J. Zhong, W. C. Boicourt, S. L. Zhang, and D. L. Zhang, 2007: Hurricane-induced destratification and restratification in a partially-mixed estuary. *Journal of Marine Research*, **65,** 169-192.

Lin, W., L. P. Sanford, and S. E. Suttles, 2002: Wave measurement and modeling in Chesapeake Bay. *Continental Shelf Research*, **22,** 2673-2686.

Lopez, F. and M. Garcia. 1998. Open-channel flow through simulated vegetation: suspended sediment transport modeling. *Water Resources Research*, **34**, 2341-2352.

MacCready, P. and P. B. Rhines, 1993: Slippery bottom boundary layer on a slope. *Journal of Physical Oceanography*, **23,** 5-22.

MacCready, P., 1999: Estuarine adjustment to changes in river flow and tidal mixing. *Journal of Physical Oceanography*, **29,** 708-726.

Madsen, O. S., 1994: Spectral wave-current bottom boundary layer flows. *Proceedings 24th International Conference on Coastal Engineering, ASCE, Kobe*, **1,** 384-398.

Marchesiello, P., J. C. McWilliams, and A. Shchepetkin, 2001: Open boundary conditions for long-term integration of regional oceanic models. *Ocean Modeling*, **3,** 1-20.

Martin, W., P. MacCready, and R. Dewey, 2005: Boundary layer forcing of a semidiurnal cross-channel seiche. *Journal of Physical Oceanography*, **35,** 1518-1537.

Mendez, F. J. and I. J. Losada. 2004. An empirical model to estimate the propagation of random breaking and nonbreaking waves over vegetation fields. *Coastal Engineering*, **51**, 103-118.

Mendez, F. J., I. J. Losada, and M. A. Losada. 1999. Hydrodynamics induced by wind waves in a vegetation field. *Journal of Geophysical Research-Oceans*, **104**, 18383-18396.

Mied, R. P., R. A. Handler, and T. F. Donato, 2002: Regions of estuarine convergence at high Rossy number: A solution in estuaries with elliptical cross sections. *Journal of Geophysical Research*, **107**.

Monismith, S. G., 1986: An experimental study of the upwelling response of stratified reservoirs to surface shear stress. *Journal of Fluid Mechanics*, **171,** 407-439.

Monismith, S. G., W. Kimmerer, J. R. Burau, and M. T. Stacey, 2002: Structure and flow-induced variability of the subtidal salinity field in northern San Francisco Bay. *Journal of Physical Oceanography*, **32,** 3003-3019.

Nepf, H. M. 1999. Drag, turbulence and diffusion in flow through emergent vegetation. *Water Resources Research*, **35**, 479-489.

Nepf, H. M. and E. R. Vivoni. 2000. Flow structure in depth-limted, vegetated flow. Journal of Geophysical Research, **105**, 28,547-28,557.

Newell, R. I. E. and E. W. Koch. 2004. Modeling seagrass density and distribution in response to changes in turbidity stemming from bivalve filtration and seagrass sediment stabilization. *Estuaries*, **27**, 793-806.

North, E. W., S.-Y. Chao, L. P. Sanford, and R. R. Hood, 2004: The Influence of Wind and River Pulses on an Estuarine Turbidity Maximum: Numerical Studies and Field Observations. *Estuaries*, **27,** 132-146.

Nunes, R. A. and J. H. Simpson, 1985: Axial convergence in a well-mixed estuary. *Estuarine, Coastal, and Shelf Science*, **20,** 637-649.

Ota, T., N. Kobayashi, and J. T. Kirby. 2004. Wave and current interactions with vegetation. Proceedings of 29th International Conference on Coastal Engineering, Lisbon, September, pp. 508-520.

Ott, M. W. and C. Garrett, 2002: Frictional estuarine flow in Juan de Fuca Strait with implications for secondary circulation. *Journal of Geophysical Research*, **103,** 15657-15666.

Peterson, C. H., R. A. Luettich Jr, F. Michelli, and G. A. Skilleter. 2004. Attenuation of water flow inside seagrass canopies of differing structure. *Marine Ecology Progress Series*, **268**, 81-92.

Phillips, O. M., 1970: On flows induced by diffusion in a stably stratified fluid. *Deep Sea Research*, **17,** 435-443.

Phillips, O. M., J. Shyu, and H. Salmun, 1986: An experiment on boundary mixing: mean circulation and transport rates. *Journal of Fluid Mechanics*, **173,** 473-499.

Resio, D., S. Bratos, and E. Thompson, 2002: Meteorology and wave climate. USACE Coastal Engineering Manual.

Rybicki, N. B., H. L. Jenter, V. Carter, R. A. Baltzer, and M. Turtora. 1997. Observations of tidal flux between a submersed aquatic plant stand and the adjacent channel in the Potomac River near Washington, DC. *Limnology and Oceanography*, **42**, 307-317.

Sanay, R., 2003: Wind-induced exchange in semi-enclosed bains, Department of Ocean, Earth, and Atmospheric Sciences, Old Dominion University.

Sanay, R. and A. Valle-Levinson, 2005: Wind-induced circulation in semienclosed homogeneous, rotating basins. *Journal of Physical Oceanography*, **35,** 2520-2531.

Sanford, L. P., 1994: Wave-Forced Resuspension of Upper Chesapeake Bay Muds. *Estuaries*, **17,** 148-165.

Sanford, L. P. and J. P. Halka, 1993: Assessing the paradigm of mutually exclusive erosion and deposition of mud, with examples from upper Chesapeake Bay. *Marine Geology*, **114,** 37-57.

Sanford, L. P., 2008: Modeling a dynamically varying mixed sediment bed with erosion, deposition, bioturbation, consolidation, and armoring. *Computer & Geosciences*, doi:10.1016/j.cageo.2008.02.011.

Sanford, L. P., S. E. Suttles, and J. P. Halka. 2001. Reconsidering the physics of the Chesapeake Bay estuarine turbidity maximum. *Estuaries*, **24**, 655-669.

Schoellhamer, D. H., 1996: Factors affecting suspended-solids concentrations in South San Francisco Bay, California. *Journal of Geophysical Research*, **101,** 12087-12095.

Scoffin, T. P. 1970. The trapping and binding of subtidal carbonate sediments by marine vegetation in Bimini Lagoon, Bahamas. *Journal of Sedimentary Petrology*, **40**, 249-273.

Scully, M. E., C. T. Friedrichs, and J. M. Brubaker, 2005: Control of Estuarine Stratification and Mixing by Wind-induced Straining of the Estuarine Density Field. *Estuaries*, **28,** 321-326.

Sharples, J., J. H. Simpson, and J. M. Brubaker, 1994: Observations and modelling of periodic stratification in the Upper York River Estuary, Virginia. *Estuarine, Coastal, and Shelf Science*, **38,** 301-312.

Shi, F., I. A. Svendsen, J. T. Kirby, and J. M. Smith. 2003. A curvilinear version of a Quasi-3D nearshore circulation model. *Coastal Engineering*, **49**, 99-124.

Shi, F., J. T. Kirby, and D. Hanes. 2006. An efficient semi-implicit scheme for a quasi-3D nearshore circulation model in generalized curvilinear coordinates, submitted to *Coastal Engineering*.

Simpson, J. H., J. Brown, J. Matthews, and G. Allen, 1990: Tidal straining, density currents, and stirring in control of estuarine stratification. *Estuaries*, **13,** 125-132.

Smith, R., 1980: Bouyancy effects upon longitudinal dispersion in wide well-mixed estuaries. *Philosophical Transactions of the Royal Society of London. Series A, Mathematical and Physical Sciences*, **296,** 467-496.

Stacey, M. T., J. R. Burau, and S. G. Monismith, 2001: Creation of residual flows in a partially stratified estuary. *Journal of Geophysical Research*, **106,** 17,013-17,037.

Stanley, D. W. and S. W. Nixon, 1992: Stratification and bottom-water hypoxia in the Pamlico River estuary. *Estuaries*, **15,** 270-281.

Svendsen, I.A., K. Haas, and Q. Zhao. 2000. Quasi-3D nearshore circulation model, SHORECIRC, Version 1.3.6, Documentation and User's Manual, Center for Applied Coastal Research. University of Delaware, Newark.

Teeter, A. M. 2001. Sediment resuspension and circulation of dredged material in Laguna Madre, Texas. Technical Report, U.S. Army Engineer Research and Development Center, Vicksburg, MS, U.S.A.

Teeter, A. M., B. H. Johnson, C. Berger, G. Stelling, N. W. Scheffner, M. H. Garcia, and T. M. Parchure. 2001. Hydrodynamic and sediment transport modeling with emphasis on shallow-water, vegetated areas (lakes, reservoirs, estuaries and lagoons). *Hydrobiologia*, **444**, 1-24.

Trowbridge, J. H. and S. J. Lentz, 1991: Asymmetric behavior of an oceanic boundary layer above a sloping bottom. *Journal of Physical Oceanography*, **21,** 1171-1185.

Trowbridge, J. H., 1992: A simple description of the deepening and structure of a stably stratified flow driven by a surface stress. *Journal of Geophysical Research*, **97,** 15,529-15,543.

Tyler, M. A. and H. H. Seliger, 1978: Annual subsurface transport of red tide dinoflagellate to its bloom area - water circulation patterns and organism distribution in Chesapeake Bay. *Limnology and Oceanography*, **23,** 227-246.

U.S. Army Corps of Engineers, 2002. Coastal Engineering Manual. Engineer Manual 1110-2-1100, U.S. Army Corps of Engineers, Washington, D.C. (in 6 volumes).

Valle-Levinson, A., C. Li, K. C. Wong, and K. M. M. Lwiza, 2000: Convergence of lateral flow along a coastal plain estuary. *Journal of Geophysical Research*, **105,** 17045-17061.

Valle-Levinson, A., C. Reyes, and R. Sanay, 2003: Effects of bathymetry, friction, and rotation on estuary-ocean exchange. *Journal of Physical Oceanography*, **33,** 2375-2393.

van Katwijk, M. M. and D. C. R. Hermus. 2000. Effects of water dynamics on *Zostera marina*: transplantation experiments in the intertidal Dutch Wadden Sea. *Marine Ecology Progress Series*, **208**, 107-118.

Wang, D.-P., 1979: Wind-Driven Circulation in the Chesapeake Bay, Winter 1975. *Journal of Physical Oceanography*, **90,** 564-572.

Wanless, H. R. 1981. Fining upwards sedimentary sequences generated in seagrass beds. *Journal of Sedimentary Petrology*, **51**, 445-454.

Ward, L. G., W. M. Kemp, and W. E. Boynton. 1984. The influence of waves and seagrass communities on suspended particulates in an estuarine embayment. *Marine Geology*, **59**, 85-103.

Warner, J. C., W. R. Geyer, and J. A. Lerczak, 2005: Numerical modeling of an estuary: A comprehensive skill assessment. *Journal of Geophysical Research*, **110,** C05001 (1-13).

Warner, J. C., C. R. Sherwood, H. G. Arango, and R. P. Signell, 2005: Performance of four turbulence closure models implemented using a generic length scale method. *Ocean Modeling*, **8,** 81-113.

Weisberg, R. H., 1976: The nontidal flow in the Providence River of Narragansett Bay: A stochastic approach to estuarine circulation. *Journal of Physical Oceanography*, **6,** 721-734.

Weatherly, G. L. and P. J. Martin, 1978: On the structure and dynamics of the oceanic bottom boundary layer. *Journal of Physical Oceanography*, **8,** 557-570.

Wigand, C., J. C. Stevenson, and J.C. Cornwell. 1997. Effects of different submersed macrophytes on sediment biogeochemistry. *Aquatic Botany*, **56**, 233-244.

Wilcock, P. R., D. S. Miller, R. H. Shea, and R. T. Kerkin. 1998. Frequency of effective wave activity and the recession of coastal bluffs: Calvert Cliffs, Maryland. *Journal of Coastal Research*, **14**, 256-268.

Willmott, C. J., 1981: On the validation of models. *Physical Geography*, **2,** 184-194.

Winant, C. D., 2004: Three-dimensional wind-driven flow in an elongated, rotating basin. *Journal of Physical Oceanography*, **34,** 462-476.

Wong, K. C., 1994: On the nature of transverse variability in a coastal plain estuary. *Journal of Geophysical Research*, **99,** 14,209-14,222.

Wong, K. C. and J. E. Moses-Hall, 1998: The tidal and subtidal variations in the transverse salinity and current distributions across a coastal plain estuary. *Journal of Marine Research*, **56,** 489-517.

Woodruff, J. D., W. R. Geyer, C. K. Sommerfield, and N. W. Driscoll, 2001: Seasonal variation of sediment deposition in the Hudson River estuary. *Marine Geology*, **179,** 105-119.

Wunsch, C., 1970: On oceanic boundary mixing. *Deep Sea Research*, **17,** 293-301.

Zheng, L. and R. H. Weisberg, 2006: Tide, buoyancy, and wind-driven circulation of the Charlotte Harbor estuary: A model study. *Journal of Geophysical Research*, **109**.

Zhong, L. and M. Li, 2006: Tidal energy fluxes and dissipation in the Chesapeake Bay. *Continental Shelf Research*, **26,** 752-770.